Electro-mechanical analysis of thin-film substrate fuses using finite element methodology.

WILNIEWCZYC, Mariusz Pawel.

Sheffield Hallam University

Electro-Mechanical Analysis of Thin-Film Substrate Fuses Using Finite Element Methodology

Mariusz Paweł Wilniewczyc

A thesis submitted in partial fulfilment of the requirements of
Sheffield Hallam University
for the degree of Doctor of Philosophy.

Electronics Research Group
School of Engineering
Sheffield Hallam University
Sheffield, UK

July 1999

Collaborating Organisation:
General Electric Power Controls Ltd., Liverpool UK

Acknowledgements

I would like to express my deepest gratitude to General Electric Power Controls Ltd., Liverpool UK, and to General Electric Company plc, which preceded it, for sponsoring this project throughout its three-year duration, for providing test facilities and supplying fuse samples and experimental data to support this project. In particular I would like to thank Nick Allen, Józef Żugaj and Dave Crellin for their interest in the project and constant support.

I wish to express my heartfelt gratitude to Professor Peter M McEwan, who initiated and supervised this project, and without whose guidance, interest, constructive criticism and encouragement the successful completion of this project would not have been possible. I would also like to thank my second supervisors Prof. John Atkinson and Dr Upul Fernando for their advice and valuable discussions on stress analysis and fatigue. Thanks are also expressed to John Burgan, John Stanley and John Bradshaw for their technical support. Sincere thanks to my colleagues at the *Electronics Research Group* and to all my friends who helped make my stay in Sheffield enjoyable, especially to Hui.

The Author

The author received his Master's Degree in Electrical Engineering from the Department of Electrical Engineering of the Technical University of Gdańsk in September 1995. In October 1995 the author moved to Sheffield (UK) to undertake a one-year research scholarship at the School of Engineering Information Technology at Sheffield Hallam University, and in October 1996 the author embarked on the three-year Ph.D. research project, presented in this thesis.

The author's email address is m.p.wilniewczyc@iee.org

Declaration

I hereby declare that this thesis is entirely my own work, and has not been submitted in support of an application of another degree or qualification of this, or any other university, institute of learning or industrial organisation.

Mariusz Wilniewczyc

27 June, 1999.

Abstract

In this thesis the electro-thermo-mechanical behaviour and withstand performance of constricted high-breaking capacity thin/thick film substrate fuse elements is examined. Three-dimensional time-varying non-linear CAD finite element modelling and simulation techniques were used to investigate the current-carrying capacity of a variety of single-layer and multi-layer fuse geometries for DC and repetitive currents. The critical electro-thermally-induced stresses and strains were identified, and the techniques to achieve a reduction in the magnitude of these stresses & strains were investigated. Computational tools were developed to enable the prediction of the lifetime of thick-film substrate fuses subjected to cyclic-current loading conditions. The lifetime of a manufactured substrate fuse, subjected to a range of pulsed currents, was determined theoretically and correlated with the experimental findings. The onset of crack formation, conductive film de-bonding and lifting from the substrate and fatigue were studied computationally and experimentally. Photographic evidence of crack formation and propagation in the conductive film, film de-bonding from the substrate, metal dislocation and deformation in thin-thick film substrate fuse elements subjected to current pulses is presented.

List of Figures

①

List of Tables

Glossary of Abbreviations

Acronym	Description
3D	three dimensional
LE	linear elastic
FE	finite element
TTFSF	thin-thick film substrate fuses
SBF	substrate-bonded film
MBF	metal-bonded film
LMBF	lower metal-bonded film
UMBF	upper metal-bonded film
SMD	surface mount device
PCB	printed circuit board
CLF	conductive lithographic film
LCF/HCF	low/high cycle fatigue
BC(s)	boundary condition(s)
MFC	minimum fusing current
MSF	manufactured substrate fuse

ABAQUS output variable identifiers

EPOT	electrical potential
EPGM	magnitude of the electrical potential gradient vector
EPG*n*	component *n* of the electrical potential gradient vector ($n = 1, 2, 3$)
ECDM	magnitude of the electrical current density vector
ECD*n*	component *n* of the electrical current density vector ($n = 1, 2, 3$)
JENER	energy dissipated because of the flow of electrical current, per unit volume
HFLM	magnitude of the heat flux vector
HFL*n*	component *n* of the heat flux vector ($n = 1, 2, 3$)

NT11	temperature
Sij	ij-component of stress ($i \le j \le 3$)
MISES	MISES equivalent stress
TRESCA	TRESCA equivalent stress
PRESS	equivalent pressure stress
Eij	ij-component of strain ($i \le j \le 3$)
EEij	ij-component of elastic strain ($i \le j \le 3$)
PEij	ij-component of plastic strain ($i \le j \le 3$)
THEij	ij-component of thermal strain ($i \le j \le 3$)
Un	component n of the displacement vector ($n = 1, 2, 3$)

List of Principal Symbols

Symbol	Definition
δ	electrical conductivity
φ	electrical potential
q	heat flux
T	temperature
c	thermal capacity
K	thermal conductivity
h	coefficient of surface heat transfer (film coefficient)
u_i	i^{th} component of the displacement degree of freedom ($1 < i \leq 3$)
θ_i	i^{th} component of the rotational degree of freedom ($1 < i \leq 3$)
α	thermal expansion coefficient
E	modulus of elasticity
G	shear modulus
υ	Poisson's ratio
ε	direct strain
σ	direct stress
γ	shear strain
τ	shear stress
$\Delta\sigma/2$	stress amplitude
$\Delta\gamma/2$	shear strain amplitude
σ_m	mean stress
$2N_f$	number of cycles to fatigue failure
$2N_t$	transition fatigue life
f	frequency
t	time

ϕ	mark space ratio
σ_f'	fatigue strength coefficient
b	fatigue strength exponent
ε_f'	fatigue ductility coefficient
c	fatigue ductility exponent

Subscripts

el.	elastic
pl.	plastic
avg.	average
c-avg.	cycle average
c-min.	cycle minimum
c-max.	cycle maximum

Superscripts

st.	stabilised
m	mean

Table of Contents

Chapter 1.

Introduction

1.1. The Purpose of this Thesis.

In this thesis the electro-thermo-mechanical behaviour of constricted high-breaking capacity thin-thick film single and multi-layer substrate fuse elements was investigated. Methods to computationally predict the lifetime of thin-thick film substrate fuses subjected to intermittent current-carrying conditions were also devised.

The study embodied the following analyses of thick film current-carrying fuse elements:

- current distribution;
- temperature distribution;
- stress/strain/deformation distributions;
- lifetime prediction (fatigue analysis).

Previous studies on theoretical fuse lifetime prediction did not include substrate fuses. The work done so far involved the theoretical and experimental lifetime prediction for wire and strip fuse elements. For unconstricted geometries the simplified approach, wherein the strain is assumed to be proportional to the temperature rise, can be adopted. For the purpose of this study, wherein the thermal expansion of the fuse element is constrained by the substrate, full scale simulation techniques had to be used in order to accurately predict the stresses and strains. Consequently, three-dimensional time-varying non-linear CAD finite element modelling and simulation techniques were adopted. Experimental work was carried out to verify the theoretical lifetime predictions against the experimental results.

1.2. Contents of this Thesis

Chapter 2 provides a brief general background to fuses. It describes fuses for semiconductor protection in more detail and provides an overview of fatigue and fuse life-time prediction studies found in literature. Chapter 3 provides the theoretical background to all the stages adopted for this study, i.e. electro-thermal analysis, thermal stress analysis, and fatigue (lifetime prediction). Chapter 4 describes the results of the studies into the electro-thermo-mechanical behaviour of thin-thick film substrate fuse elements. Critical stress/strain components, their location and their effect on the fuse withstand performance were identified. Various substrate and film materials along with single and multi-layer film geometries were studied to determine the effect of varying the material properties and fuse element geometry on the magnitude of the stresses. Chapter 5 describes the work undertaken to construct a model capable of the prediction of the number of cycles to fatigue failure (fuse operation) for any shape of the intermittent current loading. Samples of a manufactured substrate fuse were tested experimentally to determine the fuse's withstand performance under pulsed current working conditions. The theoretical life-time predictions were validated against experimental results. The samples tested were subsequently examined using microscopy and scanning electron microscopy for evidence of fatigue deterioration.

Chapter 2.

Review of High Breaking Capacity Low Voltage Electric Fuses

This Chapter provides a brief background to electric fuses, with special reference to semiconductor protection fuses and, especially, thin-thick film substrate fuses (TTFSF). A summary of previous research on failure mechanisms in thin conductive films, fatigue, crack initiation and propagation, and fuse lifetime under cyclic-current loading is provided.

2.1. Electric Fuse Characteristics

The modern high breaking capacity (HBC) electric fuse is a small device used for short-circuit and current overload protection of electric circuits and their components. In its simplest form a fuse consists of a short piece of wire of cross-sectional area normally far smaller than the cross-sectional area of conductors in the protected circuit. When current exceeds a so called safe level the fuse wire melts, arcing is initiated and extinguished, following which the fuse is said to have 'blown', or operated. Where the fuse is correctly co-ordinated with the circuit parameters, the protected circuit is not damaged and, hence, only the fuse has to be replaced.

2.1.1. General Behaviour.

One of the main characteristics describing fuse behaviour is the time/current (I:t) characteristic. The I:t characteristic defines the time lag between the instant when the current increases above a certain minimum level, termed the minimum fusing current (MFC), and the instant when the fuse operates and the current is forced down to zero, Figure 2-1.

The minimum fusing current is the current level at which the fuse operating time would theoretically be infinite. Semiconductor fuses are 'faster', i.e. compared to general purpose low voltage fuses of the same rating, for a given fault current the operating time is shorter. Semiconductor fuses are discussed in Paragraph 2.2, p.5.

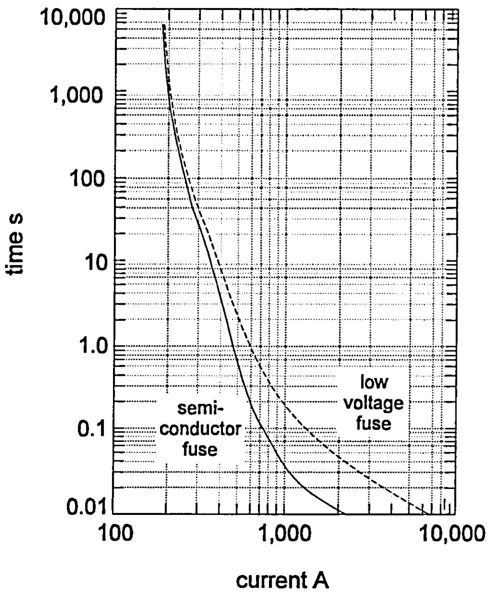

Figure 2-1. Comparison of typical time/current characteristics of standard and semiconductor fuses.

2.1.2. Pre-Arcing Behaviour

The duration from the instant when current commences until the melting and vaporisation of the element has taken place, is known as the pre-arcing period, Figure 2-2. The time from the instant when arcing is initiated until current is brought down to zero is called the arcing period.

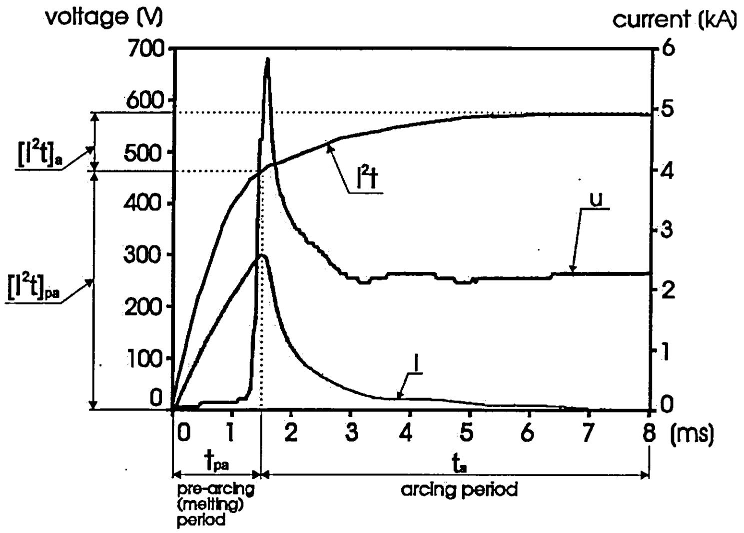

Figure 2-2. Typical short circuit performance of a high speed fuse.

Under short-circuit conditions the period required for the fuse element to reach its melting temperature is normally very short and adiabatic Joulean heating can be assumed. This means that heat losses from the element to the filler, end-caps and other parts of the fuse can usually be neglected. Hence all energy dissipated during the pre-arcing period under short-circuit conditions will be contained in the element and all the Joulean energy will contribute to its temperature rise. The energy, per unit volume termed the specific energy, required to raise the element temperature from ambient to melting temperature is called the *pre-arcing* I^2t and is represented by the following integral equation [1]: $[I^2t]_{pa} = \int_0^{t_p} i^2 dt = K_m S^2$, where K_m – Meyer's constant, and S – cross-sectional area of conductor.

The I^2t quantity is commonly referred to as the specific let-through energy. The means to reduce the pre-arcing time and the pre-arcing let-through in TTFSF will be studied in further chapters.

2.1.3. Arcing Behaviour

At the instant when arcs are initiated in a fuselink there is a significant increase in the voltage drop across it [1]. The rising arc voltage causes the current to fall and eventually reach zero, Figure 2-2. There exist several theoretical arcing models, however given that this thesis essentially concentrates on the pre-arcing behaviour of TTFSF, the arcing models will not be elaborated here.

2.1.4. Fuse Co-ordination

In applications, e.g. where semiconductor devices must be protected, fuses are often used in conjunction with circuit breakers or contactors. This combination is justified by the characteristics of these devices, Figure 2-3, which shows that overcurrents would normally be cleared by the circuit breaker, whereas short-circuit currents are cleared by the fuse. The use of circuit breakers and semiconductor fuses connected in series gives a current-clearing capability over the full-time range. This allows the design parameters of each device to be more accurately related to the time-range of the design operation.

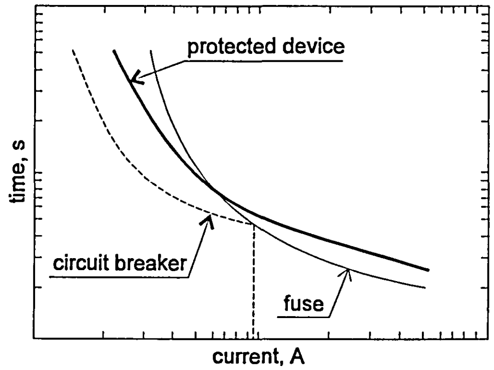

Figure 2-3. Typical fuse and circuit breaker characteristics.

2.2. Fuses for Semiconductor Protection

The use of power semiconductor devices expanded rapidly since they were first marketed in the early 50s. They are relatively small devices, its terms of their power to mass ratio, and low thermal capacities of semiconductor junctions coupled with the high resistivities of semiconductor materials limit their ability to withstand surge overloads, because the heat generated at the junction cannot be transferred quickly or easily away from the junction. For safety reasons semiconductor devices frequently require individual fuse protection. However, given that under fault conditions the device can fail in a shorter time than it takes for a standard fuse to clear the fault, a special range of very fast-acting fuses had to be developed. Semiconductor fuses are, therefore, specially designed to provide protection for power semiconductor devices. Over the years the ratings of power diodes, thyristors and other power electronics devices have been improved enormously, particularly as regards their current and voltage ratings. However, their inherent withstand weakness to overload current remains, and individual fuse protection is therefore still widely used [18].

Semiconductor fuse elements can be operated at temperatures of 200~300°C. The high running temperature of the fuse elements poses special problems. For example, the resulting increased body temperature may restrict some applications, where a number of semiconductor fuses operate in close proximity to one another. Secondly, oxidation effects are far more severe at elevated temperatures and this necessitates the use of more expensive precious metals, and thirdly, high operating temperatures can reduce the element life-span due to combined thermal and mechanical fatigue and fracture effects. The above-mentioned oxidation effects can be reduced without recourse to the use of precious metals, for example by the use of silver-plated copper strips in which the total silver content is only about 1% [6], but as a rule, silver is the preferred element material for these fuses.

The maximum permissible current rating of diodes and thyristors during short-circuits may be characterised in the form of the device $I^2t|_{Th}$ parameter. Czucha [46], for example, proposed appropriate $I^2t|_{Th\text{-}max}$ correction factors for cases where the duration of the short-circuit is less than 10ms.

2.2.1. Requirements Placed Upon Fuses for Semiconductor Protection

Semiconductor fuses must fulfil the following requirements [7]:

- the rated RMS load must be carried indefinitely without premature fuse operation or the fuse exceeding specified temperature;
- short duration overloads should not produce element deterioration;
- a range of cyclic loading must be endured without excessive deterioration;
- the peak current, peak voltage, energy let-through and operating temperatures during operation must be below the corresponding withstand values of the protected device.

2.2.2. Notched Strip Fuses

Power semiconductor fuses must be designed to operate rapidly without generating high arc voltages, which could damage semiconductor components. The rapid operation is ensured by the use of very thin restrictions along the fuse element, the number and length of the restrictions being chosen to ensure that the total arc voltage is sufficient to exceed the system voltage without leading to excessive reverse overvoltages during operation [3].

A typical semiconductor fuse element is composed of a thin wide strip with several short and narrow restrictions, Figure 2-4.

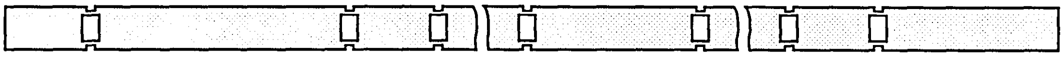

Figure 2-4. GEC semiconductor fuse element design.

Many other element designs exist, some of which are illustrated in Figure 2-5. As elements are prone to damage during handling or under harsh working conditions, it has been found advantageous to use a smaller number of wider elements having a double-bridge arrangement of restrictions. Such arrangements are also necessary for increased current ratings.

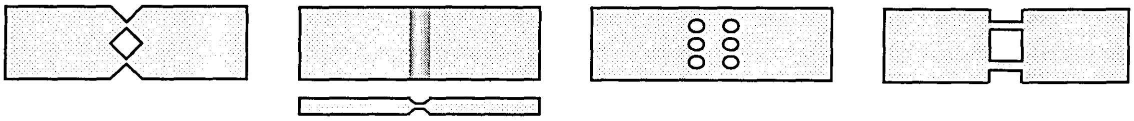

Figure 2-5. Other strip element designs.

2.2.3. Thin-Thick Film Substrate Fuses

Rapid melting of semiconductor fuse elements necessitates that they possess a large ratio of the cross-sectional area of the plain part to the cross-sectional area of the reduced section. The cross-sectional area of the notched part is typically smaller than 0.0005 mm^2 in practice [3], and notched strip elements are consequently vulnerable to mechanical deterioration in service. Elements of this size are prone to cracking along the restriction and, unless supported, therefore be the cause of nuisance operation.

The continuing development of power semiconductor devices necessitated new fuse designs, which were required to minimise the I^2t let-through whilst increasing the fuse rating. It was found that further reductions of the reduced cross-sectional area of unsupported strip fuses was not a feasible solution. Hence, manufacturers looked at the application of thin film technology to fuse design. Bussmann, for example, has produced a thin-film (Z-type) fuse [12] which, according to the manufacturer, allows for very high current density, low I^2t and can be used under the most severe working environmental conditions e.g. vibration, mechanical shock, thermal shock, cyclic loading etc., Figure 2-6.

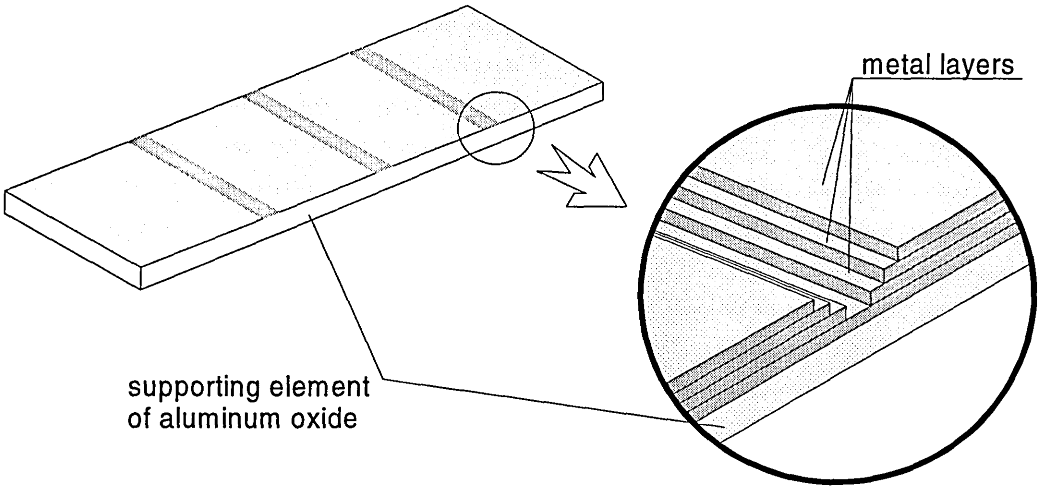

Figure 2-6. BUSSMANN melting element construction.

NEC (Japan) have also produced semiconductor fuses. These fuses utilise copper film bonded on to a ceramic substrate [13]. The geometry of the restrictions is typical of conventional unsupported elements but are much thinner in section, Figure 2-7

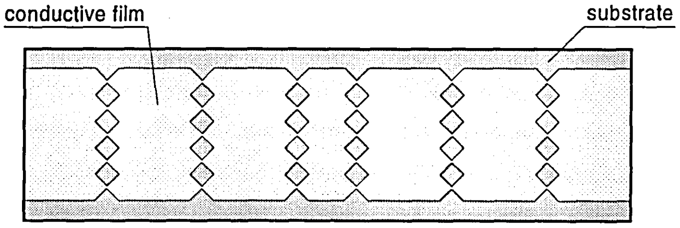

Figure 2-7. NEC (Japan) substrate fuse.

Other manufacturers considered substrate fuses as possible semiconductor fuse designs. These studies, however, have not resulted in new product designs and so far most semiconductor fuses still contain unsupported strip elements [16].

Experimental studies on single- and multi-layer substrate fuses have been carried out at the Electrotechnical Institute in Gdańsk [3]. The Gdańsk researchers have also investigated sandwich fuse elements, wherein the conductive film is trapped between two substrates, the advantage being that arc extinction occurring in narrow gaps is much faster and the resulting arcing I^2t is much reduced. Multi-layer fuse element designs shapes are reported, but no detailed data regarding the thicknesses of the layers or materials used is currently available.

More elaborate substrate fuse designs have been patented by Laur et al. [27] and Dorman Smith Fuses Ltd. [28]. The latter patent presents a design approach, namely where layers of conductive material are deposited on the cylindrical surface of the substrate, using thick-film deposition techniques, chemical deposition, dipping, spraying or electroplating.

Conductive Film Materials

From the electro-thermal point of view, the conductive element material ought, ideally, to be characterised by:

- good electrical properties;
- good thermal properties;
- good solderability;
- high melting point;
- low oxidation;
- acceptable cost.

Several materials were compared against the criteria and summarized in Table 2-1.

Table 2-1. Comparison of the electro-thermal properties of typical element materials.

Material	Electrical resisitivity	Thermal conductivity	Melting point	Relative cost
	10^{-8} Ohms/m	W/m°C	°C	Silver=100
Silver	1.47	428	961	100
Copper	1.55	403	1083	3.1
Gold	2.05	319	1063	675
Aluminium	2.5	236	659	2.84
Zinc	5.5	117	420	1.35
Tin	11.5	68	232	8.1
Lead	19.2	36	328	1.62

Given the above range of element materials, zinc, lead and tin are ruled out as suitable fuse element material on grounds of their low melting point, low thermal conductivity and high electrical resisitivity. Copper has good thermal and electrical properties but it oxides easily at elevated temperatures. It could still be used if the conductive film was protected from oxidation e.g. using inert protective coatings such as SiC [96]. Aluminium has inferior thermal and electrical properties and it also oxides easily when exposed to air. Gold has good thermal and electrical properties, it is also chemically stable but it has poor adhesion properties and is also very expensive. Of all the metals silver has the best overall electro-thermal physical properties, i.e.: low electrical resisitivity, high thermal conductivity, high melting point and high resistance to oxidation. This choice is consistent with the general belief that silver is the most commonly used metal in semiconductor fuse design [15], for conventional semiconductor fuses, despite its relatively high cost.

From the mechanical point of view, the choice of element material is somewhat more difficult because conductive film properties should be considered in connection with the mechanical properties of the substrate.

The conductive element material ought, additionally, to be characterised by:

- good adherence to the substrate;
- low Young's modulus;
- thermal expansion coefficient ideally comparable with that of the substrate;
- high yield stress;
- high creep strength.

Again, several materials were compared against the criteria and summarized in Table 2-2.

Table 2-2. Comparison of the mechanical properties of typical element materials.

Material	Thermal exp. coefficient	Young's modulus	Yield stress	Creep		
				Stress	Rate of steady-state creep	T
	10^{-6} °C^{-1}	GN/m^2	MN/m^2	MN/m^2	ε, %/s	°C
Silver	19.1	82.7	29.4	N/A	N/A	N/A
Copper	17	130	69–287	N/A	N/A	20
Gold	14.1	78.5	29.4–39.2	N/A	N/A	N/A
Aluminium	23.5	70.6	35.3	49.0	N/A	20
Zinc	31.0	104.5	104	20.6	N/A	20
Tin	23.5	49.9	N/A	N/A	N/A	N/A
Lead	29.0	16.1	4.9–9.8	0.98	1.7×10^{-5}	20

Silver, gold and copper have relatively small thermal expansion coefficients. Of these three silver and gold exhibit very low yield stress. Zinc and lead have high thermal expansion coefficients, moreover lead has very low yield stress. Since metals with good electrical conductivity usually have poor adherence to substrate material, neither silver nor copper exhibit particularly good adhesion properties to ceramic substrates. However, intermediate layers of titanium, chromium or nichrome can be used to enhance the adherence property [96]. The conclusion is such that only copper, and possibly silver, have favourable mechanical properties.

The general conclusion is such that silver and copper exhibit the best combined electro-thermo-mechanical properties. These two metals are, therefore, most likely to be used in TTFSF design.

Substrate Materials

The substrate, essentially, provides a mechanical platform to support the element, which also conducts away the heat generated in the current-carrying conductive film. It is therefore desirable that the substrate should have good thermal properties at ambient and working temperatures and less favourable thermal properties at elevated temperatures. This is because at high temperatures, which occur under short circuit conditions, an increase in the thermal time constant speeds up the fuse operation.

The substrate material ought to be characterised by:

- good electrical insulation properties;
- good thermal properties;
- high melting point;
- good mechanical strength;
- good resistance to thermal shock;
- relatively high surface smoothness;
- low cost.

The range of suitable available substrate materials and their properties is presented in Table 2-3.

Table 2-3. Comparison of suitable substrate materials.

Material	Melting point	Thermal conductivity	Thermal exp. coefficient	Young's modulus
	°C	W/m°C	10^{-6} °C^{-1}	GN/m^2
Alumina	2540	40	5.7	340
Beryllia	2550	300	9.63	330
Magnesia	2864	53	11	303
Silica	1610	1.33	0.41	73
Pyrex	925	1.4	3.2	64

Barring pyrex, all the substrate materials presented in Table 2-3 have sufficiently high melting points. The other thermal properties, however, differ considerably. For example, thermal conductivity of beryllia is seven times larger than that of alumina and over two hundred times larger than that of pyrex. Silica has very small thermal expansion coefficient hence, in combination with a current-carrying metal film, the thermal stresses in the substrate would be larger. It is also interesting that whilst most materials have a negative temperature coefficient, glass and silica have positive coefficients, Figure 2-8. Low thermal conductivity combined with positive temperature coefficient render glass and silica theoretically unsuitable for substrate fuse applications. Beryllia has superb thermal properties (high thermal conductivity and a negative temperature coefficient), but it poses a substantial health hazard (i.e. toxic dust).

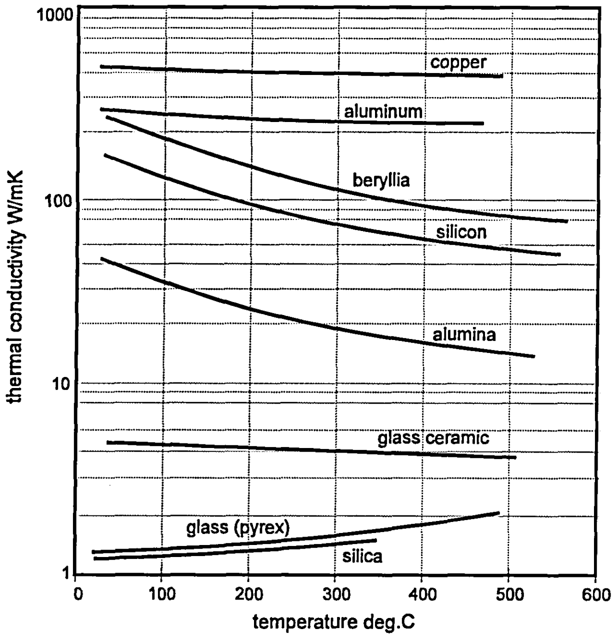

Figure 2-8. Comparison of the thermal properties of different substrate materials (metals: copper and aluminium included for comparison).

The substrate ought to exhibit high surface smoothness if the thickness of the deposited film is intended to be small, e.g. alumina exhibits much smaller surface smoothness (~10,000Å ÷ ~15,000Å) than glass (<250Å), limiting the practical thickness of the conductive film to a minimum of about 1.5μm. Alumina can be polished and, when the grain size is small, the resulting surface smoothness is comparable with that of glass. Small-grain alumina substrates are difficult to obtain, however, and the polishing procedure can be expensive. Relatively high surface roughness can, however, be advantageous in, for example, electroless plating because it allows good mechanical bonding [97].

It can be concluded that, from the point of view of pre-arcing thermal absorption, alumina is the best substrate material. Pyrex has inferior thermal properties, but it has superior elastic properties. Consequently, in this study alumina and pyrex were selected for the substrate material and their suitability for TTFSF, e.g. the magnitudes of the stresses produced by the two substrates, was evaluated (Paragraphs 4.4.5 & 4.5.3).

Generally, the interdependence of the thermal, electrical and mechanical properties of the conductive film and the substrate is complex and the selection of the conductive film material should be made taking into account *all* the critical electro-thermo-mechanical properties of the conductive film *and* the substrate at the same time. It follows that the presented choice of materials and characteristics for the conductive film and the substrate is, inevitably, limited. The four possible combinations of silver/copper films on alumina/pyrex substrates were considered to have the best overall electro-thermo-mechanical properties, hence these combinations were chosen to form the core of the study presented in this thesis.

Surface Mount Fuses.

The fast incorporation of surface mount devices (SMDs) in many types of electronic circuit created a demand for SMD components, including SMD fuses [19]. Most leading manufacturers have, therefore, recognised the need for fuses to be compatible with SMD assembly technique and now offer leadless, moulded fuses, for standard SMD assembly, e.g. BUSSMANN [12] offers a range of Subminiature Surface Mount Fuses, as illustrated in Figure 2-9.

1. Glass Stripe
2. Fused Glass Cover
3. Metal Film Fusible Element
4. Silver Termination Pad
5. Silver End Termination
6. Nickel Barrier
7. Tin-Lead Plating
8. Ceramic Substrate

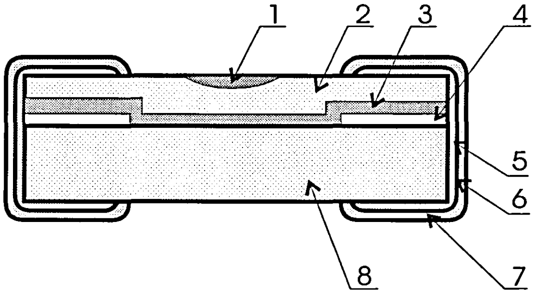

Figure 2-9. Bussmann Surface Mount Fuse construction.

Although the current rating of the SMD fuses available today is too small to deem them suitable for use in semiconductor device protection applications, the inherent problem of the interfacial stresses resulting from the film/substrate composite thermal expansion mismatch remains.

Element Manufacture Techniques.

PRINTED CIRCUIT BOARD

Thin-film fuses can be fabricated using standard copper laminated printed circuit board (PCB) sheets, and by subsequent etching. This method of manufacture is relatively cheap, and the purity and the quality of the copper foil (pits, scratches, depressions etc.) are ensured by the standards, to which PCBs are manufactured (e.g. MIL-P-13949) [109].

VAPOUR DEPOSITION.

In this method the substrate is placed in a vacuumed chamber. The material to be deposited is also placed in the chamber and heated until it melts and begins to evaporate. Gaseous atoms then condense on the cooler substrate surfaces, producing an even film. A shaped element can be made by using a suitable mask. Alternatively, by deposition and subsequent etching, a required shape can be obtained.

SPUTTERING

A method similar to vapour deposition. In this method, however, the metal to be deposited is bombarded with inert gas ions, which eject atoms from the metal giving a flux of atoms which, as in the previous case, are deposited on surfaces within the vacuum chamber. The disadvantage of both the vapour deposition and sputtering techniques is that the films produced are relatively thin (4~5 microns). This creates problems when making electrical connections to the film, which need to carry high currents. Mechanical rigidity is also difficult to achieve with this type of film.

SCREEN PRINTING.

This method is used on a wide scale in the electronics industry, particularly for the SMD. Conductive paste or ink is laid on the substrate using a squeegee through a fine wire mesh mask. The mask is then removed and the printed circuit fired in a furnace. The paste contains glass frit which bonds well to the substrate giving excellent film adhesion properties. The inclusion of the bonding frit, however, reduces the electrical conductivity of the film.

ELECTROPLATING.

Electroplating may be defined as the production of metal coatings on electrically conductive media through the action of an electric current. Electroplating on electrically non-conductive media necessitates prior deposition of a thin conductive layer, using e.g. sputtering. This, as will be shown later, can be advantageous, since the incorporation of a thin intermetallic resistive layer improves the adherence of the main conductive layer.

Electroless plating may be defined as the production of metal coatings on electrically non-conductive media through the action of a chemical process. In the electronics industry electroless plating has been used in the production of printed circuit boards (PCB). The process of producing a continuous Cu film consists of several steps and its chemical reactions are described in [96].

2.3. Fatigue, Crack Growth and Lifetime Prediction Studies in Literature.

One of the main reliability issues in thick-thin film fuses is the nuisance operation due to phenomena such as ageing and fatigue. Dasgupta et al. [37] provided a comprehensive overview of material failure mechanisms. He named large elastic deformation, yield, thermal buckling, interfacial de-adhesion, fatigue, diffusion and creep as possible sources of element material failure. With reference to failure mechanisms for cyclic fatigue Dasgupta [38] named cyclic stress & strain ranges as the main damage parameters used for engineering design. Above a certain temperature there is interaction between fatigue and creep effects, and it is found that up to approximately half the melting temperature, fatigue is the criterion of fracture, whereas at higher temperatures, creep becomes the cause of failure [85]. A further interesting feature is that a material having a fatigue limit characteristic at ambient temperature will lose this at high temperatures.

The issue of reliability exists not only in thin film fuses, but it is one of the major problems faced by the thin-film electronics industry. The following section provides a brief summary of the failure mechanisms in thin films reported in literature.

2.3.1. Failure Mechanisms in Thin Films.

Various failure mechanisms in thick-thin films were reported in literature [30-34]. Cięż [31], for example, stated that failure can have constructional, production and technological, and exploitational factors, and pointed out that natural ageing mechanism contributes to only 5~7 % of the total failure cases. He named physical and chemical processes, which are responsible for the degradation effect: interdiffusion, oxidation, corrosion and electrodiffusion. With respect to thin-film electronic packages Dasgupta et al. [37] cited buckling, interfacial de-adhesion, fatigue and interdiffusion as possible sources of failure. He pointed out that the mechanical strength of the interface is characterised and measured in terms of the interfacial fracture toughness. This is a unique interfacial property between any pair of materials and can be measured for common choices of material combinations. Bacher [32] investigated firing-process related failure mechanisms in copper multi-layers. Thick film conductor compositions generally contain Bi_2O_3 and PbO as components of the binder system. If the organic materials are not burnt out completely during the firing process then carbonaceous residues are trapped in the film. Bismuth forms a continuous brittle film in the grain boundaries, which destroys the ductility of copper. As a result, cracks can develop on thermal cycling of the bismuth embrittled copper conductor. Perecherla et al [33] indicated that good bonding between the thick film and the substrate is ensured by an adequate reaction between the thick film binder phase and the substrate. However, severe reactions can result in deeper reaction zones, which in turn are correlated with lower adhesion strength. Perecherla suggested that in evaluating the thick film adhesion it is useful to classify the fracture into three types: metal fracture within the thick film conductor, corresponding to the weakest fracture mode; glass fracture at the substrate/thick film interface; and, finally, substrate fracture within the substrate, corresponding to the strongest fracture mode. Perecherla reported that with Al_2O_3 substrates, the failures occurred at the substrate/thick film interface.

Milgram [34] studied the adhesion strength of screen printed silver films. This reference is primarily dedicated to the investigation of metallic diffusion in soldered silver electrodes, but it reports the interesting fact: that the adhesion strength for thinner films is smaller, due to the lack of sufficient glass binder, Figure 2-10.

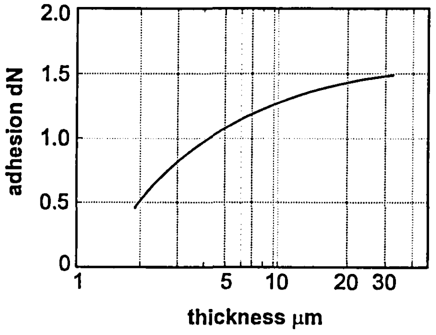

Figure 2-10. Peel strength of silver film fired onto N-750 ceramic [34].

Another important failure mechanism in thin metal films is electromigration. When an electric current passes through a thin metal film, collisions between the conduction electrons and the metal ions lead to drift of the ions. This process is known as electromigration. If there is a divergence in the flux of ions at a point, a void or hillock forms. Voids grow and overlap until conduction ceases and electrical failure is complete. Electromigration-induced damage in a polycrystalline metal film is an irreversible kinetic process, since the damage cannot be repaired simply by reversing the current [47].

Cogan [48] observed that non-linear thermal effects are responsible for premature failure in metal film resistors when operated under pulsed conditions. He attributed this failure mode to thermal run-away processes. Szeloch [51] attributed the experimentally observed propagation of micro-cracks in thin-film resistors to the presence of hot-spots or other weak points in the thin-film layer.

2.3.2. Endurance of Semiconductor Fuses under Cyclic Loading.

Premature operation of fuses subjected to pulsed-current loading has been observed and reported in literature [13, 50, 54-56]. This paragraph gives an overview of the possible causes of fuse failure and summarises the findings presented by other researchers.

Semiconductor fuses are often subjected to repetitive overload and pulsed-current duties. Under such conditions the element temperature rises, which with large overloads may approach the melting temperature of the conductive film. Repetitive currents cause mechanical stresses to change continually in the conductive film and in the substrate, which result in the development of fatigue cracks. In particular, the large film/substrate interfacial shear stresses and strains, responsible for the film debonding from the substrate, also change continually.

Wilkins [50] simulated the peak-to-peak temperature excursions, and consequent fluctuating thermal stress. The stress caused the element to deflect laterally, resulting in thermal strain, whose magnitude depended upon the temperature rise. Wilkins established the number of cycles to failure as $N = K\left[\frac{\Delta T}{T_{av}^{x}}\right]^{-1/m}$, where $K = \left[\frac{\mu}{\beta\gamma}\right]^{1/m}$ and is a constant for a given fuse design, and γ is the thermal expansion coefficient. Wilkins established the values of the x and m coefficients from empirical data: x=0.171 and m=0.26.

Daadler [52] investigated the ageing properties of silver-tin bimetallic systems by microscopic and resistance measurement techniques. The Ag-Sn system is usually used in fuses to achieve a low melting point, and is termed the M-Effect. However, at elevated temperatures, even without current cycling, the Ag_3Sn intermetallic diffusion zone develops at the Ag-Sn interface. Daadler gave three possible consequences diffusion has on ageing: i) local increase in resistivity, which may cause runaway effects; ii) reduction in mechanical strength at the M-Effect/metal boundary; iii) changes in the time/current characteristic. Arai [54] observed bends developing in straight wires subjected to cyclic loading. He also observed fatigue crack growth and fatigue fracture and attributed the failure to repeated expansion and contraction of the fuse element under cyclic pulse current. One important finding of Stevenson [55] is that the S-N curve for silver fuses is not asymptotic, i.e. silver has no fatigue limit. The importance of stress relief bends for the lifetime of a given fuse was also presented.

Meng [56] investigated short pulsed-current induced fatigue effects in wire and notched strip fuses. The work concentrated on the low-cycle fatigue domain, with many of the experimental number of cycles to failure being smaller than 10. Meng detected deformation and displacement of fuse elements subjected to a number of current pulses, and observed that plastic deformation was situated in the notch, and that the damage increased with the number of pulses. For notched strip fuse elements Meng estimated that the number of pulses to failure is given by $N = k_0 \frac{10^{16}}{t^4} \left(\frac{I_n}{I} \right)^{25.3}$, where k_o=2.51, t is the ON time, I is the ON current and I_n is the rated current of the fuse. Meng found that the number of pulses to failure, as estimated by the above equation, was in good agreement with experimental data.

Harrison [4] reported crystallisation and agglomeration of the conductive film material in the notched region in substrate fuses subjected to 50Hz AC loading for 200~500 hrs. The growth of random whisker-like crystals, also reported in the work, was attributed to ion movement in the grain boundaries.

2.3.3. Crack Growth under Cyclic Loading

Newman [58] studied crack-growth behaviour under monotonic and cyclic loading using 2D finite element modelling. The crack growth criterion was based on crack-tip strain. Crack growth was found to be dependent upon the mesh size, and the material strain hardening had a significant influence on the crack-growth behaviour.

2.4. Summary

In Chapter 2 the background to thin-thick film substrate fuses was presented and current trends in semiconductor protection substrate fuse technology were identified. The electro-thermo-mechanical properties of several substrate and element materials were evaluated. Several techniques of conductive film deposition were presented and their suitability to fuse element manufacture was investigated.

The section also presented a literature review of failure mechanisms, fatigue, crack growth and lifetime prediction studies of thin conductive films laid on non-conductive substrates, with special reference to thin-film substrate fuses subjected to pulsed-current loading.

Chapter 3.

Background to 3D Finite Element Electro-Thermal, Thermal Stress and Fatigue Analyses

This Chapter presents the theoretical background to finite element electro-thermal & thermal stress analyses and thermal fatigue. Major modes of thin-thick film substrate fuse failure and critical stress/strain components contributing to the failure are identified. A summary of previous research relevant to FE interfacial stress analysis is provided and basic requirements of computer modelling and simulation techniques are explained. The assumptions made for the study are discussed and, finally, the procedures used to ensure convergence of the highly non-linear electro-thermal analysis are given.

3.1. Introduction

A comprehensive FE analysis of crack formation and growth in thick-film substrate fuses is rather complex. For example, thermal conductivity affects electrical conductivity, which in turn affects the current density distribution; both electrical and thermal properties influence the temperature magnitude and distribution which, combined with the mechanical properties of the film/substrate materials, affects the magnitude of physical deformation. The magnitude of the deformation and the mechanical properties of the conductive film and the substrate affect the stress/strain distributions, which in turn affect the electrical properties of the conductive film and so on, to repeat the cyclic dependence. Add to this the effects of crack formation or film de-bonding from the substrate on the current/temperature distribution and the picture becomes very complex. It follows that fully comprehensive and legitimate modelling of crack formation/propagation in thick-film substrate fuses would require the application of a concurrent analysis of current/temperature/stress distribution *and* crack formation/growth.

This, however, is impossible to achieve in ABAQUS. Consequently, the problem was divided into three major parts and analysed sequentially. These are:

- coupled electro-thermal analysis;
- thermal stress analysis;
- fatigue life prediction.

The coupling of the electrical & thermal analysis is essential for accurate temperature prediction. The errors introduced by the de-coupling of the thermal-stress analysis from the thermal-electrical analysis are small and were assumed to be negligible (Paragraph 3.7.2, p.29). Short cracks have little effect on the temperature magnitude & distribution, hence their effect on the thermal-electrical solution was also assumed to be negligible. Long cracks, however, can significantly affect the electro-thermal solution. Since the problem studied in this thesis concerns mainly high-cycle fatigue, wherein crack initiation is considered to constitute a dominant portion of total life, the effect of time spent propagating a crack on total time to operation was also assumed to be negligible.

3.2. Coupled Electro-Thermal Analysis

Previous studies of notched substrate fuses used transmission line matrix (TLM) [4, 21] finite element [9] or finite difference [7, 50] modelling, and also experimental thermochromic [4], thermocouple [24] and infrared thermal imaging [25, 26] techniques to predict the temperature distribution and/or magnitude in the fuse element. In the study presented in this thesis FE modelling techniques were used to predict the temperature magnitude and distribution. The main advantage of the FE technique is such that the temperature distribution obtained from the electro-thermal analysis can subsequently be used for the thermal stress and thermal fatigue analyses.

The thermal-electrical equations were solved concurrently for both temperature and electrical potential using the ABAQUS **Coupled thermal-electrical* procedure. Coupling of the electrical and thermal equations arises from two sources: the electrical conductivity is temperature dependent and, hence, the internal heat generated is a function of electrical current and temperature. All electrical energy dissipated in the conductive film was assumed to be converted to thermal energy (ABAQUS option **Joule heat fraction*).

3.2.1. Prescribed Initial and Boundary Conditions

The boundary conditions applied at the external surfaces of the models studied are given by $\mathrm{T} = \mathrm{T}(\mathbf{P}, \mathrm{t})$ and $\mathrm{h} = \mathrm{h}(\mathbf{P}, \mathrm{T})$, where $\mathbf{P} = \mathrm{P}(x, y, z)$ and h is the coefficient of surface heat transfer (film coefficient). The value of the film coefficient h will be later established by fitting computational results to experimental data. Electric current was applied at all nodes on the input surface. At t=0 all nodes were assumed to be at the ambient temperature, except in cases where the analysis commenced from a 'hot-start' initial condition (Paragraph 5.7, p.98).

3.3. Thermal Stress Analysis

3.3.1. Definition of the Critical Stress/Strain Components Contributing to Fuse Failure

Two major modes of failure can occur in thin-film fuses subjected to pulsed-current loading. The first mode is film de-bonding and lifting from the substrate, due to the interfacial thermal shear stresses produced by the mismatch of the mechanical properties of the film and the substrate. The second mode is fatigue crack formation and crack growth due to the thermally induced cyclic stresses and strains, i.e. thermal fatigue. The two failure modes are schematically illustrated in Figure 3-1.

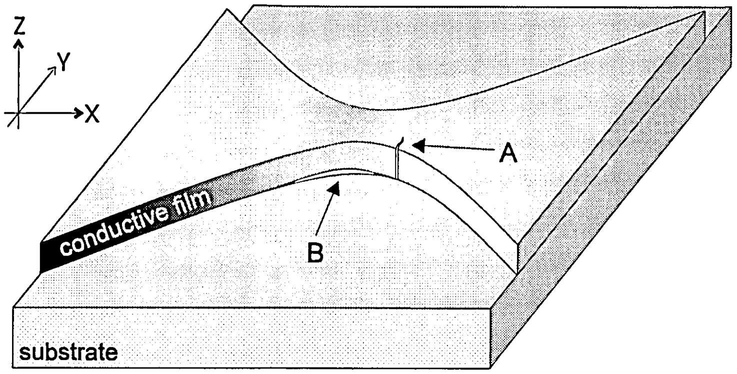

Figure 3-1. Major modes of failure in thin-film fuses. A - part-through crack; B - conductive film de-bonding from the substrate

Both failure modes can cause electro-thermal runaway processes: a crack developing across the notch increases the electrical resistance of the notch. Assuming constant current, this results in more Joulean heat being generated in the notch and, consequently, the rising temperature increases the resistance still further. If the film is de-bonding from the substrate then the film/substrate thermal path and cooling is impaired. Consequently, the notch temperature rises which can result in the runaway process described above. The development of these processes depends on the magnitude of the degradation and the overall thermal properties of the fuse and its environment. If the extraction of the heat is sufficient, a new thermal equilibrium will be realised. For the thermal runaway process to take place it is, therefore, necessary that the crack length or the extent of the film de-bonding exceed specific threshold.

At substantially elevated temperatures the notched parts of the fuse element experience plastic deformation. Since for ductile materials, exhibiting yielding and subsequent plastic deformation, the *shear-strain-energy* (VON MISES) theory correlates best with material behaviour [85] the VON MISES (MISES) yield criterion was used in this study. The MISES equivalent stress is given by $S_{mises} = \frac{1}{\sqrt{2}}\sqrt{(\sigma_1 - \sigma_2)^2 + (\sigma_2 - \sigma_3)^2 + (\sigma_3 - \sigma_1)^2}$, where principal stresses σ_1, σ_2, and σ_3 are the three roots of:

$$\sigma_i^3 - \left(S_{xx} + S_{yy} + S_{zz}\right)\sigma_i^2 + \left(S_{xx}S_{yy} + S_{yy}S_{zz} + S_{zz}S_{xx} - S_{xy}^2 - S_{yz}^2 - S_{zx}^2\right)\sigma_i$$

$$- \left(S_{xx}S_{yy}S_{zz} - S_{xx}S_{yz}^2 - S_{yy}S_{zx}^2 - S_{zz}S_{xy}^2 + 2S_{xy}S_{yz}S_{zx}\right) = 0$$

The critical stress components contributing to film de-bonding are the planar shear stresses σ_{zy} and σ_{zx}. Consequently, the *maximum-shear-stress* (TRESCA) was adopted as the criterion for film de-bonding: $\tau_{max} = \frac{\sigma_1 - \sigma_3}{2}$, where σ_1 is the algebraically largest and σ_3 is the algebraically smallest principal stress. Cracking was presumed to initiate at the interfacial film/substrate point where the maximum shear strain is largest (the critical point). Maximum shear strain, at the critical point, is given by: $\gamma_{max} = \sqrt{(\varepsilon_{22} - \varepsilon_{33})^2 + \gamma_{23}^2}$. The pressure equivalent stress (PRESS), defined as $p = -\frac{1}{3}\mathrm{trace}(\sigma) = -\frac{1}{3}(\sigma_{xx} + \sigma_{yy} + \sigma_{zz})$, was used to obtain the scalar direct stress field. A negative value of the pressure equivalent stress indicates a tensile stress, and a positive value indicates a compressive stress, hence giving an indication of which parts of the fuse are subjected to compressive and tensile stresses.

3.3.2. Governing Equations

The six stress-strain relationships for a 3D body under thermal stress are [85]:

$$\left.\begin{aligned} \varepsilon_x &= \frac{\sigma_x}{E} - \frac{\upsilon}{E}(\sigma_y + \sigma_z) + \alpha(T - T_a) \\ \varepsilon_y &= \frac{\sigma_y}{E} - \frac{\upsilon}{E}(\sigma_x + \sigma_z) + \alpha(T - T_a) \\ \varepsilon_z &= \frac{\sigma_z}{E} - \frac{\upsilon}{E}(\sigma_x + \sigma_y) + \alpha(T - T_a) \end{aligned}\right\} \quad \text{[Eq. 3-1]}$$

$$\gamma_{xy} = \frac{\tau_{xy}}{G}, \qquad \gamma_{yz} = \frac{\tau_{yz}}{G}, \qquad \gamma_{zx} = \frac{\tau_{zx}}{G}$$

The stresses can be expressed explicitly in terms of the strains, the relations in question are:

$$\left.\begin{aligned}\sigma_x &= \lambda e + 2\mu\varepsilon_x - (3\lambda + 2\mu)\cdot\alpha(T - T_a)\\ \sigma_y &= \lambda e + 2\mu\varepsilon_y - (3\lambda + 2\mu)\cdot\alpha(T - T_a)\\ \sigma_z &= \lambda e + 2\mu\varepsilon_z - (3\lambda + 2\mu)\cdot\alpha(T - T_a)\\ \tau_{xy} &= 2\mu\gamma_{xy}, \quad \tau_{yz} = 2\mu\gamma_{yz}, \quad \tau_{zx} = 2\mu\gamma_{zx}\end{aligned}\right\} \quad \text{[Eq. 3-2]}$$

where:

$\lambda = \frac{\nu E}{(1+\nu)(1-2\nu)}$ and $\mu = \frac{E}{2(1+\nu)} = G$ are Lamé elastic constants.

These equations will be used in Chapter 4 to verify the accuracy of ABAQUS predictions.

3.3.3. Prescribed Boundary Conditions

The kinematic boundary conditions (BCs) can be divided into internal symmetry BCs and external BCs. Internal symmetry BCs exist where systems are composed of symmetrical elements, and only the symmetrical part of the system needs to be modelled. External BCs exist due to external constrains imposed on the model.

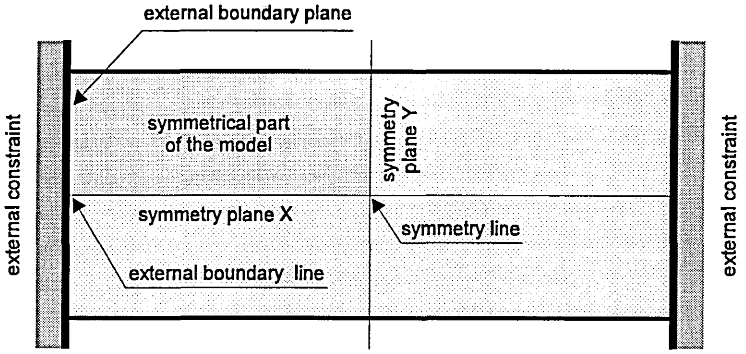

Figure 3-2. Definitions of symmetry and external boundaries.

The displacement degrees of freedom (u_x, u_y, u_z) were modelled. Since no large magnitudes of rotation occur in substrate fuses, the rotational degrees of freedom (θ_x, θ_y, θ_z) were assumed to be negligible and were neglected. The external boundary constraints represent the mechanical substrate/end-cap connection. In the problem considered the fuse element was connected to the end-cap (electrically, thermally and mechanically) by soldering. However, it would not be feasible to model the solder bond in detail, given that its exact geometry varies from fuse to fuse, hence simplified modelling was adopted. This methodology assumed that there was no solder bond, and that the fuse element and the substrate were directly attached to the end-cap.

There are several possible modes of constraining the fuse element. These are explained in Figure 3-3.

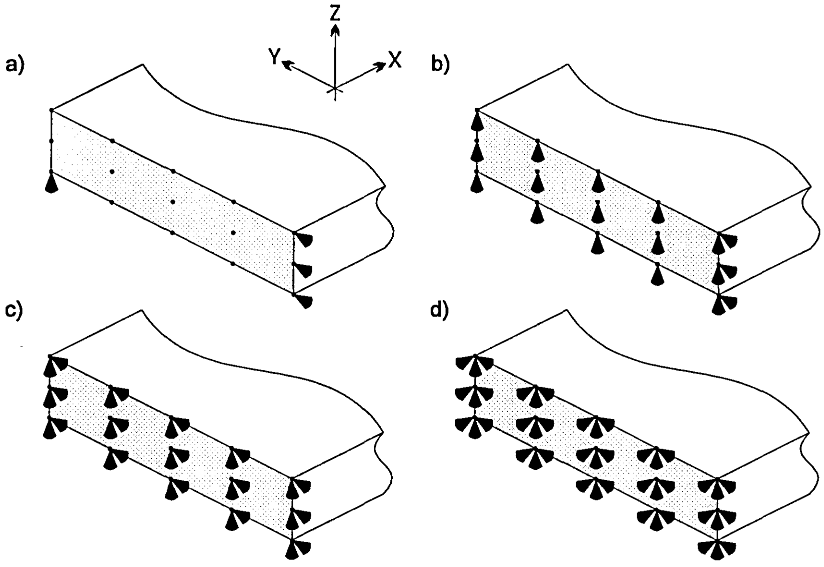

Figure 3-3. Possible modes of constraining the fuse element (conductive film omitted for clarity). a) fuse element completely free to expand; b) fuse element virtually free to expand; c) fuse element can expand freely in the X-direction only; d) fuse element rigidly fixed.

The type of the constraining mode has a significant effect on the magnitude of the deformation, Table 3-1. The effect of the constraining mode on the magnitude of the stress was found to be similar for modes *a*, *b*, and *c*. However, overconstraining the model resulted in an increase in the magnitude of the stress and a reduction in the magnitude of the deformation. Modes *b* and *c* produced almost identical results, and for the purpose of this study the type of the constraining mode presented in Figure 3-3 b) was adopted.

Table 3-1 The effect of the constraining mode on the magnitudes of solution variables.

Type of constraining mode as illustrated in Figure 3-3 x, where x:	Magnitudes of solution variables		
	U3	MISES	TRESCA
a)	6.02×10^{-4}	279	313
b)	5.38×10^{-4}	280	313
c)	5.40×10^{-4}	279	313
d)	3.21×10^{-4}	291	320

Table 3-2 indicates the degrees of freedom which were constrained with reference to Figure 3-2.

Table 3-2. Structural boundary conditions.

Boundary	Constrained degree of freedom		
	u_x	u_y	u_z
symmetry plane Y	✓		
symmetry line	✓	✓	
symmetry plane X		✓	
external boundary line		✓	✓
external boundary plane			✓

3.4. Thermal Fatigue, Crack Initiation and Crack Propagation

The ageing of wire and strip fuses was previously investigated and reported in literature [4, 50÷56]. Still, little information is available with regard to the ageing of substrate fuses. Moreover, previous studies on theoretical life-time prediction used simplified methods to determine the magnitudes and amplitudes of the stresses and strains, which have paramount effect on fuse life-time under cyclic-current loading. These methods directly linked the magnitude of the strain with the temperature using thermal expansion co-efficient. In this study, the stresses and strains are accurately determined using finite element techniques. Non-linear temperature-dependent material properties were used to refine the accuracy of the predictions.

Under normal operating conditions the temperature of the constricted regions of the fuse element may reach several hundred °C. Consequently, parts of the notch may experience plastic deformation, in which case the strain-life (ϵ-N) method, taking into account both elastic and plastic strains, gives most accurate predictions. As a result the ϵ-N method was adopted for this study.

3.4.1. Crack Propagation

Linear elastic fracture mechanics (LEFM) methods are normally used to model crack propagation. Modelling of crack propagation in 2D models is relatively easy and was reported in literature [58]. Such modelling normally uses crack tip strain or critical stress or crack opening displacement as the criterion for node de-bonding. However, although in ABAQUS v.5.6 crack propagation analysis is available, it is limited to 2D and axisymmetric cases only. Since all the FE models used in this study were three dimensional and not axisymmetric, crack propagation analysis was not performed.

3.5. Interfacial Stress Analysis – Literature Review

Interfacial stress arises in physical composite systems where two materials of different mechanical properties are in contact, and either external mechanical force is applied to the composite or the temperature of the system is raised. The problem of interfacial stress affects many applications, including thin-film substrate fuses. For example they range from dentine bonding systems to thin-film electronics to space shuttle coatings. The common question the designers of all such systems have to address is: 'Will the interfacial stresses impair the characteristics of the system?' and, in the extreme cases, 'Will the interfacial stresses cause failure of the component?'. This section provides an overview of the research into broadly defined interfacial stress analysis, found in the literature.

Kline [59] investigated adhesively bonded joints. He found that peak stresses developed at the joint's edges and that Young's modulus had the most pronounced effect on the magnitude of the stress, with the use of a lower modulus resulting in a large decrease in peak stress values at the edge of the bonded joint. Li et al [60] studied the stress distribution in adhesive bonded tee joints using elastic finite element method. The influence of the geometry of the joint on the stress distribution was investigated. The main finding was that the geometry of the joint, in particular the overlap length and adhesive thickness, significantly affect the stress distribution and that the stress concentrations occur, not surprisingly, in the corner of the plate. Meera et al [61] presented a more complex study of notch tip stresses and strains in elastic-plastic isotropic bodies subjected to multi-axial loading. Zsary [62] emphasised the fact that for the design engineer testing the developing stress distribution, stating the magnitude and location of the stress peaks and determination of the direction of stresses can be more important than determining the precise magnitude of the stress, as on the basis of this information product design can be modified. Bacmann [63] investigated residual stresses in sputtered thin films. The knowledge of the residual stress level is important because compressive stresses may result in adhesion loss by buckling, while tensile stresses may lead to film failure and interfacial cracks. Bacmann found that the residual stresses in sputtered films decreased with the thickness of the film. Wakasa [64] investigated the distribution of the interfacial stress in dentine bonding systems by means of finite element analysis. The study showed that the distribution of the interfacial stress was highly non-uniform, with maximum stress at the edge of the resin composite/bonding area interface. The analysis also showed that a non-uniform stress developed at the interface, despite the uniform mode of the tensile load. Wakasa also found that the higher the elastic modulus of the bonding area the higher the magnitude of the interfacial stresses.

Ozmat [65] studied thermal fatigue life of leaded ceramic chip carriers, using finite element non-linear and rate dependent material characteristics methods. Ozmat suggested that the results of his work on two-dimensional FE models show that when appropriate material laws and the correct boundary conditions of the thermal fatigue problem are included in the models, encouraging results can be obtained. Ozmat appreciated that more accurate modelling would require further development of the FE models to include temperature dependent elastic, plastic and creep deformation behaviour of materials used, and three-dimensional representation of the model geometry.

Aivazzadeh [66] indicated that classical displacement or equilibrium FE interface models do not ensure all the required continuities, for example in the displacement model the continuity of the displacements are satisfied, whereas the equilibrium model leads to continuous stress but discontinuous displacements. Aivazzadeh developed new rectangular interface finite elements, with four degrees of freedom at each node on the interface (two displacement and two transverse components of stresses). He concluded that compared to results obtained from classical constant stress elements, the new interface finite elements give satisfactory values with fewer elements. However, given the assumptions Aivazzadeh has made (2D linear elasticity), the new elements could not be used in modern FE models.

Other work on the interfacial stress analysis includes the linear elastic 2D FE analysis of copper thin-film structure on glass/ceramic substrate (Kapur [67]), and non-linear 3D FE thermal stress analysis of tape automated bonding packages and interconnections (Lau [68]). Lau indicated that his models showed excellent agreement between the analytically predicted and the experimentally observed failure mechanisms.

The main conclusions that can be drawn from the presented literature review above are:

- Simple methods, utilising 2D and/or LE techniques, are only suitable in cases where approximate or semi-qualitative results are satisfactory. For accurate prediction of stress distribution and stress magnitudes 3D elasto-plastic temperature-dependent modelling is essential. The inclusion of creep and rate-dependent properties (e.g. cyclic softening/hardening) is advantageous, but the major problem is with obtaining accurate material properties.
- In order to ensure that the results of the analysis are independent of the FE mesh, particular care must be taken concerning its quality. Inadequate mesh quality will result in erroneous predictions.
- Several authors indicated that the stress is largest at the edges/corners of the interfacial system. The location and the relative magnitude of the stress are seen as more important than the precise magnitude of the stress.

3.6. Principles of Computer Modelling and Simulation

Simulation is a numerical technique for conducting experiments on a computer that involve certain types of mathematical and logical models to emulate the behaviour of a system. The purpose of systems study through *modelling* is to aid the analysis, understanding, design, operation, prediction or control of systems without actually constructing and operating the real system or thing. A *model,* in this context, is a virtual representation of a system (or process or theory) intended to enhance our ability to understand, predict and possibly control the behaviour of the system. *Validation* is the process of substantiating that the model is sufficiently accurate for the intended application. Without validation, a model is of very little practical use. *Verification* is a procedure to ensure that the model is built according to specifications and to eliminate errors in the structure, algorithm and computer implementation of the model [98, 99].

In this thesis, *finite element* modelling was used. Validation of this technique requires that i) correct behaviour of the finite elements is ensured; ii) the geometric quality of the finite elements is adequate; and iii) the refinement of the finite element mesh is adequate. The ABAQUS FE software was used to solve the electro-thermal equations [104]. Correct behaviour (field distribution and accuracy) of the finite elements was initially verified by the software developer (HKS). The geometric quality of the finite elements (e.g. angle between isoparametric lines, edge angle, aspect ratio, warp) and the refinement of the mesh (the proportion of the mesh density to the expected magnitudes of variable differentials) were verified for each model by the author.

The accuracy of the ABAQUS predictions was verified, initially, by the software developer [104]. The accuracy of the ABAQUS coupled electro-thermal prediction was also verified by comparing ABAQUS results with the results produced by an independent model of current-currying fuse wire, surrounded by a quartz-sand filler [8], and experimental data [102] [Appendix B].

3.7. Assumptions made for the Studies

The main aim of the FE thermal fatigue study was to determine the substrate fuse lifetime under pulsed-current loading conditions. However, to achieve this the following interrelated fields had to be analysed first: electric current distribution, temperature distribution and stress/strain distribution. Due to the interdisciplinary character of the study and the complexity of the problem some simplifying assumptions were necessary. These are discussed below.

3.7.1. Restrictions Imposed by the Software/Hardware

ABAQUS ver. 5.6 can solve non-linear time-varying coupled thermal-electrical problems. ABAQUS cannot compute all three (electrical, thermal and structural) fields simultaneously. Hence, the change in model geometry due to thermal expansion was assumed to have a negligible effect on the electrical solution. This assumption is valid, given that the effect of the change in the model dimensions due to thermal expansion on the resistance is very much smaller than the increase in resistance due to the high operating temperature.

In the models developed to solve problems in this study, great care was taken to ensure that the mesh density was adequate with regard to the expected distribution and magnitudes of the solution variables. The largest stress differentials occur in the vicinity of the notch across the conductive film/substrate interface, hence accurate prediction of the stress distribution requires the use of fine mesh at the interface. However, finer mesh entwines more finite elements and increases computer run-times and storage. These conflicts necessitate a compromise on storage, speed and accuracy. The effect of the mesh size on the accuracy of the prediction was studied using small models, and the results indicated that the finite element models used in this project give accurate predictions, and that the mesh refinement of all the FE models was more than satisfactory to ensure sufficient accuracy of the electro-thermal prediction.

3.7.2. Restrictions Resulting from Approximate Properties of Materials

It is estimated that the greatest error in the finite element modelling was introduced by imprecise values for the physical properties of the materials analysed. Temperature dependent data for some materials was unknown (e.g. the temperature dependent thermal properties of compacted quartz sand filler or the plastic properties of gold). In those cases ambient or lump values were used.

The factors which affect the properties of thin conductive films include:

- dependence of electrical conductivity on the thickness of the conductive film;
- dependence of electrical conductivity on the frequency of the current;
- dependence of electrical conductivity on stress;
- temperature coefficient of resistance in very thin films;
- effect of oxidation;
- residual stresses in the film/substrate;
- elasto-plastic properties of thin films v. bulk material;
- the conductive film was assumed to be isotropic.

These are discussed below.

The resistivity and the temperature coefficient of resistance of pure metals are influenced by a significant reduction in one of the dimensions of the specimen, as is the case with thin films [95]. These effects become significant if the thickness of the film is less than ~30nm. The minimum film thickness used in this study was 120nm, hence, the effect of the film thickness on resistivity was assumed to be negligible.

The electrical conductivity of thin-films is known to increase significantly when the frequency of the supply source exceeds ~10^6Hz. The maximum frequency used for the pulse-load studies was 2.07Hz, hence, the effect of frequency was assumed to be negligible.

The effect of stress on the resistance of a thin film may be divided into two: that due to the change in dimensions and that due to the change in resistivity [97]. The main reason for resistivity being a function of stress is that the lattice vibrations are moderated as the sample is compressed, resulting in a lowered resistivity. A 1% change in resistance can be induced by a strain of only 0.5% [95]. Although this change is significant on its own, it is negligible in comparison with the change in resistivity produced by the increase in temperature (approximately sixfold increase between ambient and melting for copper), hence the change in resistivity due to stress was neglected.

The temperature coefficient of resistance of very thin but moderately conductive films rarely approaches the bulk value and, in fact, it is rarely even positive [95]. The coefficient decreases rapidly with increasing film resistivity and, therefore, with decreasing film thickness. Negative temperature coefficients do not occur in continuous metal films unless impurities are present. The effect of negative temperature coefficient is significant only in very thin films (<5μm), hence it was neglected in this study.

Unless suitably protected, thin conductive films heated in air precipitate increase in resistance due to surface oxidation. It has been found that the increase in resistance of a film due to oxidation is considerably greater than can be accounted for on the basis of only the reduced thickness of the conductive portion of the film [95]. Oxidation occurs along grain boundaries, internally due to migration of trapped oxygen, as well as externally, due to absorbed oxygen from the surface. Films that have undergone grain-boundary oxidation are not, therefore, electrically homogenous, even though at a macroscopic level they are physically continuous.

Intrinsic stresses are trapped in thin films during the deposition process [95]. Nearly all films, laid down by whatever process, are found to be in some state of internal stress. In thin film heated by current the existence of tensile residual stresses in the film is cancelled out by the compressive Joulean thermal stress and, hence, is advantageous. In general electroplating or evaporation processes produce tensile residual stress, while compressive residual stresses are observed in sputtered films. In 'impure' films, in which oxygen and other materials are incorporated into the structure during growth, the resultant stresses are usually sufficiently high to overshadow any of the 'pure film' effects. Intrinsic stresses are largest in very thin films, however, the stress decreases as the film thickness increases. The maximum stress occurs when the film changes from discontinuous islands to a continuous layer. For example in a silver film 25nm thick deposited on silica the intrinsic stress was found to be close to 200 N/mm^2. The stress decreases monotonically as the film thickness increases and for a 0.1μm film thickness the intrinsic stress is only 20 N/mm^2 [24]. Using extrapolation the intrinsic stress, therefore, can be assumed to be even smaller in still thicker films (the thickness of the main conductive films in this study are in the range 10÷15μm). It can be concluded that owing to the difficulties with the estimation of the sign and the precise magnitude of the residual stresses, and because the intrinsic stresses are considered to be much smaller than the thermally induced stresses, the effect of the residual stresses was omitted from the finite element models. All models were consequently assumed to be stress-free prior to the thermal stress analysis.

The elastic properties of thin films are quite different from those of the bulk material. For example, the strengths (i.e. yield stress) exhibited by some films may be as much as 200 times as great as for well-annealed bulk samples, and are usually several times the magnitude of the corresponding strengths of severely worked bulk material [97]. The expression for the yield stress as a function of thickness is given by $\sigma^{*}_{\mathrm{film}} = \sigma_{\mathrm{bulk}}\left(1+\frac{K}{d_f}\right)$, where K is a constant and d_f is the film thickness, i.e. the yield stress increases as the film thickness decreases.

In this study the conductive film was assumed to be isotropic. In a non-cubic metal lattice this assumption may not be valid, since resistivity and mechanical properties are functions of the crystallographic orientation, and there may be a preferred orientation of these crystallites in the film, causing the resistivity to depend on the growth profile of the film.

At temperatures exceeding roughly half the melting temperature, creep becomes the main cause of failure [85] and should be taken into consideration. In this study the average temperature of the element did not exceed ~250°C, well below half the melting temperature of copper (T_m=1083°C). At 204°C the creep rate for oxygen free copper (Cu 99.99+) rod loaded at 51 N/mm^2 is 0.215% per 1,000 h [88]. In this particular case creep related elongation (1.08%) constituted only about 20% of the total elongation of 4.58%, for the test duration of t=5,000h. In this thesis the maximum testing time for the manufactured fuse was 611h, hence the ratio of creep related strain to total strain can be assumed to be smaller than ~10%. Although creep behaviour can be included in material definition in a static creep analysis, ABAQUS does not provide a way to include time-varying nodal temperatures from the electro-thermal analysis in the thermal stress analysis. Given all the above considerations creep related effects were omitted from the computer models.

3.8. Abaqus Loading and Convergence Studies

In ABAQUS convention in a steady-state analysis, by default the loading curve varies linearly from nought, at t=0, to maximum, at t=1.0, where t is the normalised ABAQUS 'time' scale. In simple FE models this is sufficient to produce convergence for most types of analysis. The electro-thermal response of current-carrying fuses, however, is highly non-linear, with greatest gradients occurring towards the 'end' of the analysis. In this case linearly increasing loading is unlikely to produce convergence, or it could lead to an excessive number of cutbacks and equilibrium iterations. The loading curve, therefore, had to be modified in order to equalise the temperature increments (the model used for this verification is described in Paragraph 5.2, p.87).

The results of the analysis for three models:

i) model A, with loading increasing monotonically from nought to maximum (ABAQUS default);

ii) model B, with loading increasing monotonically from 80% of full load to full load (Load I_2);

iii) model C, with non-linear loading (Load I_1),

are presented in Figure 3-4 and Table 3-3.

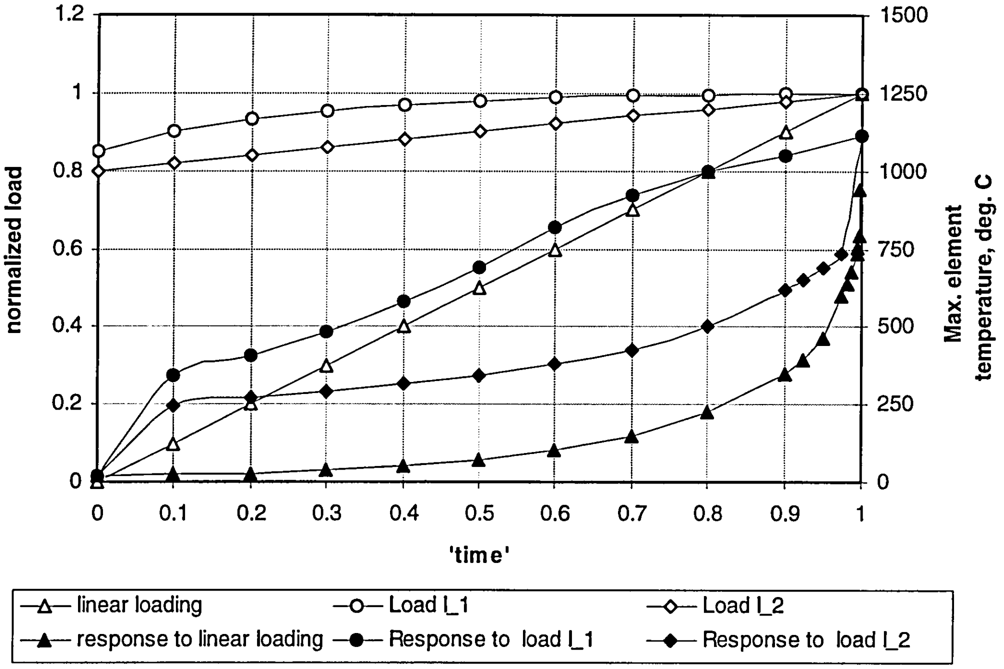

Figure 3-4. Linear and non-linear loading curves and the computed increase in maximum element temperature.

Model A produced several cut-backs and in the end the analysis was terminated due to very small time increment required. Hence, the default loading could not be used to analyse the type of problem discussed. The response of model B was much better than the response of model A, but the temperature curve was still highly non-linear, which may sometimes result in divergence. Barring the initial jump, temperature increments for model C were approximately equal, and the convergence was smooth with no cut-backs. The total number of iterations for this model was also smaller compared to model B, Table 3-3. Consequently, non-linear increasing loading (Load I_1) was adopted for the electro-thermal studies.

Complex FE models, wherein various non-linearities interact, can initially produce irregular convergence, Figure 3-5. By default, the convergence check (identifier: $\mathrm{I_o}$), i.e. $min\left(\left(r^{\alpha}_{max}\right)^{i},\left(r^{\alpha}_{max}\right)^{i-1}\right) > \left(r^{\alpha}_{max}\right)^{i-2}$ where r is the residual, α is the field and i is the iteration counter, begins at iteration No.4 (the dashed line in Figure 3-5 b).

Table 3-3. ABAQUS electro-thermal prediction for linear and non-linear current loading.

Model A			Model B (load I_2)			Model C (load I_1)	
time step	Max. temperature deg. C	notes	time step	Max. temperature deg. C	notes	time step	Max. temperature deg. C
0	21.6		0	21.6		0	21.6
0.1	23.33		0.1	246.6		0.1	344
0.2	28.09		0.2	267.4		0.2	403
0.3	36.81		0.3	290.1		0.3	482
0.4	50.52		0.4	314.9		0.4	578
0.5	71.22		0.5	343.5		0.5	688
0.6	103.3		0.6	378.3		0.6	818
0.7	150.6		0.7	423.6		0.7	920
0.8	228.3		0.8	504		0.8	998
0.9	345.1	cut-back	0.9	620.2	cut-back	0.9	1,052
0.925	391.5		0.925	650.6		1.0	1,112
0.95	461.7		0.95	685.9		total No of iterations: 42	
0.975	600.6	cut-back	0.975	733.7			
0.981	635.7		1.0	1,112			
0.987	676.8		total No of iterations: 44				
0.994	733.5	cut-back					
0.995	755						
0.997	791.7						
0.998	941.9	cut-back					
analysis terminated solution not obtained total No of iterations: 46							

Hence, the use of the default value for I_o (the iteration after which the check is made that the residuals are not increasing in both of two consecutive increments) would result in an excessive number of premature cut-backs and iterations (Note: in the problem presented in Figure 3-5, if default settings had been used, the solver would have unnecessarily terminated the increment at iteration No.4).

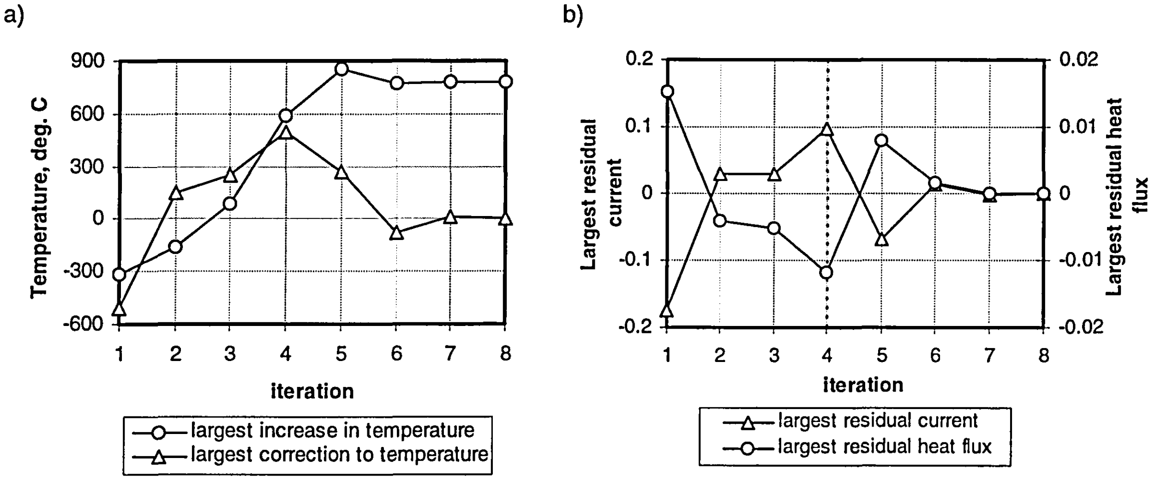

Figure 3-5. Abaqus response to a 10% increase in current loading (time step 0.9–1.0) – verification of the rate of convergence; a) largest increase in temperature; b) largest residuals.

Likewise, in the highly non-linear electro-thermal problem studied, the logarithmic rate of convergence, i.e. $ln\left(\left(r^{\alpha}_{max}\right)^{i}/\left(r^{\alpha}_{max}\right)^{i-1}\right)$, may not be achieved after I_r iterations (I_r is the equilibrium iteration number at which logarithmic rate of convergence check begins, by default I_r=8), Figure 3-6. Again, the use of the default value for I_r would result in an excessive number of premature cut-backs and iterations (Note: in the problem presented in Figure 3-6 the solver unnecessarily terminated the increment at iteration No.8 – the solution would otherwise have converged at iteration No.10).

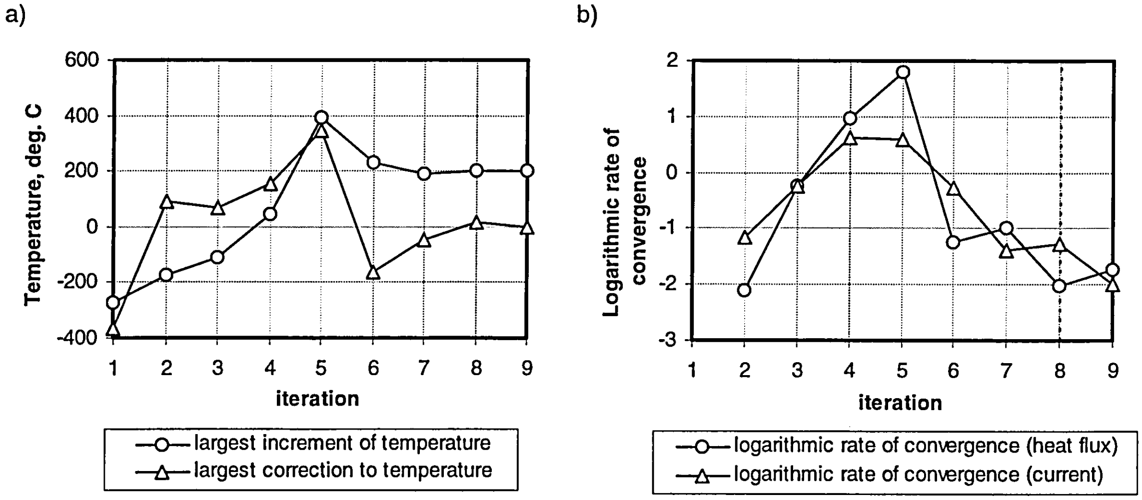

Figure 3-6. Abaqus response to a 10% increase in current loading (time step 0.9–1.0) – verification of the logarithmic rate of convergence; a) largest increase in temperature; b) largest residuals.

It was also observed that the ABAQUS solver sometimes produced chaotic convergence (or in some cases no convergence) even for a very small increase in current loading, Figure 3-7.

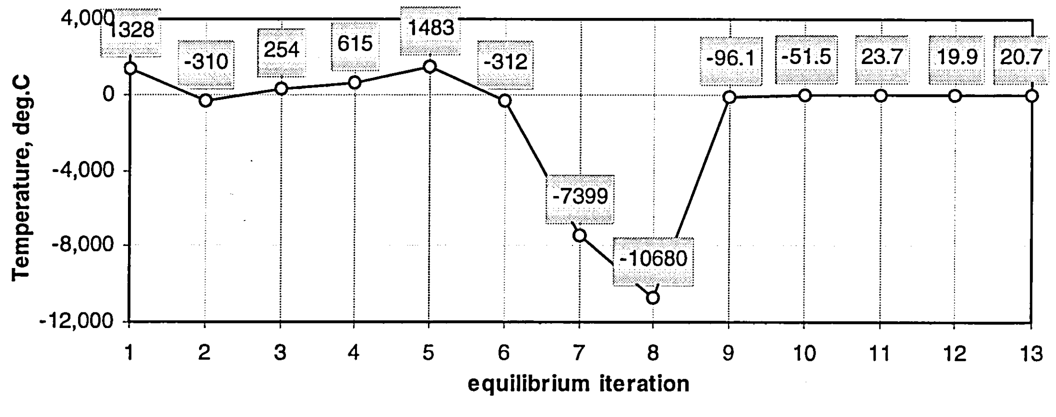

Figure 3-7. Largest increment of temperature for a 2% increase in current loading. The solution has converged at the equilibrium iteration No.13.

Finally, it was observed that ABAQUS behaviour can sometimes be rather unpredictable. For example, a slight modification of the electrical properties of the conductive film material may lead to cut-backs, excessive number of iterations or even the termination of the analysis, Table 3-4.

Table 3-4. The effect of slight modification of the electrical properties of the conductive film on the efficiency of ABAQUS convergence.

Parameter/Case	Case 1	Case 2	Case 3	Case 4
σ_1 Smm^{-1}	25,740.3	25,739.9	25,739.5	25,739.1
N° of iterations	36	56	56	45
Increments	10	20	19	14
N° of cut-backs	0	9	9	2
Solution obtained ?	yes	no	no	yes
Analysis time, hrs	14.3	42.2	43.6	22.1

The exceptional behaviour of the electro-thermal analysis for FE models comprising various non-linearities, necessitated the modification of some of the ABAQUS solution controls. The following controls were reset from their default values:

- since convergence may sometimes be initially irregular (Figure 3-5) to avoid premature cut-backs of the time increment, the equilibrium iteration after which the check is made that the residuals are not increasing (I_o) was reset to 7 (default is 4);
- the equilibrium iteration number at which the logarithmic rate of convergence check begins (I_r), was reset to 12 (default is 8);
- to prevent ABAQUS from increasing the time increment after cut-back the maximum number of equilibrium iterations in consecutive increments for the time increment to be increased, was reset to 1 (default is 4).

3.9. Summary

In Chapter 3 the methodology to predict the lifetime of TTFSF subjected to intermittent electric currents was presented. The methodology, adopted for this study, is based on finite element modelling of the electro-thermo-mechanical behaviour of TTFSF. The predicted amplitudes of the electro-thermally-induced stresses are used as the basis for subsequent fatigue analysis. The convergence of the electro-thermal procedure of the FE solver (ABAQUS) was investigated.

Chapter 4.

Finite Element Electro-Thermal Stress Analysis in Single-Layer and Multi-Layer Thin-Thick Film Substrate Fuse Elements

The electro-thermo-mechanical behaviour applied to single-layer and multi-layer thin/thick film substrate fuse elements is analysed in this Chapter. The electrical current density distribution, the temperature distribution due to Joulean heating of the conductive film, and the thermally induced stresses and deformation are examined using 3D FE non-linear methodology. The effects of the fuse element and substrate material properties and the geometry of the element on the magnitude of the critical stress components are also investigated. The results of the following studies form the foundation for the more comprehensive analysis of the life-time prediction of conductive films subjected to pulsed-current loading conditions of a typical commercially-available substrate fuse design (Chapter 5).

4.1. Model of the Substrate Fuse

4.1.1. Model Geometry

The substrate fuse geometry[1] investigated initially is shown in Figure 4-1.

---

[1] The dimensions of the geometry, representative of a feasible substrate fuse design, were provided by the Electrotechnical Institute in Gdańsk, Poland.

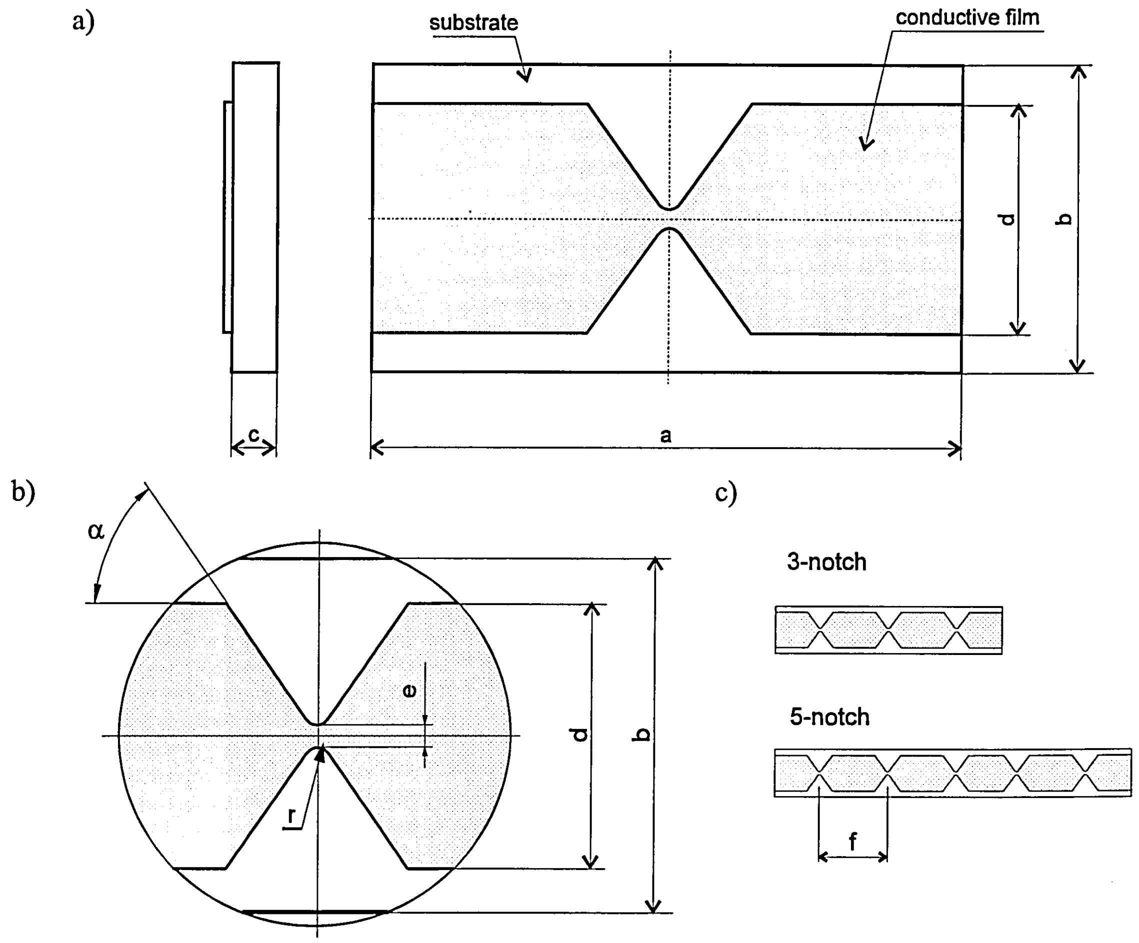

Figure 4-1. Substrate fuse models; a) substrate fuse geometry investigated; b) detailed geometry of the notch; c) derived 3-notch and 5-notch substrate fuse elements; dimensions: a=8mm, b=4mm, c=0.6mm, d=3mm, e=0.3mm, f=6mm, r=0.2mm, α=60°.

Single-notch, three-notch and five-notch geometries (Figure 4-1) were investigated. The length of the 3-notch fuse element was 20mm and that of the 5-notch fuse element was 32mm. The spacing between the notches (f) was 6mm. The fuse element was assumed to be surrounded completely by quartz sand filler (omitted in the above diagrams for clarity), typically used in HBC fuses. The planar geometry of the fuse element was identical for all models studied. The varying parameters were: fuse element length (number of notches), number of conductive films; thickness(es) of the conductive film(s); thickness of the substrate; electro-thermo-elastic properties of the conductive film(s) and, finally, the thermo-elastic properties of the substrate.

4.1.2. Finite Element Models

The FE model of the substrate fuse investigated essentially comprised the conductive film, substrate and filler. Due to symmetry only a symmetrical quarter of the fuse needed to be modelled. The conductive film was modelled using the DC3D8E 8-node linear coupled thermal-electrical elements (brick element). The substrate and the filler were modelled using the DC3D8 8-node linear heat transfer brick element. For the electro-thermal studies, FE models comprising one FE layer per conductive film and five FE layers in the substrate were constructed. Such an approach is valid, because the electro-thermal solution in the conductive film is planar[2] and, as a result, the analysis computational wavefront of these FE models is relatively small. However, for the thermal stress studies a more detailed FE model was required. This detailed model is now described.

The comprehensive FE model, Figure 4-2, was constructed to accommodate all the film/substrate geometric combinations previously referred to.

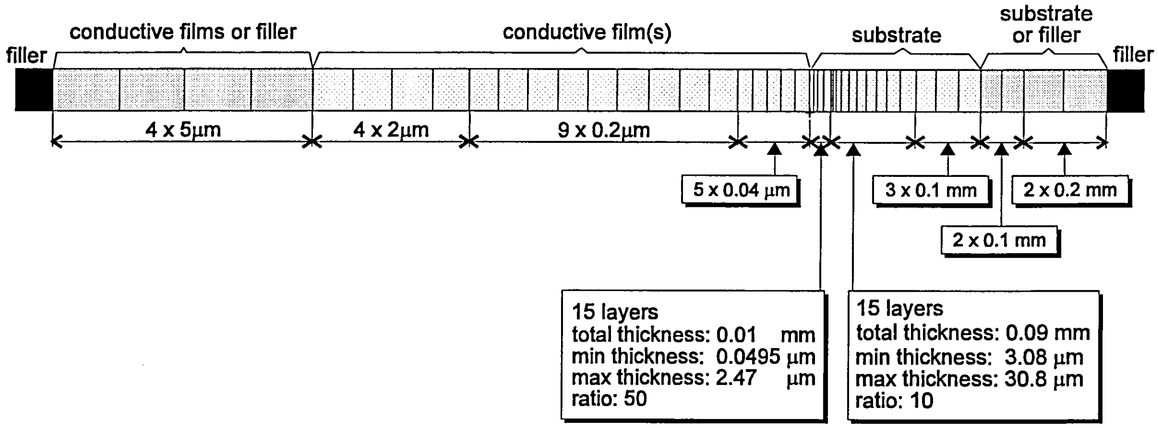

Figure 4-2. Mesh distribution model.

The FE model conforms to the following requirements:

- mesh density is finer around the notched region (in the 'x-y' plane);
- mesh density increases gradually towards the film/substrate interface (from both sides of the interface);
- the thickness of the conductive film can be varied within required limits (from 40nm to 30µm);
- additional substrate bonded (and metal bonded) film(s), whose thickness(es) can be varied within required limits, may be accommodated;
- the thickness of the substrate can vary within the required limits (from 0.4mm to 1.0mm).

The complete finite element model of the fuse element is shown in Figure 4-3 (Note that the filler is omitted in the figure for visual clarity purposes only).

---

[2] Some solution variables, such as the heat flux across the film thickness, exhibit significant differentials *within* the conductive film, in the third (Z) dimension (normal to the surface of the conductive film). Given that the exact profile of, for example, the heat flux within the conductive film is not the primary objective of this study, the single-FE-layer-per-conductive-film approach was, therefore, considered to be legitimate.

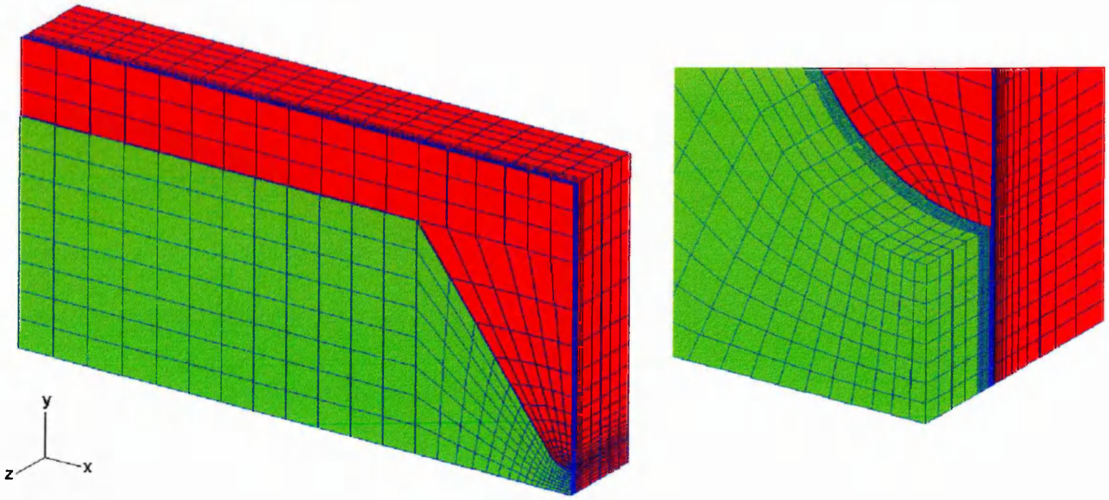

Figure 4-3. Finite element model of the symmetrical part of the fuse element.

The finite elements constituting the conductive film are plotted in green and those constituting the substrate are plotted in red. The mesh density increases gradually (in the 'x-y' plane) towards the notch, because this is the area where the physical changes are most pronounced. In particular, as high interfacial stress differentials occur across the film/substrate boundary, it is crucial that the mesh density across the film/substrate interface is sufficiently fine to enable computation of corresponding stress differentials within acceptable accuracy. Figure 4-4 shows the mesh density in the critical area of the film/substrate interface. This figure also shows the additional FE layers (plotted in pink and brown), which can be designated to the conductive film group(s), hence to permit films of up to 30μm in thickness to be modelled.

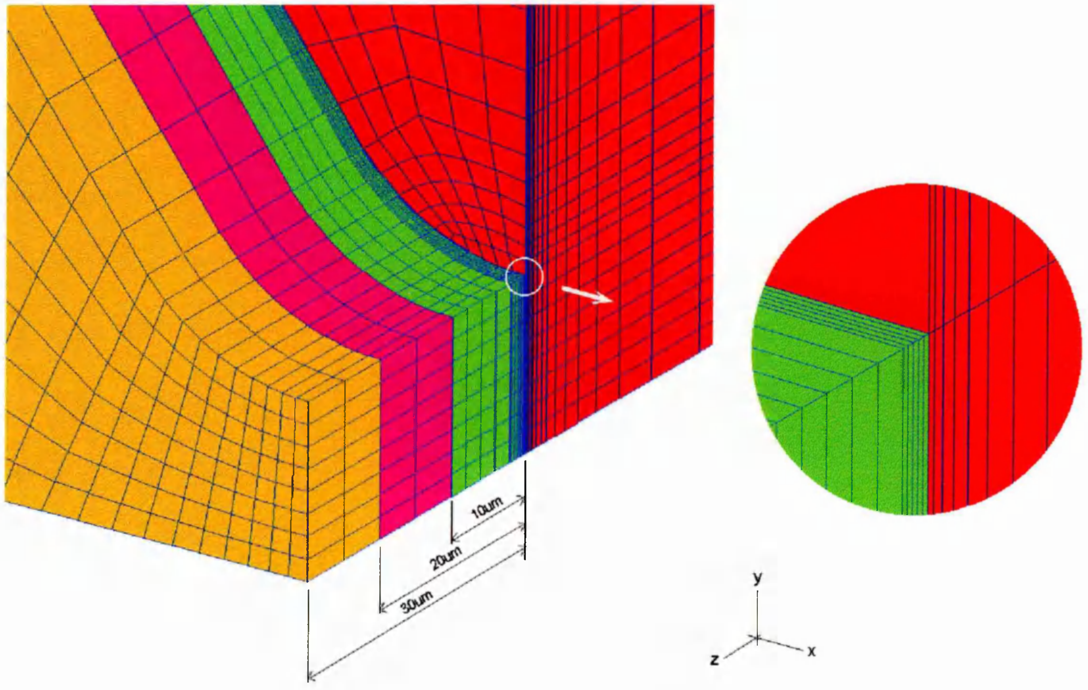

Figure 4.4. Mesh distribution in the vicinity of the notch – for clarity the FE mesh is magnified 10× in the 'Z' dimension.

The fuse element was assumed to be surrounded by an isotropic quartz sand filler. The filler was modelled as a solid (3D) body. The mesh was made much coarser in the filler and its density was reduced the further away from the fuse element. The complete fine-mesh FE model of the fuse (Figure 4-5), including the surrounding filler, was represented by 34,164 nodes and 31,157 elements.

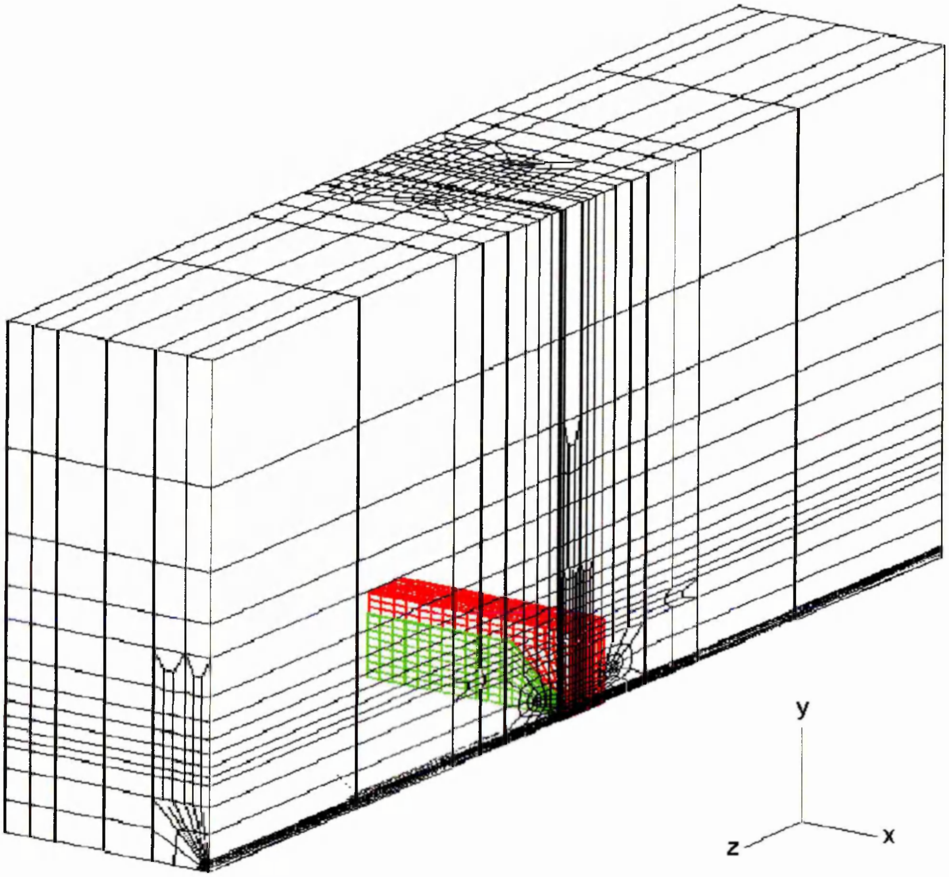

Figure 4.5. Complete finite element model of the symmetrical part of the fuse geometry. For clarity, the mesh of the fuse element and the substrate are shown through the mesh of the filler (plotted in red and green).

4.1.3. Verification of the Quality of the Mesh

The electrical solution was found to be very accurate even for badly distorted mesh. The temperature prediction was also very accurate. However, predicted magnitudes and distribution for the structural variables (thermal stress analysis) were found to be dependent on mesh quality, Figure 4-6. Consequently, greater care was taken to ensure that the quality of the mesh used for the thermal stress analysis (i.e. mesh of the conductive film and the substrate) was adequate, Table 4-1.

a)

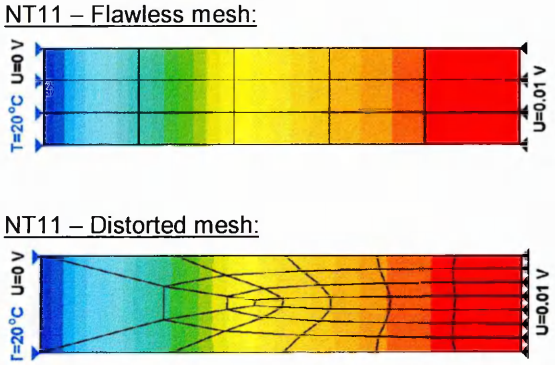
NT11 – Flawless mesh:

NT11 – Distorted mesh:

Variable magnitudes:

Variable	Flawless mesh	Distorted mesh	Error %
ECDM A/mm^2	378	378	0
JENER W/mm^3	2.268	2.268	0
NT11 deg. C	90.3	89.7	-0.66
HFLM W/mm^2	10.2	9.07	-11.1

b)

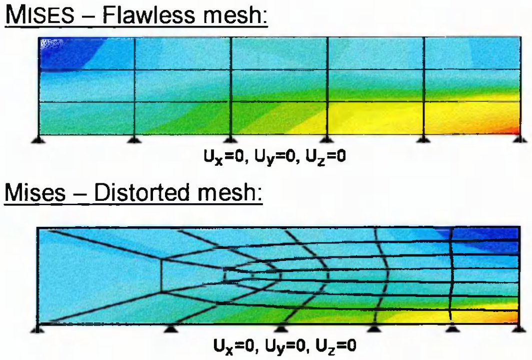
MISES – Flawless mesh:

Mises – Distorted mesh:

Variable magnitudes:

Variable	Flawless mesh	Distorted mesh	Error %
MISES N/mm^2	315	381	20.9
TRESCA N/mm^2	358	438	22.3
U_1 mm	2.06×10^{-3}	2.09×10^{-3}	1.4
U_2 mm	1.99×10^{-3}	1.89×10^{-3}	-5.02

Figure 4-6. Verification of the quality of the mesh; a) temperature distribution and variable magnitudes for flawless and distorted mesh (thermal-electrical analysis, element type: DC3D8E); b) MISES stress distribution and variable magnitudes for flawless and distorted mesh (thermal stress analysis, element type: C3D8).

Table 4-1. Verification of the quality of the mesh.

Test	Number of finite elements which failed the test	
	in the vicinity of the notch	in the film/substrate group
aspect ratio	N/A	N/A
edge angle	3	209
face skew	0	121
face taper	1	1
face warp	0	0
twist	0	0

4.2. Thermal-Electrical Analysis

The analysis commences by computing the electrical current density distribution in the conductive film for steady-state current flow. As previously referred to, the computation of the electrical field must be performed contemporaneously with the computation of the thermal field. This was achieved using the **Coupled thermal-electrical* option of ABAQUS (Appendix E). The single-notch and the three-notch fuse elements were examined on this basis.

4.2.1. Prescribed Boundary Conditions

The boundary constraints include both sets of electrical and thermal boundary conditions (BCs). The two electrical BCs include voltage symmetry U=0V applied to all nodes of the conductive film co-incident with the 'Y' plane of symmetry at the reduced section, and the nodal input voltage (or input current) applied to all nodes at the edge of the wide section of the conductive film, Figure 4-7. For the single-notch fuse model the input current boundary condition was used and the electric current was applied to all nodes at the edge of the wide section. The magnitude of the electric current of 22.3A (11.15A due to symmetry) was chosen to produce a maximum element temperature of 200°C under steady-state conditions. For the 3-notch fuse model the input voltage boundary condition was used and a voltage of 0.15V was applied to all nodes at the edge of the wide section.

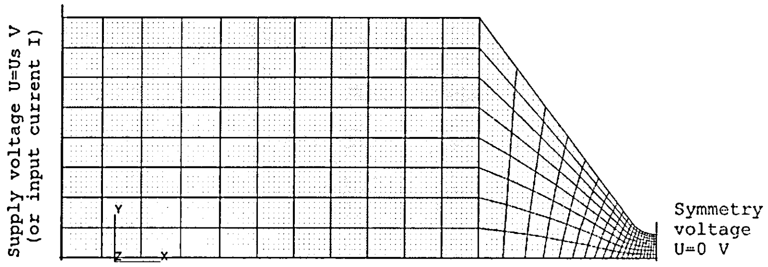

Figure 4-7. Applied electrical boundary conditions (the same methodology applies to the 3-notch fuse element).

The two thermal boundary conditions which apply are therefore:

- no heat flow (flux) occurs across the symmetry planes;
- the external surfaces of the fuse model are fixed at the ambient temperature (20°C).

4.3. Results of the Thermal-Electrical Analysis

4.3.1. Results of the Analysis in the Electrical Domain

The results of the analysis in the electrical domain include the distribution of the:

- electrical potential;
- electrical potential gradient;
- electric current density;
- energy dissipated per unit volume due to the flow of the electric current.

The last item is most important, as it has paramount effect on the heat generated in the conductive film. The results for the 3-notch fuse model are given in Figures 4-8 through 4-11.

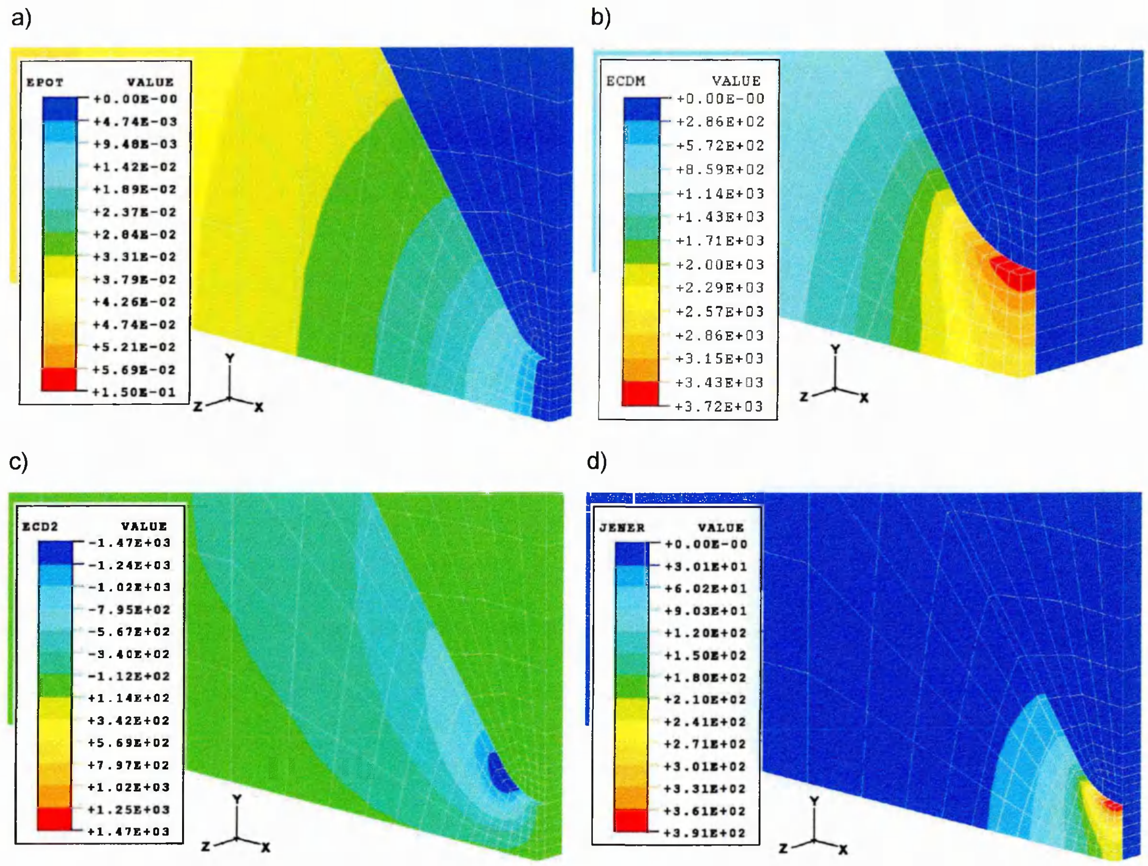

Figure 4-8. The results of the coupled thermal-electrical analysis of the 3-notch substrate fuse in the electrical domain – central notch.

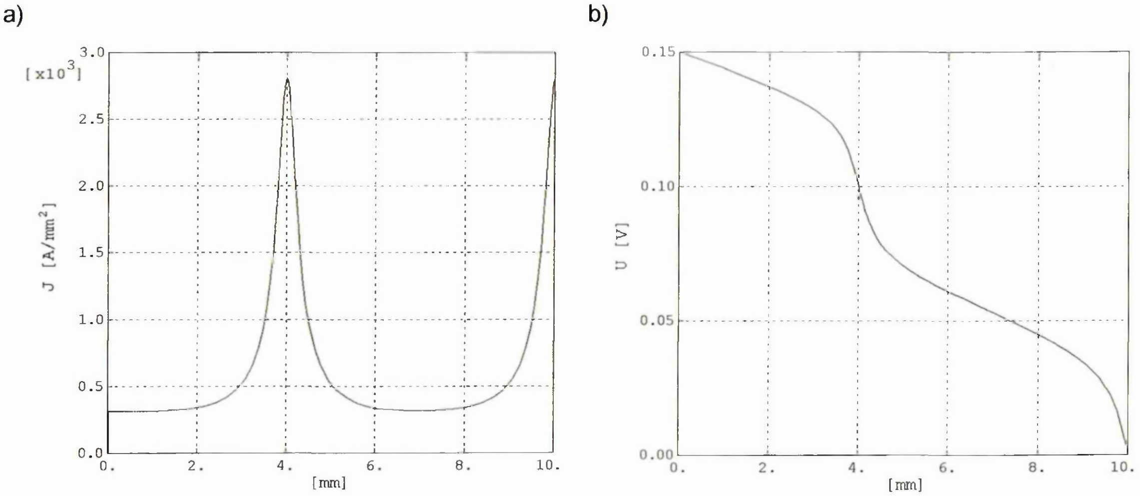

Figure 4-9. Electrical current density magnitude (a) and electrical potential (b) in the 3-notch fuse element along the symmetry line of the conductive film.

The results of this analysis indicate that:

- the electrical boundary conditions are satisfied (Figures 4-8 a, 4-8 c & 4-9 b);
- the magnitude of the electrical current density vector is, naturally, largest in the notches, (Figure 4-9 a); as a consequence the largest voltage gradients are located in the notches, (Figure 4-9 b);

- considering one notch only, current density is largest at the side of the notch, consequently the magnitude of the generated Joulean heat is largest at the side of the notch[3] (Figure 4-10 a);
- since the temperature of the middle notch is higher than the temperature of the side notch, more Joulean heat is generated in the middle notch (Figures 4-10 b & 4-11) despite the magnitude of the current density being the same in all notches (Figure 4-9 a).

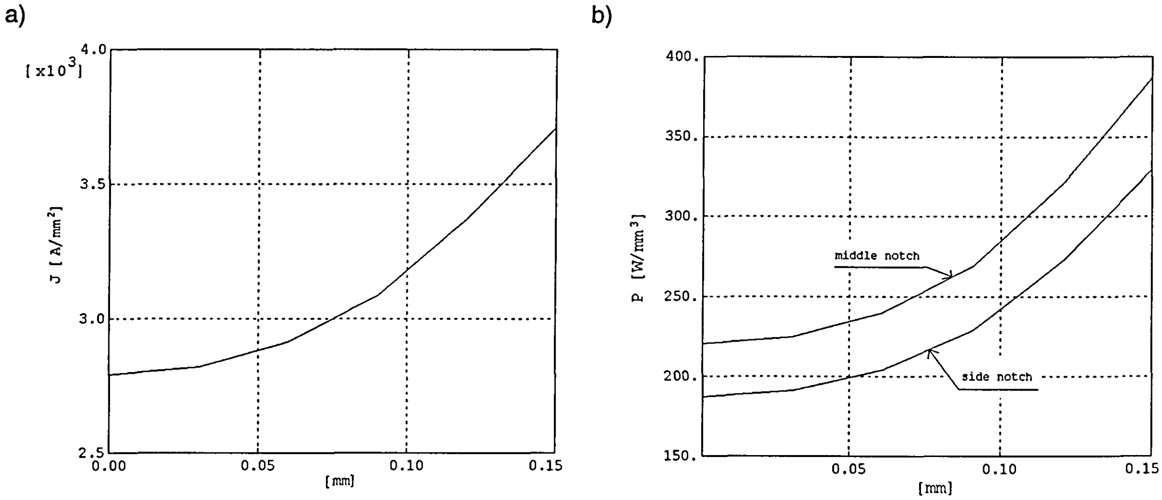

Figure 4-10. Electrical current density distribution across the notch along the 'Y' axis (a), and electrical power dissipated per unit volume across the middle and side notches along the 'Y' axis (b).

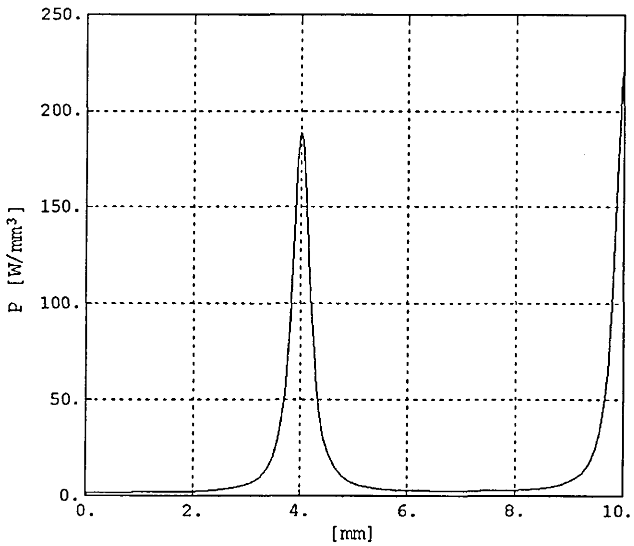

Figure 4-11. Electrical power dissipated per unit volume along the symmetry line of the conductive film.

---

[3] This finding is consistent with the results obtained by Rosen [6].

4.3.2. Results of the Analysis in the Thermal Domain

The amount of the generated heat is proportional to the magnitude of the current and the resistance of the conductive film. The resistivity of the conductive film material was allowed to vary with temperature, and for the film material studied (silver), it increases sharply with the temperature (Appendix G). The heat is conducted away from the notch to the element wider section and through the substrate and the filler. For any steady current below the minimum fusing current thermal equilibrium is established, whereupon the total heat generated equals the total heat conducted from the element. The computed steady-state temperature distribution profile in the 1-notch fuse element, carrying a DC current of 22.3/11.15A, is shown in Figure 4-12.

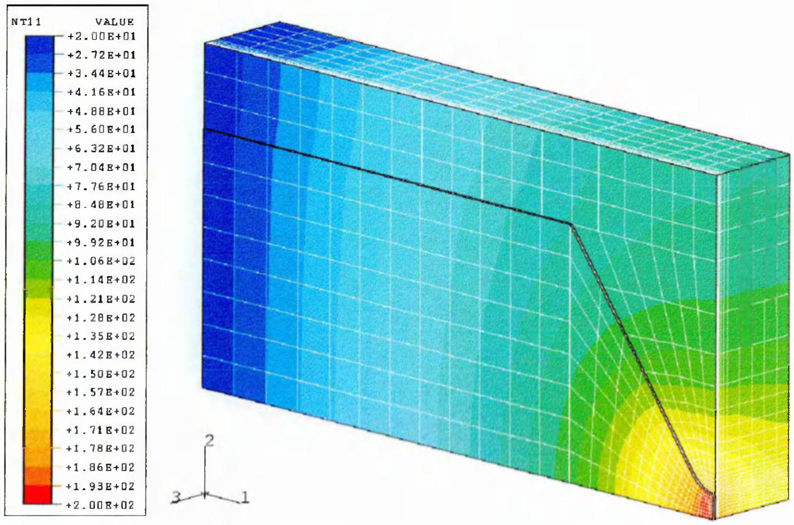

Figure 4-12. Steady-state temperature distribution in the fuse element carrying a DC current of 22.3/11.15A.

The magnitude and the distribution of the temperature in the vicinity of the notch have significant effect on the magnitude of the critical stresses and strains, which precipitate de-bonding or crack initiation at the weakest (most susceptible) section of the element geometry (Figure 4-13).

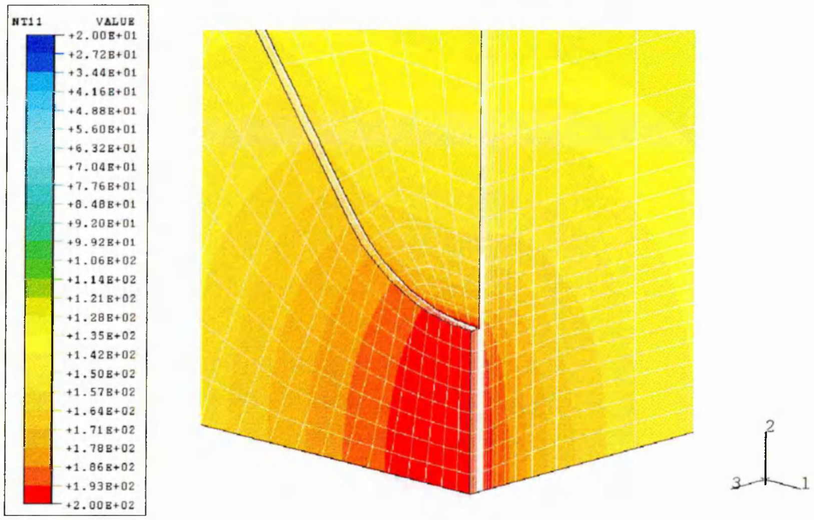

Figure 4-13. Temperature distribution in the vicinity of the notch.

The results for the 3-notch fuse element are presented below in greater detail, because the electro/thermal solution is more revealing in the 3-notch fuse element, compared to the 1-notch fuse element, and the coupling of the electrical field with the thermal field is more evident. The computed temperature distribution on the cross-section of the fuse element and the filler is shown in Figure 4-14.

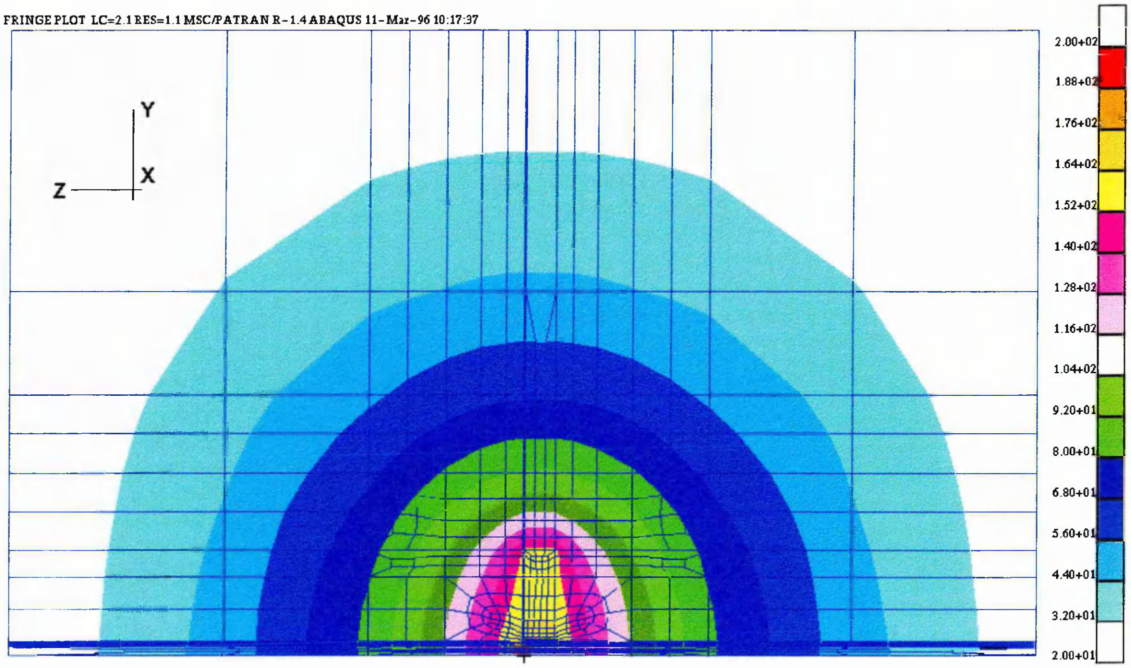

Figure 4-14. Temperature distribution on the 'Y' symmetry plane.

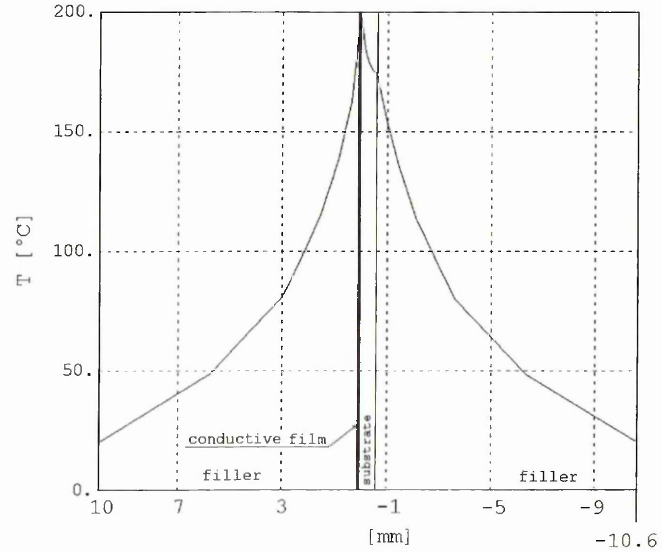

Figure 4-15. Temperature profile through the conductive film, substrate and filler, along the 'Z' axis of model symmetry, for the 3-notch fuse elements.

The temperature distribution in the fuse element is plotted in Figure 4-16. The temperature profiles along the conductive film and the substrate are shown in Figure 4-17.

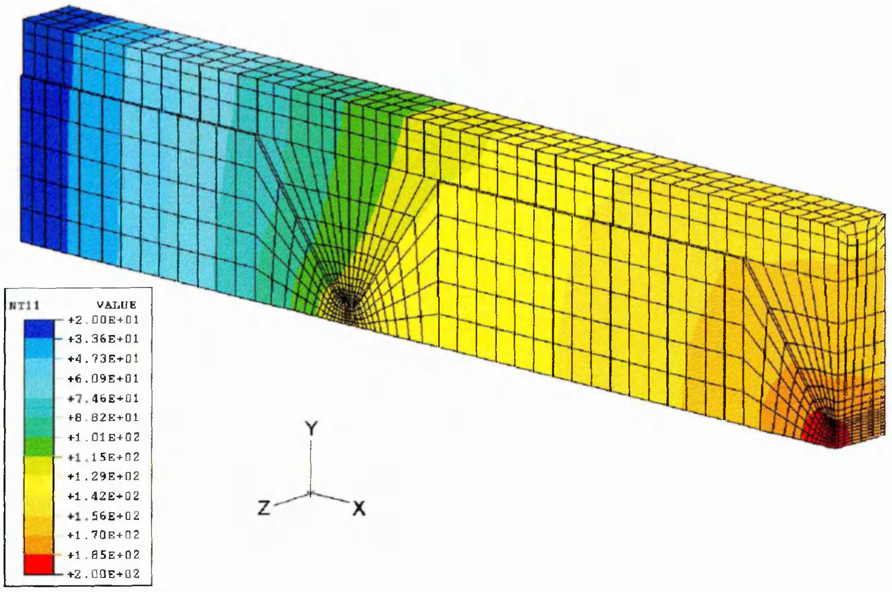

Figure 4-16. Temperature distribution in the 3-notch fuse element (filler omitted for clarity).

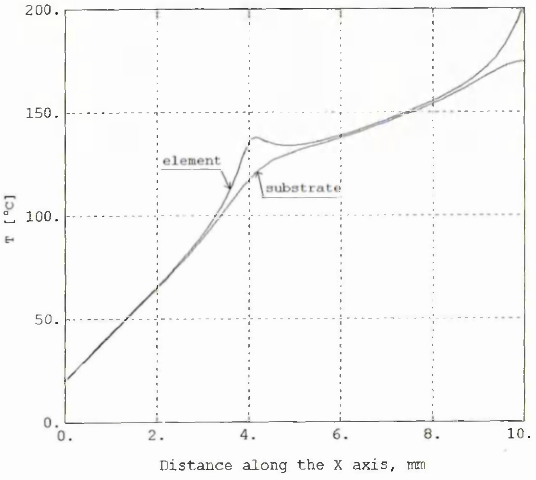

Figure 4-17. Temperature profiles in the conductive film along the 'X' axis of the element symmetry, and in the substrate along the 'X' axis of the substrate symmetry.

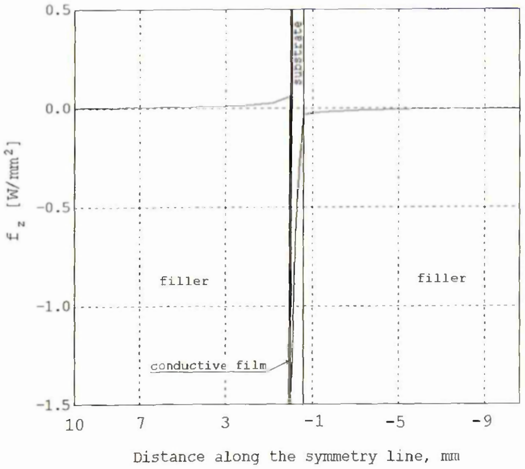

Figure 4-18. Heat flux in the conductive film, substrate and the filler along the symmetry line.

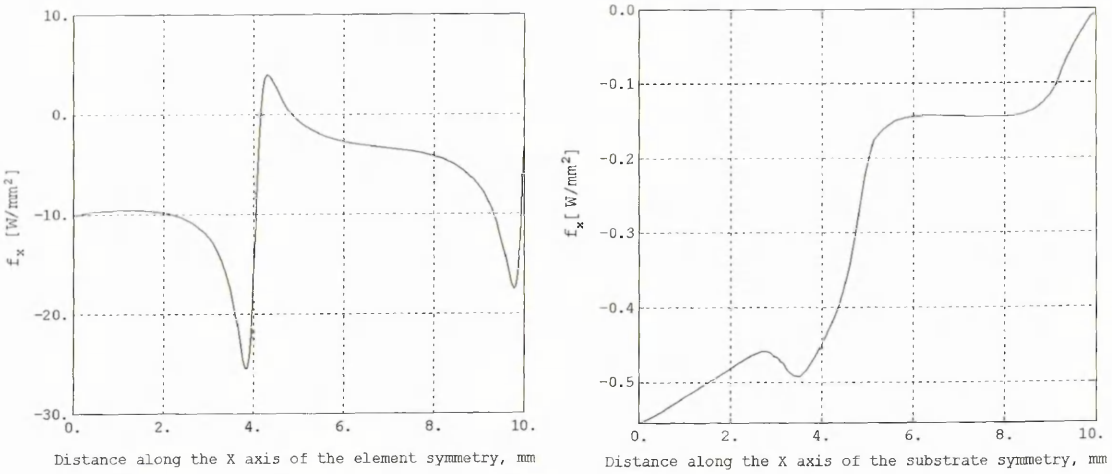

Figure 4-19. Heat flux along the symmetry line of the conductive film (a) and the average heat flux along the 'X' axis in the substrate (b).

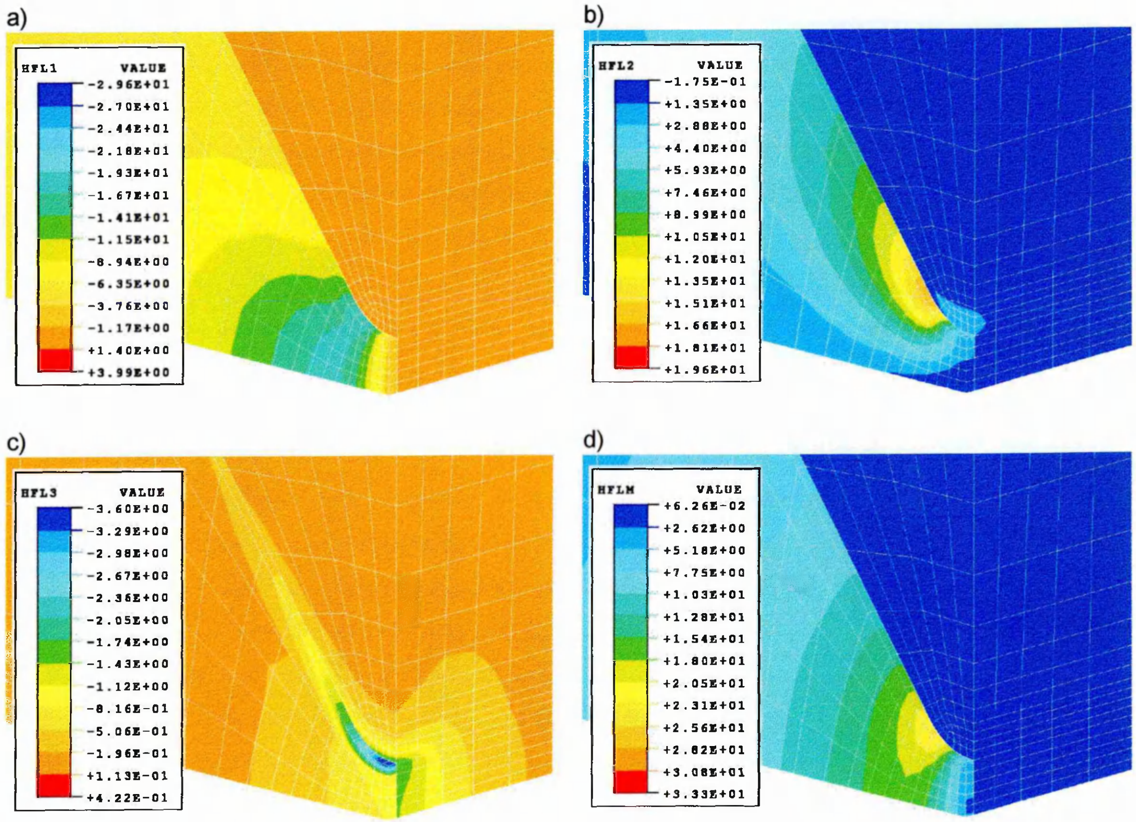

Figure 4-20. Heat flux components and magnitude in the vicinity of the middle notch (filler omitted for clarity). HFL_1, HFL_2, HFL_3 – the 'X', 'Y' and 'Z' components of the heat flux vector; HFLM – the magnitude of the heat flux vector.

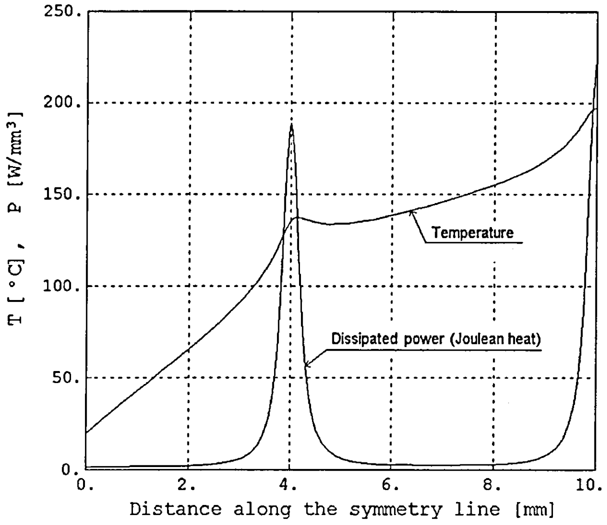

Figure 4-21. Effect of the temperature on the magnitude of the Joulean heat dissipated in the conductive film.

The results of the analysis indicate that:

- the mesh refinement is adequate for the electro-thermal problem investigated (e.g. Figures 4-13 & 4-14);
- the thermal boundary conditions are satisfied (e.g. Figures 4-12, 4-19 & 4-20);
- under steady-state conditions, maximum temperature can be found in the centre of the middle notch (Figure 4-13) despite the fact that the current density is largest at the side of the notch (Figure 4-10);
- since the thermal conductivity of the filler is very small, the heat flux through the filler is, consequently, very small (Figure 4-18);
- the heat flux through the substrate is much larger than the heat flux in the filler, and the heat flux in the conductive film is again much larger than the heat flux in the substrate, relative to the value of their respective thermal conductivities (Figures 4-19 and 4-20);
- on aggregate, however, the amount of the heat leaving the substrate across its external surface is more than twice the amount of the heat leaving the conductive film (across its external surface) (Figure 4-19);
- detailed examination of the heat flux vector field in the vicinity of the middle notch, shows that the heat flux is largest in the conductive film, where it is on average ten times larger than that in the substrate (Figure 4-20);
- The effect of the coupling of the electrical and thermal solutions is evident in Figure 4-21.

4.3.3. Dependence of the Temperature Distribution on the Thermal Properties of the Substrate

The thermal properties of the substrate affect the temperature distribution in the fuse element. The results of studies for two substrate fuse models comprising a 10μm silver film laid onto i) alumina and ii) pyrex substrates are now given. In both models the electric current was chosen to produce a maximum element temperature of 200°C. The value of the current was 13.8/6.9A for the pyrex-substrate sample, and 22.3/11.15A for the alumina-substrate sample. The temperature profiles through the conductive film and substrate thickness along the 'Z' axis of model symmetry are shown in Figure 4-22.

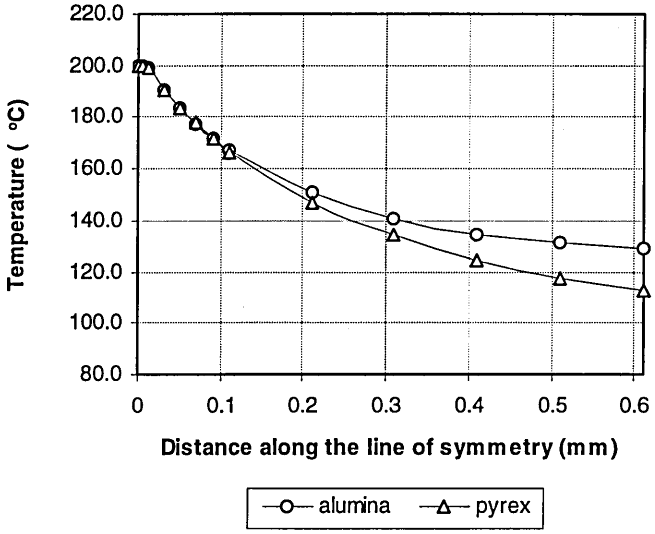

Figure 4-22. Temperature profiles along the 'Z' axis of model symmetry through the element and substrate thickness for two identical 10μm conductive films laid on alumina and pyrex substrates.

The different temperature profiles indicate that the magnitude and distribution of the stress, elaborated further in Paragraph 4.4.1, is affected by the elastic properties of the substrate and by the actual temperature distributions.

4.3.4. Comparison of the Current-Carrying Capacity and Short-Circuit Performance of Strip Fuses and Substrate Fuses

The pre-arcing thermal response to a short-circuit current in strip fuses was compared with the response of two substrate fuses. In the first case the fuse element was entirely surrounded by a quartz sand filler, in the other two cases the fuse element was laid respectively on to alumina and pyrex substrates. The fuse element in all cases was 10μm thick silver film. The pre-arcing time was found to be smallest for the pyrex-substrate fuse, and only slightly larger for the strip fuse. The pre-arcing time was largest for the alumina-substrate fuse, Figure 4-23.

This behaviour can be attributed to the thermal properties of the surrounding media (Appendix G). Alumina has larger thermal conductivity and thermal capacity compared to both pyrex and quartz sand, hence more heat is absorbed by alumina substrates and, consequently, the response is slower.

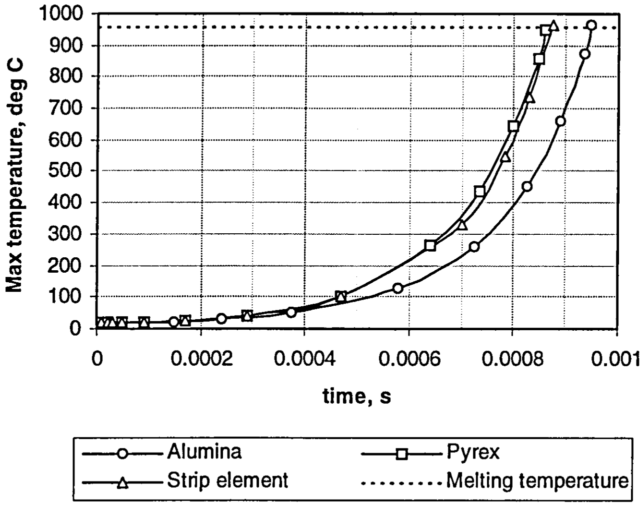

Figure 4-23. Comparison of the response to a short-circuit condition for a single-notch strip fuse and two substrate fuses; injected current: I=2,000A DC at t=0, circuit time constant τ=2ms.

Table 4-2. Pre-arcing times for alumina and pyrex substrate fuses compared to strip fuses.

Type of fuse	Pre-arcing time
	ms
strip element	0.875
pyrex substrate	0.860
alumina substrate	0.946

Although the pre-arcing time of alumina substrate fuses is slightly longer compared to strip fuses of the same geometry (Table 4-2), the substrate provides a heat sink and, consequently, under steady-state conditions more heat is conducted away from the notches through the substrate and, hence, the nominal current of fuse elements laid on substrates can be increased. This is demonstrated in Figure 4-24, where the maximum element temperature is shown versus steady-state RMS current for the three fuses discussed.

If the three fuses were to be operated at the maximum temperature of 300°C then the increase in current-carrying capacity would be such as illustrated in Table 4-3.

Table 4-3. Comparison of current-carrying capacity for alumina, pyrex and strip fuses.

Sample	Nominal current	Increase in nominal current compared to strip fuse element
	A	%
strip element	15.1	0
pyrex substrate	15.8	4.6
alumina substrate	24.8	64.2

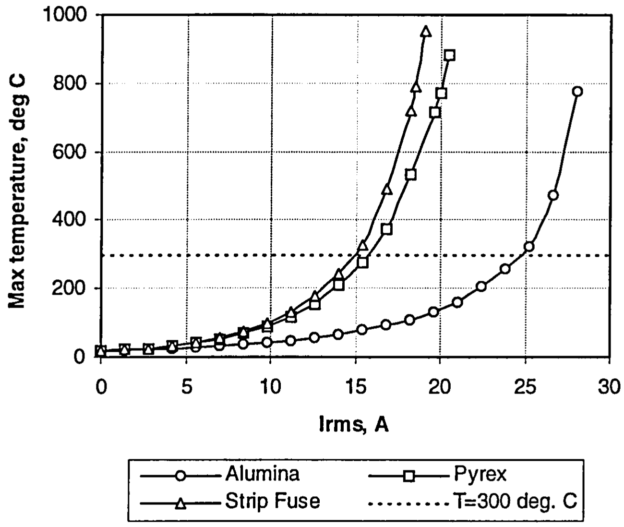

Figure 4-24. Comparison of the maximum element temperature versus the RMS current for a strip fuse and two substrate fuses.

The current-carrying capacity of alumina-based substrate fuses can be further enhanced by the use of wide and thin notches, which in effect increases the critical area in contact with the substrate, and improves heat transfer from the element to the substrate. The results of the studies on this phenomenon can be found in [4].

4.3.5. Substrates with Additional Heat Sink and Sandwiched Fuse Elements

The effect of attaching an additional heat sink to the bottom side of the substrate, and the effect of sandwiching the fuse element between two substrates on the current-carrying capacity of substrate fuses were studied. The substrate material was alumina and the heat sink material was copper. The silver film thickness was 11.1μm. The four samples analysed are illustrated in Figure 4-25.

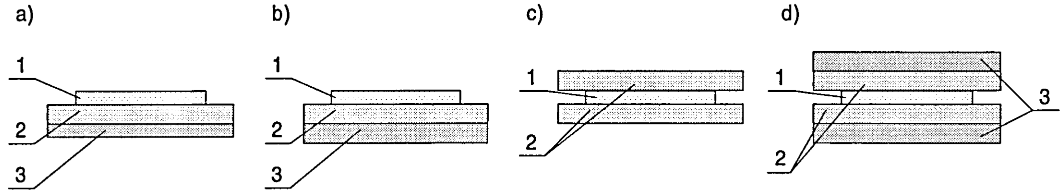

Figure 4-25. Fuse samples with additional heat sink(s) and sandwiched fuses. 1–conductive film, 2–substrate, 3–heat sink; a) heat sink thickness 0.2 mm; b) heat sink thickness 0.4 mm; c) fuse element sandwiched between two substrates; d) fuse element sandwiched between two substrates with two heat sinks each 0.4 mm thick.

The amount of heat transferred from the conductive film to the upper substrate is smaller compared to the amount of heat transferred from the film to the main substrate, because the film is deposited onto the main substrate, and the upper substrate is only mechanically pressed to the surface of the film. This property was modelled using a thin layer between the conductive film and the upper substrate. The thermal conductivity of this layer was arbitrarily chosen as half that of the substrate.

The maximum steady-state element temperature versus the RMS current for the four samples analysed is shown in Figure 4-26.

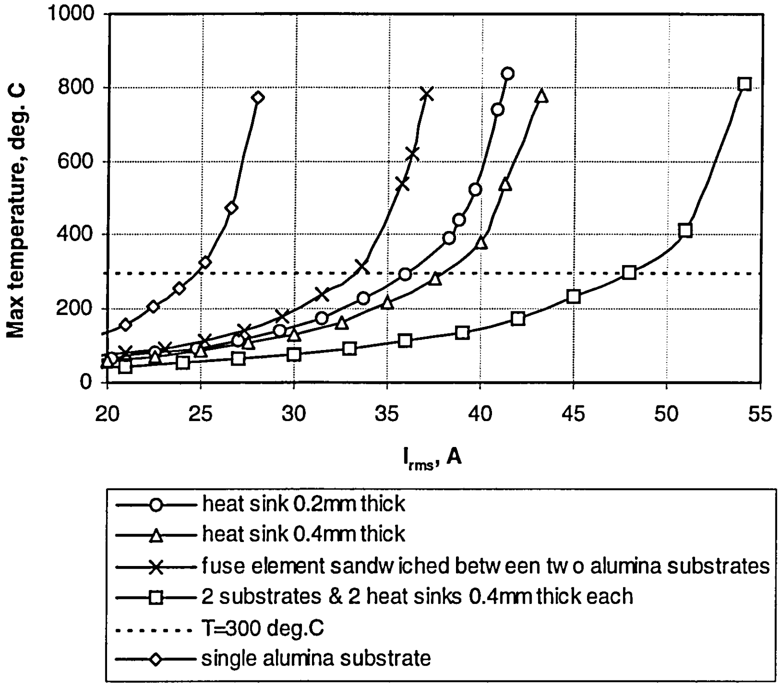

Figure 4-26. Current-carrying capacity of sandwiched fuses and fuses with additional heat sink(s); I=36/18A DC.

Temperature profiles through the filler, fuse element and substrate along the 'Z' axis of model symmetry, for the four models discussed (Figure 4-25) and, for comparison, for the single alumina substrate model, are presented in Figure 4-27. The effect of the additional heat sink(s) and the effect of sandwiching the fuse element between two substrates on the temperature magnitudes and temperature profiles are evident in this figure.

It is evident that the application of additional heat sink(s) and sandwiching the fuse element provide a means to increase the pre-arcing current-carrying capacity of the fuse. The computed pre-arcing time of t=1.34ms for the sandwich sample with two substrates and two heat sinks (Figure 4-25 d) was only 11.1% greater than the pre-arcing time for the single substrate sample (Figure 4-25 a). Sandwiching the fuse element between two substrates with two heat sinks, therefore, radically increases the current capacity (by a massive 217% compared to the strip fuse element), without a significant increase in the pre-arcing time, Table 4-4.

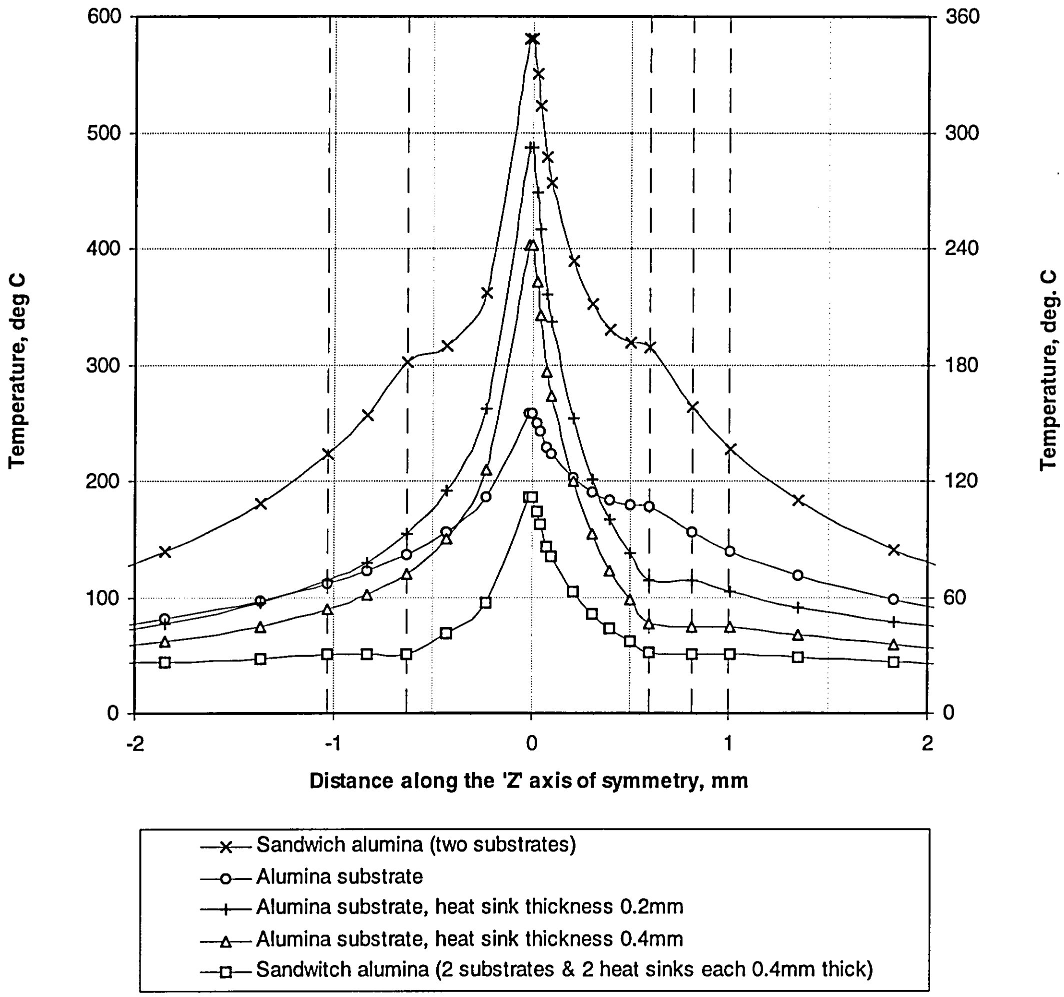

Figure 4-27 Temperature profiles along the 'Z' axis of model symmetry for sandwiched fuses and fuses with additional heat sink(s); left-hand scale for the sandwich alumina (2 substrates) model, right-hand scale for all other traces; injected current: alumina substrate model: 22.3/11.15A, all other models: 36/18A

Table 4-4. Comparison of current-carrying capacity for sandwiched fuses and fuses with additional heat sink(s).

Sample	Nominal current	Increase in nominal current compared to strip fuse element
	A	%
heat sink 0.2 mm thick	36.1	139
heat sink 0.4 mm thick	37.9	151
fuse sandwiched between two alumina substrates	33.3	120
sandwich fuse with two heat sinks 0.4 mm thick	47.9	217

Sandwiching the fuse element between two substrates is also advantageous from the arcing viewpoint, as it improves the arcing characteristics of the fuse, i.e. reduces the arcing let-through [3].

4.4. Thermal Stress Analysis of Single-Layer Substrate Fuse Elements

The models analysed in this section permit computation of the stress magnitude and distribution in single layer current-carrying fuse elements and the dependence of the maximum interfacial stresses and maximum deformation on the variation of the film thickness and the substrate thickness. The thermal stress analysis assumes that plasticity is neglected. In order to enable comparison of structural variables the magnitude of the electric current for all models presented in this section was chosen to produce a maximum element temperature of 200°C.

4.4.1. Stress/Strain and Displacement Distributions in Single Layer Fuse Elements

The combination of the elevated non-uniform temperature distribution, due to the flow of electric current (Figure 4-12) and the effect of external constraints, as previously discussed, generates internal thermal stresses in the fuse element. The whole of the conductive film was found to be in compressive stress, due to the large thermal expansion coefficient of silver. The bulk of the substrate is also in compressive stress (Figures 4-28 & 4-29).

In the 1-notch model, in the vicinity of the conductive film constriction, the substrate was found to be in compression. This is because the geometry of the 1-notch fuse element is almost square and both ends of the fuse element are fixed in the 'Z' direction. For longer fuse elements, however, the expected transition from tensile to compressive stress, at the film/substrate interface, is discernible (Figure 4-30).

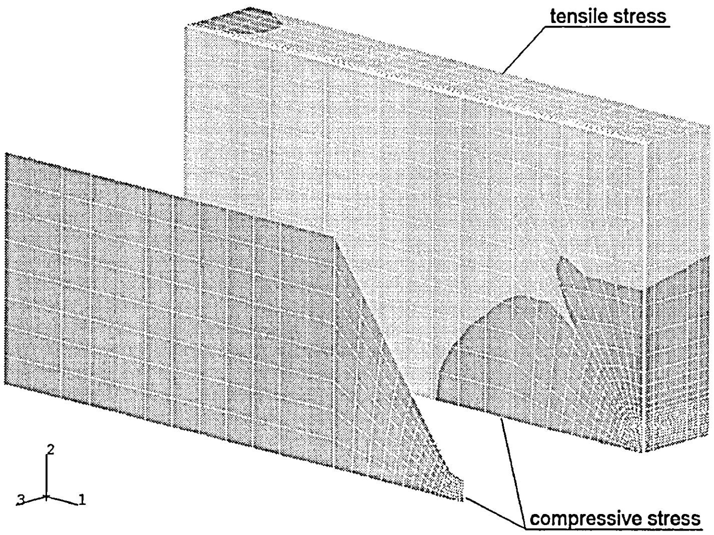

Figure 4-28. Equivalent pressure stress (PRESS) distributions showing parts of the model in compression (dark grey) and tension (light grey).

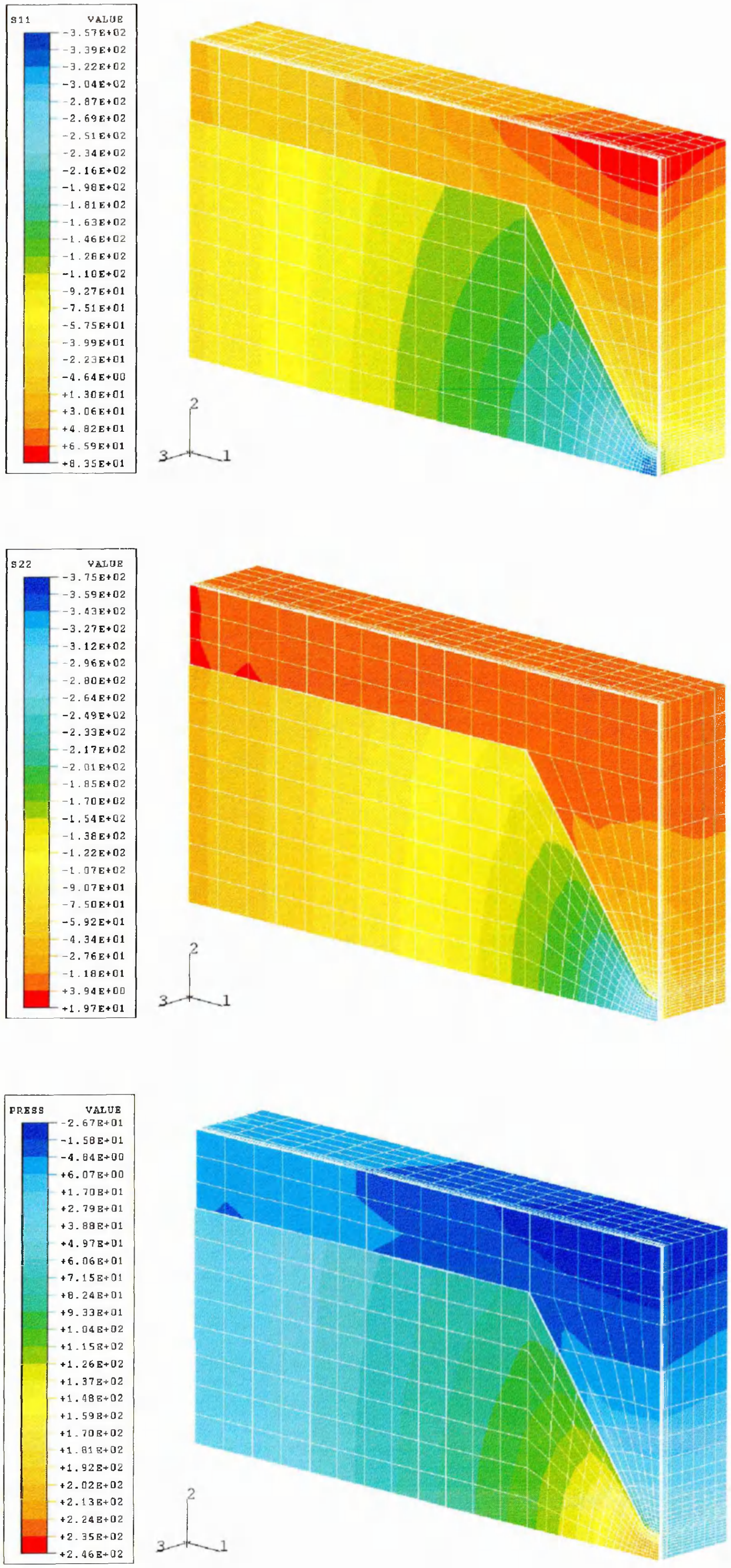

Figure 4-29. Direct stresses S_{11} and S_{22} and the equivalent pressure stress PRESS distributions.

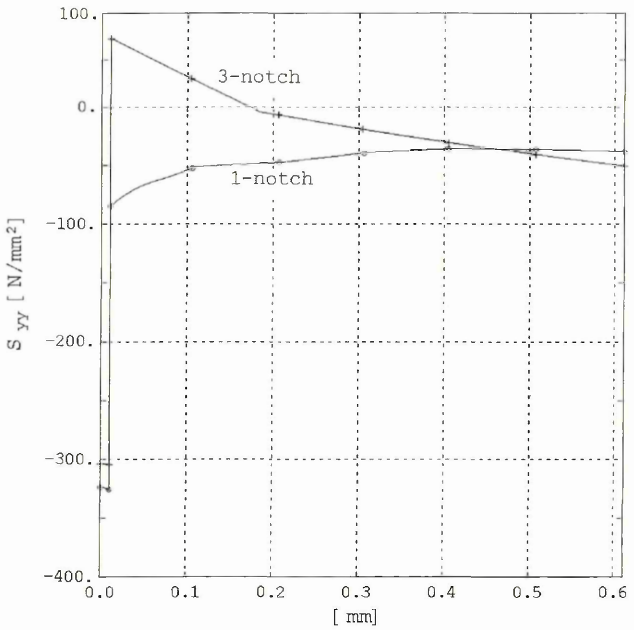

Figure 4-30. Stress S_{yy} profiles through the element and substrate thickness for the 1-notch and 3-notch fuse elements.

Let us consider the profiles of several components of the strain tensor along the symmetry line (see Appendix A for definitions of critical axes), through the element and substrate thickness (Figure 4-31).

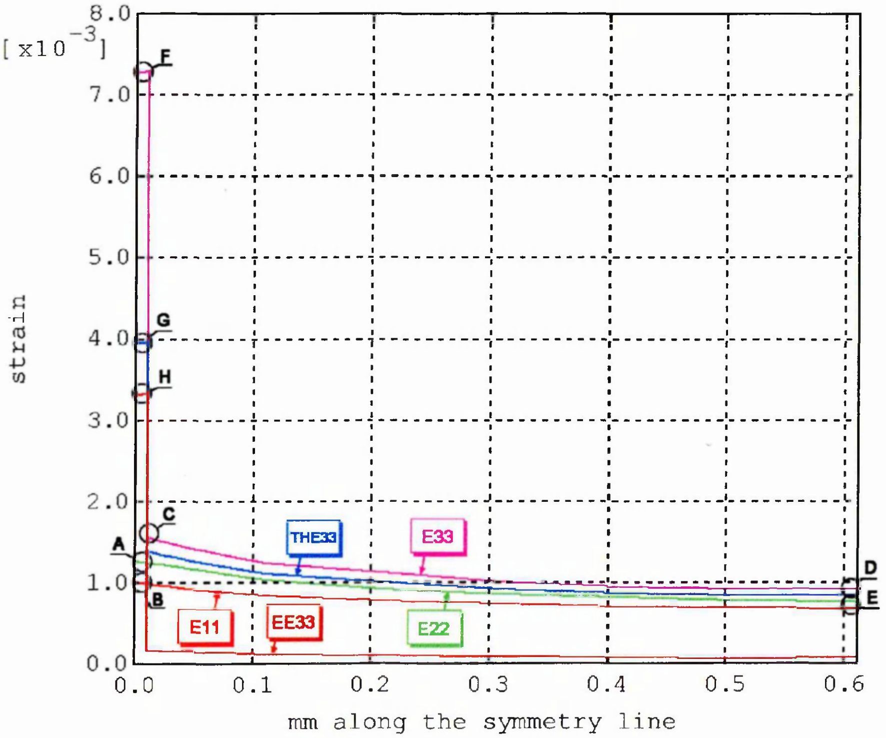

Figure 4-31. Profiles of the components of direct strain E_{11}, E_{22} and E_{33}, along the symmetry line, through the conductive film and substrate thickness; Also included is component THE_{33} of the thermal strain tensor; Components THE_{11} and THE_{22} are exactly equal to THE_{33} at all points, and are omitted or clarity; Also included is elastic strain EE_{33}. Elastic strains EE_{11} and EE_{22} were omitted for clarity;

The profiles of the direct strains E_{11}, E_{22} and E_{33}, and component THE_{33} of the thermal strain tensor along the 'Z' axis of model symmetry (Figure 4-31) indicate that:

- The fuse element is subjected to a combination of thermal and elastic strains (compare E_{33} with THE_{33} and EE_{33}). Elastic strain (*EE*) is defined as the difference between total strain and thermal strain, $EE_{ij} = E_{ij} - THE_{ij}$.
- Since the conductive film is rigidly fixed to the substrate, and the film cannot expand freely on the 'X-Y' plane, no discontinuity is allowed for the E_{11} and E_{22} functions, at the film/substrate interface. The results of the computational prediction are therefore valid (points A and B).
- Discontinuity at the film/substrate interface is allowed for the E_{33} function, because the conductive film can expand freely in the 'Z' direction (point C).
- The results indicate that the substrate can expand almost freely in the 'Z' direction, i.e. elastic strain EE_{33} is small.
- Strains E_{11} and E_{22} are smaller than the E_{33} strain throughout the substrate thickness, which indicates that the free expansion of the substrate on the 'X-Y' plane is restricted by the end terminations (e.g. at point E strain E_{11}=0.69×10^{-3}, which is 24% less than the value of strain E_{33} at that point, and E_{22}=0.78×10^{-3}, which is 14% less than E_{33}. If the expansion was not restrained then $E_{11}=E_{22}=E_{33}$).
- The value of total strain E_{33} at point F is $E_{33} = 7.25\times10^{-3}$. The thermal strain accounts for $THE_{33}^{(\text{Point G})} = 200^\circ\text{C}\cdot1.99\times10^{-5}\,\frac{1}{^\circ\text{C}} = 3.98\times10^{-3}$ of the total strain (Point G).

  The remaining portion of the strain is the elastic strain $EE_{33} = 7.25\times10^{-3} - 3.98\times10^{-3} = 3.27\times10^{-3}$ (Point H). This strain is due to the restrictions in the free expansion of the conductive film.
- The accuracy of the computer prediction can be quickly verified, e.g. thermal strain THE_{33} at point D should be: $THE_{33}^{(\text{pointD})} = 129^\circ\text{C}\cdot6.6\times10^{-6}\,\frac{1}{^\circ\text{C}} = 8.51\times10^{-4}$

  (temperature at Point D obtained from Figure 4-22, also note that $\alpha_{\text{Al}_2\text{O}_3}^{T=129^\circ\text{C}}$ was used, i.e. temperature dependent material properties). The computer prediction indicates $THE_{33} = 8.5\times10^{-4}$ (point D), i.e. the error is smaller than 0.1%.

Let us now consider the direct stress profiles along the 'Z' axis of symmetry, Figure 4-32:

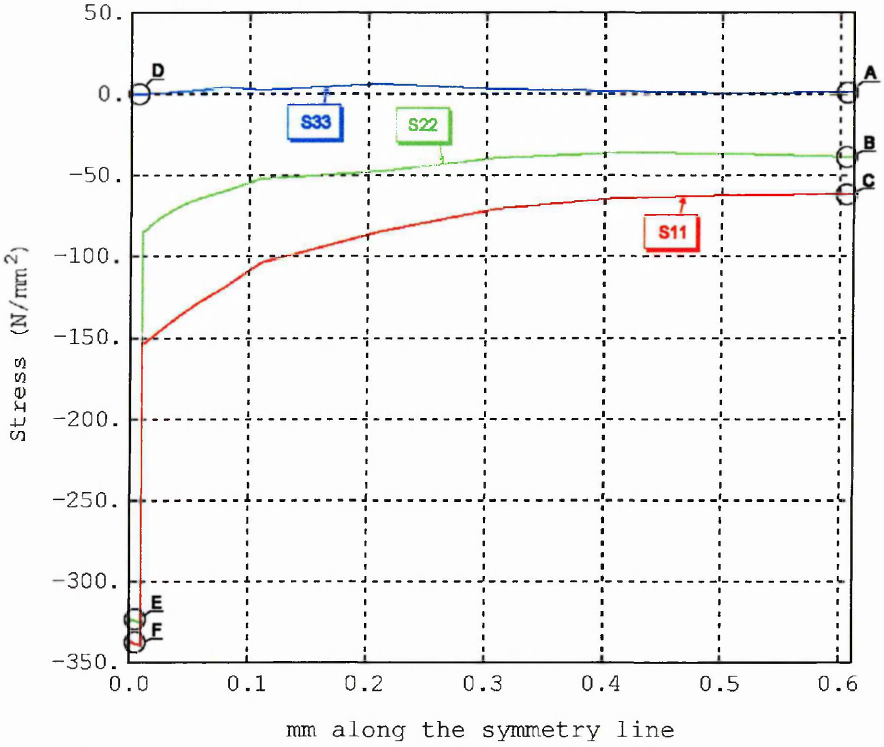

Figure 4-32. Direct stress profiles S_{11}, S_{22} and S_{33} along the symmetry line through the element and substrate thickness.

The profiles of the direct stresses S_{11}, S_{22} and S_{33} along the 'Z' axis of model symmetry (Figure 4-32) indicate that:

- The element can practically expand freely in the 'Z' direction; the direct stress S_{33} is, therefore, very small throughout the conductive film and substrate thickness (e.g. at Points A and D).
- The stresses S_{11} and S_{22} in the conductive film are very large, because the free expansion of the film is restricted by the substrate and the external constraints (Points E and F). The S_{33} stress, however, is very small, because the conductive film is not constrained in the 'Z' direction (Point D).
- The accuracy of the computer prediction can be quickly verified using the stress-strain relations (Paragraph 3.3.2, p.22), from which, for example, the S_{11} stress at Point C is calculated as:

$$S_{11} = \lambda e + 2\mu\varepsilon_{xx} - (3\lambda + 2\mu)\cdot\alpha(T - T_a) = 125{,}062\cdot 0.00239 + 2\cdot 135{,}484\cdot 6.9\times 10^{-4} - \\ -(3\cdot 125{,}062 + 2\cdot 135{,}484)\cdot 6.56\times 10^{-6}\cdot 129 = -60.9\ \mathrm{N/mm^2}$$

where:

$$\lambda = \frac{\nu E}{(1+\nu)(1-2\nu)} = \frac{0.24\cdot 336{,}000}{(1+0.24)(1-2\cdot 0.24)} = 125{,}062\,,$$

$$\mu = \frac{E}{2(1+\nu)} = \frac{336{,}000}{2\cdot(1+0.24)} = 135{,}484$$

and $e = \varepsilon_{xx} + \varepsilon_{yy} + \varepsilon_{zz} = 0.69\times10^{-3} + 0.78\times10^{-3} + 0.92\times10^{-3} = 2.39\times10^{-3}$.

Using the same procedure, the S_{22} and S_{33} stresses, at Point B and Point A, are respectively: $S_{22} = -36.5$ N/mm^2 and $S_{33} = 1.4$ N/mm^2. The computer prediction indicates that $S_{11} = -61$ N/mm^2 (Point C), $S_{22} = -38$ N/mm^2 (Point B), and $S_{33} = 1.4$ N/mm^2 (Point A). The computer prediction is, therefore, accurate and satisfactory in these respects.

As both silver and alumina have positive thermal expansion coefficients, the whole fuse element expands with rising temperature. Given that the thermal expansion coefficient of silver is approximately 3 times larger than that of alumina the whole assembly, therefore, tends to buckle upwards (in the 'Z' direction). The magnitude of the deformation can be quantified by the displacement vector field $\mathbf{U} = \mathrm{U}(x,y,z)$, Figure 4-34.

The U_1, U_2 and U_3 components of the displacement vector field (Figure 4-34), clearly indicate that: i) the applied displacement boundary conditions are legitimate; and ii) as envisaged, the fuse element buckles in the 'Z' direction. The actual displacements are very small, in the order of several microns. The deformation is more pronounced in longer fuse element, Figure 4-33.

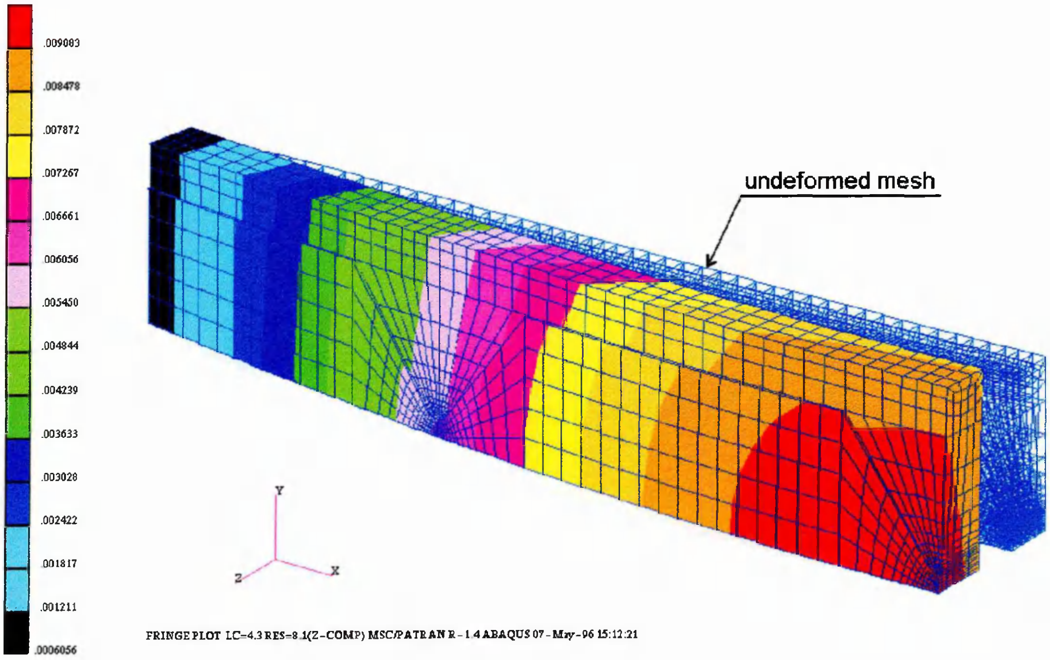

Figure 4-33. Deformation (U_3) of a 3-notch substrate fuse element (for clarity the magnitude of the deformation was magnified 150x).

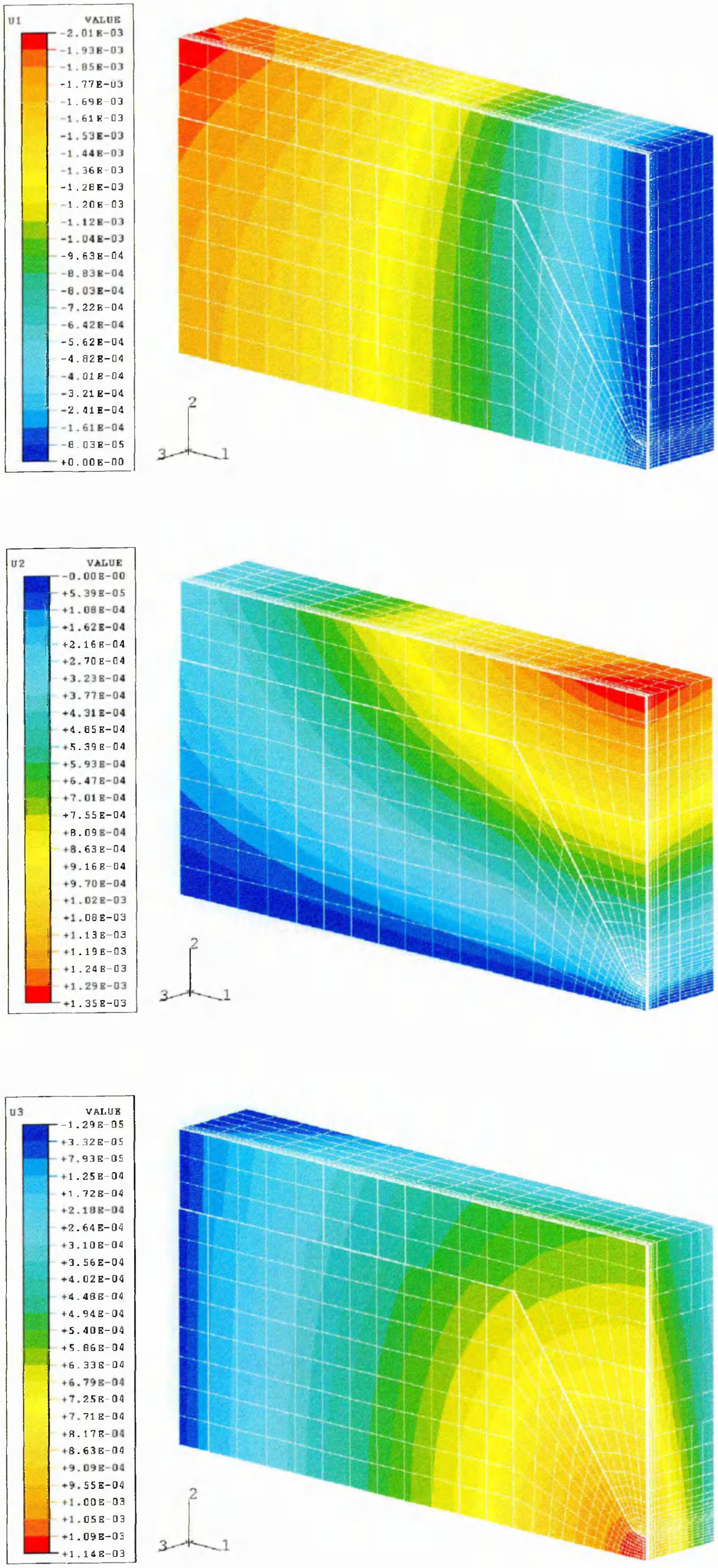

Figure 4-34. Displacement components U_1, U_2 and U_3.

The results presented to this point summarise the physical structural behaviour of the whole substrate fuse element carrying steady-state electric current. It is apparent also that the critical stresses and strains affecting fuse lifetime are located in the most narrow regions of the element notch. Moreover, for film de-bonding the film/substrate interfacial stresses are the most critical and they are dependent on the shape of the notch. These respective critical stresses/strains are elaborated below.

The mechanical forces trapped in the conductive film resulting from the film/substrate thermal expansion coefficient mismatch generate planar shear stresses at the film/substrate interface. The shear stresses (Figure 4-35) are, as expected, largest at the interfacial film/substrate notch edge. The S_{31} and S_{32} components are the most critical for film de-adhesion, because they act in the 'X-Y' plane. The S_{12} component of the shear stress is, naturally, much smaller. The maximum shear stress (TRESCA) is shown in Figure 4-35 d).

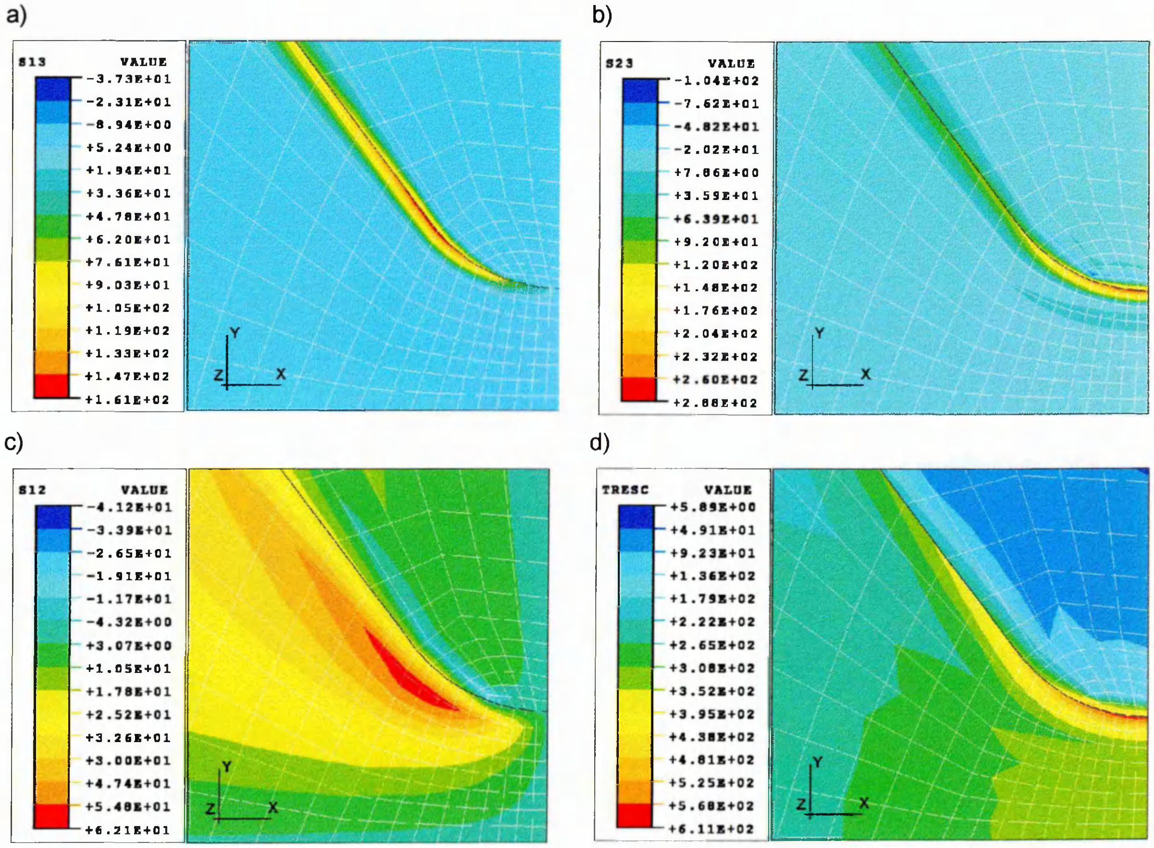

Figure 4-35. Shear stress components S_{13}, S_{23}, S_{12} and maximum shear stress (TRESCA) distributions at the conductive film/substrate interface (conductive film omitted for clarity).

The TRESCA, S_{31} and S_{32} shear stresses are most pronounced along the interfacial film/substrate notch edge, the actual stress profiles along that line are shown in Figure 4-36. The S_{32} and the TRESCA stresses are maximum at the point of the minimum cross-section of the notch – the critical point (Points A & D in Figure 4-36). The S_{31} shear stress is zero at the critical point (Point B), and is maximum at Point C. The precise location of the maximum depends on the temperature distribution and on the geometrical shape of the conductive film. As the temperature falls away from the notch all shear stresses decrease in magnitude.

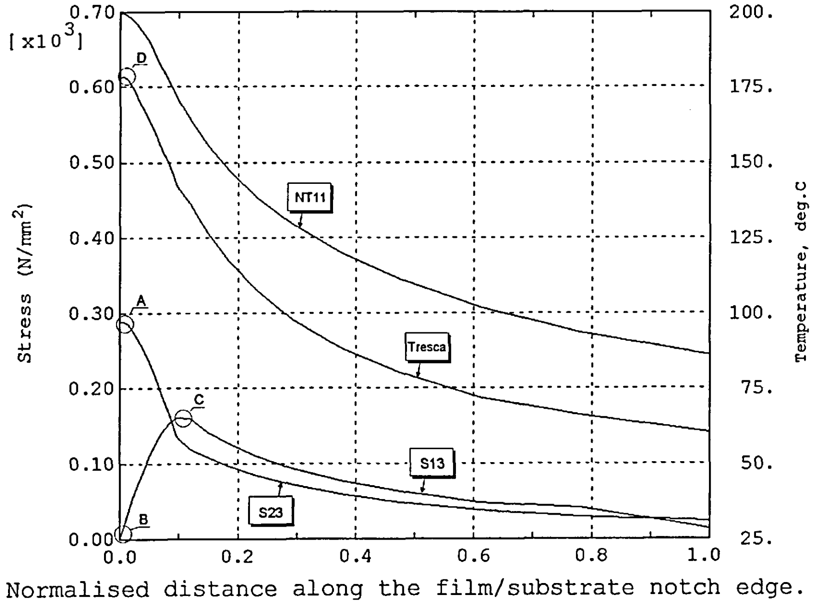

Figure 4-36. Maximum shear stress (TRESCA) and shear S_{13} and S_{23} stress profiles in the conductive film along the film/substrate notch edge.

The shear stresses are also very small within the conductive film and the substrate the further away they are measured from the film/substrate interface (Figure 4-37).

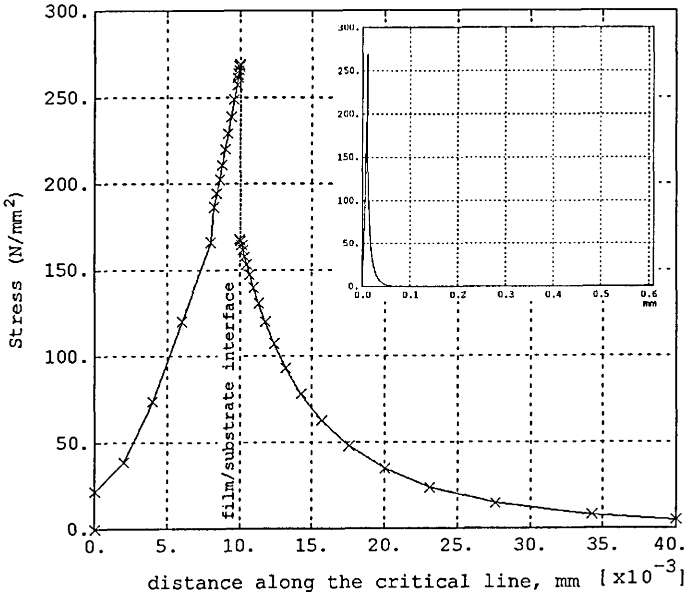

Figure 4-37. Shear stress S_{zy} along the critical line.

It is postulated that film de-bonding will commence at the point of the maximum shear stress acting along the film/substrate interface (the critical point). Theoretically, when the value of the shear stress exceeds the adhesion bonding strength the film will de-bond from the substrate.

In an idealised case the point of the maximum shear stress will, subsequently, commute to the next node on the interfacial film/substrate line, Figure 4-38.

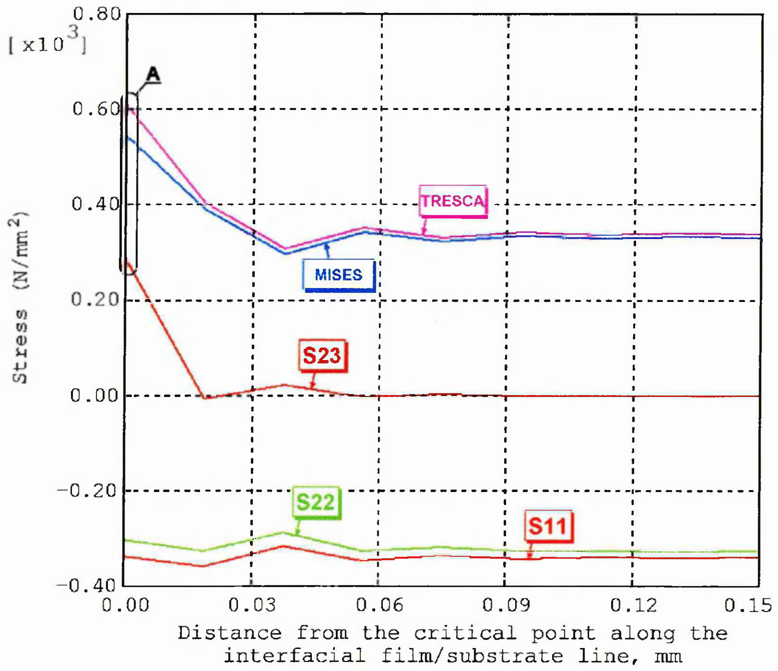

Figure 4-38. Stress profiles at the film/substrate interface along the ‘Y’ axis.

The distribution of the direct strains E_{11} and E_{22}, in the vicinity of the notch (Figure 4-39 & 4-41), indicates that the conductive film cannot expand freely on the ‘X-Y’ plane. It is only along the conductive film edge that the film can expand freely, hence the direct strains are largest along this edge.

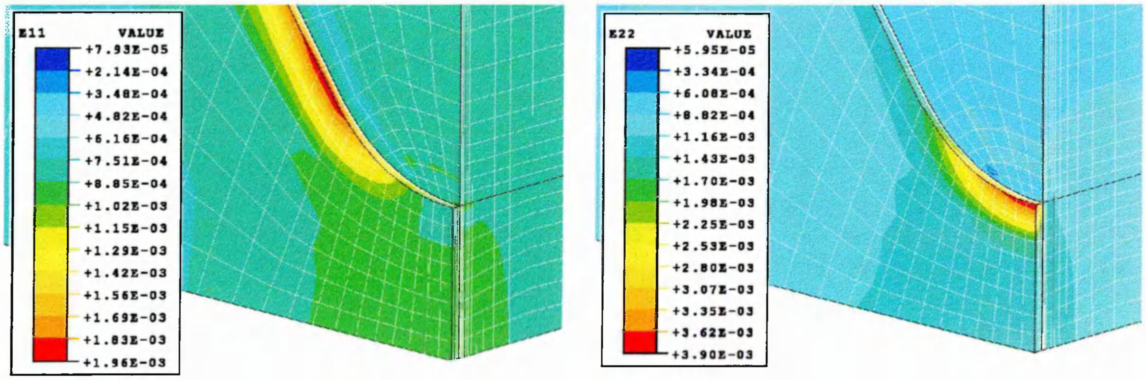

Figure 4-39. Direct strains E_{11} and E_{22} in the vicinity of the notch.

The expanded view of the magnitude of the deformation/strain in the conductive film clarifies this finding (Figure 4-40).

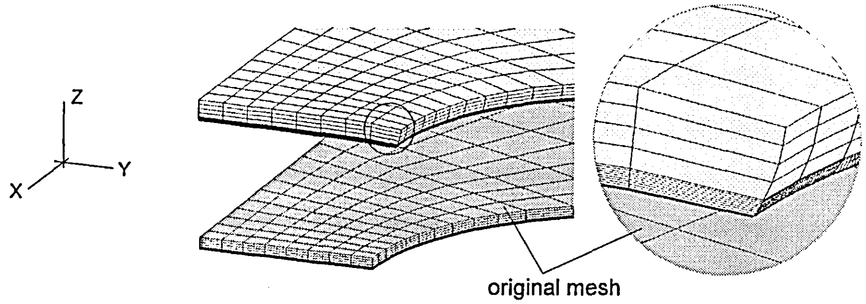

Figure 4-40. Magnitude of the deformation in the conductive film in the vicinity of the notch, deformation magnified 100x (substrate mesh omitted for clarity).

The shear strains E_{13} and E_{23} are largest along the interfacial film/substrate notch edge, and the direct strains E_{11} and E_{22} are largest along the film notch edge (Figure 4-41).

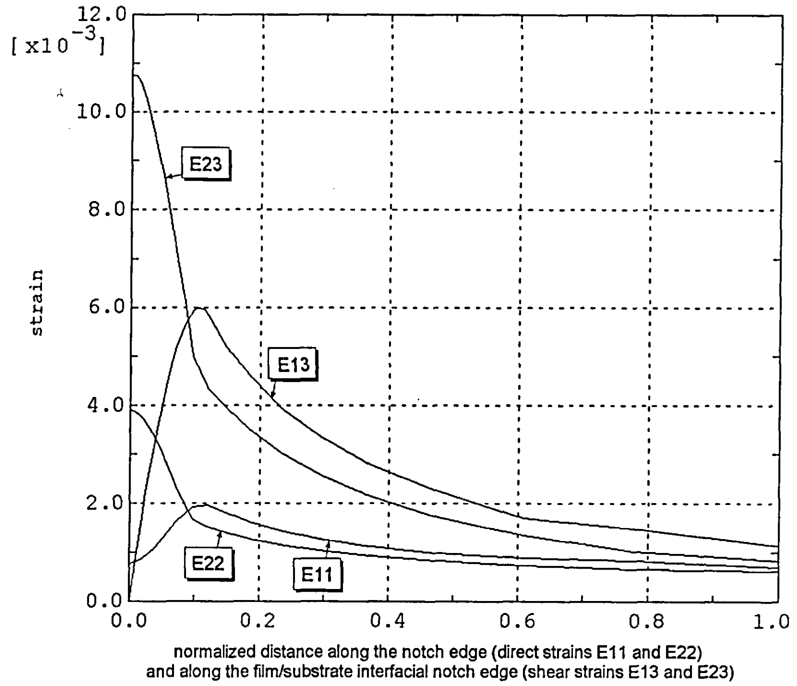

Figure 4-41. Direct strains E_{11} and E_{22} along the notch edge; shear strains E_{13} and E_{23} along the interfacial film/substrate notch edge.

The direct and shear strains cannot be overlooked because, at substantially elevated temperatures, parts of the notch experience plastic deformation and the magnitude of the stress alone no longer reflects the exact elastic/plastic behaviour of the specimen.

4.4.2. Dependence of the Magnitude of the Deformation on the Length of the Fuse Element

Single-notch, 3-notch and 5-notch fuse elements (see Figure 4-1 c) were analysed to verify the effect of the length of the fuse element on the magnitude of the deformation. The results of the computational study indicate that the magnitude of the deformation increases with the length of the fuse element (Figure 4-42).

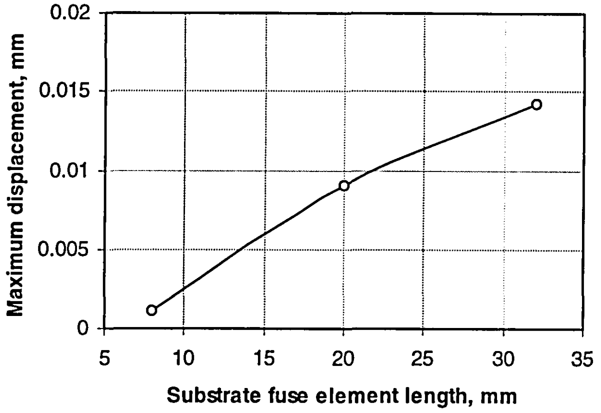

Figure 4-42. Dependence of the magnitude of the deformation on the length of the fuse element.

4.4.3. Dependence of the Magnitude of Stress and Deformation on the Thickness of the Conductive Film

Three fuse elements were analysed. The geometry and dimensions of the fuse elements were identical for all cases, except for the thicknesses of the single conductive film layers studied: these being 11μm, 21μm and 31μm. The results of the computer simulation are presented in Table 4-5 and graphically in Figures 4-43 & 4-44.

Table 4-5. Results of the variable film thickness analysis.

Sample No	Film thickness	Max. interfacial MISES stress	Max. interfacial shear stress S_{ZX}	Max. interfacial shear stress S_{ZY}	Maximum shear stress TRESCA	Max. displacement U_Z
	μm	N/mm^2	N/mm^2	N/mm^2	N/mm^2	mm ×10^{-3}
1	11	494	133	245	544	1.21
2	21	582	188	317	657	1.65
3	31	638	217	358	727	2.03

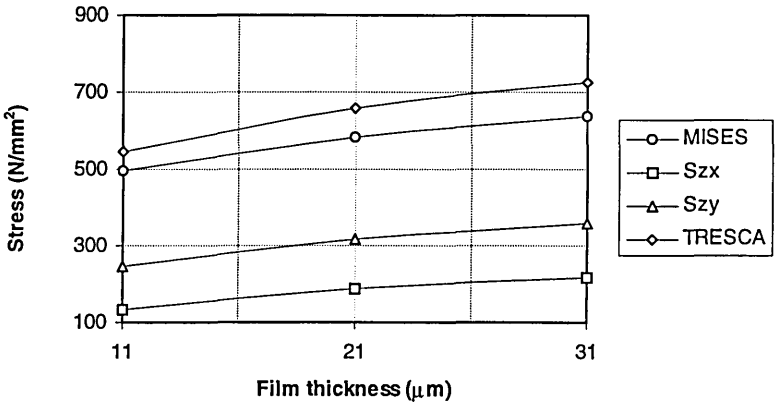

Figure 4-43. Dependence of the maximum MISES, TRESCA, S_{zx} and S_{zy} stresses on the film thickness.

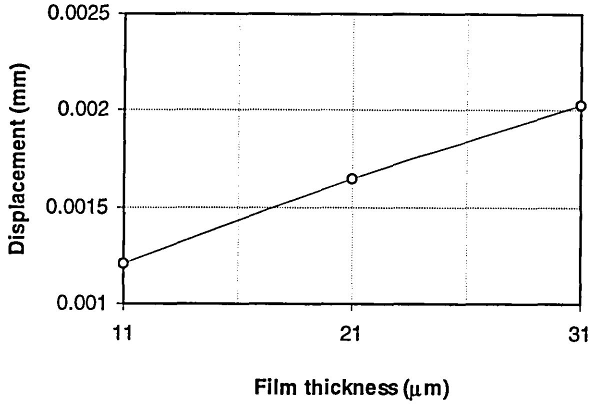

Figure 4-44. Dependence of the maximum displacement U_3 on the film thickness.

Figures 4-43 and 4-44 indicate that increasing the film thickness produces greater trapped stress in the film and increased deformation and that the trapped stress produces greater interfacial shear stresses when the film thickness is increased. Thin conductive films are, therefore, superior to thick films in this respect, i.e. thinner films produce smaller deformation and also all significant stress components are smaller in thinner film fuse elements.

4.4.4. Dependence of the Magnitude of Stress and Deformation on the Thickness of the Substrate

Three fuse elements of different substrate thickness were analysed. The silver film thickness (11μm) was unchanged. The geometry and dimensions of the alumina substrate (except for its thickness) were also unchanged for all cases analysed.

The results of the analysis are summarised in Table 4-6 and in Figures 4-45 & 4-46.

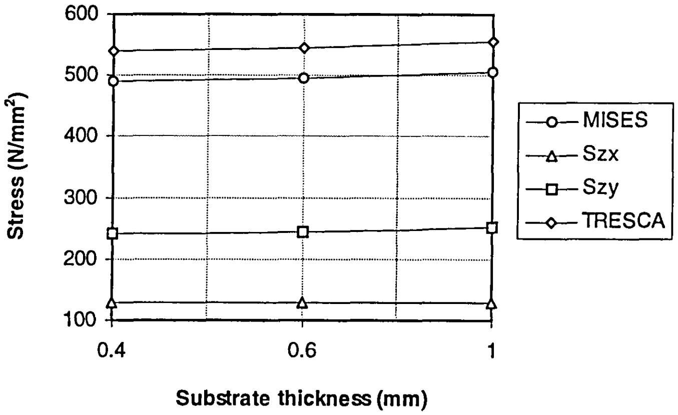

Figure 4-45. Dependence of the maximum interfacial MISES, TRESCA and S_{zx} and S_{zy} stresses on the substrate thickness.

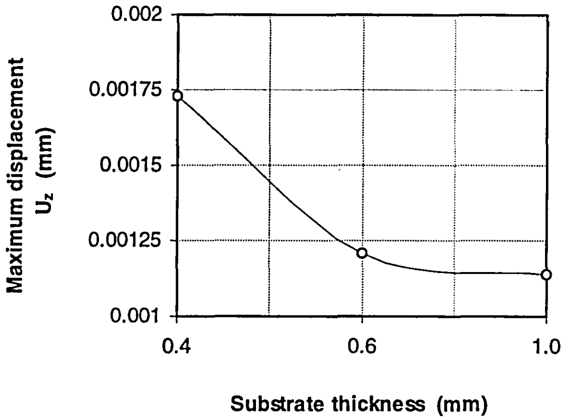

Figure 4-46. Dependence of the maximum displacement *Uz* on the substrate thickness.

Table 4-6. Results for the variable substrate thickness analysis.

Sample No	Substrate thickness	Maximum interfacial MISES stress	Maximum interfacial shear stress S_{ZX}	Maximum interfacial shear stress S_{ZY}	Maximum shear stress TRESCA	Maximum displacement Uz
	mm	N/mm^2	N/mm^2	N/mm^2	N/mm^2	mm ×10^{-3}
1	0.4	491	128	242	540	1.73
2	0.6	494	128	245	544	1.21
3	1.0	505	129	251	556	1.14

From Figures 4-45 & 4-46 it is observed that, in general, varying the substrate thickness has no significant effect on the maximum interfacial shear stresses S_{zx} and S_{zy} and that thin substrates are more flexible which results in increased deformation. As the maximum interfacial MISES stress and maximum interfacial shear stresses TRESCA, S_{zx} and S_{zy} all decrease when the thickness of the substrate is decreased, thin substrates are recommended to minimise stress. However, thin substrates are vulnerable to increased deformation. As the reduction in stress in thinner substrates is not significant, and the increase in maximum displacement $\hat{U}_3$ is evident, the thickness of the substrate should not be smaller than approx. 0.4mm, if exaggerated deformation is to be avoided.

4.4.5. Dependence of the Magnitude and Profile of the Stresses on the Elastic Properties of the Substrate

The results of varying the properties of the substrate material on the stress distribution for two single-layer fuse elements were examined. The geometry and dimensions of the fuse element and the substrate were identical for both cases. The main thermal and mechanical properties of the substrate materials studied are given in Table 4-7. The results of this analysis are presented in Table 4-8 and Figure 4-47.

Table 4-7. Main properties of the substrate materials studied.

Substrate material	Thermal conductivity	Thermal exp. coefficient	Young's modulus
	W/mm°C	$10^{-6}\,°C^{-1}$	N/mm^2
Alumina[4]	0.025	6.0	339,000
Pyrex[5]	0.0011	3.3	64,000

Table 4-8. Results of the analysis of the effect of varying the thermo-elastic properties of the substrate on the magnitude of the interfacial stresses.

Substrate material	Maximum Interfacial MISES Stress	Maximum Interfacial Shear Stress S_{ZX}	Maximum Interfacial Shear Stress S_{ZY}	Maximum Shear Stress TRESCA	Maximum Displacement U_Z
	N/mm^2	N/mm^2	N/mm^2	N/mm^2	$mm \times 10^{-3}$
Alumina	494	133	245	544	1.21
Pyrex	517	135	240	539	2.89

As previously referred to (Paragraph 4.3.3, p.50) the temperature distributions (Figure 4-22) in the two samples are different due to different thermal properties of the substrate materials. Consequently, the stress distribution and stress magnitudes are affected by both the elastic properties of alumina and pyrex, and by the actual temperature distributions.

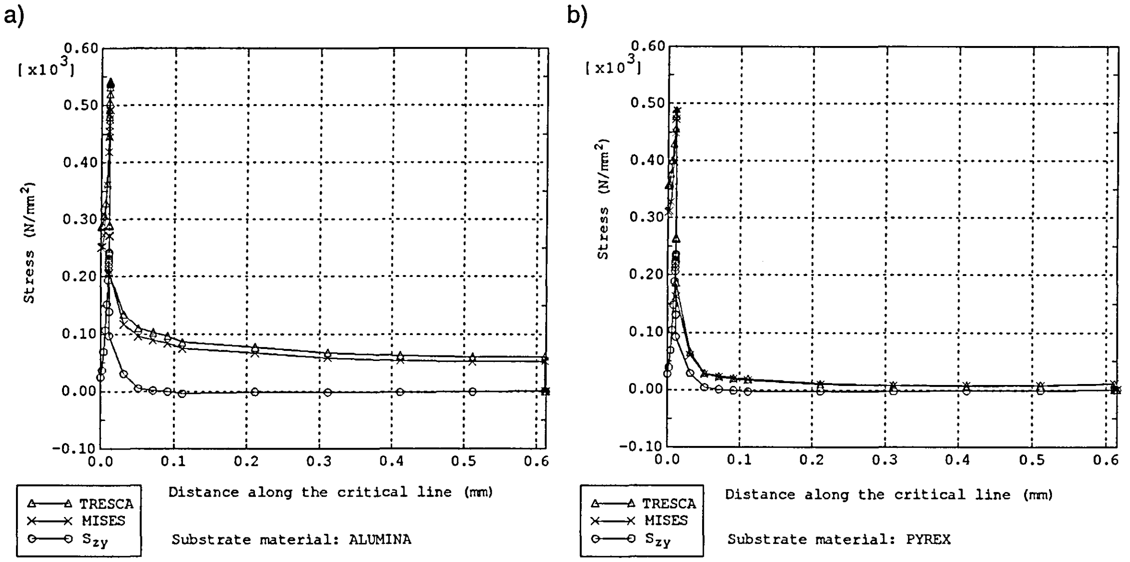

Figure 4-47. MISES, TRESCA, and S_{ZY} stress profiles along the critical line for alumina (a) and pyrex (b).

The main findings are:

- The MISES stress along the critical line through the substrate thickness (Figure 4-47) is significantly smaller for pyrex, because its Young's modulus is more than five times

---

[4] Group A6 alumina, nominal Al_2O_3 content 96.5 – 99 %

[5] Pyrex borosilicate glass, SiO_2 – 81%, B_2O_3 – 13%, Na_2O – 4%, Al_2O_3 – 2%

smaller than that of alumina. This result indicates that, neglecting the large interfacial stresses, the life-span of a pyrex fuse element would be longer.

- The different modulus of elasticity (Table 4-7) is the reason for increased deformation, given that a smaller value of Young's modulus indicates a more flexible material.
- The maximum values of the critical stress components (Table 4-8) are not significantly different for the two samples studied. However, this may be different for other metal film/geometry combinations and for longer fuse elements.

Results of the studies on the dependence of the maximum values of the critical stress components on the substrate material properties for multi-layer fuse elements can be found in Paragraph 4.5.3, p.76.

4.5. Thermal Stress Analysis of Multi-Layer Substrate Fuse Elements

Multi-layer films are commonly used in thin film technology to reduce the substrate-film interfacial stress and improve the adhesion strength of the composite [97], because: i) resistive films have better adhesion properties with ceramic substrates; ii) the magnitude of the interfacial shear stresses can be transferred from the metal film/substrate interface to the interfacial metal film/metal film interface[6]; iii) due to alloying at the metal/metal interface the adhesive strength of that interface is much larger than the adhesive strength of the metal film/substrate interface. From the mechanical viewpoint it would also be advantageous to have the resistive substrate bonded film (SBF) deposited over the whole of the substrate, because the temperature at the edge of the weak SBF/ceramic interface would be much smaller than the maximum temperature in the notch. This type of fuse would, however, have poor arcing characteristics and, consequently, was not analysed. To summarise, with proper selection of materials, multi-layer films offer greater adhesion strength and a reduction in peel-off.

Thirty three different combinations of multi-layer films were analysed. For all samples analysed silver was chosen as the main conductive layer for its thermal/electrical properties. The choice of the metals for the additional layers was based mainly on their mechanical properties. The results of the study presented in subsequent sections are restricted to the dependence of the interfacial stress in two-layer and three-layer fuse elements on the thickness and mechanical properties of the additional film(s) and the properties of the substrate.

---

[6] This characteristic is limited to cases where the area of the SBF is larger than that of the MBF.

The principal aims of the study were to:

- investigate the means to achieve a reduction in the magnitudes of the critical stress components in two-layer and three-layer metal combinations;
- analyse the dependence of the interfacial stresses on the thickness of the substrate bonded film;
- analyse the dependence of the interfacial stress on the mechanical properties of the substrate bonded film and the (lower/upper) metal bonded film(s);
- evaluate materials so that a reduction in the maximum value of all significant stress components can be achieved.

4.5.1. Dependence of the Interfacial Stress on the Thickness of the Substrate Bonded Film

Three Au-Ag film samples were analysed initially. The Au-Ag combination was used purely as an example of two noble metals and a benchmark verification of the FE solution. The principal metal film properties and thicknesses are those given in Table 4-9. In all samples the thicknesses of the SBF and the MBF were chosen to produce a total film thickness of 11μm.

Table 4-9. Properties of the samples used in the analysis of the dependence of the interfacial stress on the thickness of the substrate bonded film.

Sample No	Substrate Bonded Film thickness and material	Metal Bonded Film thickness and material
	μm	μm
1	0.1 Gold	10.9 Silver
2	0.5 Gold	10.5 Silver
3	0.9 Gold	10.1 Silver

The results of the computational analysis for the above samples are given in Table 4-10 and Figure 4-48.

Table 4-10. Results of the analysis for varying substrate-bonded film thickness.

Sample No	Maximum interfacial MISES stress	Maximum interfacial shear stress S_{ZX}	Maximum interfacial shear stress S_{ZY}	Maximum shear stress TRESCA	Maximum displacement U_Z
	N/mm^2	N/mm^2	N/mm^2	N/mm^2	$mm \times 10^{-3}$
1	484	138	245	531	1.27
2	463	136	241	506	1.27
3	446	134	238	500	1.26

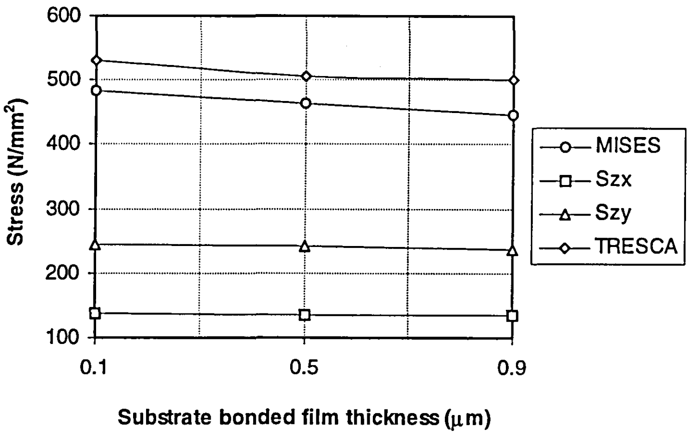

Figure 4-48 Dependence of the maximum interfacial MISES, S_{ZX}, S_{ZY} and TRESCA stresses on the thickness of the substrate bonded film.

From Table 4-10 it is observed that as the substrate bonded film thickness is increased a small reduction in all stresses is observed. For example the reduction in MISES and TRESCA stresses is 7.8% and 5.8% respectively, and the reduction for both shear S_{zx} and S_{zy} stresses is 2.8%. From the same table it is clear that the two-layer sample (No 3, Table 4-9) is superior to the single-layer sample of the same geometry (Table 4-8). The maximum MISES stress is reduced by 9.7%, the maximum TRESCA stress is reduced by 8.1%, the shear stress S_{zx} is practically the same and the shear stress S_{zy} is reduced by 2.8%. The declination (Figure 4-48) indicates that a further reduction in stress would be possible if the thickness of the substrate bonded film was increased.

4.5.2. Dependence of the Interfacial Stresses on the Elastic Properties of the Substrate Bonded Film

Six different metals were used for the substrate bonded film and analysed to evaluate the effect of their mechanical properties on the computed interfacial stresses. The metal bonded film was silver throughout and its thickness was 10μm for all samples. The thickness of the substrate bonded film was also fixed at 0.5μm for all samples, hence the total thickness of all the two-layer films was 10.5μm. The main properties of the metals analysed are given in Table 4-11 and the results of the analyses are given in Table 4-12 and Figure 4-50. Silver was also used as a substrate bonded film to enable comparison of the results obtained with the single layer film and two-layer film models and as a benchmark for accuracy of the FE model and methodology.

Table 4-11. Main properties of the metal films analysed.

Sample No	Substrate Bonded Film material	Electrical conductivity	Melting point	Thermal exp. coefficient	Young's modulus
		S·mm × 10^3	°C	10^{-6} °C^{-1}	N/mm^2
1	Gold	45.4	1,064	14.1	78,500
2	Aluminium	37.4	660	23.5	70,600
3	Magnesium	23.8	649	26	44,700
4	Titanium	1.8	1,667	8.9	120,200
5	Copper	59.0	1,084	17	130,000
6	Molybdenum	17.5	2,615	5.1	324,800
7	Tungsten	18.5	3,387	4.5	411,000
8	Silver	61.3	961	19.1	82,700

Table 4-12. Results of the analysis of the dependence of the interfacial stress on the elastic properties of the SBF.

Sample No	Maximum interfacial MISES stress		Maximum interfacial shear stress S_{ZX}		Maximum interfacial shear stress S_{ZY}		Maximum shear stress TRESCA		Maximum displacement U_Z
	N/mm^2	± %	N/mm^2	± %	N/mm^2	± %	N/mm^2	± %	mm ×10^{-3}
1	434	- 9.2	125	- 1.6	230	- 1.7	485	- 7.4	1.17
2	519	+ 8.6	128	+ 0.8	236	+ 0.8	560	+ 6.9	1.18
3	432	- 9.6	124	- 2.4	225	- 3.8	484	- 7.6	1.17
4 ☺	**413**	**- 13.6**	**125**	**- 1.6**	**230**	**- 1.7**	**461**	**- 12.0**	**1.16**
5 ☹	**550**	**+ 15.1**	**131**	**+ 3.1**	**243**	**+ 3.8**	**584**	**+ 11.4**	**1.18**
6	436	- 8.8	129	+ 1.6	239	+ 2.1	494	- 5.7	1.16
7	518	+ 8.4	131	+ 3.1	244	+ 4.3	597	+ 13.9	1.15
8	478	100.0	127	100.0	234	100.0	524	100.0	1.18

The main conclusions to be drawn from the results presented in Table 4-12 are:

- Two-layer films produce smaller maximum MISES and TRESCA stresses with some materials (titanium, magnesium, gold, molybdenum), but with other materials (tungsten, copper, aluminium) the maximum interfacial MISES and TRESCA stresses increase;
- The maximum displacement is primarily affected by the elastic properties of the metal bonded film and the substrate, and not greatly affected by the properties of the substrate bonded film (because it is much thinner);
- Of the seven metals studied titanium produced the smallest substrate/film interfacial stresses. This finding is consistent with the general application of resistive pastes to improve adhesion (electrical conductivity of titanium is approximately 30 times smaller than that of silver) [96].

The effect of varying the elastic properties of the SBF on the overall stress magnitude was also examined. The overall stress magnitude, in this case, is defined as the normalised scalar sum of the critical stress components: TRESCA, MISES, S_{zx}, and S_{zy}. No relationship was found between neither the magnitude of the overall stress and the thermal expansion coefficient, nor between the magnitude of the overall stress and the Young's modulus. However, the overall stress is a function of the product of the thermal expansion coefficient and the Young's modulus (Figure 4-49). This behaviour can be explained as follows:

- The larger the thermal expansion coefficient the larger the build-up of the elastic strain (defined as the difference between the thermal strain and total strain) and, consequently, the stress;
- The larger the Young's modulus the larger the magnitude of the stress (for a given magnitude of strain which, as was shown above, is linked to the elastic properties of the substrate and the metal bonded film).

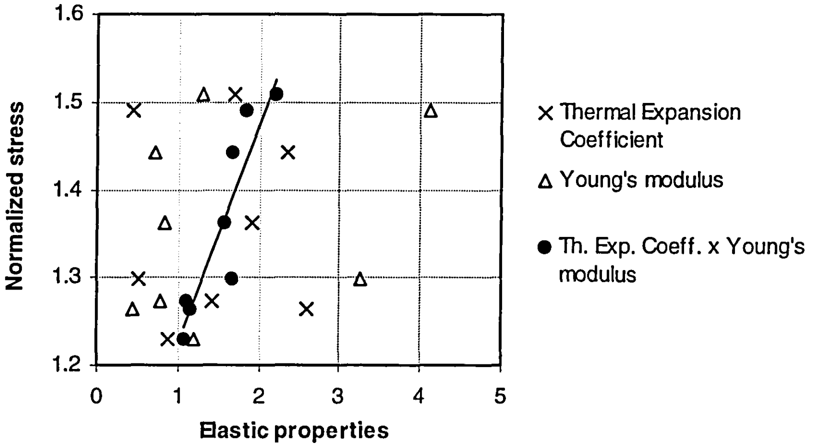

Figure 4-49. The effect of varying the elastic properties of the SBF on the overall magnitude of the stress.

The presented relationship indicates that to achieve a reduction in stress magnitude both the thermal expansion coefficient and the Young's modulus have to be considered concurrently.

The stress profiles along the symmetry and critical lines for two two-layer samples (Ag-Cu and Ag-Ti) were compared with the stress profiles obtained for a single layer (Ag) sample. The above mentioned metal combinations were chosen from the selection of the two-layer samples analysed (Table 4-12), because they clearly demonstrate the greatest positive and greatest negative effect the additional SBF has on the magnitude of the critical stress components (Figure 4-50).

From Figure 4-50 it is clear that the interfacial shear stresses in the Ag-Cu sample are much larger than the stresses in a single layer silver sample of the same geometry. However, the Ag-Ti combination produced smaller interfacial stresses. Moreover, the MISES stress differential along the symmetry line between the substrate and the substrate bonded film in the Ag-Cu sample (Figure 4-50 d) is larger than the equivalent stress differential between the substrate and the silver film in a single-layer sample (Figure 4-50 b). In the Ag-Ti sample practically the whole of the MISES stress differential is contained between the substrate bonded film and the metal bonded film (Figure 4-50 f). This, therefore, is advantageous, because the adhesion strength of the metal/metal combination is much stronger than the adhesion strength of the metal/ceramic combination.

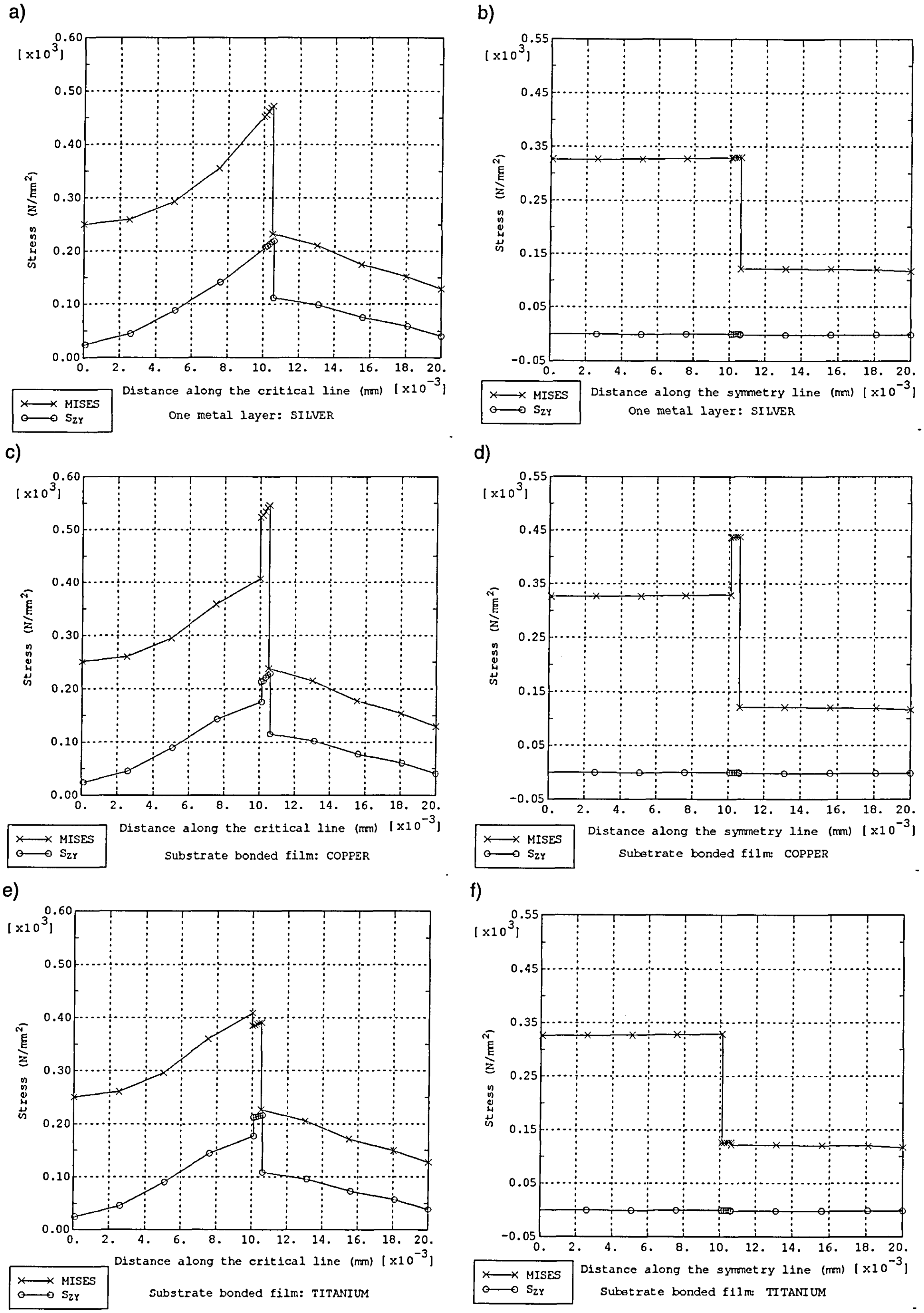

Figure 4-50. MISES and shear stress S_{zy} along the critical (left) and symmetry (right) lines; a & b) single layer silver film; c & d) substrate bonded film: copper; e & f) substrate bonded film: titanium.

4.5.3. Dependence of the Interfacial Stresses in Three-Layer Fuse Elements on the Elastic Properties of the Substrate, Substrate Bonded Film and Lower Metal Bonded Film

Twenty three-layer fuse element samples were analysed of which half were different combinations of metals for the substrate bonded film and the lower metal bonded film (LMBF). These metal combinations were analysed using alumina and pyrex material for the substrate. The metal combinations and the results of the analyses are presented in Tables 4-13 and 4-14

Table 4-13. Results of the analysis of the dependence of the interfacial stresses in 3-layer fuse elements on the elastic properties of the substrate, SBF and LMBF. Substrate material: Alumina.

Sample No	Metal combination		Maximum interfacial MISES stress	Maximum interfacial shear stress S_{ZX}	Maximum interfacial shear stress S_{ZY}	Maximum shear stress TRESCA	Maximum displacement U_Z
	SBF	LMBF	N/mm^2	N/mm^2	N/mm^2	N/mm^2	mm-×10^{-3}
1	Cu	Mo	547	139	247	580	1.26
2	Mo	Cu	557	146	261	593	1.27
3	Ti	Mg	458	136	239	497	1.27
4	Ti	W	535	141	251	617	1.25
5	W	Au	536	144	256	619	1.26
6	Mg	Ti	467	134	236	509	1.26
7	Mo	W	533	141	251	615	1.25
8	W	Mo	530	141	251	612	1.25
9	Au	Ti	470	135	239	512	1.26
10	Ti	Au	465	137	243	507	1.27

Table 4-14. Results of the analysis of the dependence of the interfacial stresses in 3-layer fuse elements on the elastic properties of the substrate, SBF and LMBF. Substrate material: Pyrex.

Sample No	Metal combination		Maximum interfacial MISES stress	Maximum interfacial shear stress S_{ZX}	Maximum interfacial shear stress S_{ZY}	Maximum shear stress TRESCA	Maximum displacement U_Z
	SBF	LMBF	N/mm^2	N/mm^2	N/mm^2	N/mm^2	mm-×10^{-3}
11	Cu	Mo	598	148	263	631	2.53
12	Mo	Cu	609	154	275	643	2.57
13	Ti	Mg	483	134	239	495	2.53
14	Ti	W	693	157	280	718	2.48
15	W	Au	698	159	283	722	2.52
16	Mg	Ti	491	132	235	506	2.52
17	Mo	W	690	157	281	714	2.48
18	W	Mo	686	156	278	710	2.50
19	Au	Ti	493	132	236	508	2.51
20	Ti	Au	488	135	241	502	2.53

Main findings:

- The three-layer samples studied did not produce better results (smaller stresses) compared to the best two-layer sample (Sample No.3, Table 4-10) of the same geometry. Only the Mg-Ti SBF/LMBF combination produced comparable stresses. Due to the increased manufacturing costs the application of three-layer fuse elements could, therefore, hardly be justified.

- The magnitudes of the critical stress components indicate that there is no general rule as to whether or not pyrex should be considered superior to alumina as the substrate platform material, because the maximum stresses depend on both the properties of the substrate and on the properties of the materials used for the substrate bonded film and the lower metal bonded film. With some metal combinations the results for the two substrate materials studied are quite similar (e.g. samples 3&13, 9&19, 10&20), whereas with other metal combinations they are not (e.g. samples 1&11, 8&18, 4&14).
- The MISES stress profiles along the symmetry line indicate that most SBF/LMBF metal combinations produce a chaotic stress distribution, the worst one for the metal combinations studied is shown in Figure 4-51 a). However, if the materials for the SBF and the LMBF are carefully selected a satisfactory stress distribution can be achieved, Figure 4-51 b).

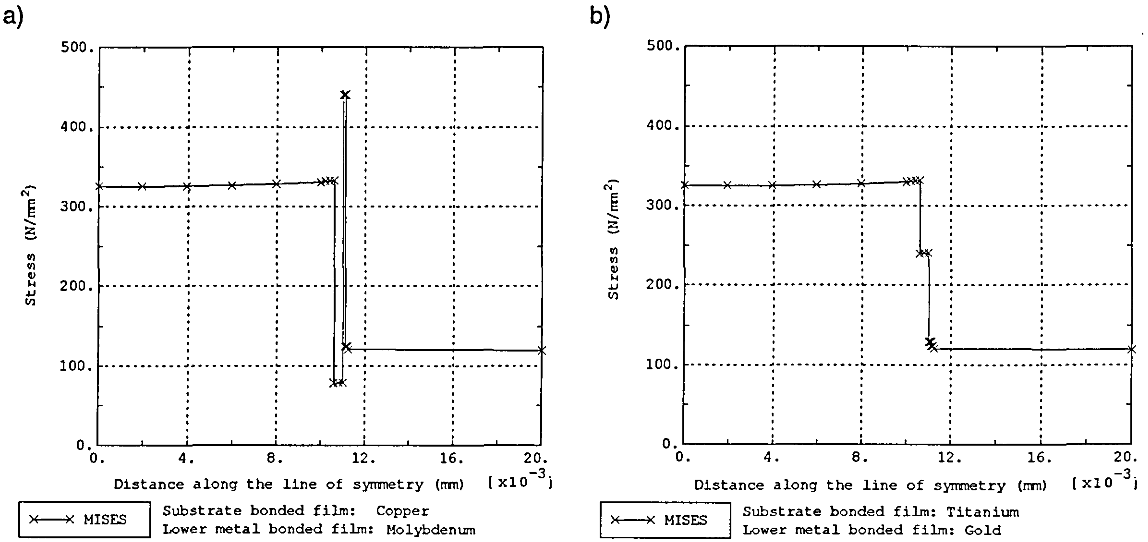

Figure 4-51. MISES stress profiles along the line of symmetry; a) worst case: SBF/LMBF metal combination CuMo, b) best case: SBF/LMBF metal combination TiAu.

4.6. Summary and Evaluation of Study

In Chapter 4 the electro-thermally-induced stresses and strains in TTFSF carrying steady-state currents were studied. The study showed that the FE techniques can be successfully utilised to analyse this class of problem. The critical stresses contributing to fuse failure were identified, their magnitude and location was computed for various film/substrate geometries and two-layer and three-layer metal combinations. These metal combinations were also examined with a view to achieving a reduction in the magnitude of the critical stress components in multi-layer substrate fuses. The effect of varying the substrate/heat sink(s) geometry on the pre-arcing current-carrying capacity of TTFSF was also examined.

The main conclusion to be drawn from the study presented in this Chapter is such that the computer predicted stresses & strains can be used for the next stage of the investigation, namely fatigue analysis. Fatigue analysis of a commercially available manufactured substrate fuse is the subject of the following Chapter.

Chapter 5.

Fatigue Analysis of the Manufactured Substrate Fuse

Intermittent currents, to which semiconductor fuses are often subjected, produce a fluctuating temperature field in the fuse, where the greatest amplitudes occur in the vicinity of the element constrictions. The temperature transients result in fluctuating stress & strain fields of amplitudes which are approximately proportional to the fluctuating temperature amplitude. The longer the pulsed-current period the greater is the amplitude of the temperature fluctuation and, therefore, the greater are the corresponding stress & strain amplitudes and, hence, the shorter is the fuse life-time. The most prevalent failure mode under these conditions is due to fatigue of the element, leading to formation of cracks and subsequent melting.

The effect of cyclic-current loading on the life-time of a manufactured substrate fuse (MSF) was investigated theoretically and experimentally. The cyclic temperature/stress/strain fields were predicted computationally. The aim was to devise a FE model to enable the prediction of the number of cycles to failure for any type of electrical loading.

5.1. The Manufactured Substrate Fuse

A commonly available thin-film substrate fuse, referred to as the manufactured substrate fuse, Figure 5-1, was used in this study. The fuse, rated at 20A, 300V, was of a conventional semi-conductor fuse construction [4]. The filler was bonded silica with water glass as the binding agent.

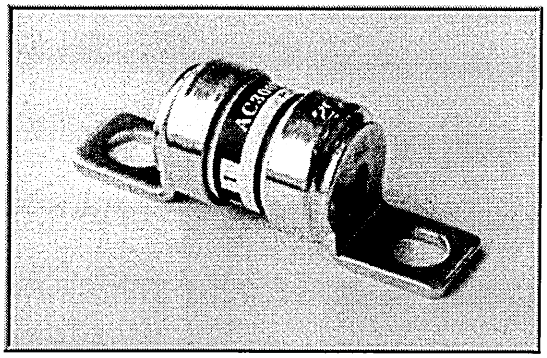

Figure 5-1. The manufactured substrate fuse investigated.

Fifteen samples of the manufactured fuse were available for this study. However, only the manufacturer's I:t fuse characteristic was available. Hence, for the purpose of the FE study it was necessary to determine: i) the external and internal dimensions of the fuse and the substrate; ii) the exact geometry of the conductive film and iii) the properties of the materials the fuse was made of. One sample of the fuse was dismantled and the solid filler was removed using a 10% solution of sodium hydroxide (caustic soda) in water. The measured dimensions of the parts of the fuse are detailed, Figure 5-2.

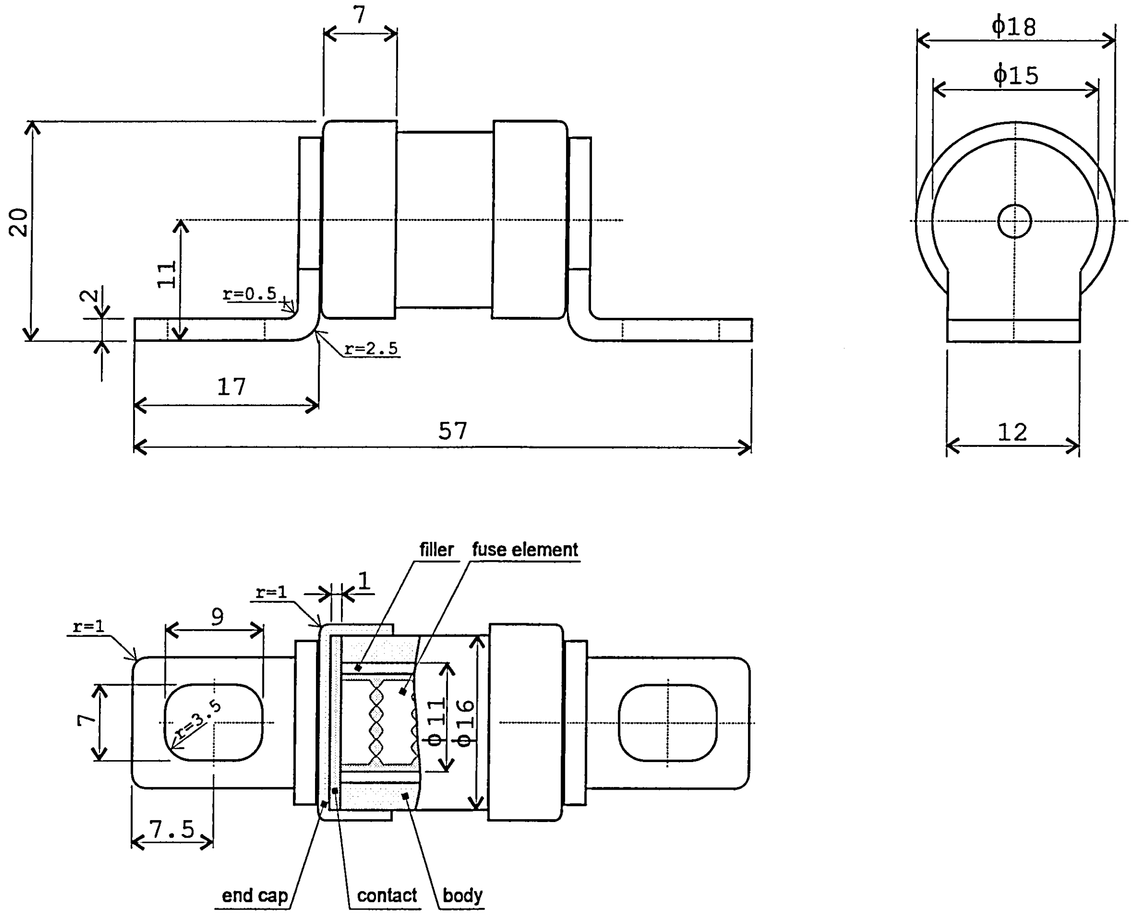

Figure 5-2. Schematic diagram of the manufactured substrate fuse investigated.

5.1.1. Geometry of the Conductive Film

The geometry and dimensions of the conductive film were determined in accordance with the following steps, Figure 5-4:

- the fuse element was scanned using a high-resolution scanner (Figure 5-4 a);
- the edges of the conductive film were determined using edge detection tools (b);
- the bitmap image was converted to vector graphics using trace-detect tools (c);
- the image was refined (noise removed) and aligned to fit the pre-determined grid (d);
- a best fit symmetrical geometry of the notch was determined (e)
- the best-fit symmetrical geometry of the notch was superimposed over the vector image to verify the validity of the proposed geometry of the notch and the location of the notches (f);
- a symmetrical section, i.e. a quarter of the proposed geometry of the notch, was extracted (g) and a set of 'x-y' data points determined for FE modelling (h);

The actual width of the notch, at 66μm ±1, was obtained using scanning electron microscope (SEM) imaging techniques (Figure 5-9 a). The reconstructed geometry of the manufactured fuse element is shown in Figure 5-3.

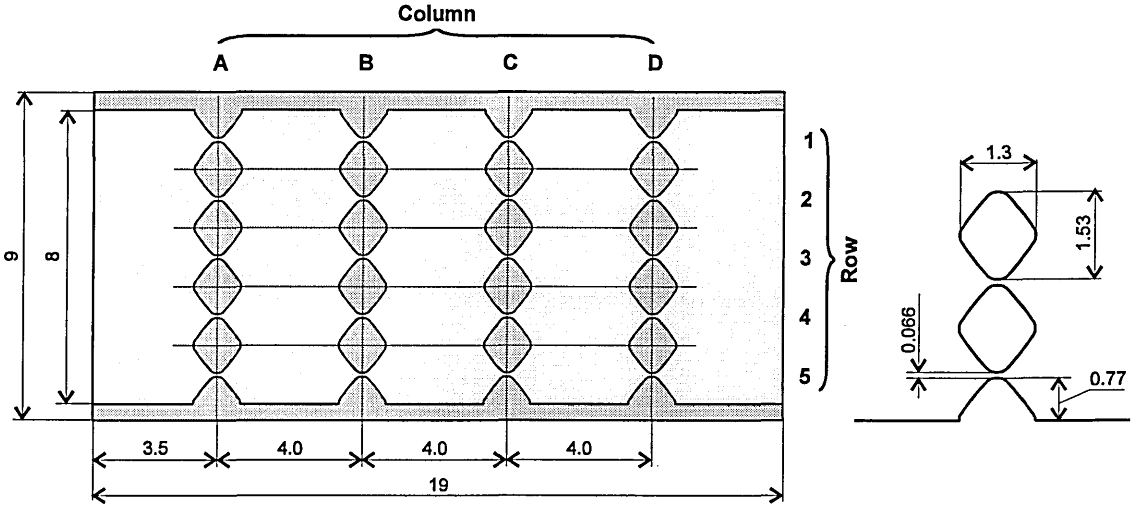

Figure 5-3. Reconstructed geometry of the manufactured substrate fuse element.

The location of the constrictions is identified by their 'column' and 'row' co-ordinates, e.g. the notch in the left-hand upper corner is identified by the A-1 label, and the notch in the right-hand bottom corner is identified by the D-5 label. Only a quarter of the geometry was used for FE modelling, Figure 5-5.

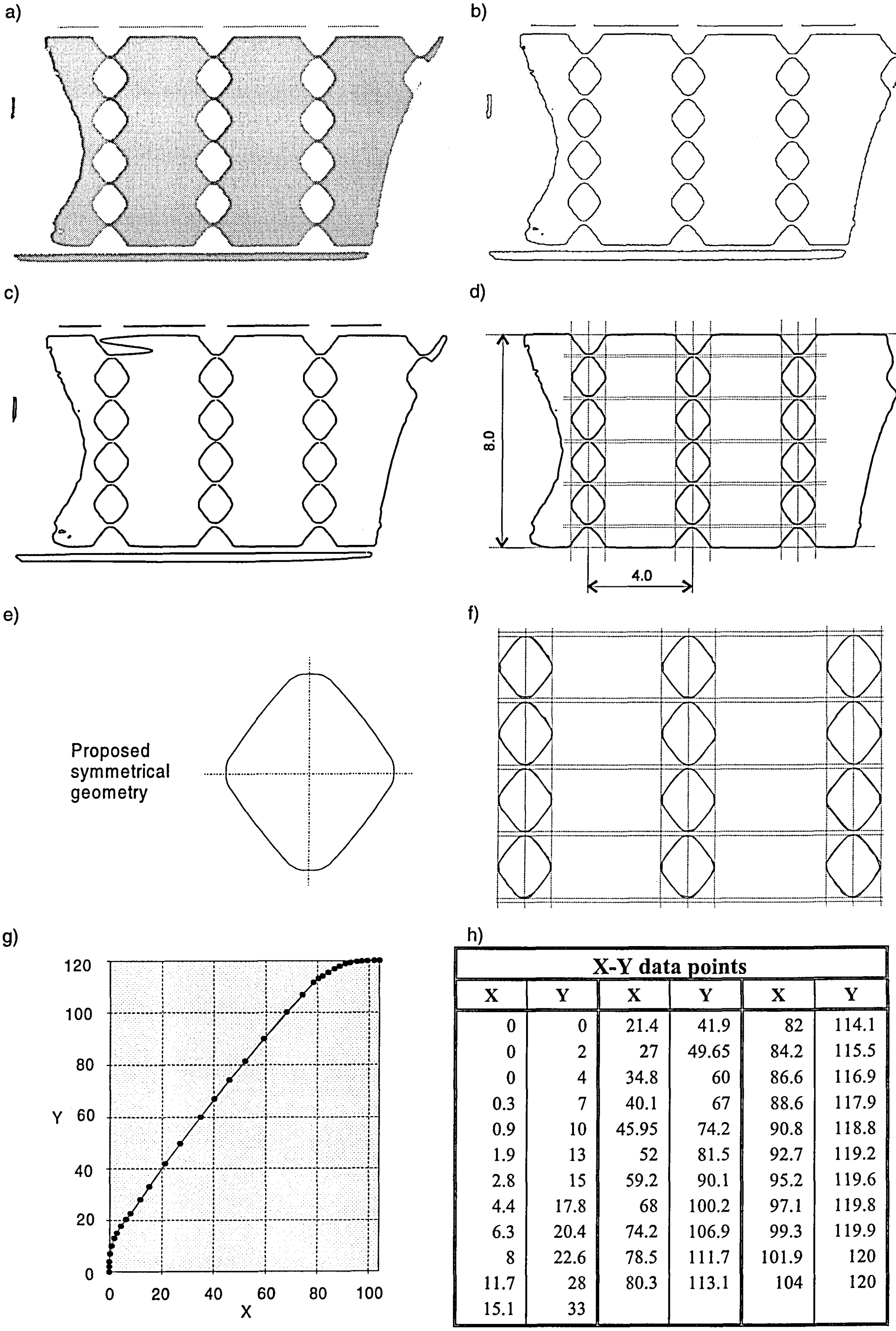

X-Y data points					
X	Y	X	Y	X	Y
0	0	21.4	41.9	82	114.1
0	2	27	49.65	84.2	115.5
0	4	34.8	60	86.6	116.9
0.3	7	40.1	67	88.6	117.9
0.9	10	45.95	74.2	90.8	118.8
1.9	13	52	81.5	92.7	119.2
2.8	15	59.2	90.1	95.2	119.6
4.4	17.8	68	100.2	97.1	119.8
6.3	20.4	74.2	106.9	99.3	119.9
8	22.6	78.5	111.7	101.9	120
11.7	28	80.3	113.1	104	120
15.1	33				

Figure 5-4. Stages of the reconstruction of the geometry of the conductive film.

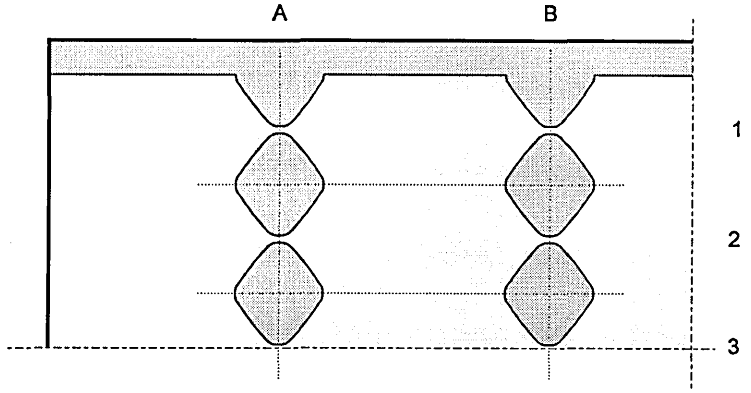

Figure 5-5. Symmetrical part of the manufactured substrate fuse element.

The thickness of the conductive film was measured by surface texture (roughness) measurement methods using a Taylor-Hobson Laser Form Talysurf – 120L instrument. The film thickness profile along the length of the fuse element mid-way between the notches is shown, Figure 5-6.

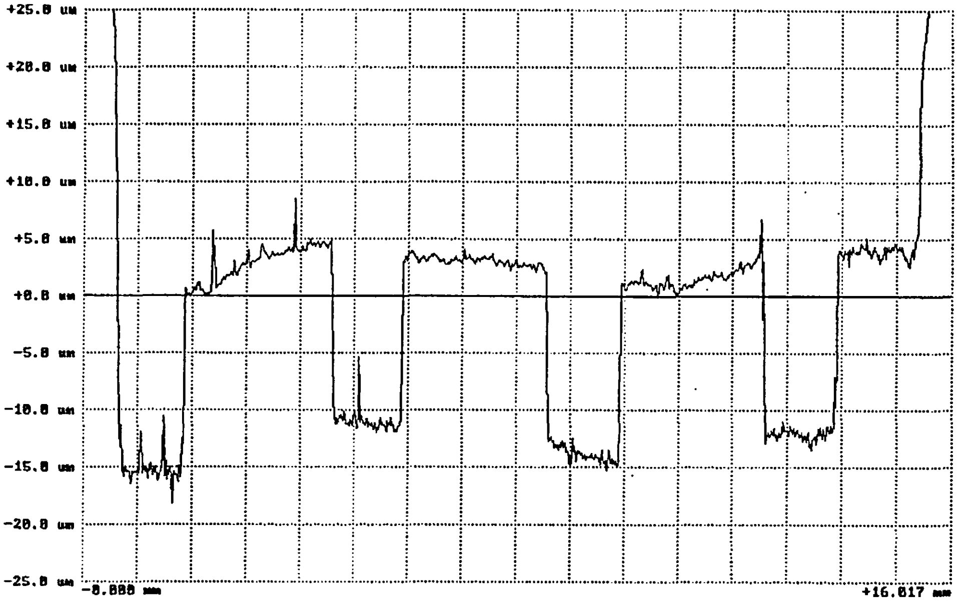

Figure 5-6. Manufactured substrate fuse – profile of the conductive film.

The 'waviness' of the fuse element in Figure 5-6, at around 5μm, can be attributed to uneven surface flatness, which for alumina is typically around 5μm/cm [97]. The roughness of the substrate, at around 1.0μm, is also typical for alumina substrates [97]. The roughness of the conductive film, at around 0.5–1.0μm, is due to the presence of a thin silicone coating [14], which protects the copper film material from oxidation (see also Figure 5-9). The thickness of the conductive film, at 15μm, is almost constant. This thickness was used for FE modelling. The effect of surface flatness variations on the fuse electro-thermo-mechanical behaviour was assumed to be negligible. The measured surface roughness has negligible effect on the electro-thermal performance of the fuse. However, its effect on the magnitude of the stresses can in some cases be significant, and is best modelled using appropriate stress concentration factors. Since at the elevated temperature the material softens and the effect of surface roughness on the magnitude of the stress decreases, the effect of surface roughness was, initially, also assumed to be negligible.

5.1.2. Microscopic and Spectral Investigation of the Conductive Film Material

The geometry and the electro-thermal-mechanical properties of the conductive film material were considered to have a paramount effect on the fuse behaviour. Thus, after the geometry and the thickness of the conductive film were determined, the composition of the conductive film was investigated using microscopy, SEM and spectral analysis techniques.

An untested sample of the manufactured fuse element was polished on a 1μm polisher/grinder to remove any stains and the protective silicone film coating from the surface of the conductive film. The sample was then etched in alcoholic ferric chloride for 15sec. A sample strip of pure copper[7] was also prepared in exactly the same way for comparison purposes.

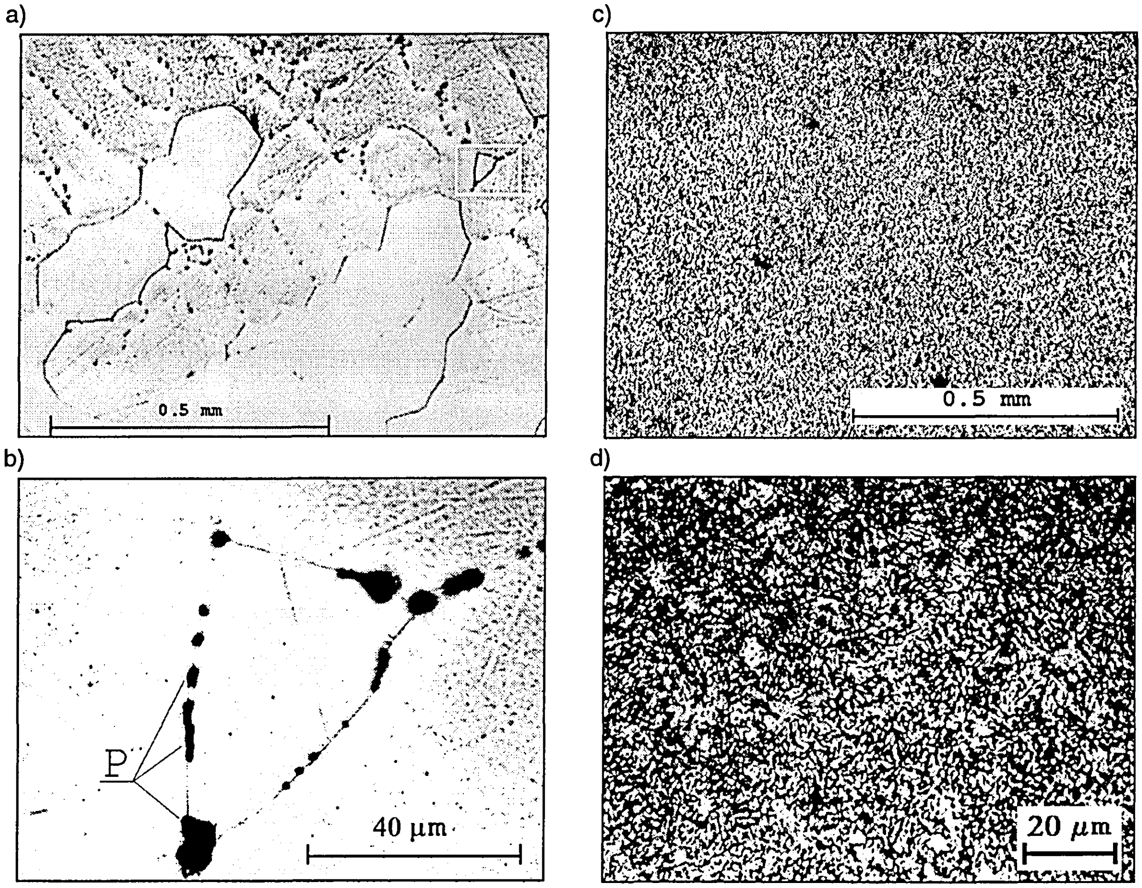

Figure 5-7. Comparison between crystal structure of pure copper and that of the manufactured substrate fuse element. a) and b) grain boundaries are easily discernible in pure copper (P - phosphorous); c) and d) grains are much smaller in the manufactured fuse sample.

---

[7] The sample was in fact a copper phosphorous alloy, with 0.02÷0.08 % phosphorus content.

Microscopic investigation showed that large grains and grain boundaries, easily discernible in bulk material (Figure 5-7 a & b), could not be observed on the manufactured fuse sample (Figure 5-7 c & d). The absence of large grains in the manufactured fuse element was attributed to the deposition process used for the manufacture of the element which, it is assumed, affected the growth of the grains. The fuse element was understood to have been manufactured using an electrolytic process [14], which typically results in columnar grain growth [95]. These columns are approximately 1µm in diameter (Figure 5-8), hence the grains on the surface appear to be very small.

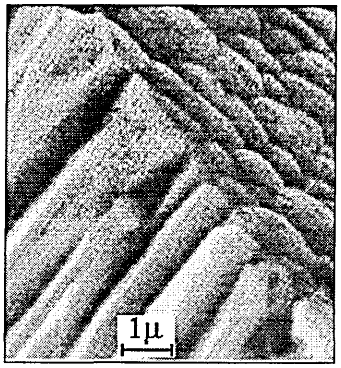

Figure 5-8. Scanning electron micrograph of Cu on Cu produced by electroplating showing columnar growth [95].

The polished fuse sample was subsequently analysed using semi-quantitative spectral analysis, Table 5-1. This study confirmed that the conductive film material was pure copper. Traces of other elements found in the sample can be attributed to the impurities in the sample. The aluminium content is due to the presence of the alumina substrate (Al_2O_3).

Table 5-1. Results of the spectral analysis of the manufactured substrate fuse.

Element	Al	Cu	Si	Mg	Ca	Hf	Ir
Mass %	49.62	48.58	0.623	0.534	0.156	0.124	0.086

5.1.3. Scanning Electron Microscope and Spectral Investigation of the Structure and Composition of the Conductive Film

SEM observations were carried out on a pristine unpolished sample. Thereupon the surface of the film was found to be covered with a thin silicone resin coating. From Figure 5-9 it is evident, however, that the coating was absent in some areas (Figure 5-9 b and c). The atomic number analysis clearly identified the smooth areas where there was no protective layer (Figure 5-9 d).

Spectral analysis revealed that the smooth areas (without the protective layer) are pure copper with only traces of carbon and other elements (Figure 5-10 a), whereas the coarse areas (including the protective layer) were found to be mainly copper, but other elements were also present in significant quantities. These elements were: Al, Si, S, Cl and K (Figure 5-10 b). However, given that the thickness of the protective layer is very small (~0.5µm), the strong showing of Cu was attributed to the underlying copper.

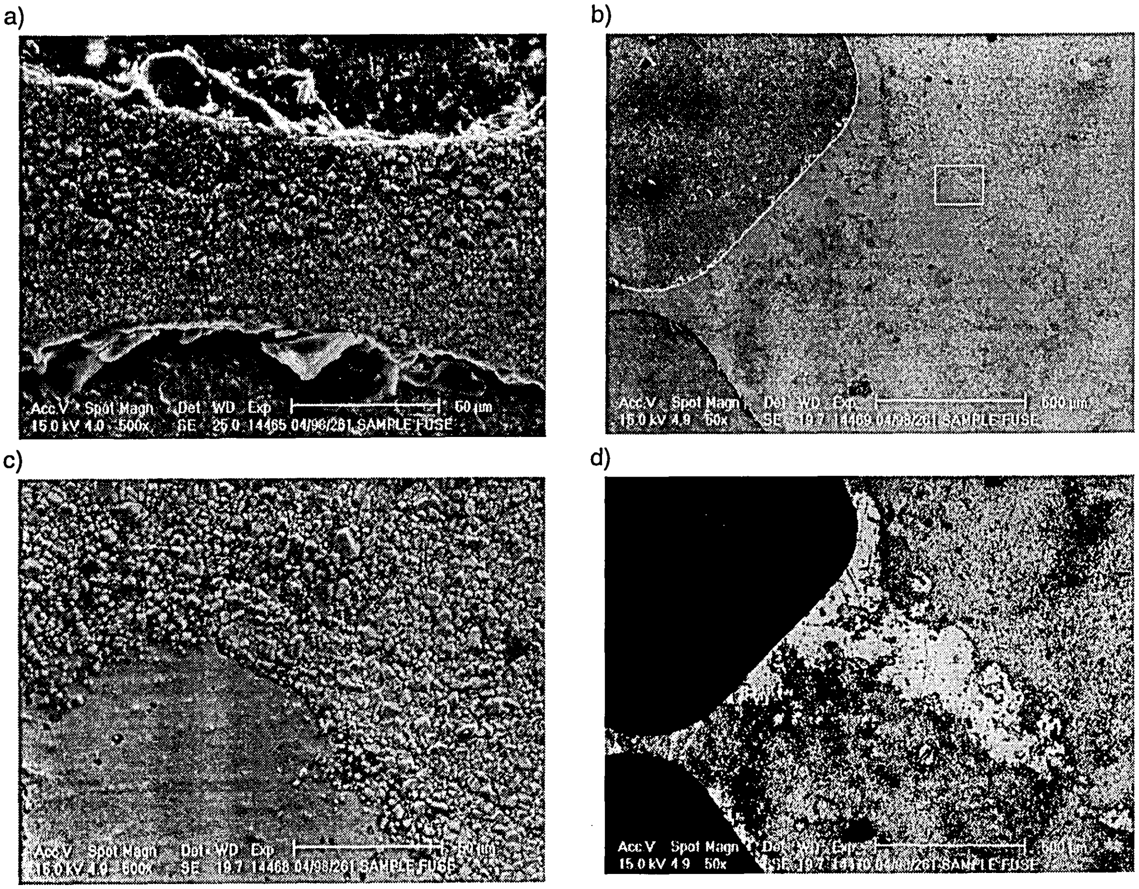

Figure 5-9. Scanning electron microscope representation of the conductive film surface of a pristine untested sample; a) the notched area; b) area where the protective coating was absent; c) high magnification of the area where the protective coating was absent; d) atomic number analysis clearly identified the areas where the protective coating was missing.

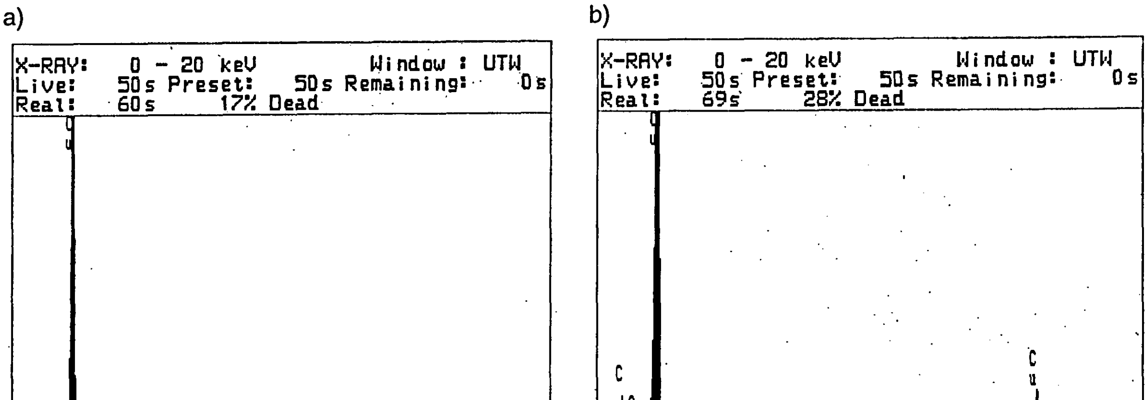

Figure 5-10. Spectral plot analysis of the conductive film; a) area without the protective coating; b) area including the protective coating.

5.2. Computer Models for the Thermal-Electrical Studies

Simplified fuse models, for example those assuming no heat losses from the element or from the fuse body, are not sufficient for accurate calculations of a fuse's transient thermal response beyond truly adiabatic heating. Consequently, computer simulation of the withstand performance (lifetime) of a fuse subjected to cyclic-current pulses, requires large-scale modelling in order to accommodate the medium- and long-duration thermal effects. For this reason all parts of the fuse were modelled. To further refine the model the test-rig copper bar, to which the fuse was fixed, was also modelled. For the FE models analysed in this section the electro-thermo-mechanical material properties were allowed to vary with temperature, i.e. compared to the FE models investigated in Chapter 4, plastic material properties were incorporated in the FE models of the MSF.

5.2.1. Geometry Models

The model used for the thermal-electrical studies comprised of: 1) conductive film, 2) substrate, 3) quartz sand filler, 4) fuse body, 5) contact, 6) end cap, 7) terminal 8) copper bar. The copper bar was also included in the model, in accordance with the anticipated fuse testing conditions [81]. All the components were assumed to significantly affect the temperature distribution and its magnitude in the fuse element, hence they all were modelled. For initial verification of the FE model, however, a FE model excluding the copper bar was used (Paragraphs 5.2.2 & 5.4).

5.2.2. Finite Element Models

Three FE models were constructed, namely: i) standard-mesh model excluding the copper bar; ii) standard-mesh model including the copper bar; and iii) fine-mesh model including the copper bar (Figure 5-11). The standard-mesh models were used for all steady-state and transient electro-thermal studies. The fine-mesh model was only used when a further thermal-stress analysis was required. The standard-mesh FE model (excluding the copper bar) comprised 21,332 nodes and 18,896 elements. The fine-mesh model comprised 60,278 nodes and 56,191 elements. In all cases, all parts of the fuse were modelled using 8-node linear finite elements: ABAQUS DC3D8E – coupled thermal-electrical bricks – for the parts of the model in which electrical and thermal conduction was permitted (both electrical and thermal degrees of freedom were activated). The DC3D8 – heat transfer brick – was used for parts of the model carrying no electric current.

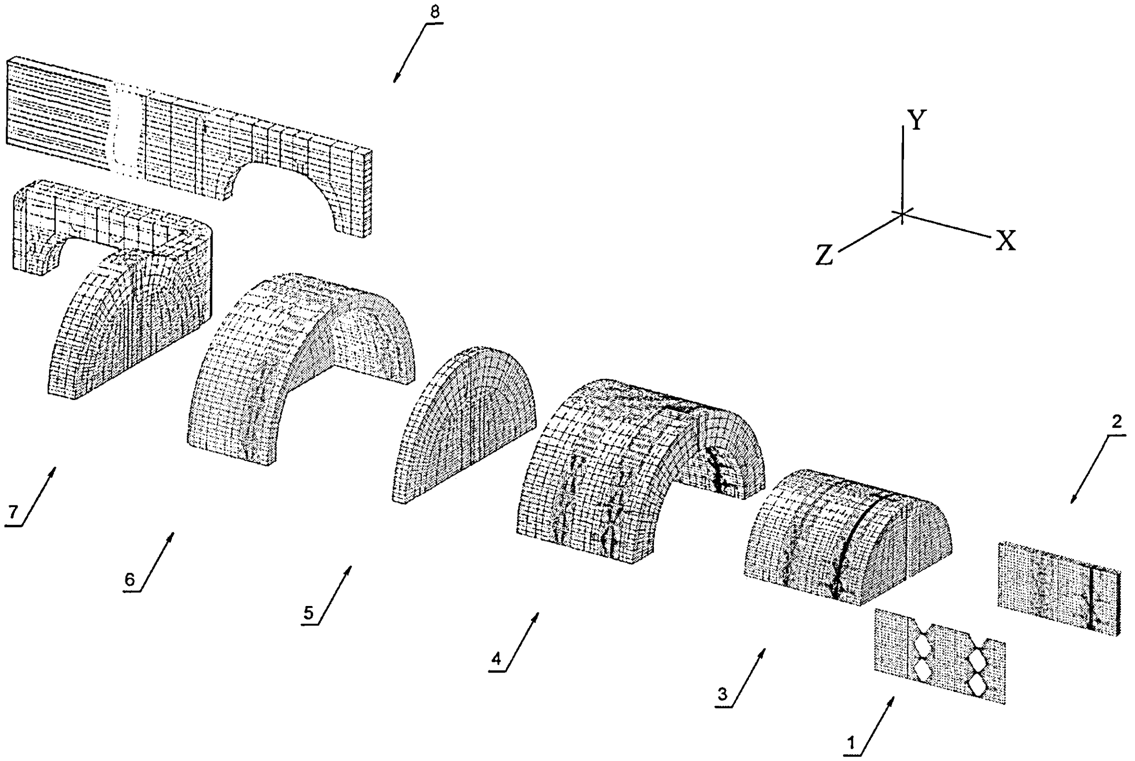

Figure 5-11. Exploded view of the manufactured substrate fuse assembly and mounting (fine-mesh FE model); 1-conductive film, 2-substrate, 3-filler, 4-fuse body, 5-contact, 6-end cap, 7-terminal, 8-test-rig copper bar.

The copper bar of the standard test-rig was 55cm long, however only 26.4cm of its length was modelled. The temperature of the bar beyond this point (further away from the fuse terminal) was found empirically to be small (Figure 5-15), hence the heat convected from the surfaces of the remaining portion of the bar was assumed to be negligible. The end of the copper bar was attached to a heat sink, the temperature of which was varied in accordance with the applied RMS current (Equation C-2, p.177).

The standard-mesh FE model is shown in Figure 5-12.

5.2.3. Applied Boundary Conditions

Current was injected at all nodes at the far end of the copper bar. All nodes of the conductive film, co-incident with the X-plane of the model symmetry, were fixed at 0 volts.

For any RMS current the temperature at the end of the bar was known (Equation C-2). This temperature was applied at the same set of nodes at which the electric current was injected, i.e. at the far end of the copper bar. Convection and radiation were incorporated on all external surfaces and no heat fluxes were allowed across the 'X' and 'Y' planes of model symmetry. The value of the film coefficient h was obtained by fitting computational results to experimental data (Paragraph 5.4.1, p.91).

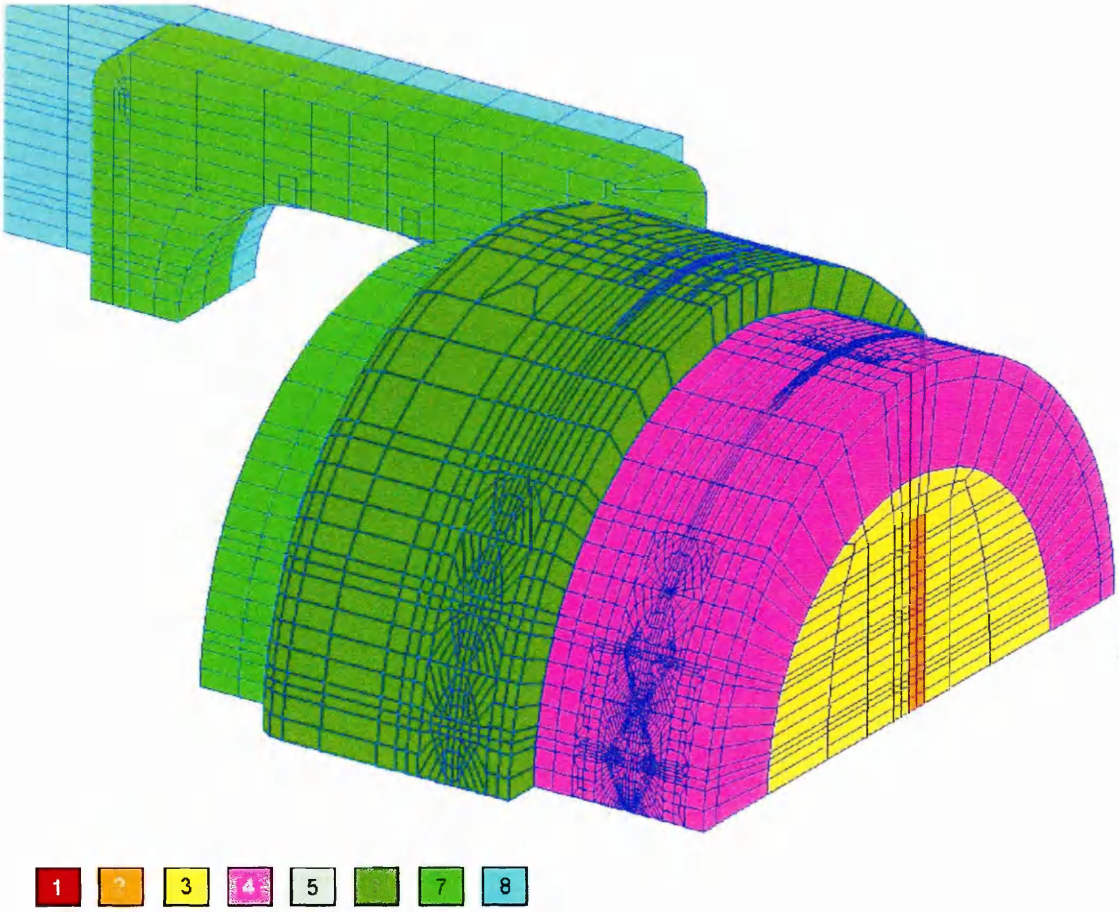

Figure 5-12. Manufactured substrate fuse assembly and mounting (standard-mesh FE model). 1-conductive film (copper), 2-substrate (alumina), 3-filler (bonded quartz sand filler), 4-fuse body (alumina), 5-contact (copper), 6-end cap (brass), 7-terminal (brass), 8-copper bar (clipped for clarity)

5.3. Computer Model for the Thermal Stress Studies

5.3.1. Geometry Model

A reduced representation of the geometry model for the thermal-electrical studies was used to construct the thermal stress model. Only the conductive film and the substrate were modelled for the thermal stress analysis. The effect of the other parts of the fuse on the stress distribution and stress magnitudes was assumed to be negligible.

5.3.2. Finite Element Model

The fine-mesh FE model used for the thermal stress studies is shown in Figure 5-13. This model is a submodel of the fine-mesh model described in Paragraph 5.2.2, for which only the elements associated with the conductive film and the substrate were retained. Very fine mesh was only used around notches B-2 and B-3, because the largest stresses & strains occur in the vicinity of the notches located close to the centre of the fuse, where the amplitude of the temperature is greatest – this approach is reflected in the mesh transitions in the conductive film and the substrate on the 'X', 'Y' and 'Z' planes in the vicinity of notches B-2 & B-3 (Figures 5-13 & 5-14). The fine-mesh FE model for the thermal-stress studies comprised 26,683 nodes and 23,507 elements.

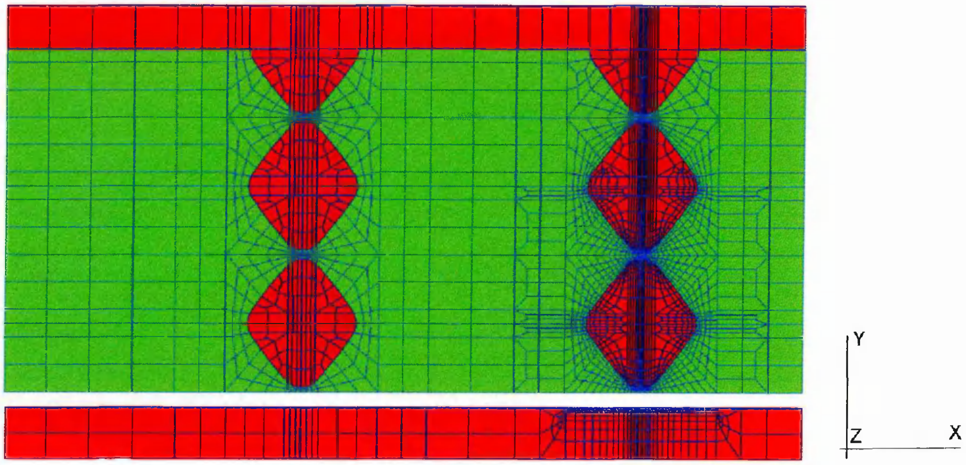

Figure 5-13. The fine-mesh FE model used for the thermal stress studies.

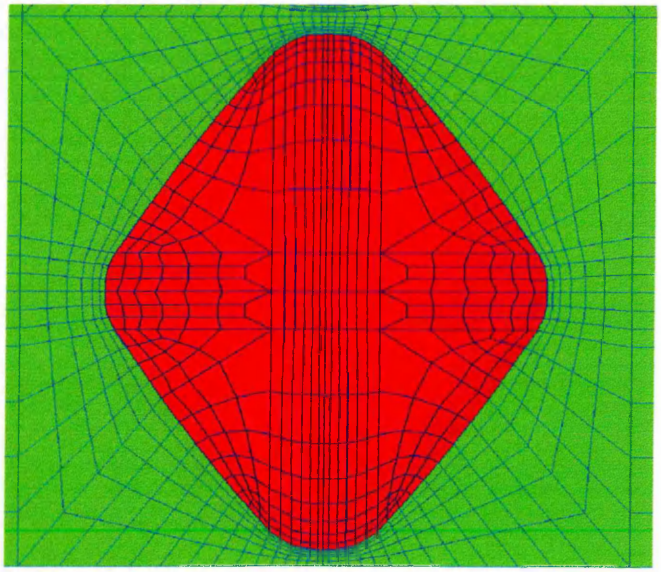

Figure 5-14. Mesh distribution in the vicinity of notches B-2 and B-3.

5.3.3. Applied Boundary Conditions

The ends of the fuse element were assumed to be fixed mechanically to the end caps in the manner described in Paragraph 3.3.3, p.23 (Figure 3-3 c). Symmetry plane boundary conditions described in Table 3-2 were used for this model.

5.4. Validation and Verification of the FE Models

The FE models were verified to ensure that the magnitudes of the end-cap temperature: i) for the standard-mesh model, match experimental data, i.e. the standard-mesh model is valid; and ii) are identical, within acceptable error, for both the standard-mesh and the fine-mesh models, i.e. all FE models are valid.

The first requirement was met by comparing the computed magnitudes of the solution variables with the experimental data, and the second requirement was satisfied by comparing the results produced by all four FE models.

The FE models incorporating the copper-bar allow for surface convection and radiation. Theoretical treatment of surface convection and radiation from the external surfaces of fuses is given elsewhere [8], however, the formulae used included specimen-related and environmental variables, which were not known. It was, therefore, decided to establish the value of the surface film coefficient, taking both convection and radiation into account, by fitting computational results to experimental data.

5.4.1. Determination of the Coefficient of Surface Heat Transfer

To determine the coefficient of surface heat transfer for the manufactured fuse a DC current of 26A was passed through the fuse for 1 hour using the experimental set-up shown in Figure C-1. Following thermal stabilisation, temperatures were recorded along the copper bar at frequent intervals, Table 5-2. From the tabulated results the increase in temperature at the upper end of the bar is attributed to the heat generated by the contact resistance of the current supply terminal.

Table 5-2. Temperature distribution along the test-rig copper bar.

Distance, cm	0	5	10	15	20	25	30	40	50	55
Temperature, °C	50.1	43.3	38.6	34.8	31.6	30.0	29.4	29.0	29.5	30.1

The temperature profile indicates whether the surface heat coefficient is finite. For example, given h=0 then there would be no heat convection from the surfaces of the copper bar and $q_x = -K_{Cu}\frac{dT}{dx} = \text{const}$, hence $\frac{dT}{dx} = \text{const}$ and the temperature distribution between the two ends of the bar would be linear. As the experimentally obtained temperature profile was not linear the h value was, therefore, significant.

The temperature profile along the copper bar was also obtained using FE modelling. Due to the large computational size of the FE model of the manufactured fuse the film coefficient was determined initially using a sub-model of the standard-mesh model, which incorporated the copper bar only. The end of the copper bar, in contact with the fuse terminal was attached to a heat source and fixed at T=50.1°C, i.e. the temperature obtained from the experiment (Table 5-2). All nodes located 26.4cm from the end of the bar (because only 26.4cm of the bar was modelled) were fixed at the heat sink temperature of 30.1°C. The average film coefficient 4×10^{-6} W/mm^2 was found to produce the same temperatures as the experimental temperature profile (Figure 5-15). This value is comparable with film coefficient values reported by other researchers for specimens located in draft-free air [104].

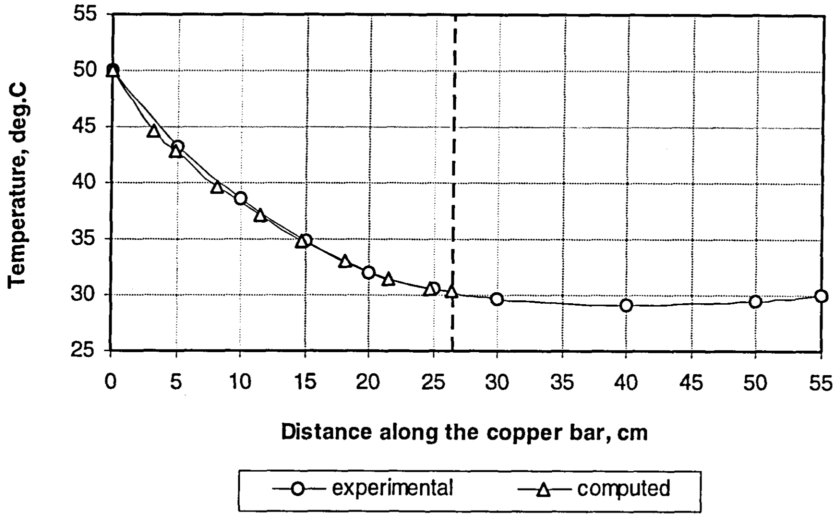

Figure 5-15. Computed and experimental temperature profiles in the test-rig copper bar.

5.4.2. Procedure of Finite Element Model Verification

Initially the standard-mesh model was used and the following analyses performed:

1. Maximum element temperature for 0A ≤ I ≤ 35A (steady-state conditions, model excluding the copper bar);
2. Top end-cap and maximum element temperatures for 0A ≤ I ≤35A (steady-state conditions, model including the copper bar);
3. Top end-cap temperature (transient analysis, model including the copper bar).

Tests 1-3 were carried out to verify that:

- the predicted maximum fuse element temperature for $I = I_{mfc}$ is $T_{max} = T_m$;
- the model including the copper bar gives the same maximum element temperatures for 0A ≤ I ≤ I_{mfc} as the FE model excluding the copper bar;
- the predicted steady-state end-cap temperatures for 20A ≤ I ≤35A match experimental data;
- the predicted transient end-cap temperatures match experimental data.

Results for the standard-mesh model excluding the copper bar.

The temperature at all nodes located on external surfaces of the fuse was varied in accordance with (Eq. C-1): $T_{end-cap} = 0.0016 \cdot I^3 - 0.001 \cdot I^2 + 0.0923 \cdot I + 21.6$.

For the theoretical minimum fusing current $I=I_{mfc}$=35A the maximum predicted fuse element temperature was 1112°C, approximately 2.7% above the melting temperature of copper ($T^{Cu}_{melt.} = 1082°C$). Alternatively, I_{mfc}=34.97A gives T_{max}=1082°C. Given that $\left.\frac{\Delta T}{\Delta I}\right|_{I \to I_{mfc}} >> 0$ and that experimental I_{mfc}=34.5±½A, the predicted MFC, being 0.086% below the theoretical MFC, is within acceptable error. The magnitude of the error is within the accuracy of experimental determination of the MFC.

The computed maximum steady-state element temperature profile versus current is shown in Figure 5-16. The temperatures between data points were interpolated and, due to large non-linearities, two best-fit third- and fourth-order polynomial functions were used to interpolate between data points. A value of 31.5A, i.e. 90% of I_{mfc}, was chosen as the dividing point.

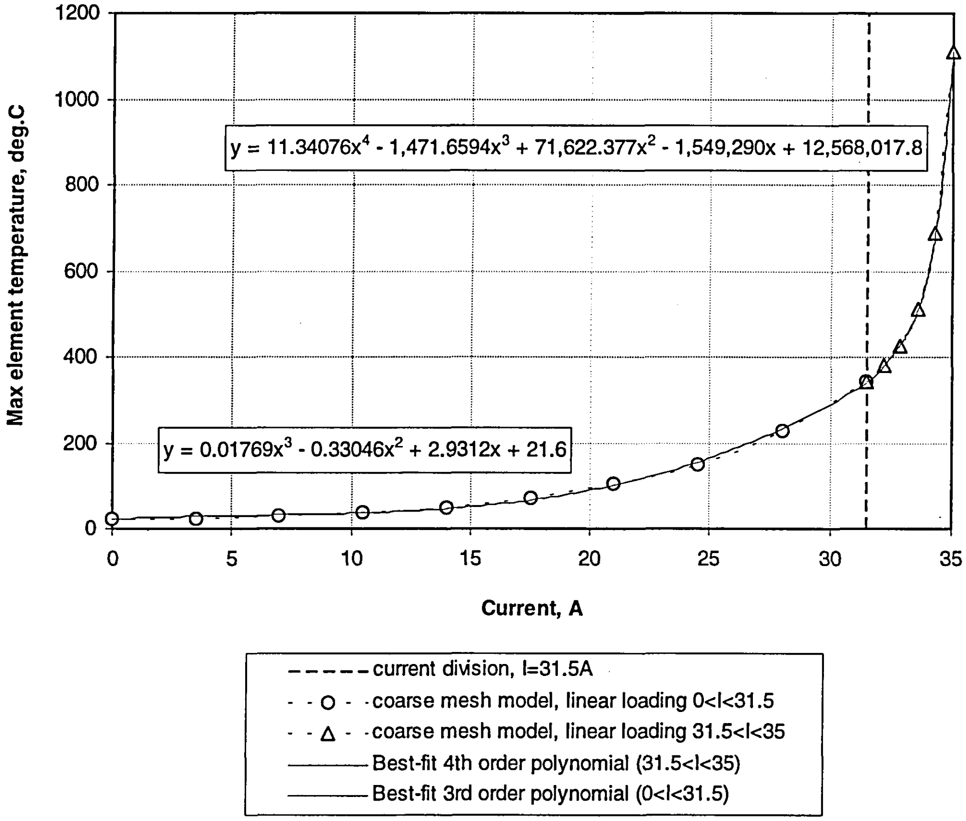

Figure 5-16. Predicted maximum element temperature versus the RMS current; the equations given are the best-fit polynomial functions, with dividing point at I=31.5 A.

The maximum element temperature versus the RMS current for the standard-mesh model, excluding the copper bar is, therefore, given by:

$$T=\begin{cases}0.01769\cdot I^3-0.33046\cdot I^2+2.9312\cdot I+21.6 & \text{for } 0\,A<I<31.5\,A\\ 11.34076\cdot I^4-1{,}471.66\cdot I^3+71{,}622.38\cdot I^2-1{,}549{,}290\cdot I+12{,}568{,}018 & \text{for } 31.5\,A<I<35\,A\end{cases}\qquad \text{[Eq.5-1]}$$

Results for the standard-mesh model including the copper bar.

Steady-state maximum element and end-cap temperatures for the FE model including the copper bar were compared with the temperatures obtained for the FE model, without the copper bar and, additionally, with experimental end-cap temperatures, Figure 5-17.

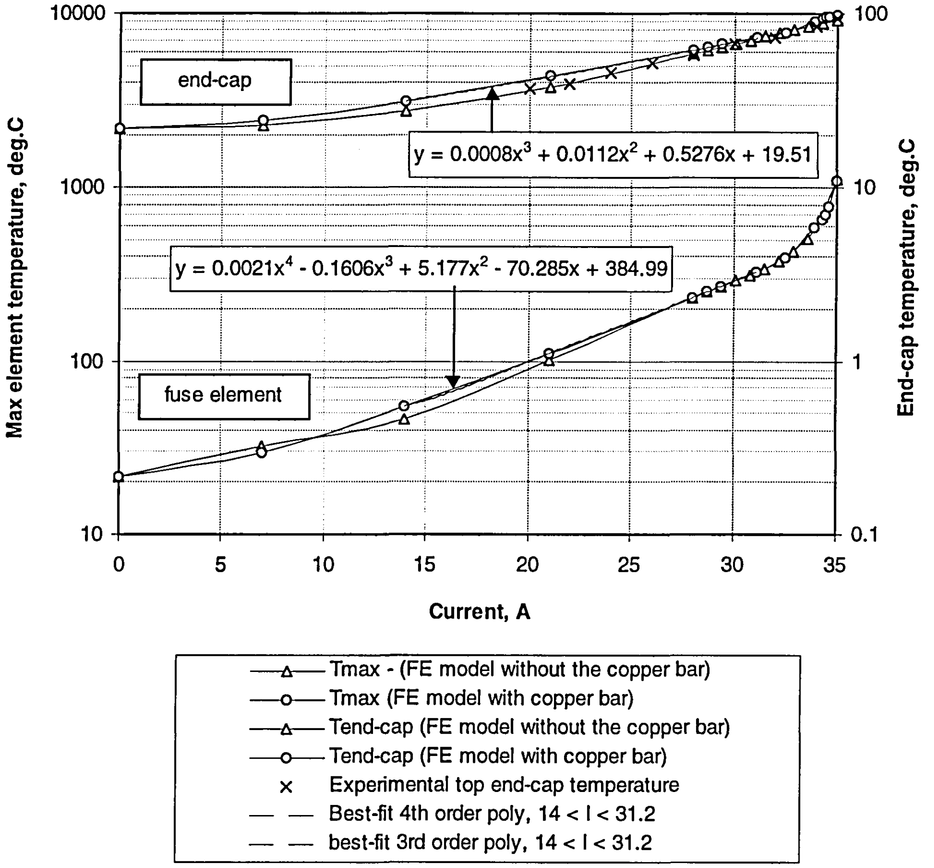

Figure 5-17. Verification of the accuracy of the electro-thermal prediction: top endcap and maximum element temperatures versus current (steady-state conditions).

The end-cap and the element temperatures versus current for the standard-mesh model, including the copper, bar are, therefore, given by:

$$T=\begin{cases}0.0008\cdot I^3-0.0112\cdot I^2+0.5276\cdot I+19.51 & \text{- end-cap}\\ 0.0021\cdot I^4-0.1606\cdot I^3+5.177\cdot I^2-70.285\cdot I+385 & \text{- element}\end{cases}\qquad \text{[Eq.5-2]}$$

These results indicate that the steady-state electro-thermal prediction produced by the FE model including the copper bar is almost identical to the corresponding prediction obtained for the FE model excluding the copper bar. Generally, the discrepancy produced by the two models is small, $\Delta T_{max}^{(\text{end-cap})}=5.4^{\circ}C$ and $\Delta T_{max}^{(\text{element})}=8.8^{\circ}C$, and was, therefore, neglected.

It is worth noting that using the formula given in Eq.5-2, it is clear that for the rated current of 20A the maximum element temperature is 101°C, which is very low (normally 200~250°C) for this class of fuse.

Results for the transient prediction.

To verify the accuracy of the model's transient thermal constants in the medium- and long time regions, the computed end-cap temperature was verified against experimental data, Figure 5-18. Experimental data was obtained for an applied current of 25A DC, using the standard test-rig (Figure C-1).

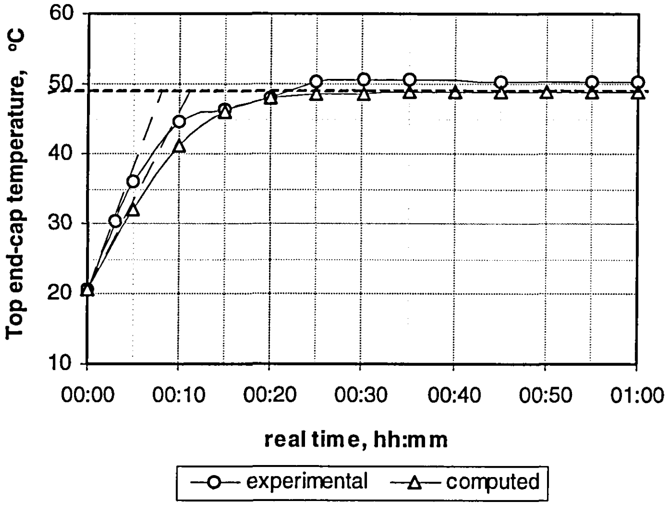

Figure 5-18. Verification of the validity of the FE model's transient thermal constants: comparison of computed and experimental top endcap temperature versus current (I=25A).

From Figure 5-18 the computed thermal constant is slightly smaller than the experimental one, however, in both cases the steady-state condition was obtained after ~50min, i.e. $\tau \approx 10$min. Given that experimental temperature measurements are subject to error, it can be concluded that in this respect the computer prediction is accurate and that the FE model is valid.

Results for the fine-mesh model including the copper bar

Test No.2 was also performed using the fine-mesh FE model and the results obtained from this analysis were compared with the results produced by the standard-mesh FE model. This procedure was carried out mainly to verify whether the predictions using the two models are identical (within acceptable error) and, hence, to validate the assumptions made in Paragraph 5.2.2.

The comparison of the results produced by the standard-mesh and the fine-mesh models is given in Figure 5-19, from which it is observed that the difference in computed temperature for both models smaller less than 2°C at any point and, hence, the assumptions made in Paragraph 5.2.2 are valid.

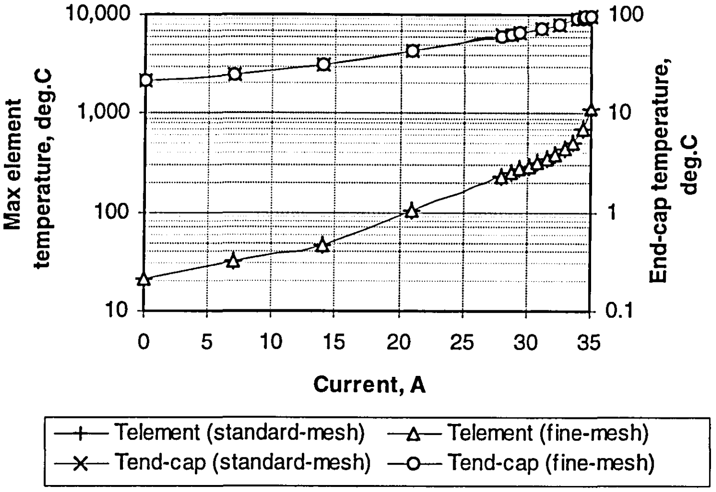

Figure 5-19. Comparison of the computed end-cap and maximum element temperatures produced by the standard-mesh and the fine-mesh FE models.

5.5. Time/Current Characteristic Prediction

The I:t characteristic of the manufactured fuse was predicted using the standard-mesh FE model including the copper-bar. The I:t characteristic, compared with the published manufacturer's I:t characteristic, is shown in Figure 5-20, from which it is observed that the discrepancy between the two characteristics is relatively small and can be neglected, given that manufacturer's I:t characteristics are only accurate to within ±5%.

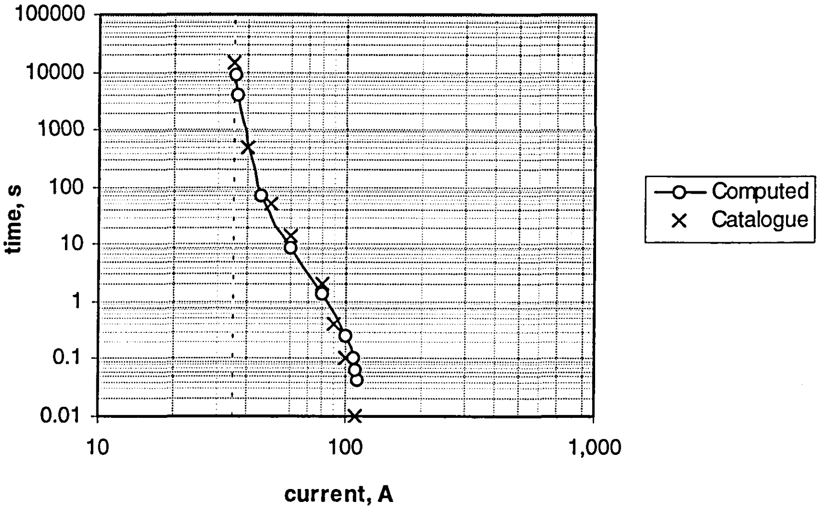

Figure 5-20. Predicted I:t characteristic of the manufactured substrate fuse compared with published manufacturer's characteristic; the dashed line indicates the minimum fusing current.

5.6. Temperature Distribution in the Fuse Element Carrying Steady-State DC Current

The standard-mesh model was used for the steady-state DC thermal-electrical analysis. Figure 5-21 shows the temperature distribution in the fuse element carrying a steady-state current of 28.3/14.15A, which is the RMS value of the current used for the theoretical and experimental symmetrical pulsed-current loading studies.

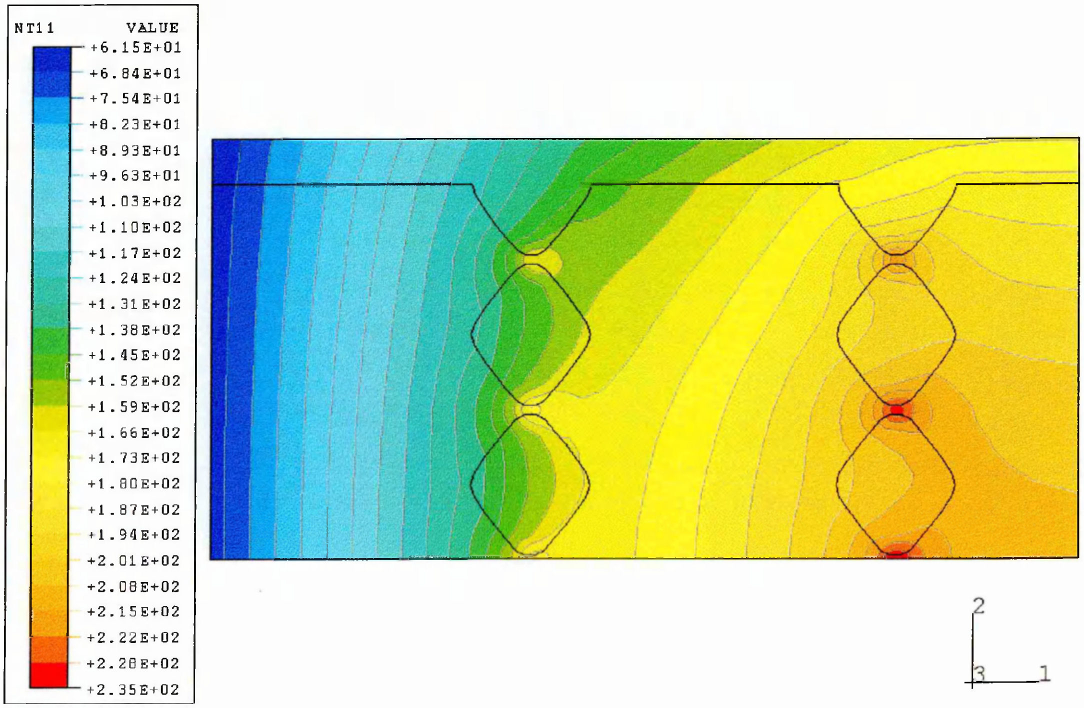

Figure 5-21. Temperature distribution in the manufactured fuse element carrying steady-state DC current (I=28.3/14.15A).

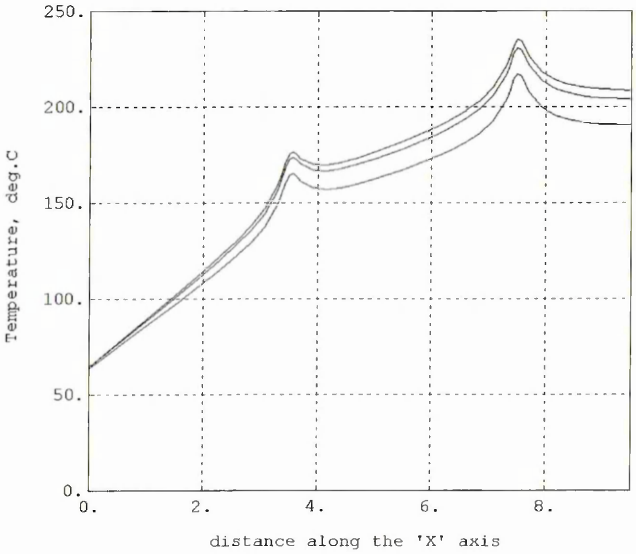

Figure 5-22. Temperature profiles in the conductive film, through the notches, along the 'X' axis; the manufactured substrate fuse is carrying a steady-state DC current of 28.3/14.15A.

Figure 5-22 shows temperature profiles in the conductive film, through the notches, along the model's 'X' axis. The temperature is largest in the vicinity of notch B-3, hence the stresses & strains are also largest in notch B-3. Consequently, this notch was chosen as the focus of the thermal-stress investigation (Paragraphs 5.8 & 5.9).

5.7. Cyclic-Current Transient Thermal-Electrical Analysis

The cyclic-current transient electro-thermal analysis was carried out initially using the standard-mesh FE model (including the copper bar) and, subsequently, using the fine-mesh model. The main aim of this study was to obtain the amplitude of the temperature variation in the fuse element, after stabilisation. The analysis was performed in a single step while the magnitude of the injected current was varied using the ABAQUS **Amplitude* [104] command.

5.7.1. Symmetric Pulsed-Current Loading Duties

The loading duties for samples S-1÷S-8 were set to the same loading duties used for fuse samples E-1÷E-8 (Table 5-13), to enable correlation of the computed temperatures and lifetimes with the corresponding experimental lifetimes (Paragraph 5.11.5, p.123).

Rectangular current pulses were used with the t_{ON}/t_{OFF} mark/space ratio set at ϕ=50% constant for all tests. The ON current was 40A, which resulted in an RMS current of 28.3A. From equation 5-2 the computed maximum cycle average element temperature (i.e. T_{max} for $f \rightarrow \infty$) is 240.8°C and the end-cap temperature is 60.5°C. Detailed pulsed-current loading data for samples S-1÷S-8 is given in Table 5-3.

Table 5-3. Pulsed-current loading data – symmetric current duties.

Sample	Δt	f
	s	Hz
S-1	18	0.0(5)
S-2	10	0.1
S-3	6	0.1(6)
S-4	3	0.(3)
S-5	2	0.5
S-6	1.46	0.68
S-7	1.06	0.94
S-8	0.487	2.05

Since the cyclic temperature amplitude is greatest for Sample S-1 and smallest for Sample S-8, the results for these two samples are presented below, graphically, in greater detail.

The computed transient temperature profiles for Sample S-1, for the initial period of 234s, are given in Figure 5-23 and, are given following stabilisation, in Figure 5-24.

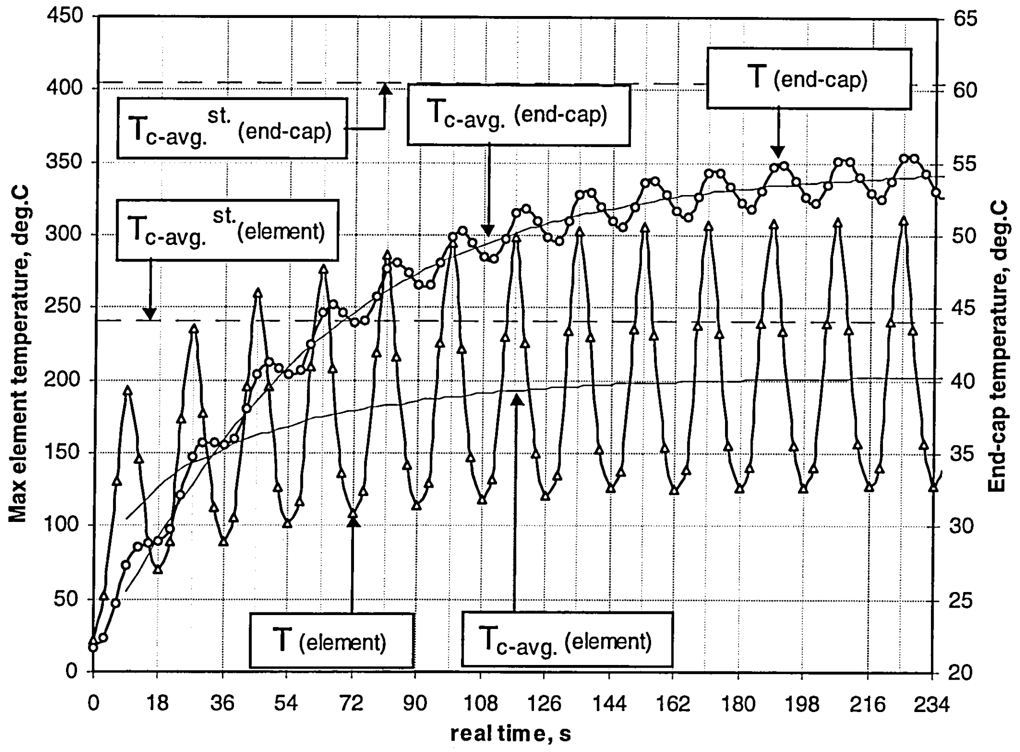

Figure 5-23. Transient maximum element and end-cap temperature profiles; Sample S-1, real time $0< t <234s$, $I_{on}=40A$, $\phi=50\%$, $t_{on}=9s$, $t_{off}=9s$, $f=0.0(5)$ Hz.

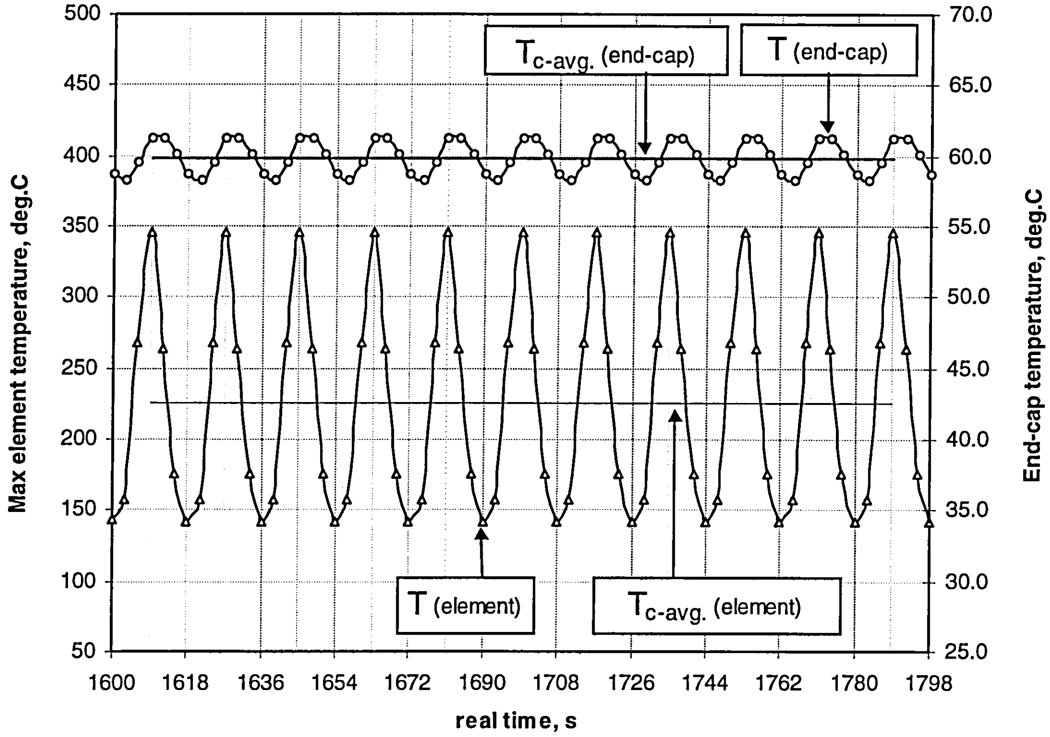

Figure 5-24. Transient maximum element and end-cap temperature profiles; Sample S-1, real time $1600< t <1798s$, $I_{on}=40A$, $\phi=50\%$, $f=0.0(5)$ Hz.

Figure 5-23 shows that the initial temperature range (peak-to-peak temperature excursion) gradually increased due to the variations in the fuse temperature-dependent material properties. Since the temperature amplitude is the most important variable for predicting fatigue failure, to obtain accurate predictions the computing time can be excessive, especially when the period of the cycle is short. The temperature profiles presented in Figure 5-24 were obtained only after a lengthy computer simulation[8]. Computer running times can be significantly reduced if 'hot-start' initial conditions are applied. In this case the temperature distribution in the model was initially obtained for steady-state conditions under DC loading of the same RMS value of the current (28.3A), and subsequently applied at the start of the pulsed-current loading transient analysis. The solution was assumed to have attained stabilised condition when all of the following equations were satisfied for both the end-cap and the element temperatures:

$$\left.\begin{aligned} \left|T^{n}_{c-avg.} - T^{n-1}_{c-avg.}\right| &\leq \lambda \cdot T^{n-1}_{c-avg.} \\ \left|T^{n}_{c-max.} - T^{n-1}_{c-max.}\right| &\leq \lambda \cdot T^{n-1}_{c-max.} \\ \left|T^{n}_{c-min.} - T^{n-1}_{c-min.}\right| &\leq \lambda \cdot T^{n-1}_{c-min.} \end{aligned}\right\} \quad \text{[Eq.5-3]}$$

where: $\lambda=0.002$ is the maximum allowed temperature error and n is the cycle counter. Transient temperature profiles obtained for Sample S-1 using 'hot-start' initial conditions are presented in Figure 5-25. The initial transient oscillation decayed fairly rapidly and fully stabilised conditions (as defined above) were obtained after 21 cycles. If less restrictive convergence criteria were to be applied, the analysis could be terminated after only a couple of cycles, hence significantly reducing the computing time.

The computed transient temperature profiles for Sample S-8 are given in Figures 5-26 and 5-27. In this case, using 'hot-start' initial conditions, stabilisation was obtained after 37 cycles.

---

[8] Assuming stabilisation is obtained after t=1,800s, at 3s time step (Sample No.1) the required number of increments is 600 and, approximately, 2,100 iterations. On a SunSparc10 workstation with 128MB RAM and 350MB SWAP RAM the analysis took about 336 hrs. For Sample No.7, where the required time step increment is 0.162s, the total number of increments to stabilisation is 11,088. The projected analysis time would, therefore, be 6,209 hrs and, clearly, is unacceptable. The 'hot-start' initial condition was consequently used to reduce the computer running times. Computer running time can also be shortened by increasing the time increment, hence reducing the number of data points per cycle (to a minimum of two points), but this option was not used in this study, because the 'hot-start' solution proved to be sufficient.

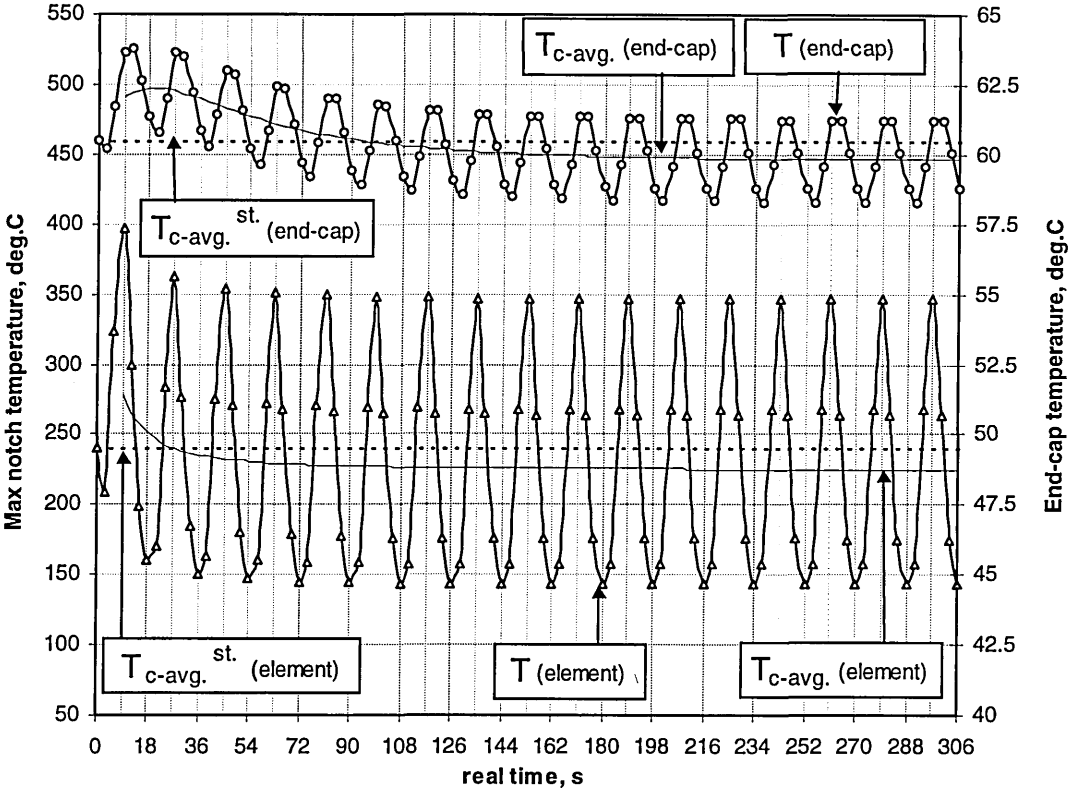

Figure 5-25. Transient maximum fuse element temperature and end-cap temperature profiles; Sample S-1, 'hot-start' initial conditions, real time 0<t<306s, I_{on}=40A, ϕ=50%, f=0.0(5) Hz.

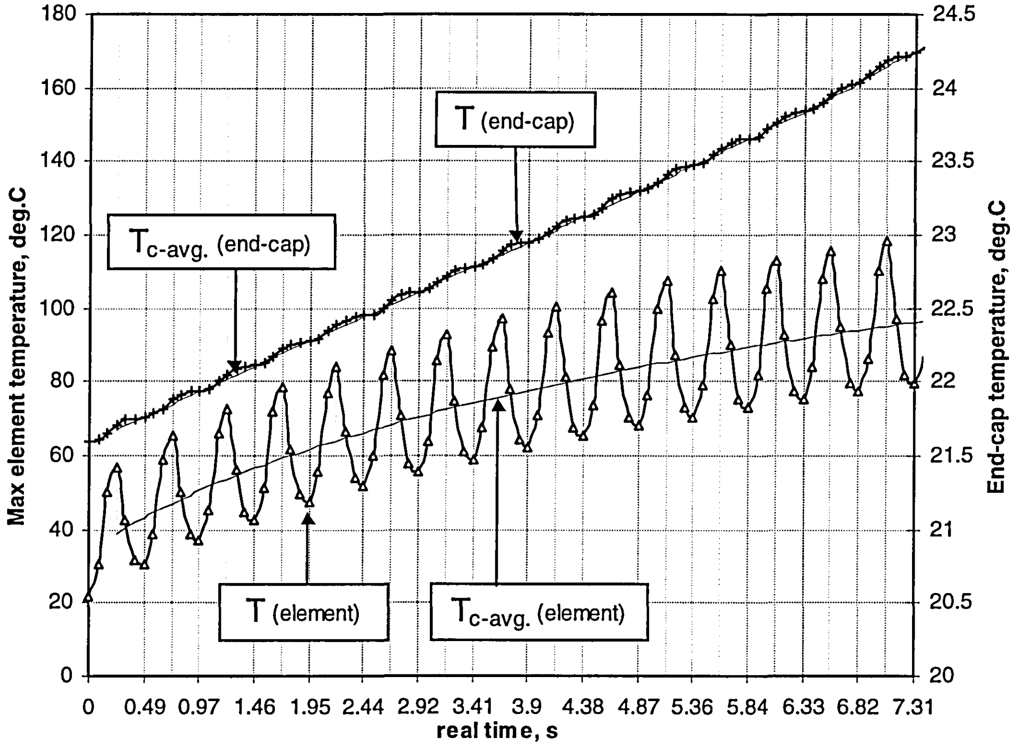

Figure 5-26. Transient maximum fuse element temperature and end-cap temperature profiles; Sample S-8, real time 0<t<7.305s, I_{on}=40A, ϕ=50%, t_{on}=0.2435s, t_{off}=0.2435s, f=2.05 Hz.

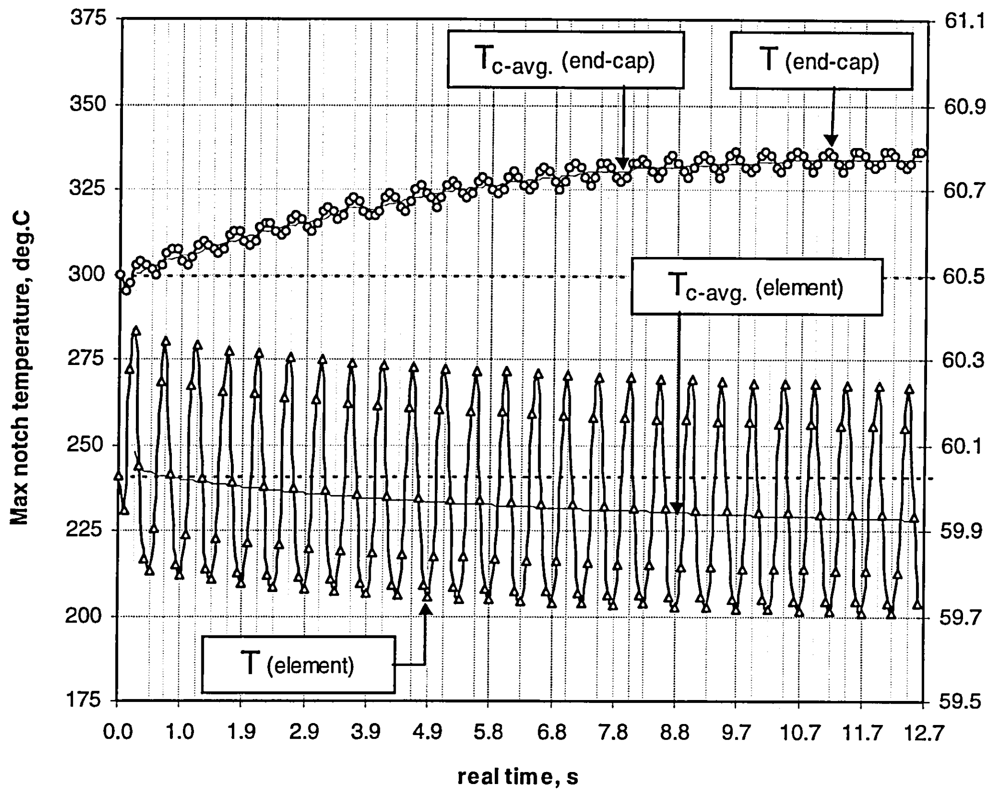

Figure 5-27. Transient maximum fuse element temperature and end-cap temperature profiles; Sample S-8, 'hot-start' initial conditions, real time 0<t<12.66s, I_{on}=40A, ϕ=50%, t_{on}=0.2435s, t_{off}=0.2435s, f=2.05 Hz.

Comprehensive results in the thermal domain for all samples are presented in Table 5-4. These results show that temperature $T_{c\text{-avg.}}$ was identical (within acceptable error) for all samples, and that the $\Delta T_c^{st.}$ increased with increase in the cycle period.

Table 5-4. Results of the transient pulsed-current loading analysis for samples S-1 ÷S8 (thermal domain).

Sample	$T_{c-min.}^{st.}$	$T_{c-max.}^{st.}$	$T_{c-avg.}^{st.}$	$\Delta T_c^{st.}$
	°C	°C	°C	°C
S-1	142.6	346.0	225.4	203.4
S-2	158.5	316.6	223.2	158.1
S-3	170.1	298.5	223.0	128.4
S-4	183.7	283.7	225.1	100.0
S-5	189.2	277.0	225.5	87.8
S-6	191.6	272.4	224.9	80.8
S-7	196.0	269.4	226.3	73.4
S-8	200.9	266.9	228.9	66.0

The computed thermally-induced stresses & strains for samples S-1÷S-8 are presented in Paragraph 5.9.1 (p.109).

5.7.2. Asymmetric Pulsed-Current Loading Duties

The main aim of the study presented in this section was to demonstrate that the procedure developed for the symmetric pulsed-current loading duties can also be used for life prediction for any other intermittent current-loading duty.

Two cases of intermittent loading were considered, namely i) the I_{ON} current was kept constant and the mark/space ratio ϕ was varied, hence the I_{rms} increased as ϕ increased; and ii) both the I_{ON} current and ϕ were varied, but the I_{rms} was constant at 20A (rated current of the fuse).

Case 1.

As stated, rectangular current pulses were used for this study, where the t_{ON}/t_{OFF} mark space ratio was varied from ϕ=0.1 to ϕ=0.9 and the period of Δt=10s was held constant for all samples. The I_{ON} current was fixed at 30A and 'hot-start' initial conditions were used for all samples. Detailed data pertaining to pulsed-current loading for samples A-1÷A-5 and the results of the computational study, in the thermal domain, are both given in Table 5-5.

Table 5-5. Pulsed-current loading data and results of the analysis in the thermal domain – asymmetric current pulses, samples A-1÷A-5.

Sample	I_{on}	ϕ	t_{on}/t_{off}	I_{rms}	$T^{st.}_{c-min.}$	$T^{st.}_{c-max.}$	$T^{st.}_{c-avg.}$	$\Delta T^{st.}_{c}$
	A	%	s/s	A	°C	°C	°C	°C
A-1	30	10	1/9	9.5	27.7	54.7	33.4	27.0
A-2	30	30	3/7	16.4	47.8	96.3	64.2	48.5
A-3	30	50	5/5	21.2	74.6	119.3	94.0	44.7
A-4	30	70	7/3	25.1	123.4	193.8	157.8	70.4
A-5	30	90	9/1	28.5	200.1	257.1	238.2	57

The effect of varying ϕ on the transient temperature profile, after stabilisation, is shown graphically in Figure 5-28.

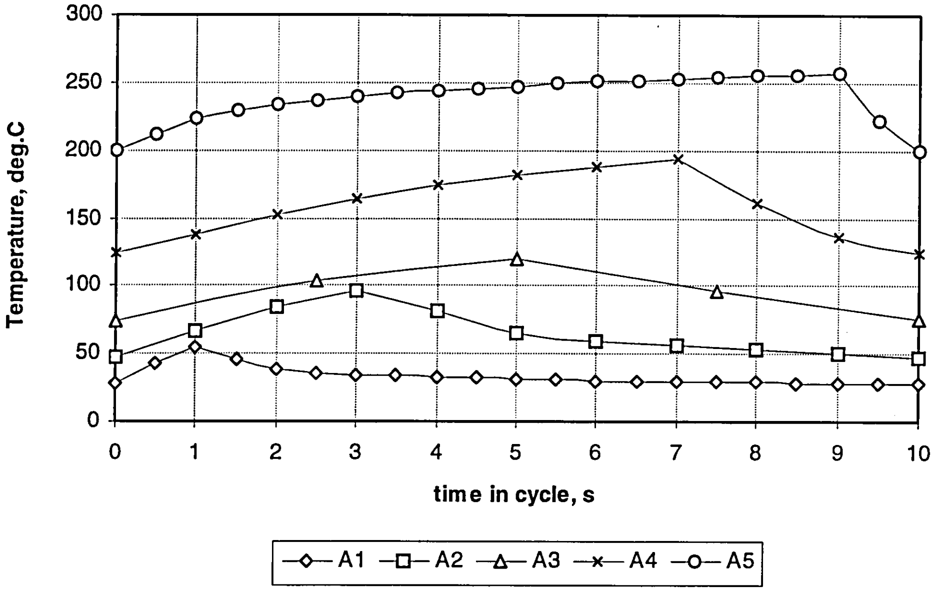

Figure 5-28. Transient maximum element temperature profiles; Samples A-1÷A-5, I_{on}=30A, Δt=10s.

Case 2.

In this study rectangular current pulses were used where both the t_{ON}/t_{OFF} mark space ratio φ and the I_{ON} current were varied to produce a constant I_{rms}=20A for all samples. The mark space ratio was varied from φ=0.1 to φ=0.9 and the I_{ON} current was varied from 21.1A to 63.2A. The period was Δt=10s and 'hot-start' initial conditions were applied for all samples. Detailed data pertaining to pulsed-current loading for samples A-6÷A-10 and the results of the computational study, in the thermal domain, are both given in Table 5-6.

Table 5-6. Pulsed-current loading data and results of the analysis in the thermal domain – asymmetric current pulses, samples A-6÷A-10.

Sample	I_{on}	φ	t_{on}/t_{off}	I_{rms}	$T^{st.}_{c-min.}$	$T^{st.}_{c-max.}$	$T^{st.}_{c-avg.}$	$\Delta T^{st.}_{c}$
	A	%	s/s	A	°C	°C	°C	°C
A-6	63.2	10	1/9	20	58.6	228.9	90.3	170.3
A-7	36.5	30	3/7	20	64.5	146.9	90.3	82.4
A-8	28.3	50	5/5	20	67.3	115.5	86.6	48.2
A-9	23.9	70	7/3	20	75.5	110.8	93.1	35.3
A-10	21.1	90	9/1	20	82.5	100.6	94.6	18.1

From Table 5-6 it is evident that as the mark/space-ratio φ is decreased ΔT increases. This is unfortunate because, for example, in a 6-pulse rectifier (i.e. typical semiconductor fuse application) φ≈1.6, hence from the fatigue life viewpoint the fuse is subjected to a significantly adverse loading.

The effect of varying ϕ for I_{rms}=const. on the transient temperature profiles, after stabilisation, is shown graphically in Figure 5-29.

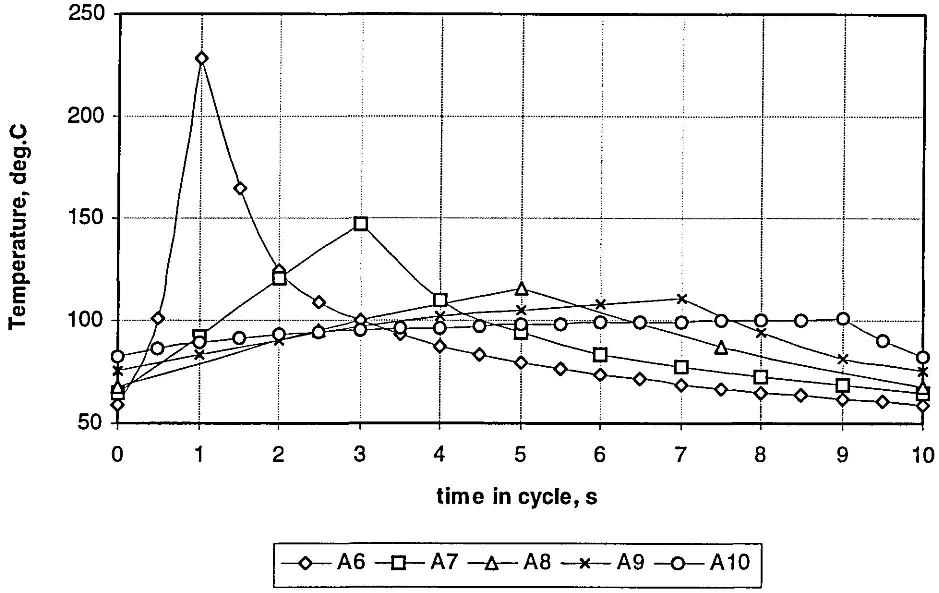

Figure 5-29. Transient maximum element temperature profiles; Samples A-6÷A-10, I_{ON}=var, I_{RMS}=20A, Δt=10s.

The predicted magnitudes of the thermally-induced stresses & strains at the thermal extremes for samples A-1÷A-10 are presented in Paragraph 5.9.2 (p.112), and the results of the study of fuse life due to cyclic-current loading are presented in Paragraph 5.10 (p.116).

5.8. Distribution and Magnitudes of the Thermally-Induced Stresses & Strains in the Manufactured Fuse Element Carrying Steady-State Rated Current

The fine-mesh FE model (including the copper bar) was used for this study. The thermal stress analysis was performed for the element carrying a rated current of 20A to ascertain the characteristic of the distribution of the stresses & strains and their magnitudes. For the rated current the maximum steady-state element temperature was previously found to be 101 °C (Eq.5-2). The magnitudes of the stresses & strains obtained for the rated current were compared with the corresponding magnitudes obtained from the pulsed-current loading analyses (Paragraph 5.9), where the RMS current was 28.3A, which enabled determination of the magnitudes of the thermo-mechanical over-load used for the accelerated ageing tests. The distributions of the critical stresses and strains, presented below, are limited to the central region of the fuse element (notches B-2 & B-3), where the magnitudes of the solution variables are largest, Figure 5-30.

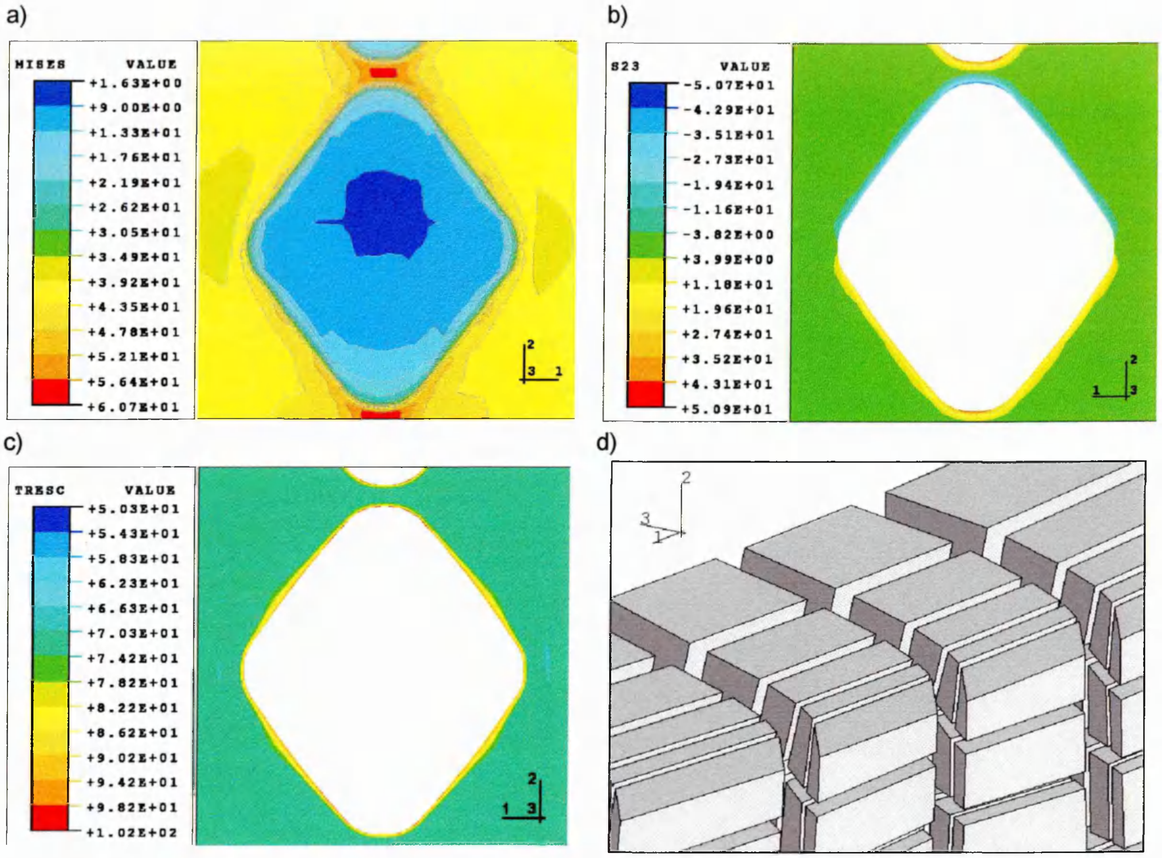

Figure 5-30. Manufactured substrate fuse – distribution of the stresses & strains and displacement distribution in the conductive film carrying steady-state rated current – 20A (notches B-2 & B-3). In a) the conductive film was omitted clarity; In b) through d) the substrate was omitted for clarity. a) MISES stress; b) shear stress S_{23}; c) TRESCA stress; d) deformed plot of the conductive film (notch B-3, mag.200x, FEs shrank by 20% for clarity).

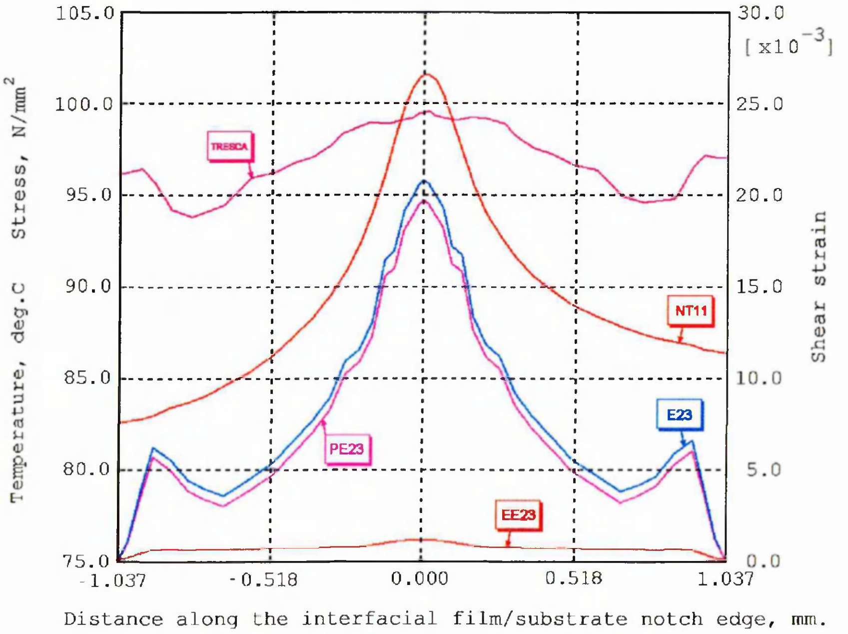

Figure 5-31. Profiles of temperature, elastic EE_{23} plastic PE_{23} and total E_{23} shear strains, maximum shear stress TRESCA along the interfacial film/substrate notch edge (notch B-3).

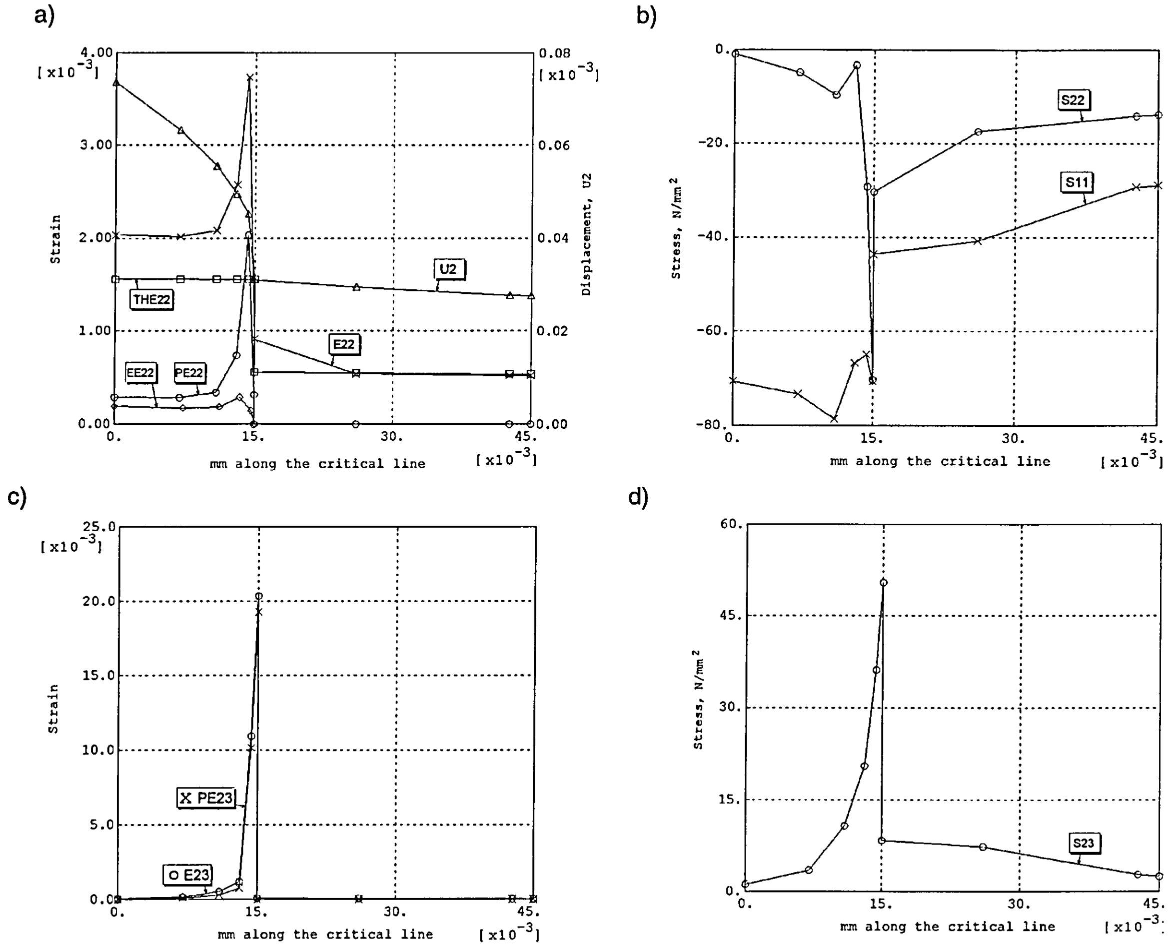

Figure 5-32. Profiles of solution variables along the critical line through the conductive film and substrate thickness in the MSF carrying steady-state rated current (notch B-3); a) direct strains THE_{22}, EE_{22}, PE_{22}, E_{22} and displacement U_2, b) direct stresses S_{11} and S_{22}, c) shear strains E_{23} and PE_{23}, d) shear stress S_{23}.

The main findings of this study are as follows:

- The MISES stress is largest in the conductive film at the centre of notch B-3, mainly due to the large direct stresses S_{11} and S_{22} (Figure 5-30 a).
- The shear stresses (S_{23} and TRESCA) were found to be largest in notch B-3 along the interfacial film/substrate notch edge. These stresses are largest at the point of the minimum cross-section of the notch – the critical point (Figure 5-30 b & c).
- The shear strains EE_{23}, PE_{23} and E_{23} are largest along the interfacial film/substrate notch edge. These strains are largest at the point of minimum cross-section of the notch, where the temperature is largest (Figure 5-31).
- Given that total strain E_{22} is the sum of the thermal, elastic and plastic strains: $\mathrm{E}_{22} = \mathrm{THE}_{22} + \mathrm{EE}_{22} + \mathrm{PE}_{22}$, at the point on the edge of the conductive film, at the minimum cross-section of the notch (Point B in Figure A-2, p.161), the thermal strain accounts for $\frac{1.58}{2.03} \cdot 100\% = 77.8\%$ of the total strain, the elastic strain EE_{22} for

$\frac{0.186}{2.03} \cdot 100\% = 9.1\%$ and the plastic strain PE_{22} for $\frac{0.288}{2.03} \cdot 100\% = 14.1\%$. These results indicate that the conductive film is subjected to a combination of thermal and mechanical (elastic and plastic) strains (Figure 5-32 a).

- The plastic strain PE_{22} is zero everywhere in the substrate, because perfect elasticity is assumed for the substrate material (Figure 5-32 a & c).
- The magnitude of the strain E_{23} at the film/substrate interface is 2.035×10^{-2}, most of which is the plastic strain which accounts for $\frac{0.01927}{0.02035} \cdot 100\% = 94.7\%$ of total strain.

  The shear stress S_{23}, however, is predominantly determined by the *elastic* shear strain EE_{23}:

  $$S_{23}^{el.} = EE_{23}^{el.} \cdot G = (E_{23} - PE_{23}) \cdot \frac{E}{2(1+v)} = (0.0203 - 0.0193) \cdot \frac{122{,}000}{2(1+0.343)} = 49.05 \text{ N/mm}^2,$$

  while $S_{23}^{max.} = 50.47$ N/mm^2, i.e. PE_{23} accounts for only 50.47–49.05 = 1.41 N/mm^2 of the total shear stress (Figure 5-32 c & d).
- Shear strains E_{23} and PE_{23} decrease rapidly the further away they are measured from the critical point (Figure 5-31 & Figure 5-32 c).

5.9. Cyclic Thermal Stress/Strain Amplitudes Under Pulsed Current Loading Conditions

For all samples (S-1÷S-8 and A-1÷A-10, Tables 5-4 & 5-6) nodal temperatures from the transient electro-thermal analysis at time instants t_{ON} and t_{OFF} (after stabilisation) were saved in data files. Subsequently, for each sample, a thermal stress analysis was performed. Using the saved nodal temperature distributions the magnitudes of the thermal stresses & strains at the thermal extremes of the current-pulse period (T_{min} at t_{ON} and T_{max} at t_{OFF}) were computed. For each sample the thermal stress analysis consisted of two steps: i) thermal loading from $T=T_{amb}$ to $T=T_{max}$ and ii) relaxation from $T=T_{max}$ to $T=T_{min}$. Electro-thermal strain-cycling was assumed not to alter material characteristics.

De-bonding and crack formation were presumed to initiate on the critical line, most likely at the critical point, where the shear stresses & strains are largest (Paragraph 5.8, p.105). The maximum shear strain was previously found in notch B-3 at the critical point. Consequently, the critical point of notch B-3 was at the centre of the investigation. The results, presented in the following sections, given at the critical point, are the average of the variable magnitudes in the conductive film, extrapolated from the integration points to the critical point.

Maximum shear strain at the critical point was calculated from:

$$\gamma_{max} = \sqrt{(\varepsilon_{22} - \varepsilon_{33})^2 + \gamma_{23}{}^2} \qquad \text{[Eq.5-4]}$$

The equivalent maximum shear stress was calculated from:

$$\tau_{max} = \pm\sqrt{\left(\frac{\sigma_{11}-\sigma_{33}}{2}\right)^2 + \tau_{23}{}^2} \qquad \text{[Eq.5-5]}$$

The cyclic strain range, the elastic strain range and the plastic strain range were calculated from:

$$\Delta\gamma = \gamma^{max}\Big|_{t=t_{OFF}} - \gamma^{max}\Big|_{t=t_{ON}} \qquad \text{[Eq.5-6]}$$

$$\Delta\gamma_{el.} = \gamma_{el.}^{max}\Big|_{t=t_{OFF}} - \gamma_{el.}^{max}\Big|_{t=t_{ON}} \qquad \text{[Eq.5-7]}$$

$$\Delta\gamma_{pl.} = \Delta\gamma - \Delta\gamma_{el.} \qquad \text{[Eq.5-8]}$$

5.9.1. Stress/Strain Differentials for the Symmetric Pulsed-Current Duties

Variable magnitudes at the critical point computed for samples S-1÷S-8 are shown in Table 5-7.

Table 5-7. The results of the transient pulsed-current loading analysis for samples S-1÷S-8 (mechanical domain).

Solution variable	Sample Unit	S-1	S-2	S-3	S-4	S-5	S-6	S-7	S-8
$S_{MISES}^{max}\big\|_{t=t_{ON}}$	N/mm^2	177	163	153	143	138	135	133	143
$S_{MISES}^{max}\big\|_{t=t_{OFF}}$	N/mm^2	140	133	130	126	124	123	123	120
$\Delta\sigma_{MISES}$	N/mm^2	37	30	23	17	14	12	10	23
σ_{MISES}^{m}	N/mm^2	158	148	142	135	131	129	128	131
$S_{TRESCA}^{max}\big\|_{t=t_{ON}}$	N/mm^2	205	188	176	164	159	156	154	165
$S_{TRESCA}^{max}\big\|_{t=t_{OFF}}$	N/mm^2	161	154	150	146	144	142	142	138
$\Delta\sigma_{TRESCA}$	N/mm^2	44	34	26	18	15	14	26	27
σ_{TRESCA}^{m}	N/mm^2	183	171	163	155	152	149	141	152
$S_{11}^{max}\big\|_{t=t_{ON}}$	N/mm^2	102	93.2	86.3	76.8	72	64.8	59.9	33.2
$S_{11}^{max}\big\|_{t=t_{OFF}}$	N/mm^2	-93.8	-91.1	-89.4	-88.0	-87.3	-86.8	-86.5	-85.2
$\Delta\sigma_{11}$	N/mm^2	196	184	176	165	159	152	146	118
σ_{11}^{m}	N/mm^2	4.1	1.1	-1.6	-5.6	-7.7	-11.0	-13.3	-26
$S_{22}^{max}\big\|_{t=t_{ON}}$	N/mm^2	100	91.2	84.3	76.3	67.1	63.8	58.1	26.2
$S_{22}^{max}\big\|_{t=t_{OFF}}$	N/mm^2	-92.7	-90.1	-88.5	-87.1	-86.4	-86.0	-85.7	-84.5
$\Delta\sigma_{22}$	N/mm^2	192.7	181	173	163	154	150	144	110.7
σ_{22}^{m}	N/mm^2	3.6	0.6	-2.1	-5.4	-9.7	-11.1	-13.8	-29.1
$S_{33}^{max}\big\|_{t=t_{ON}}$	N/mm^2	112	105	99.6	92.9	89.3	84.9	80.9	57.3

continued on next page

continued from previous page

Solution variable	Sample	S-1	S-2	S-3	S-4	S-5	S-6	S-7	S-8
$S_{33}^{max}\big\|_{t=t_{OFF}}$	N/mm^2	-101	-98.6	-97.1	-95.9	-95.3	-94.8	-94.6	-93.4
$\Delta\sigma_{33}$	N/mm^2	213	204	197	189	185	178	176	150.7
σ_{33}^{m}	N/mm^2	5.5	3.2	1.3	-1.5	-3.0	-4.9	-6.8	-18.1
$S_{23}^{max}\big\|_{t=t_{ON}}$	N/mm^2	-102	-93.7	-87.8	-81.8	-79.1	-77.2	-75.9	-73.2
$S_{23}^{max}\big\|_{t=t_{OFF}}$	N/mm^2	80.6	76.9	74.7	72.7	71.7	71.0	70.6	68.8
$\Delta\sigma_{23}$	N/mm^2	182.6	170.6	163	156	151	148	147	142
σ_{23}^{m}	N/mm^2	-10.7	-8.4	-6.6	-4.6	-3.7	-3.1	-2.7	-2.2
$E_{23}^{max}\big\|_{t=t_{ON}}$	$\times10^{-2}$	3.51	3.70	3.87	4.13	4.24	4.33	4.44	4.66
$E_{23}^{max}\big\|_{t=t_{OFF}}$	$\times10^{-2}$	6.44	6.00	5.72	5.48	5.36	5.28	5.23	5.01
$PE_{23}^{max}\big\|_{t=t_{ON}}$	$\times10^{-2}$	3.73	3.90	4.06	4.31	4.42	4.50	4.61	4.84
$PE_{23}^{max}\big\|_{t=t_{OFF}}$	$\times10^{-2}$	6.25	5.82	5.55	5.31	5.20	5.12	5.07	4.86
$EE_{23}^{max}\big\|_{t=t_{ON}}$	$\times10^{-2}$	-0.223	-0.206	-0.193	-0.181	-0.175	-0.172	-0.169	-0.182
$EE_{23}^{max}\big\|_{t=t_{OFF}}$	$\times10^{-2}$	0.191	0.180	0.173	0.167	0.165	0.163	0.162	0.157
$E_{22}^{max}\big\|_{t=t_{ON}}$	$\times10^{-2}$	0.26	0.29	0.31	0.35	0.35	0.37	0.37	0.41
$E_{22}^{max}\big\|_{t=t_{OFF}}$	$\times10^{-2}$	0.65	0.59	0.55	0.52	0.51	0.50	0.48	0.45
$E_{33}^{max}\big\|_{t=t_{ON}}$	$\times10^{-2}$	0.19	0.218	0.24	0.26	0.27	0.27	0.26	0.26
$E_{33}^{max}\big\|_{t=t_{OFF}}$	$\times10^{-2}$	0.44	0.41	0.38	0.35	0.34	0.33	0.32	0.29
$EE_{22}^{max}\big\|_{t=t_{ON}}$	$\times10^{-2}$	0.021	0.018	0.016	0.012	0.013	0.009	-0.0071	-0.0046
$EE_{22}^{max}\big\|_{t=t_{OFF}}$	$\times10^{-2}$	-0.022	-0.022	-0.022	-0.021	-0.021	-0.021	-0.021	-0.018
$EE_{33}^{max}\big\|_{t=t_{ON}}$	$\times10^{-2}$	0.034	0.032	0.033	0.036	0.035	0.033	0.033	0.031
$EE_{33}^{max}\big\|_{t=t_{OFF}}$	$\times10^{-2}$	-0.033	-0.031	-0.031	-0.029	-0.030	-0.029	-0.029	-0.028
$\gamma^{max}\big\|_{t=t_{ON}}$	$\times10^{-2}$	3.51	3.70	3.87	4.13	4.24	4.33	4.44	4.66
$\gamma^{max}\big\|_{t=t_{OFF}}$	$\times10^{-2}$	6.44	6.00	5.72	5.48	5.36	5.28	5.23	5.01
γ_{avg}	$\times10^{-2}$	4.98	4.85	4.78	4.81	4.80	4.81	4.84	4.84
$\tau^{max}\big\|_{t=t_{ON}}$	N/mm^2	-102.2	-93.9	-88.1	-82.2	-79.9	-77.9	-76.7	-83.0
$\tau^{max}\big\|_{t=t_{OFF}}$	N/mm^2	80.7	77.0	74.8	72.8	71.8	71.1	70.7	68.9
τ_{avg}	N/mm^2	-10.6	-8.5	-6.7	-4.7	-4.1	-3.4	-3.0	-7.1
$\gamma_{el.}^{max}\big\|_{t=t_{ON}}$	$\times10^{-2}$	0.223	0.206	0.193	0.181	0.175	0.172	0.169	0.182
$\gamma_{el.}^{max}\big\|_{t=t_{OFF}}$	$\times10^{-2}$	0.191	0.180	0.173	0.167	0.165	0.163	0.162	0.157
cyclic $\Delta\gamma$	$\times10^{-2}$	2.93	2.30	1.85	1.35	1.12	0.95	0.79	0.35
cyclic $\Delta\gamma_{el.}$	$\times10^{-2}$	0.414	0.386	0.366	0.348	0.340	0.335	0.331	0.339
cyclic $\Delta\gamma_{pl.}$	$\times10^{-2}$	2.516	1.914	1.484	1.00	0.78	0.615	0.46	0.011

The cyclic maximum shear-stress/maximum shear strain curves, given at the critical point, are shown in Figure 5-33. For clarity, only curves for samples S-1, S-5 and S-8 were included.

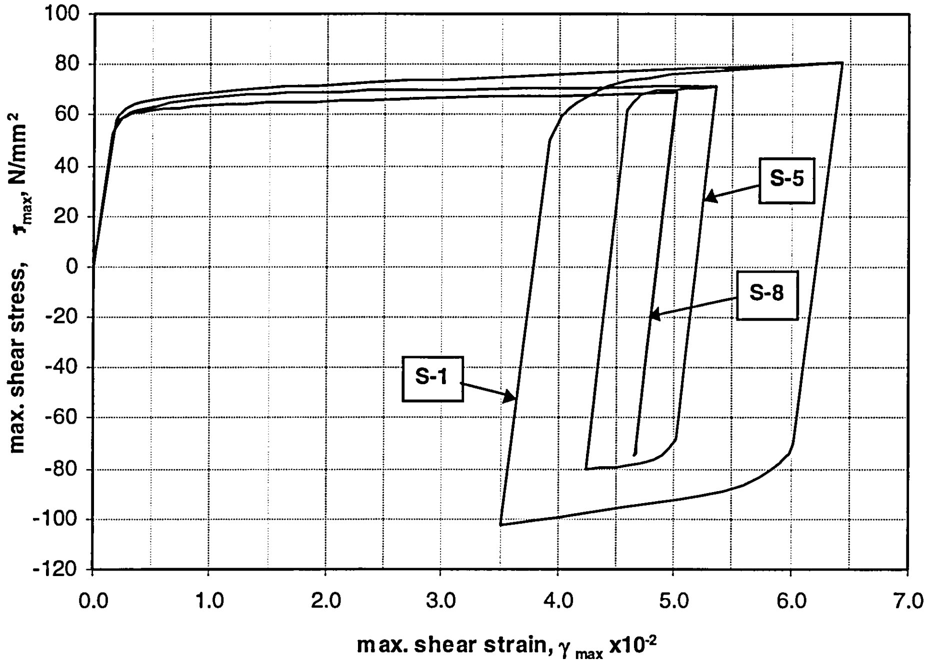

Figure 5-33. Cyclic maximum shear-stress/maximum shear strain curve, given at the critical point, for samples S-1, S-5 and S-8.

Total cyclic strain range γ, the elastic strain range $\gamma_{el.}$ and the plastic strain range $\gamma_{pl.}$, the cycle average shear strain $\gamma_{c\text{-}avg.}$ and the cycle average shear stress $\tau_{c\text{-}avg.}$ versus the current period are shown in Figure 5-34.

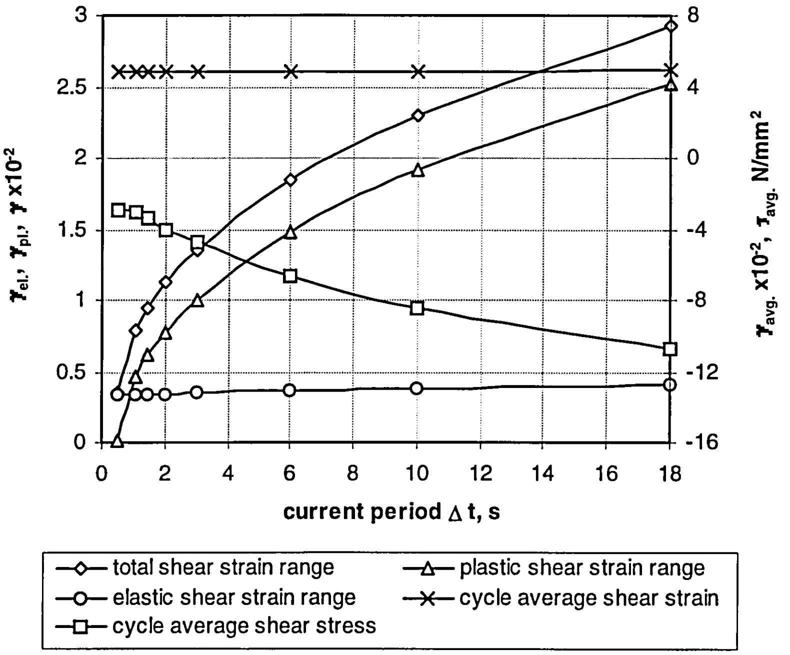

Figure 5-34. Cyclic total γ, elastic $\gamma_{el.}$ and plastic $\gamma_{pl.}$ strain ranges, cycle average maximum shear strain $\gamma_{c\text{-}avg.}$, cycle-average maximum shear stress $\tau_{c\text{-}avg.}$ versus pulsed-current period Δt.

From the results presented in Table 5-7 and Figures 5-33 & 5-34 the following conclusions can be drawn:

- Given the results for all samples, T_{off} is largest for sample S-1, hence the MISES and TRESCA stresses are largest at $t=t_{off}$ for sample S-1; amplitudes of all the cyclic stresses decreased as the current period decreased, to reflect the decreasing temperature amplitude (Table 5-7).
- All samples experienced plastic deformation. The ratio $\Delta\epsilon_{pl.}/\Delta\epsilon$ decreased as the temperature amplitude was decreased (Table 5-7, Figure 5-34).
- Direct stresses S_{11}, S_{22} and S_{33} are compressive at $t=t_{off}$ and tensile at $t=t_{on}$ – due to the thermal cyclic expansion and contraction of the film material (Table 5-7).
- The amplitude of the E_{23} and PE_{23} shear strains, $\frac{1}{2}\left(E_{23}^{max}\Big|_{t=t_{OFF}} - E_{23}^{max}\Big|_{t=t_{ON}}\right)$ and $\frac{1}{2}\left(PE_{23}^{max}\Big|_{t=t_{OFF}} - PE_{23}^{max}\Big|_{t=t_{ON}}\right)$ respectively, decreased as the current period was decreased; the elastic strain amplitude $\frac{1}{2}\left(EE_{23}^{max}\Big|_{t=t_{OFF}} - EE_{23}^{max}\Big|_{t=t_{ON}}\right)$ was approximately constant (Table 5-7).
- The cyclic maximum shear strain range $\Delta\gamma$ and $\Delta\gamma_{pl.}$ decreased as the pulsed-current period was decreased; from the $\Delta\epsilon_{pl.}/\Delta\epsilon$ trend it was also observed that completely elastic cycling would occur for current periods smaller than $\Delta t \cong 0.485$s (Table 5-7, Figures 5-33 & 5-34).
- The cycle average maximum shear strain for all samples was approximately constant, at $\gamma_{c\text{-}avg.}=4.84\times10^{-2}$ (Figure 5-33); this is because $\gamma_{c\text{-}avg.}$ is proportional to the cycle average temperature $T_{c\text{-}avg.}$, which was approximately constant for all samples (Table 5-4).
- At the critical point $\gamma_{23} >> \varepsilon_{22} \approx \varepsilon_{33}$, hence maximum shear strain $\gamma^{max.}$ is approximately equal to E_{23}: $\gamma^{max.} \cong \gamma_{23}$ (Table 5-7).
- The cycle average maximum shear stress $\tau_{c\text{-}avg.}$ for all samples is negative (compressive); $\tau_{c\text{-}avg.}$ is, however, relatively small (Figure 5-34).

5.9.2. Stress/Strain Differentials for the Asymmetric Pulsed-Current Duties

The results of the cyclic thermal-stress analysis for samples A-1÷A-5 are presented in Table 5-8 and for samples A-6÷A-10 in Table 5-9.

Table 5-8. The results of the transient pulsed-current loading analysis for samples A-1÷A-5 (mechanical domain).

Solution variable	Sample	A-1	A-2	A-3	A-4	A-5
	Unit					
$S^{max}_{MISES}\big\|_{t=t_{ON}}$	N/mm^2	76.2	94.3	104	115	131
$S^{max}_{MISES}\big\|_{t=t_{OFF}}$	N/mm^2	75.8	85.2	90.1	105	120
$\Delta\sigma_{MISES}$	N/mm^2	0.4	9.1	13.9	10	11
σ^{m}_{MISES}	N/mm^2	76.0	89.6	97.1	110	125.5
$S^{max}_{TRESCA}\big\|_{t=t_{ON}}$	N/mm^2	88.0	109	120	132	152
$S^{max}_{TRESCA}\big\|_{t=t_{OFF}}$	N/mm^2	87.3	98.2	104	121	138
$\Delta\sigma_{TRESCA}$	N/mm^2	0.7	10.8	16	11	14
σ^{m}_{TRESCA}	N/mm^2	87.7	103.6	112	126.5	145
$S^{max}_{11}\big\|_{t=t_{ON}}$	N/mm^2	5.5	38.4	30.5	57.5	43.1
$S^{max}_{11}\big\|_{t=t_{OFF}}$	N/mm^2	-59.5	-68.9	-71.8	-79.2	-85.3
$\Delta\sigma_{11}$	N/mm^2	65.0	107.3	102.3	136.7	128.4
σ^{m}_{11}	N/mm^2	-27.0	-15.3	-20.7	-10.9	-21.1
$S^{max}_{22}\big\|_{t=t_{ON}}$	N/mm^2	1.69	37.1	28.1	57.1	38.7
$S^{max}_{22}\big\|_{t=t_{OFF}}$	N/mm^2	-59.5	-68.6	-71.4	-78.7	-84.6
$\Delta\sigma_{22}$	N/mm^2	61.2	105.7	99.5	135.8	123.3
σ^{m}_{22}	N/mm^2	-28.9	-15.8	-21.7	-10.8	-22.9
$S^{max}_{33}\big\|_{t=t_{ON}}$	N/mm^2	14.7	56.7	51.6	75.4	69.5
$S^{max}_{33}\big\|_{t=t_{OFF}}$	N/mm^2	-69.3	-77.8	-80.6	-87.8	-93.5
$\Delta\sigma_{33}$	N/mm^2	-114.1	134.5	132.2	163.2	163
σ^{m}_{33}	N/mm^2	-27.3	-10.6	-14.5	-6.2	-12
$S^{max}_{23}\big\|_{t=t_{ON}}$	N/mm^2	-43.5	-53.7	-59.1	-65.5	-74.8
$S^{max}_{23}\big\|_{t=t_{OFF}}$	N/mm^2	43.4	48.9	51.8	60.3	69.0
$\Delta\sigma_{23}$	N/mm^2	86.9	102.6	110.9	125.8	143.8
σ^{m}_{23}	N/mm^2	-0.1	-2.4	-3.65	-2.6	-2.9
$E^{max}_{23}\big\|_{t=t_{ON}}$	$\times10^{-2}$	0.429	1.23	1.88	2.99	4.57
$E^{max}_{23}\big\|_{t=t_{OFF}}$	$\times10^{-2}$	0.611	1.70	2.25	3.87	5.03
$PE^{max}_{23}\big\|_{t=t_{ON}}$	$\times10^{-2}$	0.520	1.35	2.01	3.13	4.72
$PE^{max}_{23}\big\|_{t=t_{OFF}}$	$\times10^{-2}$	0.520	1.60	2.14	3.74	4.87
$EE^{max}_{23}\big\|_{t=t_{ON}}$	$\times10^{-2}$	-0.091	-0.113	-0.126	-0.142	-0.167
$EE^{max}_{23}\big\|_{t=t_{OFF}}$	$\times10^{-2}$	0.091	0.105	0.112	0.134	0.157

continued on next page

continued from previous page

Solution variable	Sample	A-1	A-2	A-3	A-4	A-5
$E_{22}^{max}\big\vert_{t=t_{ON}}$	$\times 10^{-2}$	0.0207	0.077	0.131	0.238	0.378
$E_{22}^{max}\big\vert_{t=t_{OFF}}$	$\times 10^{-2}$	0.059	0.150	0.197	0.371	0.509
$E_{33}^{max}\big\vert_{t=t_{ON}}$	$\times 10^{-2}$	0.0428	0.0248	0.0512	0.133	0.250
$E_{33}^{max}\big\vert_{t=t_{OFF}}$	$\times 10^{-2}$	0.0193	0.039	0.076	0.181	0.295
$\gamma^{max}\big\vert_{t=t_{ON}}$	$\times 10^{-2}$	0.429	1.23	1.88	2.99	4.57
$\gamma^{max}\big\vert_{t=t_{OFF}}$	$\times 10^{-2}$	0.611	1.70	2.25	3.87	5.03
γ_{avg}	$\times 10^{-2}$	0.520	1.47	2.07	3.43	4.80
$\tau^{max}\big\vert_{t=t_{ON}}$	N/mm^2	-44.0	-54.6	-60.3	-66.1	-76.4
$\tau^{max}\big\vert_{t=t_{OFF}}$	N/mm^2	43.7	49.1	52.0	60.5	69.1
τ_{avg}	N/mm^2	-0.2	-2.7	-4.1	-2.8	-3.6
$\gamma_{el.}^{max}\big\vert_{t=t_{ON}}$	$\times 10^{-2}$	0.091	0.113	0.126	0.142	0.167
$\gamma_{el.}^{max}\big\vert_{t=t_{OFF}}$	$\times 10^{-2}$	0.091	0.105	0.112	0.134	0.157
cyclic $\Delta\gamma$	$\times 10^{-2}$	0.182	0.47	0.37	0.88	0.46
cyclic $\Delta\gamma_{el.}$	$\times 10^{-2}$	0.182	0.218	0.238	0.276	0.324
cyclic $\Delta\gamma_{pl.}$	$\times 10^{-2}$	0	0.252	0.132	0.604	0.136

Table 5-9. The results of the transient pulsed-current loading analysis for samples A-6÷A-10 (mechanical domain).

Solution variable	Sample Unit	A-6	A-7	A-8	A-9	A-10
$S_{MISES}^{max}\big\vert_{t=t_{ON}}$	N/mm^2	149	107	99.1	109	15.8
$S_{MISES}^{max}\big\vert_{t=t_{OFF}}$	N/mm^2	113	95.8	89.5	88.4	86.3
$\Delta\sigma_{MISES}$	N/mm^2	36.0	11.2	9.6	20.6	70.5
σ_{MISES}^{m}	N/mm^2	131	101.4	94.3	98.7	51.1
$S_{TRESCA}^{max}\big\vert_{t=t_{ON}}$	N/mm^2	172	123	114	126	19.5
$S_{TRESCA}^{max}\big\vert_{t=t_{OFF}}$	N/mm^2	130	111	103	102	99.5
$\Delta\sigma_{TRESCA}$	N/mm^2	42.0	12.0	11.0	24.0	80.0
σ_{TRESCA}^{m}	N/mm^2	151	117	108.5	114	59.5
$S_{11}^{max}\big\vert_{t=t_{ON}}$	N/mm^2	89.9	65.1	38.5	15.7	-25.1
$S_{11}^{max}\big\vert_{t=t_{OFF}}$	N/mm^2	-82.6	-74.7	-71.4	-70.8	-69.6
$\Delta\sigma_{11}$	N/mm^2	172.5	139.8	109.9	86.5	44.5
σ_{11}^{m}	N/mm^2	3.65	-4.8	-16.5	-27.6	-47.4
$S_{22}^{max}\big\vert_{t=t_{ON}}$	N/mm^2	88.6	65.3	37.1	8.82	-28.4

continued on next page

continued from previous page

Solution variable	Sample	A-6	A-7	A-8	A-9	A-10
$S_{22}^{max}\big\vert_{t=t_{OFF}}$	N/mm^2	-81.9	-74.3	-71.1	-70.5	-69.3
$\Delta\sigma_{22}$	N/mm^2	170.5	139.6	108.2	79.3	40.9
σ_{22}^{m}	N/mm^2	3.35	-4.5	-17	-30.8	-48.9
$S_{33}^{max}\big\vert_{t=t_{ON}}$	N/mm^2	100	79.2	58.2	29.4	-22.1
$S_{33}^{max}\big\vert_{t=t_{OFF}}$	N/mm^2	-91.0	-83.5	-80.3	-79.7	-78.5
$\Delta\sigma_{33}$	N/mm^2	191	162.7	138.5	109.1	56.4
σ_{33}^{m}	N/mm^2	4.5	-2.15	-11.1	-25.2	-50.3
$S_{23}^{max}\big\vert_{t=t_{ON}}$	N/mm^2	-85.9	-61.1	-56.5	-61.9	-8.63
$S_{23}^{max}\big\vert_{t=t_{OFF}}$	N/mm^2	64.9	55.1	51.4	50.8	49.5
$\Delta\sigma_{23}$	N/mm^2	150.8	116.2	107.9	112.7	58.13
σ_{23}^{m}	N/mm^2	-10.5	-3.0	-2.55	-5.55	20.4
$E_{23}^{max}\big\vert_{t=t_{ON}}$	×10^{-2}	1.84	1.61	1.71	1.82	1.70
$E_{23}^{max}\big\vert_{t=t_{OFF}}$	×10^{-2}	4.54	2.88	2.18	2.06	1.82
$PE_{23}^{max}\big\vert_{t=t_{ON}}$	×10^{-2}	2.02	1.74	1.83	1.95	1.72
$PE_{23}^{max}\big\vert_{t=t_{OFF}}$	×10^{-2}	4.40	2.76	2.07	1.95	1.72
$EE_{23}^{max}\big\vert_{t=t_{ON}}$	×10^{-2}	-0.181	-0.129	-0.120	-0.132	-0.014
$EE_{23}^{max}\big\vert_{t=t_{OFF}}$	×10^{-2}	0.146	0.120	0.111	0.109	0.106
$E_{22}^{max}\big\vert_{t=t_{ON}}$	×10^{-2}	0.105	0.109	0.117	0.127	0.129
$E_{22}^{max}\big\vert_{t=t_{OFF}}$	×10^{-2}	0.435	0.261	0.191	0.181	0.161
$E_{33}^{max}\big\vert_{t=t_{ON}}$	×10^{-2}	0.053	0.0671	0.0452	0.0455	0.0453
$E_{33}^{max}\big\vert_{t=t_{OFF}}$	×10^{-2}	0.226	0.098	0.071	0.068	0.055
$\gamma^{max}\big\vert_{t=t_{ON}}$	×10^{-2}	1.84	1.61	1.71	1.82	1.70
$\gamma^{max}\big\vert_{t=t_{OFF}}$	×10^{-2}	4.54	2.88	2.18	2.06	1.82
γ_{avg}	×10^{-2}	3.19	2.25	1.95	1.94	1.76
$\tau^{max}\big\vert_{t=t_{ON}}$	N/mm^2	-86.1	-61.5	-57.5	-62.7	-9.2
$\tau^{max}\big\vert_{t=t_{OFF}}$	N/mm^2	65.1	55.3	51.6	51.0	49.7
τ_{avg}	N/mm^2	-10.5	-3.1	-2.9	-5.9	20.3
$\gamma_{el.}^{max}\big\vert_{t=t_{ON}}$	×10^{-2}	0.181	0.129	0.120	0.132	0.014
$\gamma_{el.}^{max}\big\vert_{t=t_{OFF}}$	×10^{-2}	0.146	0.120	0.111	0.108	0.106
cyclic $\Delta\gamma$	×10^{-2}	2.701	1.271	0.470	0.240	0.120
cyclic $\Delta\gamma_{el.}$	×10^{-2}	0.327	0.249	0.231	0.240	0.120
cyclic $\Delta\gamma_{pl.}$	×10^{-2}	2.374	1.022	0.239	0	0

From the results for samples A-1÷A-10 (Tables 5-8 & 5-9) the following conclusions can be drawn:

- For temperature amplitudes smaller than ~20°C no cyclic plasticity was observed (Sample A-1, A-9 & A-10).
- For very small temperature amplitudes (≲10°C) the direct stresses S_{11}, S_{22} and S_{33} were found to be compressive during the cycle (Sample A-10).

5.10. Theoretical Fatigue Life Predictions Under Cyclic-Current Loading Conditions

The lifetimes for Samples S-1÷S-8 were initially predicted using the cyclic strain-life methodology and fatigue properties of copper found in literature. The results of this prediction were compared with the experimental predictions. Using both the computed and the experimental predictions the value of the fatigue strength of copper was slightly increased to produce a better fit of the computed lifetimes with the experimental findings. The new set of fatigue constants was subsequently used to predict the lifetimes for Samples A-1÷A-10.

5.10.1. Lifetime Predictions for the Symmetric Loading Duties

The magnitude of the alternating strain can be related to the number of cycles to failure by the strain-life (∈-N) relation [38]:

$$\frac{\Delta\varepsilon}{2} = \frac{\sigma_f'}{E}(2N_f)^b + \varepsilon_f'(2N_f)^c \qquad \text{[Eq.5-9]}$$

where σ_f', ε_f', b and c are fatigue constants for direct strain-cycling fatigue.

Since in the problem studied shear strains have the most significant effect on fatigue life, equation 5-9 was rewritten to represent shear-strain cycling fatigue:

$$\frac{\Delta\gamma}{2} = \alpha(2N_f)^B + \beta(2N_f)^C \qquad \text{[Eq.5-10]}$$

where $\Delta\gamma/2$ is the cyclic shear strain amplitude, and α, β, B and C are material constants, determined from shear strain-cycling fatigue.

For accurate life predictions precise values of the α, β, B and C fatigue constants must be known. These constants were previously obtained experimentally for various conditions of copper (e.g. cold-worked or annealed). However, little empirical data is available for high-temperature fatigue of copper.

Given the high operating temperature of the notched parts of the fuse element material (usually >200°C), and that annealing in copper occurs around 100°C [90], the conductive film material was assumed to be annealed. Benham [76] obtained fatigue constants for annealed copper from torsional (shear) strain-cycling fatigue. Given the selection of fatigue constants for copper found in the literature [74-76, 80], the constants derived by Benham are most apt for the case investigated in this thesis and are given in Table 5-10:

Table 5-10. Fatigue constants for copper obtained from torsional (shear) strain-cycling fatigue at room temperature [76].

Fatigue constant	α	β	B	C
Value	0.0065	0.719	-0.1353	-0.492

These constants, however, were obtained at room temperature and they may be different at the elevated temperature (although probably not significantly so). Additional complexity is introduced by the fact that: i) the number of cycles to failure is known to be smaller for a thermally cycled specimen than for one mechanically cycled at the elevated temperature [43] and ii) a mean strain can, under certain conditions, reduce the subsequent life by exhausting some of the ductility available in pristine material [42]. On the other hand, at the elevated temperature the material softens and is known to be better able to withstand the plastic strain without failure [43]. These effects tend to cancel each other out. However, since the above considerations have a qualitative rather than quantitative character, their precise combined effect on life is unknown. It follows that fuse lifetimes, as predicted by equation 5-10 using fatigue constants from Table 5-10, are approximate.

From equation 5-10 the lifetimes for samples S-1÷S-8 were obtained:

Table 5-11. Lifetime predictions for samples S-1 ÷S-8.

Sample	Life $2N_f$
S-1	3,758
S-2	6,550
S-3	10,925
S-4	23,525
S-5	37,465
S-6	66,100
S-7	93,500
S-8	1,110,500

The results of the investigation are shown, graphically, in Figure 5-35. Experimental results (from Paragraph 5.11, p.121) are also shown in Figure 5-35 for comparison.

From Figure 5-35 it is observed that the computed lifetimes for samples S-1÷S-8 are in a good agreement with the empirical results. The estimated lifetimes for most samples are within a ratio of two smaller than the experimentally measured lifetimes. The shear strains for the experimental lifetimes (measured on the best-fit line) are approximately 30% larger than the corresponding computed shear strains.

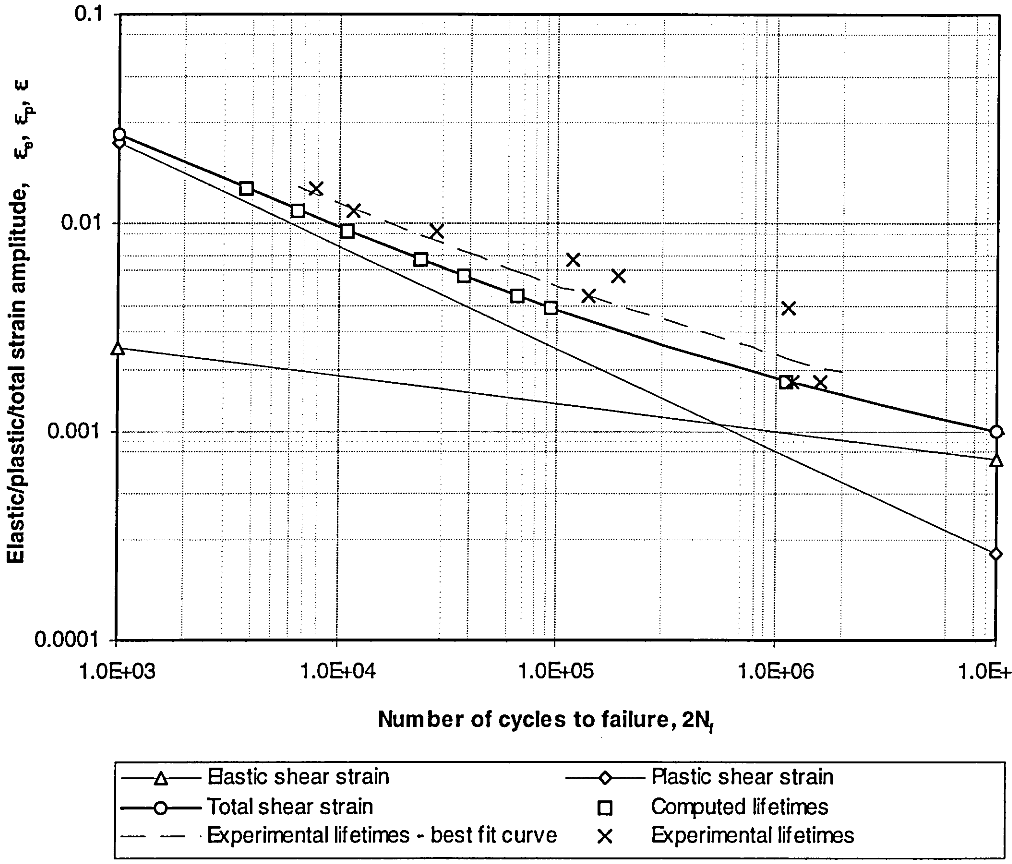

Figure 5-35. Comparison of computed and experimental lifetimes for fuse samples S-1÷S-8 & E-1÷E-8.

To refine the accuracy of the predictions the fatigue constants ought, ideally, to be obtained from an experiment reflecting the character of the fatigue presented in this thesis. An initial investigation, leading to the determination of high-temperature fatigue constants for electro-thermally shear strain-cycled copper, is presented below.

Using data from Table 5-10 the transition fatigue life was calculated:

$$2N_t = \left(\frac{\beta}{\alpha}\right)^{\frac{1}{(B-C)}} = 534{,}581 \qquad \text{[Eq.5-11]}$$

From Figure 5-34 it is observed that the transition life exists for Δt=0.68s, that is for $\gamma=0.335\times10^{-2}$ hence, from the experimental best-fit curve (Figure 5-35), $2N_t \cong 2.8\times10^5$. It is, therefore, concluded that the fatigue constants (Table 5-10) obtained from torsional strain-cycling fatigue at room temperature can only be used in the case of the substrate fuse investigated to give approximate predictions.

It is postulated that, due to metal softening, the fatigue strength of copper α at the elevated temperature is larger than at the ambient temperature and that the β, B and C constants are not significantly affected by the elevated temperature. The value of α was, consequently, evaluated using the β, B and C constants and the computed $2N_t$:

$$\alpha = \beta(2N_t)^{C-B} = 0.719 \cdot 280{,}000^{-0.492-(-0.1353)} = 0.0082$$

The new fatigue constants are given in Table 5-12.

Table 5-12. Fatigue constants for electro-thermal shear strain-cycling fatigue at $T_{c\text{-avg.}}$=240°C.

Fatigue constant	α	β	B	C
Value	0.0082	0.719	-0.1353	-0.492

Using the new fatigue constants the ϵ-N diagram was reproduced, Figure 5-36. From this Figure it is evident that the new ϵ-N curve is now very close to the experimental best-fit curve, with the difference between the predicted and experimental life being smaller than a ratio of two. This ratio can be considered to constitute a design safety margin.

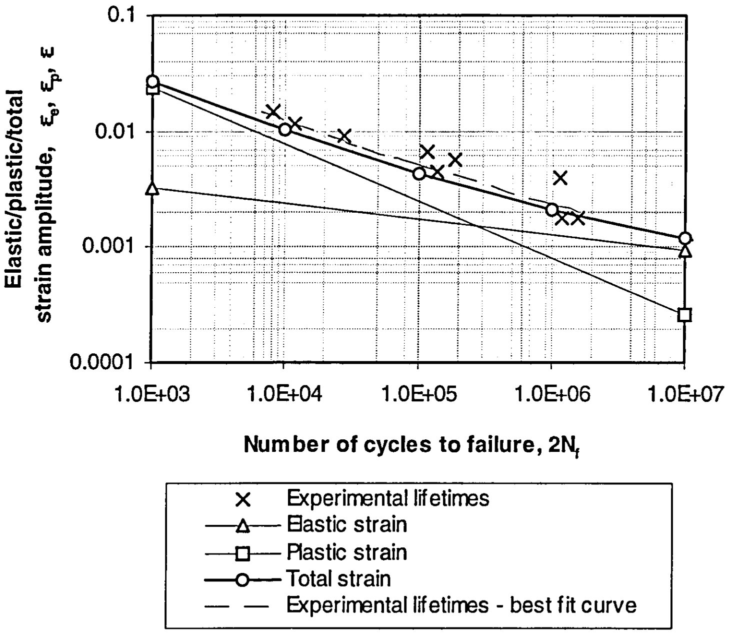

Figure 5-36. Diagram for the evaluation of high temperature fatigue constants of annealed copper.

Combining the new fatigue constants with equation 5-10 gives:

$$\frac{\Delta\gamma}{2} = 0.0082 \cdot (2N_f)^{-0.1353} + 0.719 \cdot (2N_f)^{-0.492} \qquad \text{[Eq.5-12]}$$

From equation 5-12 the life of the manufactured substrate fuse can be calculated for any type of cyclic-current loading, provided that the amplitude of the cyclic shear strain is known.

5.10.2. Lifetime Predictions for the Asymmetric Loading Duties

Equation 5-12 was used to predict the lifetimes of the manufactured substrate fuse when subjected to asymmetric cyclic-loading duties. Using the data obtained from computer simulation for samples A-1÷A-10 (Tables 5-8 & 5-9), the lifetimes for the asymmetric current-loading duties were estimated. The results of this study are presented in Table 5-13.

Table 5-13. Lifetime predictions for the asymmetric loading duties – samples A-1÷A-10.

Sample	Life	Sample	Life
A-1	37,400,000	A-6	4,975
A-2	634,000	A-7	32,360
A-3	1,516,000	A-8	634,000
A-4	88,700	A-9	9,420,000
A-5	683,500	A-10	418,500,000

From the results for samples A-1÷A-10 (Tables 5-5, 5-6, 5-8, 5-9 & 5-13) the following conclusions can be drawn:

- For constant ON current and varying ϕ (Samples A-1÷A5) the lifetime was shortest for $\phi=0.7$. It is also clear that life is primarily influenced by the temperature amplitude, hence by the cyclic shear strain amplitude, the average values of these variables having much smaller effect on life (compare, for example, the results for Samples A-2 & A-3);
- For constant RMS current the life increases as ϕ increases. This is because for constant RMS current the following relationships are valid: $\phi \to 0 \Rightarrow \Delta T \to \infty \Rightarrow 2N_f \to 0$ and $\phi \to 1 \Rightarrow \Delta T \to 0 \Rightarrow 2N_f \to \infty$.
- The lifetimes for samples which did not experience cyclic plastic strains (Samples A-1, A-9 & A-10) are much greater ($>10^6$) than the lifetimes for samples which experienced significant cyclic plastic strains (e.g. Sample A-6).

5.10.3. Conclusions

The results of the lifetime prediction analysis indicate that good agreement was found between theoretical and experimental predictions. However, in order to refine the accuracy of the predictions further work is necessary to produce accurate empirical elevated-temperature fatigue data for common fuse element materials (copper, silver).

It is postulated that equation 5-12 can be used for life prediction of other types of thin-film substrate fuses, utilising copper for the fuse element and alumina for the substrate.

5.11. Experimental Lifetime Prediction Under Pulsed Current Loading Conditions

This section presents and analyses the results of lifetime experiments conducted on the manufactured substrate fuse samples when subjected to accelerated-ageing tests. These tests were carried out to identify the fatigue deterioration effects and to verify the theoretical findings, as predicted by computer simulation (Paragraph 5.10), against experimental results. Test conditions for the experiments (Samples E-1÷E-8) were identical to the test conditions used for computer simulation (Samples S-1÷S-8), hence permitting correlation of the predictions.

Rectangular current pulses were used with the t_{ON}/t_{OFF} mark/space ratio constant at $\phi=50\%$ for all fuses tested. The RMS current, $I_{rms} = 28.3$A, was also unchanged for all fuses tested, so that the predicted life-time was only affected by the current-pulse period, and so is independent of the average and the RMS values of the current. Consequently, the effect of the mean strain on the lifetime was identical for all samples.

5.11.1. The Test-Rig Setup

The schematic diagram of the experimental test rig for the fuse lifetime prediction under pulsed-current loading is shown in Figure 5-37.

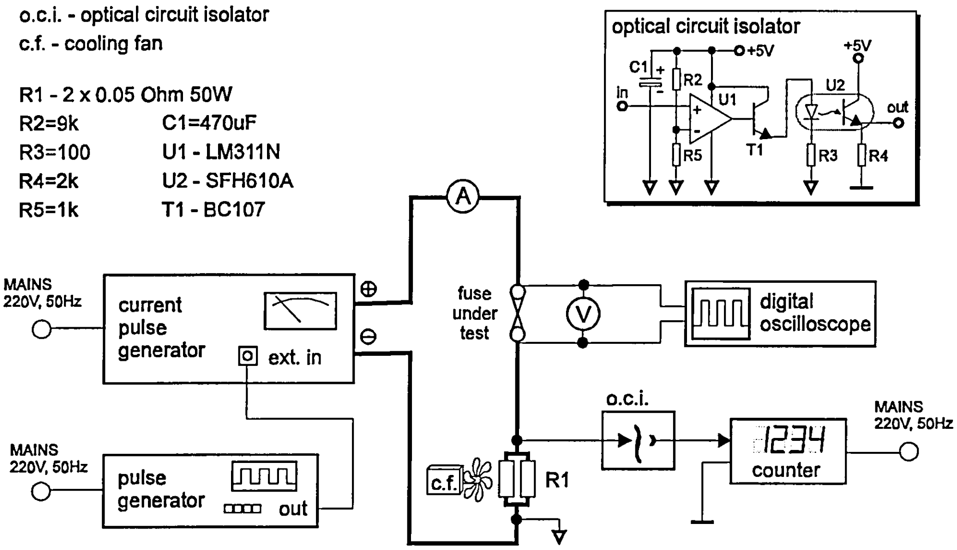

Figure 5-37. Schematic diagram of the test-rig set-up for experimental fuse lifetime prediction.

The test rig basically consisted of a current pulse generator, an additional function (pulse) generator, an optical circuit isolator and a counter. After fuse operation the total number of cycles to failure was recorded by the counter. The current pulse generator was able to generate a maximum ON current of up to 40A, over a frequency range 0.0(5) Hz to 10 Hz.

A photograph of the experimental test-rig, Figure 5-38, is that of a standard test-rig in accordance with the conditions for LV fuse testing as set out in IEC/BSI standards [81].

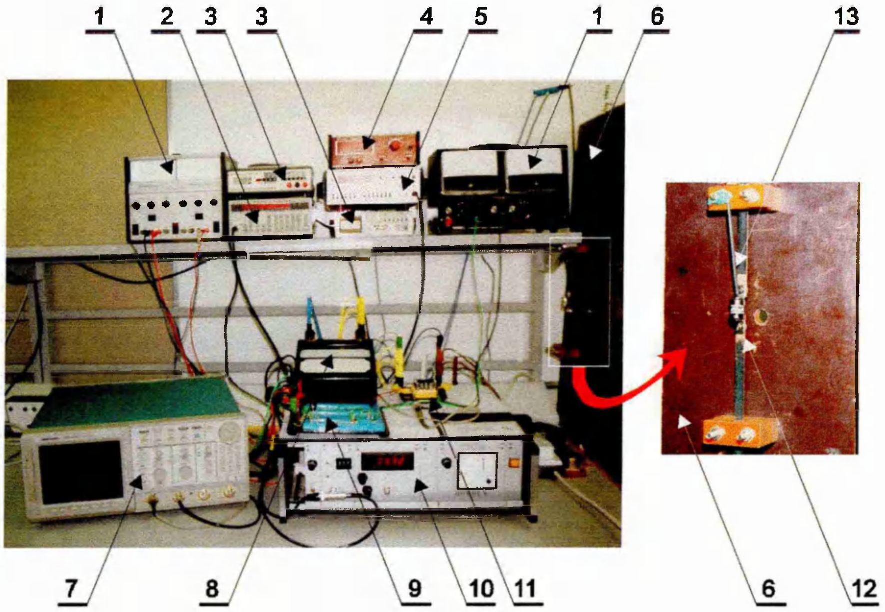

Figure 5-38. The experimental set-up for the pulsed-load life-time prediction. 1-power supply, 2-function generator, 3-multimeter, 4-digital thermometer, 5-counter, 6-standard test-rig, 7-oscilloscope, 8-ammeter, 9-optical circuit isolator, 10-current-pulse generator, 11-shunt, 12-fuse under test, 13-thermocouple

5.11.2. The Aims of the Experiment

The pulsed-current loading experiments were carried out mainly to:

- demonstrate that thin-film substrate fuses have a finite life-span when subjected to cyclic-current loading;
- establish the types of fatigue failure occurring in this class of fuse;
- determine the effect of the pulsed-current period on the fuse life-time;
- produce empirical fatigue data which could be used to verify the theoretical findings.

5.11.3. Pulsed-Current Loading Duties

For all tests the ON current was fixed at I_{ON}=40A and the I_{ON}/I_{OFF} mark/space ratio was fixed at ϕ=0.5 (50%). The equivalent RMS current was I_{RMS}=28.3A, 6.7A, below the minimum fusing current (I_{mfc}=35A). The pulsed-current period was varied from Δt=0.484s to Δt=18s (hence f_{min}=0.05Hz and f_{max}=2.07Hz).

5.11.4. Lower and Upper Limits of the Pulsed-Current Period

The pulsed-current period has limits at both lower and upper ends, Δt_{min} and Δt_{max}. The maximum period Δt_{max} is limited by the thermal time constant of the fuse. Increasing the period above a value (i.e. above Δt_{max}) for which the temperature within the fuse would fluctuate from a steady-state maximum to a steady-state minimum (ambient), would not produce any further increase in the amplitude of the temperature and, hence, would not increase the amplitude of the stresses and strains. Consequently, the life would, theoretically, remain constant for any time period greater than Δt_{max}. Additionally, since for $I_{on} \geq I_{mfc}$ melting may occur before time instant t_{off}, so the time period Δt_{max} is also limited by the thermal time constant of the fuse.

At the lower time end, the time period Δt_{min} is limited by the value of the minimum temperature amplitude below which the corresponding stress & strain amplitudes are smaller than the theoretical endurance limit where life is assumed to be infinite. However, the theoretical endurance limit measured for purely mechanical fatigue (e.g. $\Delta\varepsilon_{pl.}/2=4\text{-}5\times10^{-5}$ [74], $\Delta\sigma=103$ N/mm^2 [78]) may not be applicable to electro-thermal fatigue. Even for very small cyclic-current periods the life could be finite due to other effects, e.g. resistance increase due to oxidation, creep etc.

From the results of the computer simulation it is clear that $\Delta t^{\text{Sample E-1}} < \Delta t_{max}$ (Figure 5-25), and $\Delta t^{\text{Sample E-9}} > \Delta t_{min}$ (Table 5-7).

5.11.5. Experimental Lifetime Prediction

Nine fuse samples were tested in this study, the results for which are given in Table 5-14.

Table 5-14. Experimental lifetime prediction under pulsed-current loading.

Sample	Δt	$2N_f$	$T^{avg.}_{end-cap}$ (after 1hr)	time to operation
	s	(rounded)	°C	hrs
E-1	18	7,950	72.9	39.8
E-2	10	11.600	72.4	32.2
E-3	6	27,910	73.5	46.5
E-4	3	118,400	73.4	98.7
E-5	2	191,300	72.5	106.3
E-6	1.46	140,500	72.5	57.0
E-7	1.06	1,141,000	71.9	336.0
E-8	0.487	1,200,000	71.7	162.3
E-9	0.484	1,600,000	71.6	215.1

The experimental lifetime curve is shown in Figure 5-39. The number of cycles to operation is seen from the Figure to decrease as the pulsed-current period increases as a result of increasing the cyclic temperature, stress & strain amplitudes.

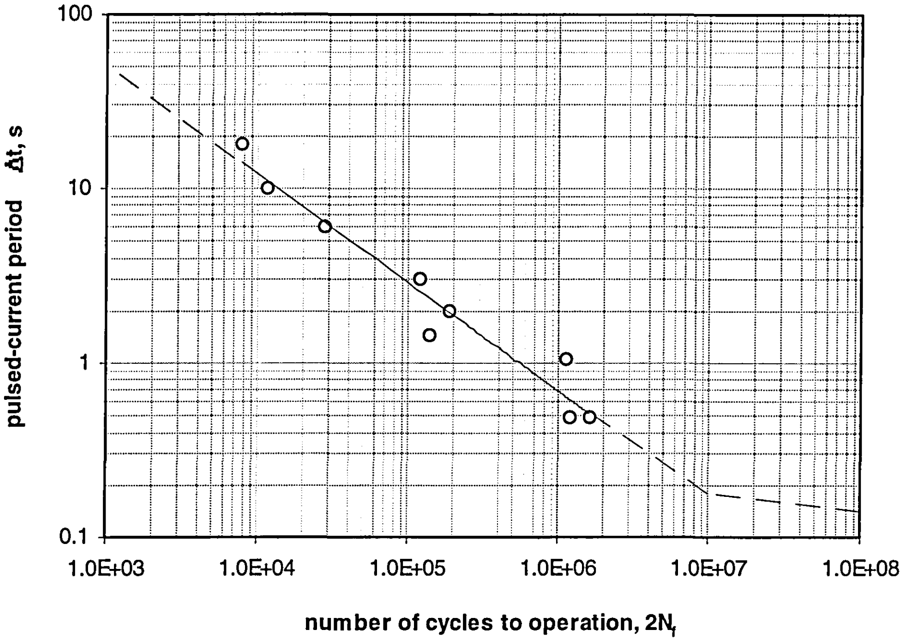

Figure 5-39. Experimental life-time prediction for the manufactured substrate fuse; the solid line is the best fit power curve (Δt-N curve); the dashed lines were extrapolated from the Δt-N curve.

Using curve fitting the experimental number of cycles to operation is given by:

$$2N_f = \left(2.7\times10^{-4}\cdot\Delta t\right)^{-1.609} \quad \text{for } 0.5 < \Delta t < 18\text{s} \qquad \text{[Eq.5-13]}$$

The dashed lines in Figure 5-39 were extrapolated from the best-fit experimental lifetime curve.

The manufactured substrate fuse was presumed to have an asymptotic endurance limit. The 'knee' is proposed for $\Delta t \approx 0.18$s, since for copper it typically occurs around 10^7 cycles [74]. Due to the very time-consuming nature of fatigue testing (the total test time to produce the above lifetime curve was 1,096 hrs), and also owing to a limited number of available fuse samples, it was not possible to determine experimentally the exact location of this transition point.

From Figure 5-39 it is observed that the scatter of test data is relatively small. However, since only one sample was tested for each point, statistical analysis was performed to obtain the magnitudes of the deviation of test data from the theoretical best-fit power curve (which was obtained using the least squares method), Figure 5-40.

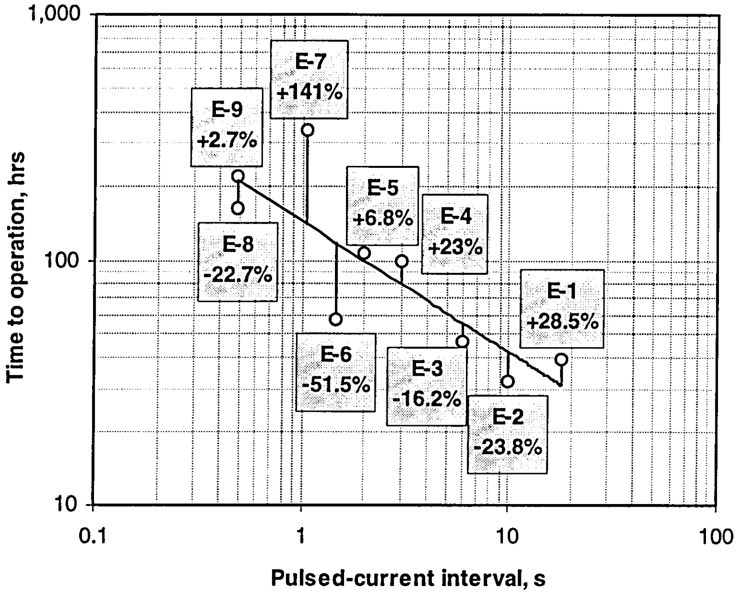

Figure 5-40. Deviation of test data from the best-fit power curve.

From Figure 5-40 it is observed that the greatest deviation exists for Sample E-7 (+141%). This finding confirms the earlier conclusions of good correlation between the computed and experimental lifetimes (Paragraph 5.10.1).

5.11.6. Results of Microscopic Observations

All the samples tested were dismantled after operation. The filler binder was dissolved using a 10% solution of caustic soda. All fuse elements experienced substantial oxidation, and had to be cleaned using a 2% solution of nital (2% solution of concentrated nitric acid), and also using an ultrasonic cleaner. Optical and scanning electron microscopy were used to locate and identify the fatigue deterioration effects. Sample numbering in this section is correlated with that presented in Table 5-14.

The following deterioration effects were observed:

- fatigue cracks of various lengths (crack initiation and propagation);
- film de-bonding and lifting off the substrate, also film warping;
- pits, craters;
- grooves;
- film deformation and dislocation.

These points are discussed below.

Crack initiation.

Thermal fatigue cracks were observed in the samples tested. Crack initiation occurred along the interfacial film/substrate edges of the notch in the region of the minimum cross-section, where the interfacial shear stress and strain are largest. Inhomogeneous film structure, an impurity in the film material, an internal defect or, most likely, surface discontinuity (e.g. grain boundaries) are most likely to be the cause of crack initiation, Figures 5-41 & 5-42. Practically all cracks initiated along the interfacial film/substrate notch edge (Figure 5-42).

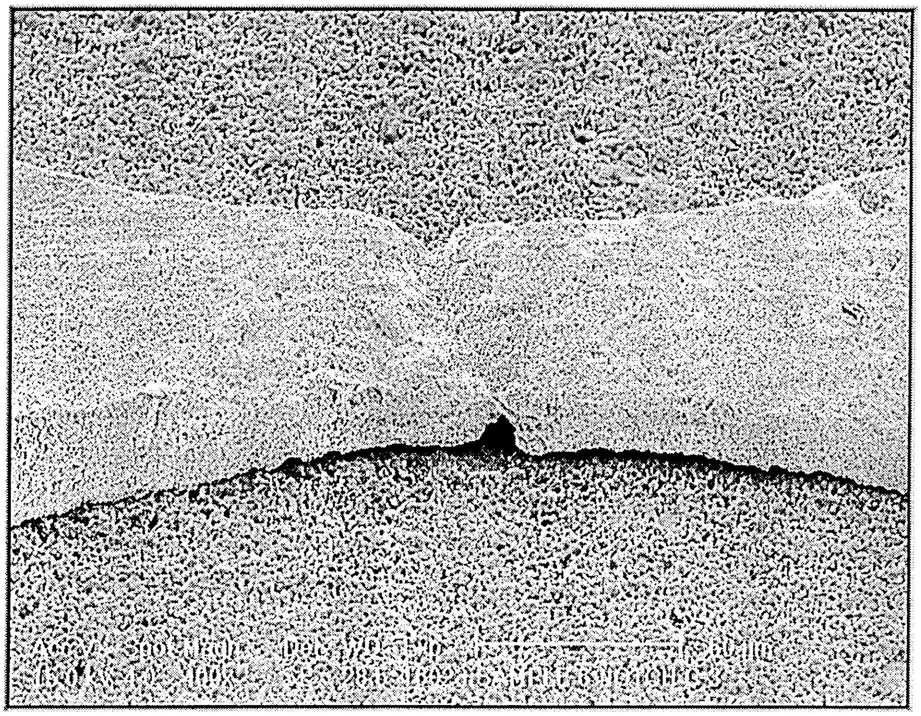

Figure 5-41. Small cracks. Sample E-2, notch C-3. Mag. 530x.

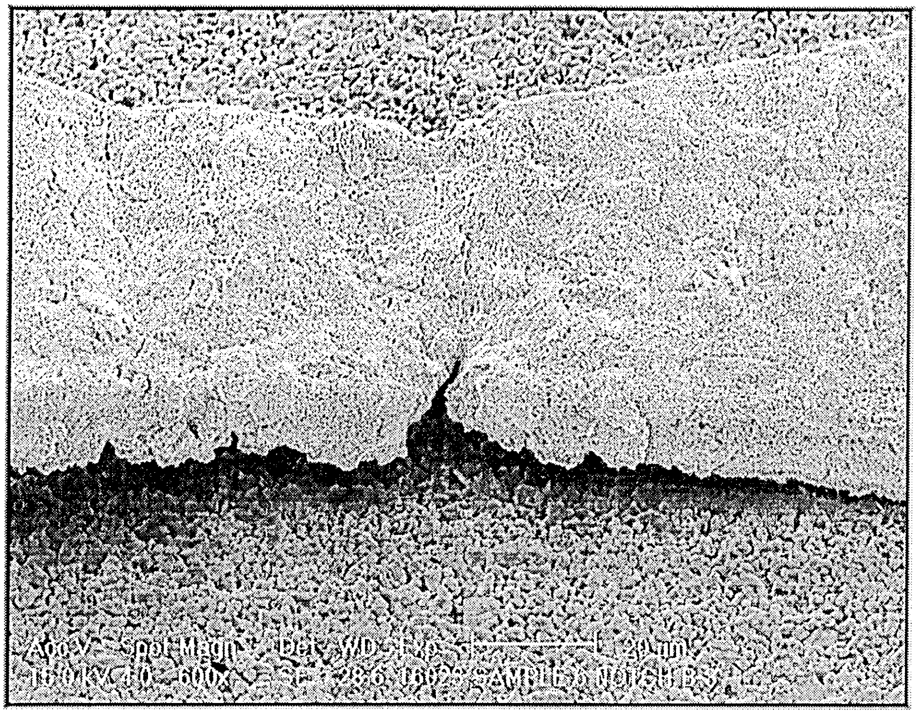

Figure 5-42. Short cracks. Sample E-2, notch B-3. Mag. 800x.

Crack propagation.

Once a crack is initiated it will propagate across the width of the notch forming a part-through crack, Figure 5-43. The rate of crack propagation ($\frac{da}{dN} = C\Delta\varepsilon_p^p a$, where C and *p* are constants), depends on the type of material, temperature and strain amplitude.

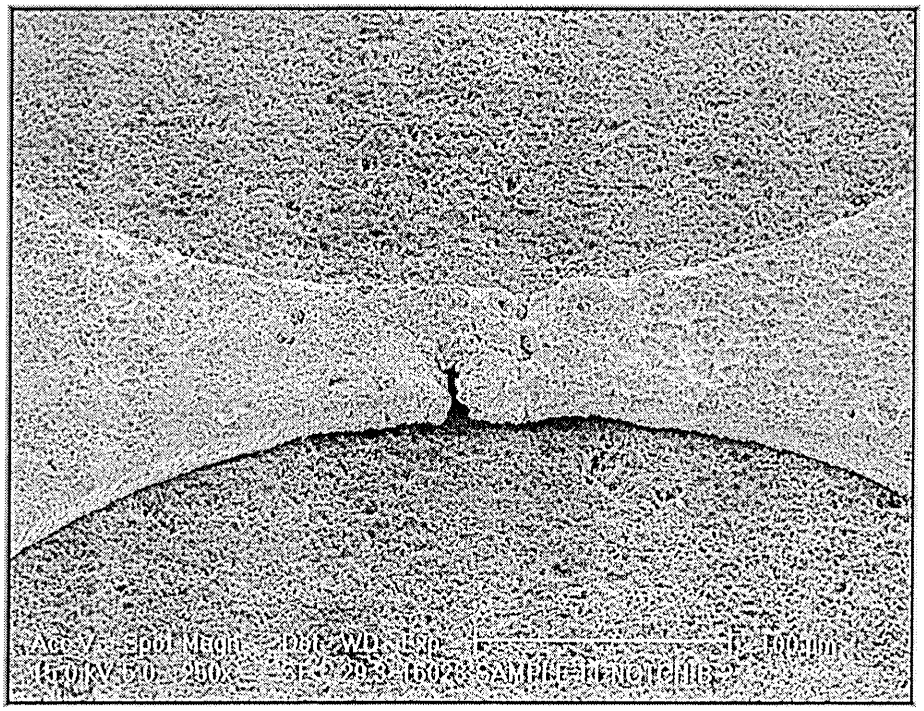

Figure 5-43. Crack propagation – part-through crack. Sample E-5, notch B-2. Mag. 330x.

If pulsed-current loading is continued, the cracks develop into long cracks which significantly alter the electrical characteristics of the fuse element (Figures 5-44 through 5-49), until an open circuit occurs (Figures 5-51). During the process of crack growth the resistance of the notch increases, consequently more current is conducted through the remaining notches in the same column, aggravating crack growth in those notches (Figures 5-43, 5-45 & 5-47, 5-50, 5-51).

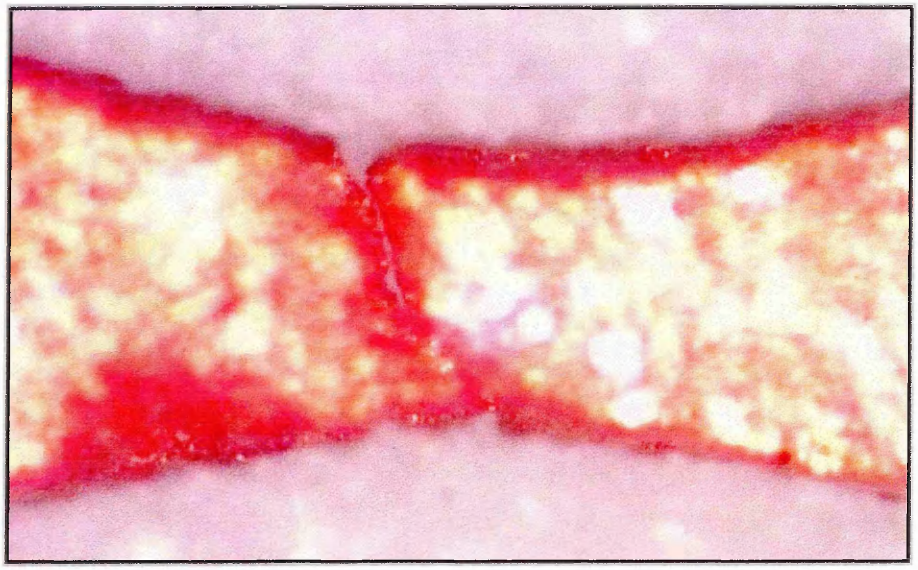

Figure 5-44. Crack propagation – long crack. Planar view, showing that the crack depth is equal to the film thickness. Sample E-6, notch D-3. Mag. 640x.

Figure 5-45. Crack propagation – long crack. Sample E-6, notch D-3. Mag. 330x.

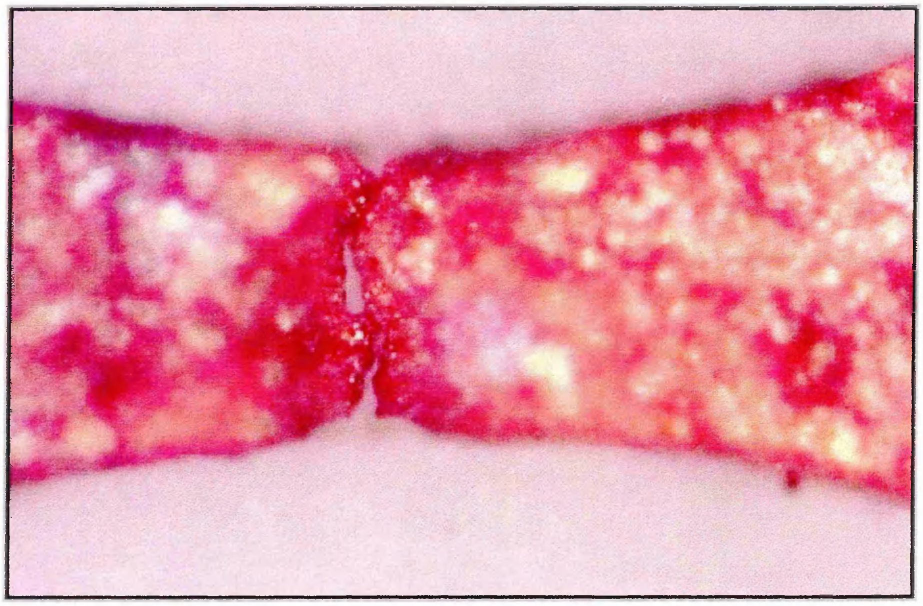

Figure 5-46. Crack propagation – long crack. Planar view. Sample E-5, notch B-5. Mag. 640x.

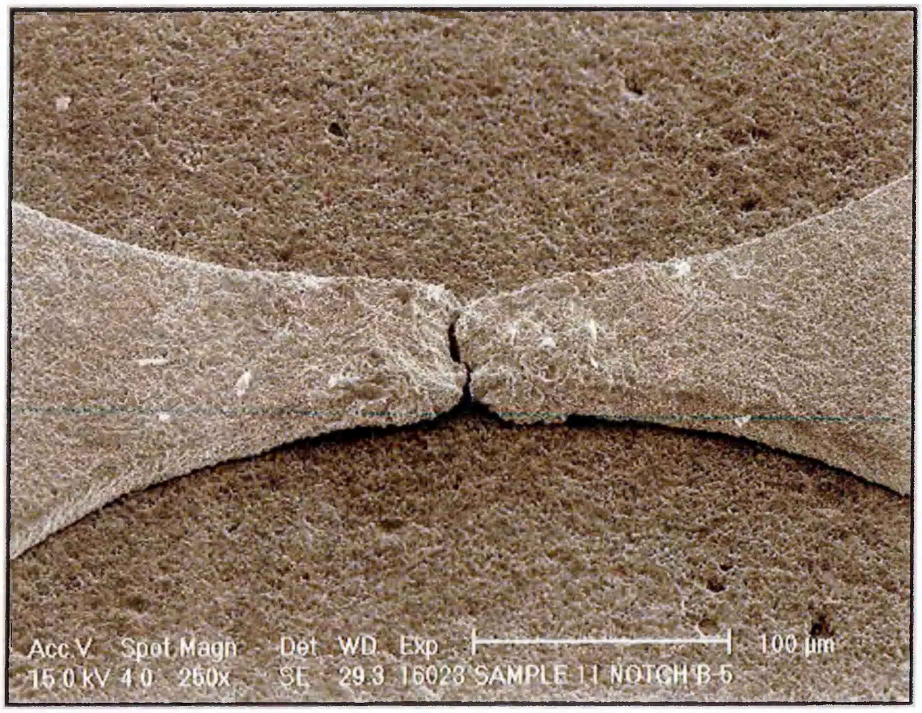

Figure 5-47. Crack propagation – long crack. Sample E-5, notch B-5. Mag. 330x.

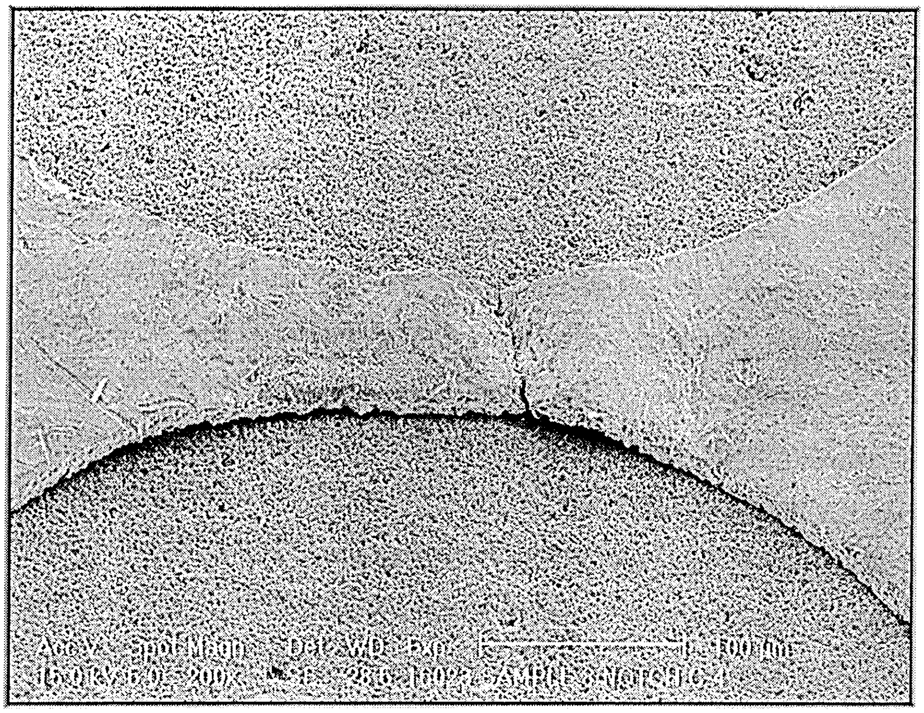

Figure 5-48. Crack propagation – long crack. Sample E-1, notch C-4. Mag. 270x.

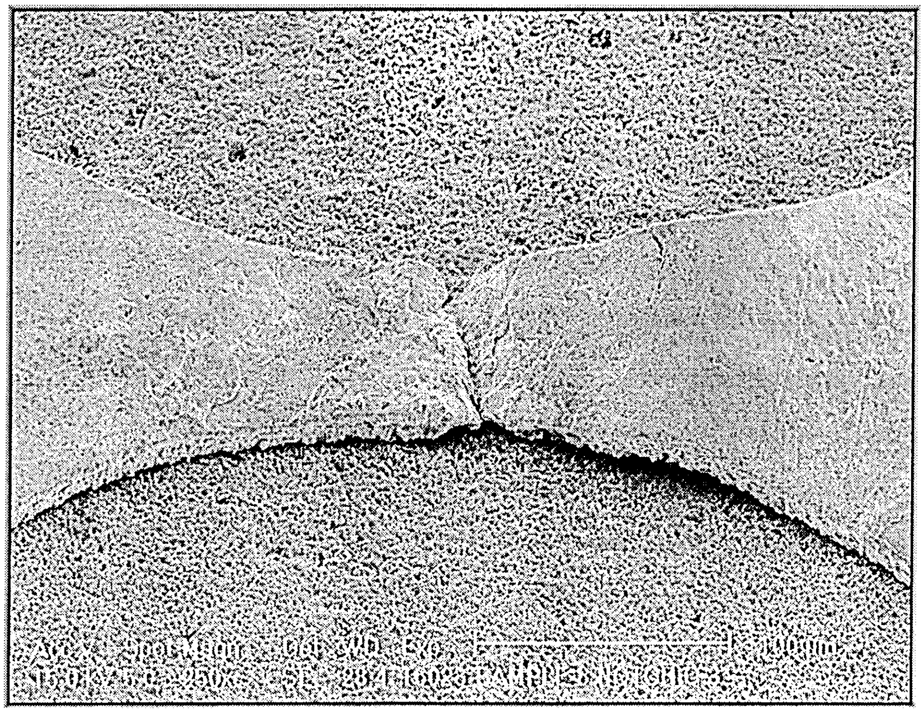

Figure 5-49. Crack propagation – long crack. Sample E-1, notch C-3. Mag. 330x.

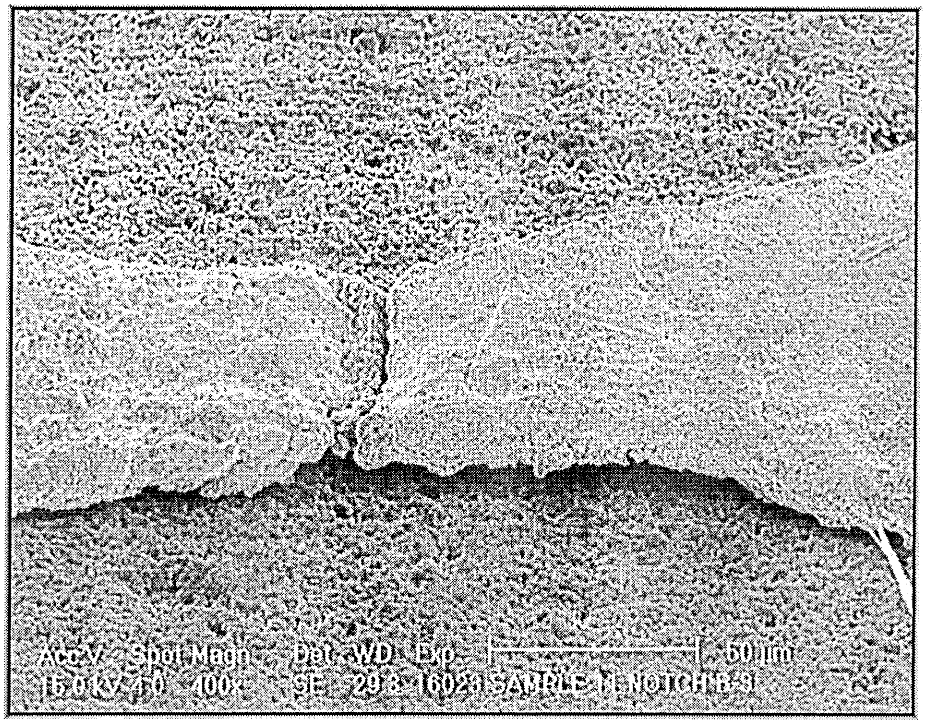

Figure 5-50. Crack propagation – long crack. Sample E-5, notch B-3. Mag. 530x.

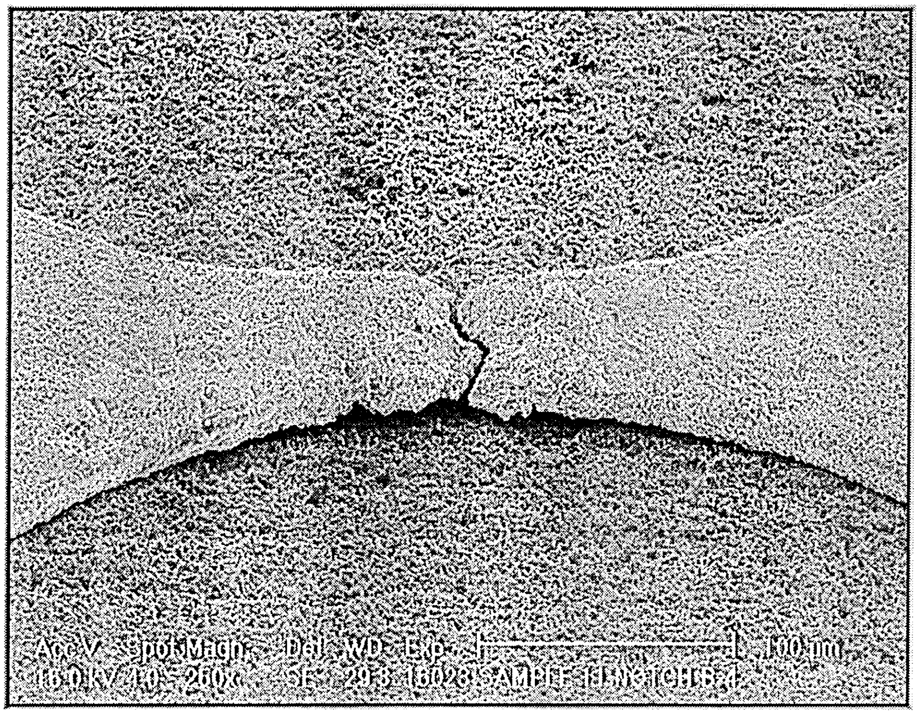

Figure 5-51. Crack propagation – long crack. Sample E-5, notch B-4. Mag. 330x.

Thermal fatigue cracks appear to be wider than the low-temperature cracks. This can be explained as follows: As the crack opens the metal comes into contact with the air (oxygen) and, due to the high temperature, the crack quickly becomes filled with oxide [44]. The oxide layer was removed during preparation of the samples, hence the cracks are wider.

Conductive film de-bonding and lifting off the substrate.

Another failure mechanism observed in the tested fuse samples was conductive film de-bonding and lifting from the substrate. Film de-bonding can be attributed to the presence of large interfacial shear stresses & strains (Paragraph 5.8, p.105), which instigate film de-adhesion (initially) along the film/substrate edge, which most likely will be at the point of maximum shear strain (the critical point). Film lifting can be attributed to the presence of large compressive stresses in the conductive film (Table 5-7), which can be released through buckling. Even though SEM observations were conducted at room temperature, in notches where film de-bonding and lifting occurred, the conductive film in the vicinity of the constrictions was found to be in a buckled state (Figures 5-52 & 5-53). This indicates that plastic deformation occurred in the metal during testing, which confirms earlier computer predictions (Paragraph 5.8, p.105).

In some notches film de-bonding and lifting was found to occur together with film cracking, Figure 5-52.

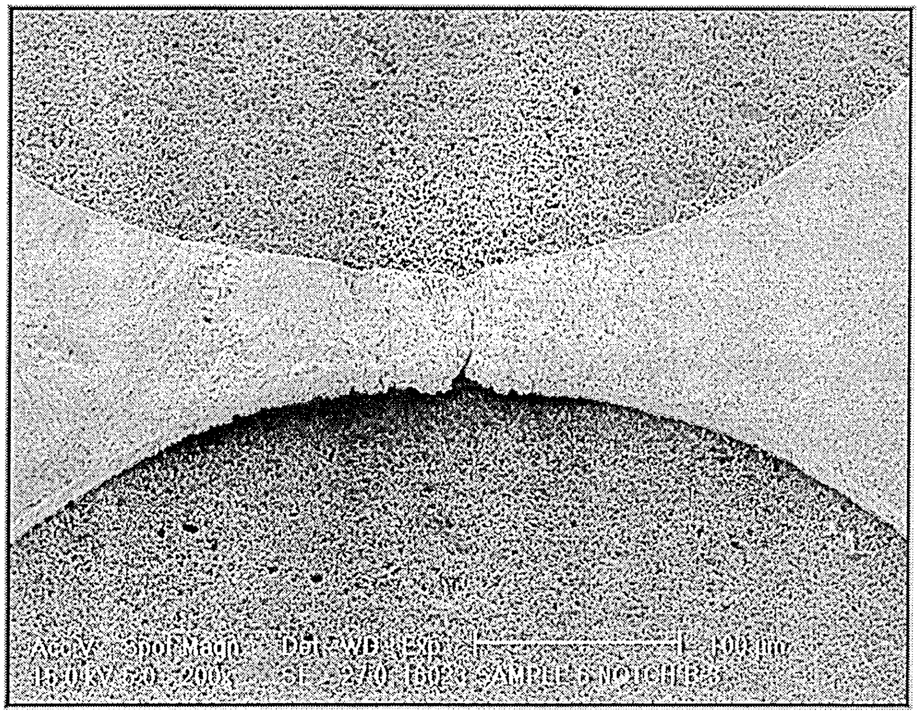

Figure 5-52. Film de-bonding. Sample E-2, notch B-3. Mag. 270x.

The enlarged view of the notched area clearly demonstrates that the film has de-bonded and lifted off the substrate, Figure 5-53 (see also Figure 5-42).

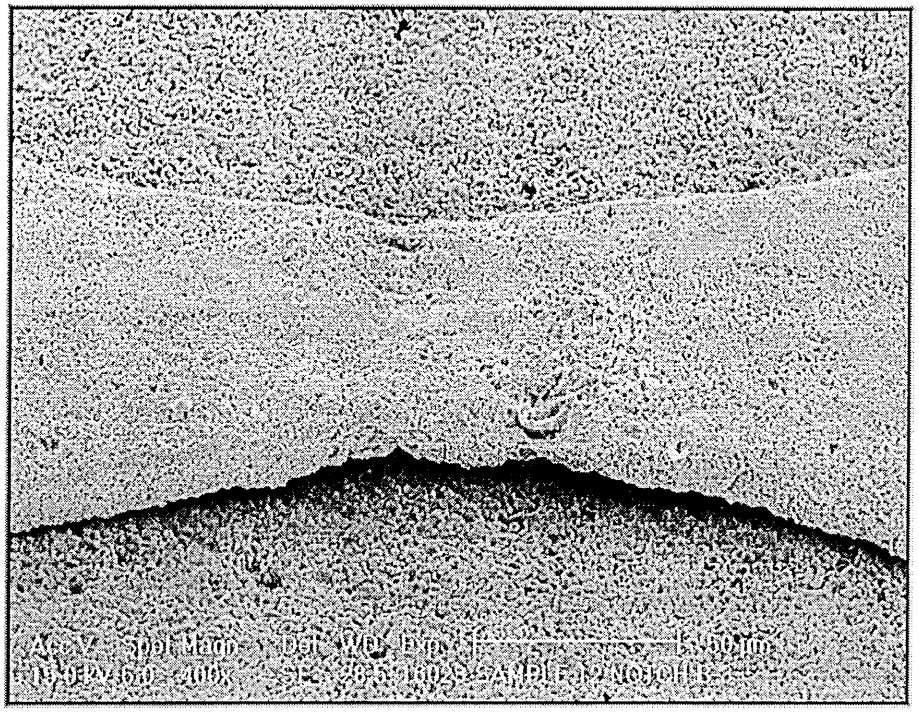

Figure 5-53. Film de-bonding and lifting off the substrate. Sample E-4, notch B-3. Mag. 530x.

In one notch the combination of several fatigue deterioration effects was particularly severe, Figure 5-54. The film de-bonded and lifted off the substrate, and in so doing caused extensive buckling and warping. Moreover, a large crack had developed across the width of the constriction.

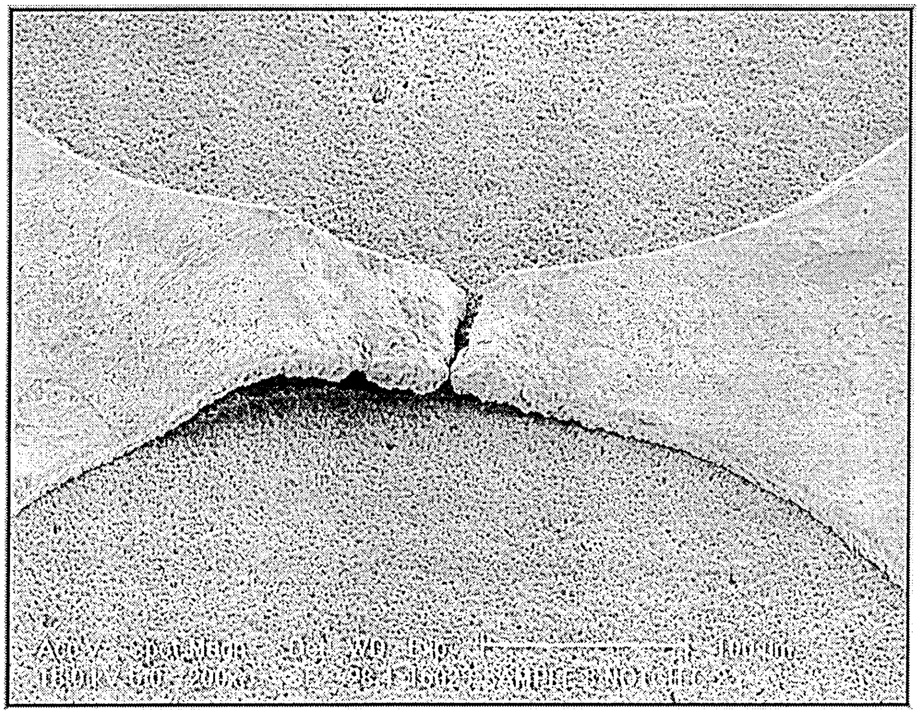

Figure 5-54. Conductive film de-bonding and buckling; film cracking. Sample E-1, notch C-2. Mag. 270x.

In one notch the conductive film was found to have de-bonded and lifted away from the centre of the notch along a groove in the film geometry, Figure 5-55.

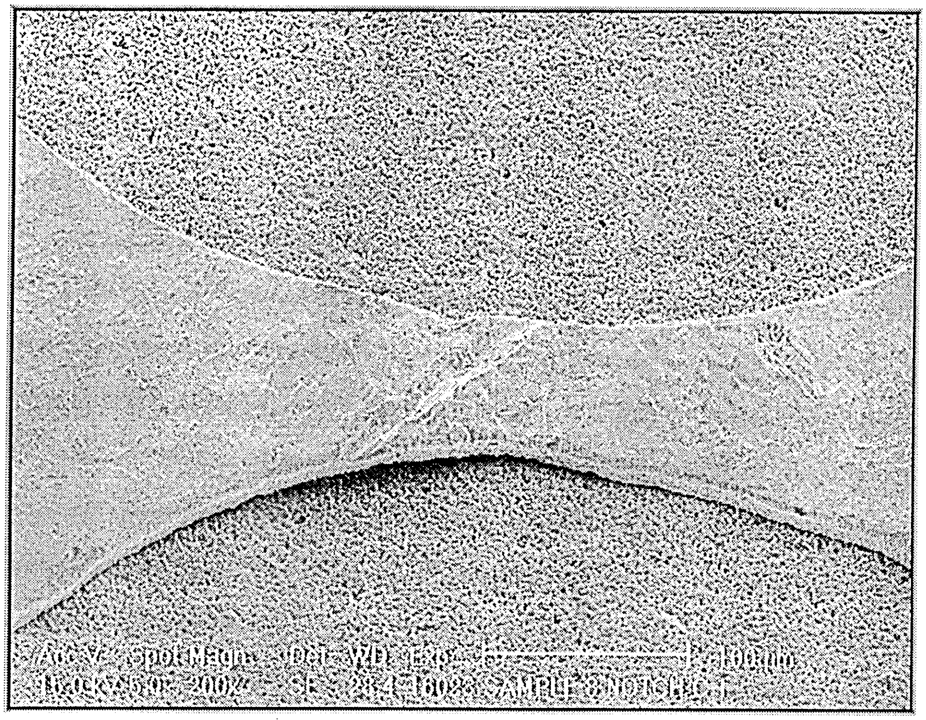

Figure 5-55. Film de-bonding and lifting along an imperfection in the film geometry (groove). Sample E-1, notch C-1. Mag. 270x.

Cavities and craters.

Another observed phenomenon was the development of cavities. These could be both relatively small (Figures 5-56 & 5-57), or large (Figure 5-58 & 5-59).

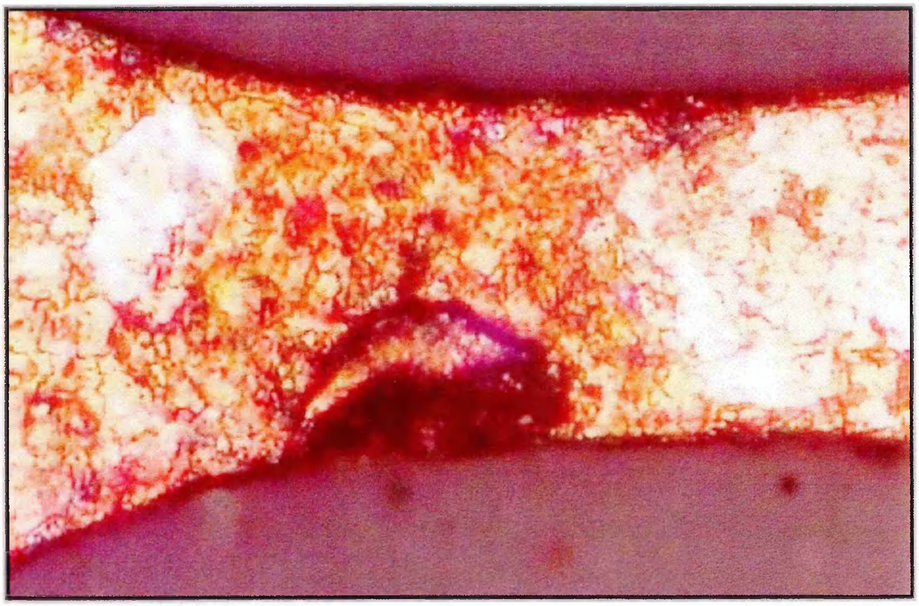

Figure 5-56. Small cavity. Planar view. Sample E-1, notch D-2. Mag. 640x.

Figure 5-57. Small cavity. Sample E-1, notch D-2. Mag. 800x.

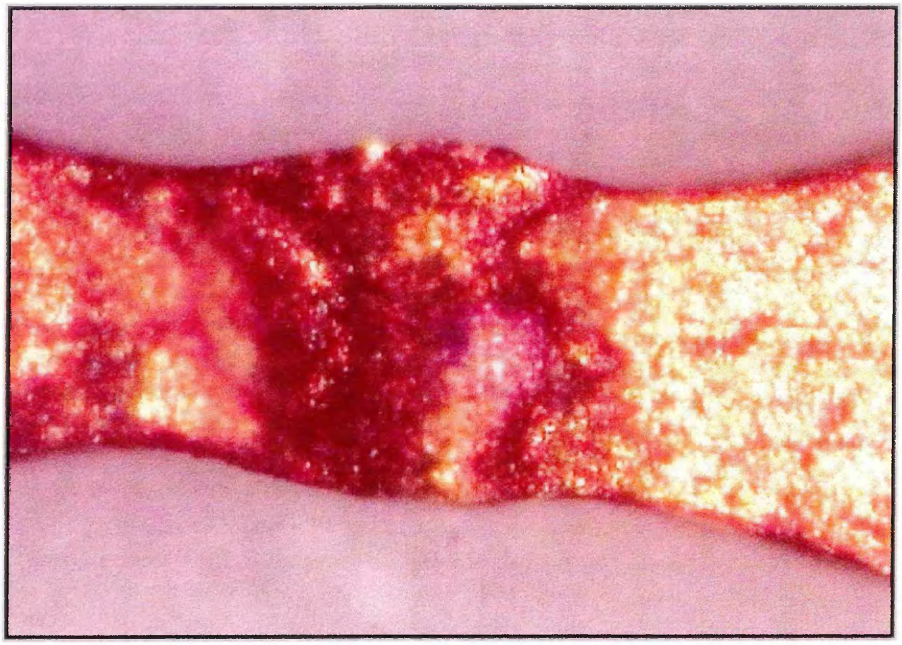

Figure 5-58. Large cavity. Planar view. Sample E-4, notch A-5. Mag. 640x.

Figure 5-59. Large cavity. Sample E-4, notch A-5. Mag. 530x.

One such cavity is thought to have extended through the thickness of the film to the substrate, forming a crater, Figures 5-60 & 5-61.

Figure 5-60. Crater. Planar view. Sample E-6, notch D-1. Mag. 330x.

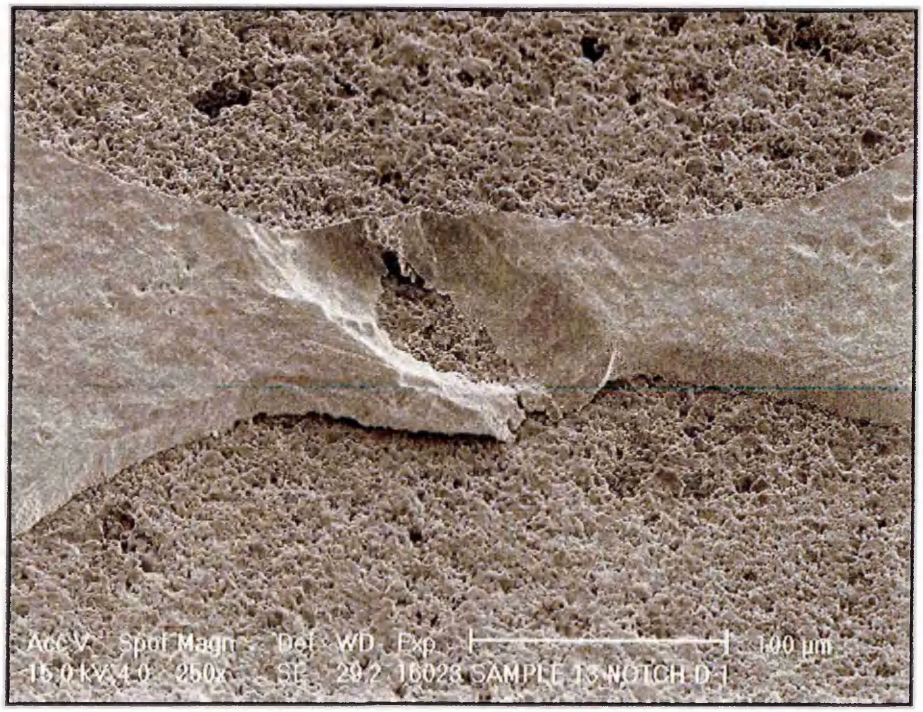

Figure 5-61. Crater. Sample E-6, notch D-1. Mag. 330x.

It is considered that the development of cavities and craters is caused by localised melting, however, the precise formation process is unknown.

Grooves.

Grooves were also found in the samples, but again the formation mechanism of grooves is unknown, Figures 5-62 through 5-64.

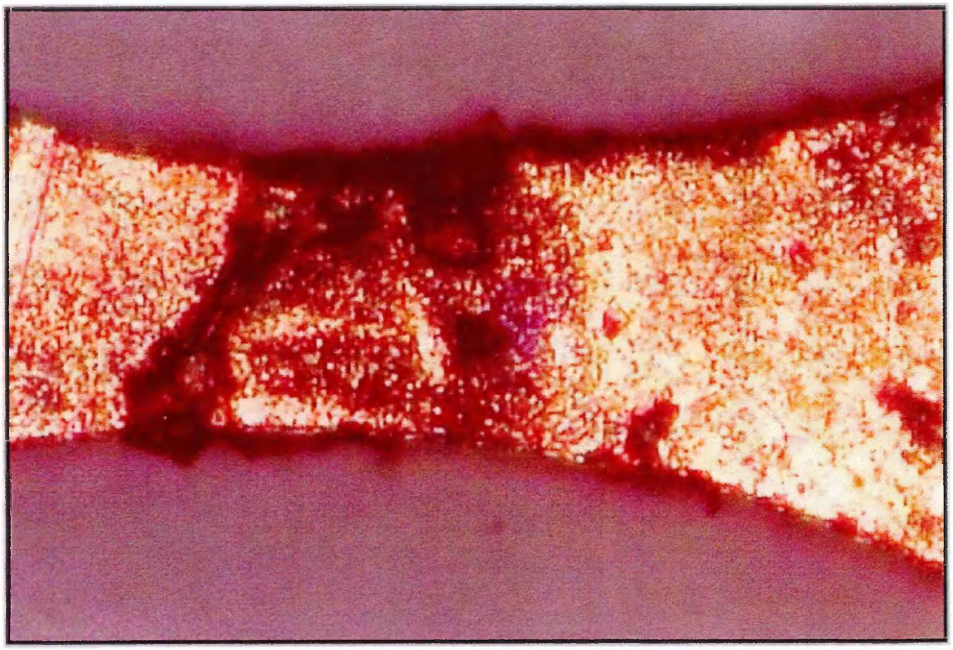

Figure 5-62. Groove. Planar view. Sample E-4, notch D-3. Mag. 640x.

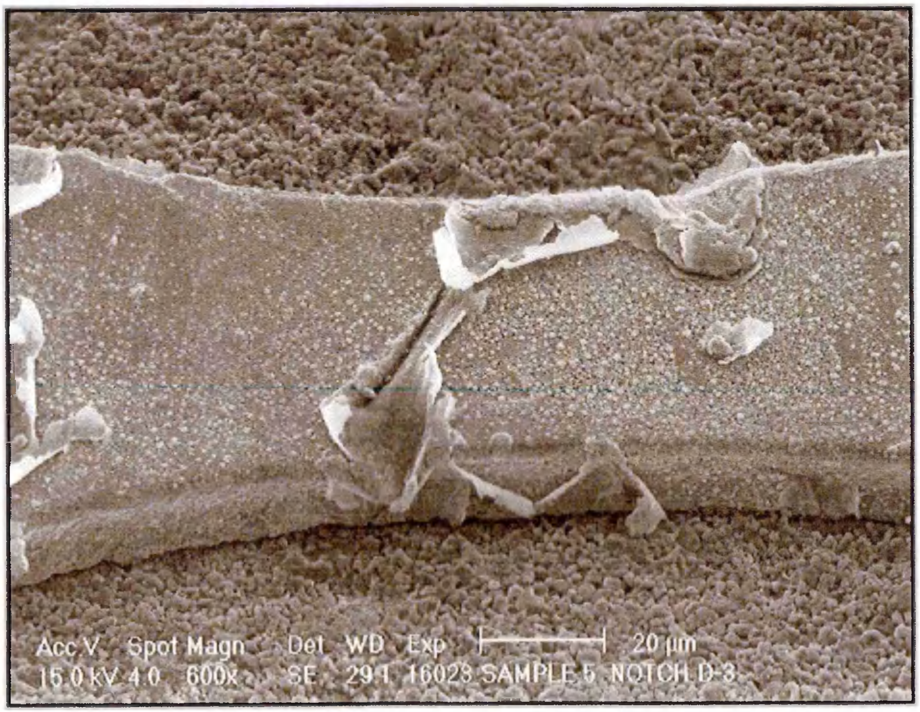

Figure 5-63. Groove. Sample E-4, notch D-3. Mag. 800x.

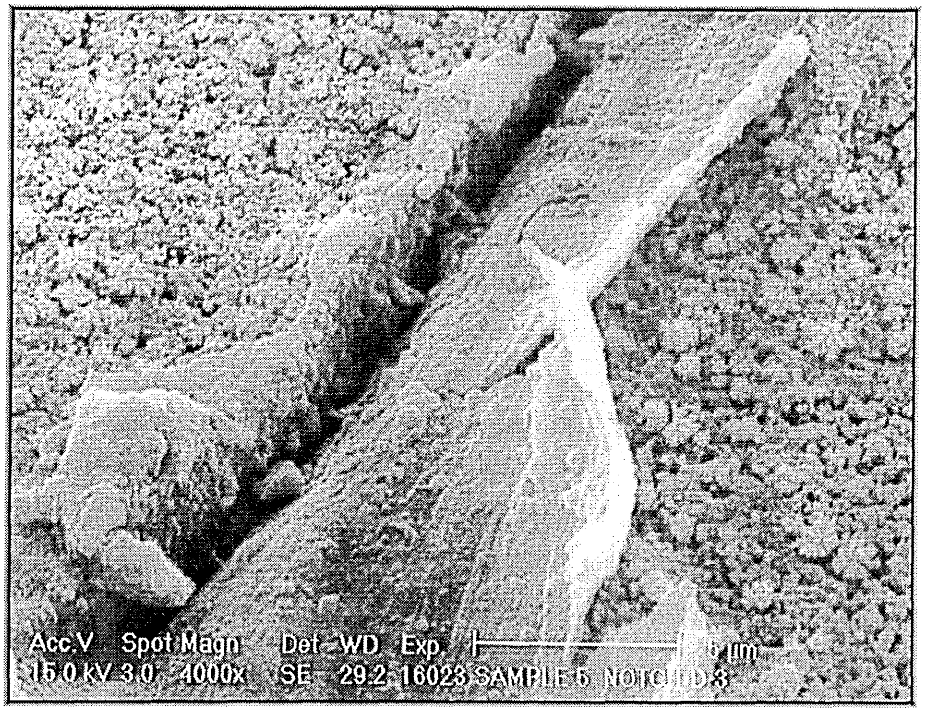

Figure 5-64. Groove. High magnification. Sample E-4, notch D-3. Mag. 5330x.

Fuse operation

Although fuse operation is not a bona fide fatigue failure process, in the fuse samples investigated the process of fuse operation was initiated by fatigue deterioration effects. When the resistance of a constriction increases above a threshold value due to the development of crack(s), film de-bonding from the substrate etc., it instigates a thermal run-away process. When the temperature of the constriction reaches the melting temperature of copper, arcing is very quickly initiated and when extinguished[9], an open-circuit forms across that particular notch. From this moment the remaining constrictions in the same column are carrying 25% more current, which aggravates the fatigue processes in these notches. Consequently, the remaining constrictions in the same column are likely to operate sequentially in a short time-span. Photographic evidence of the amount of evaporated metal in one column of notches, after fuse operation, confirms the described process, Figure 5-65.

---

[9] The reader is referred to other references [10, 11] for detailed analysis of the arcing phenomena in HRC fuses.

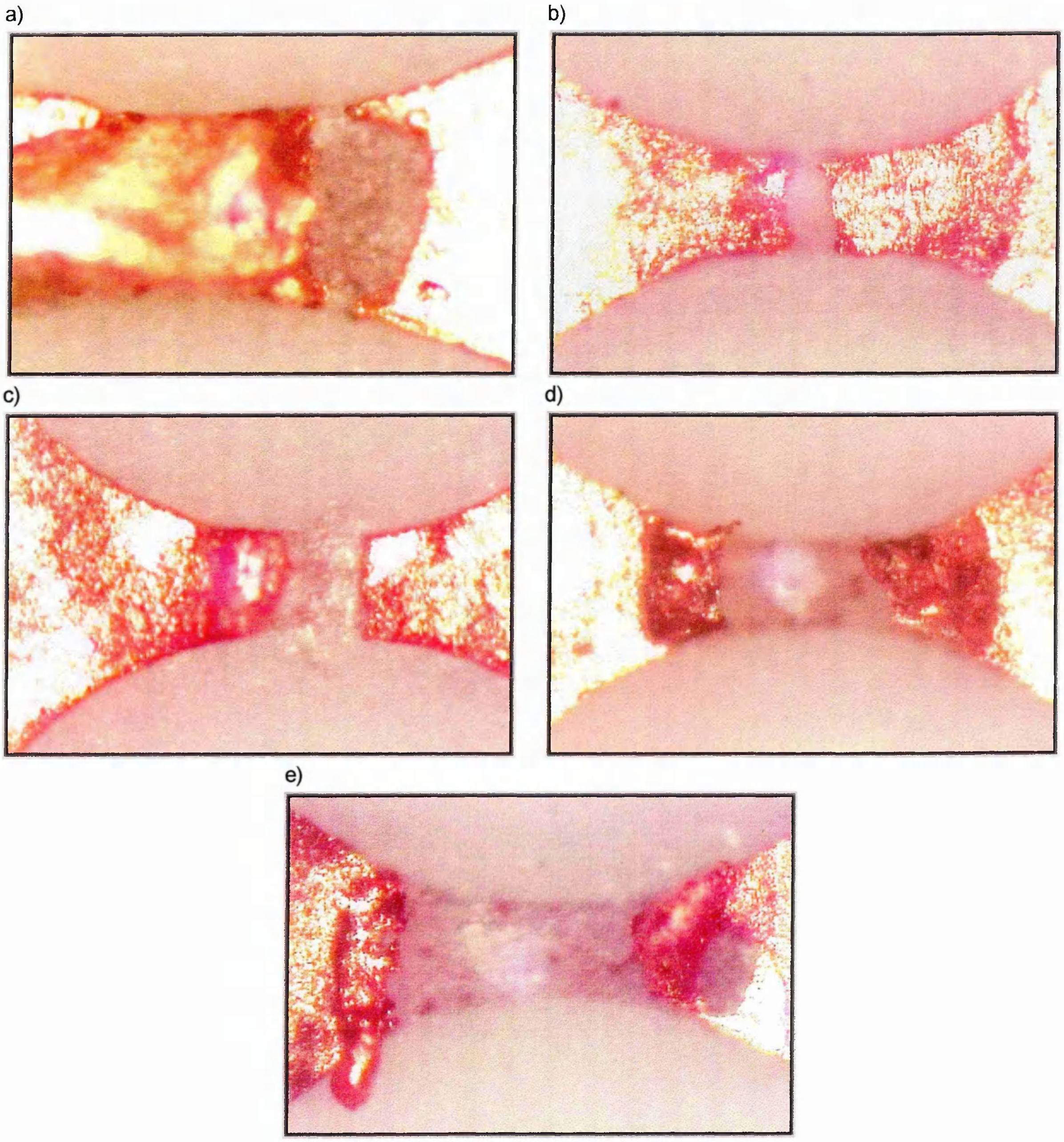

Figure 5-65. Sequence of fuse operation. Sample E-1, notch B-1 (a), B-5 (b), B-4 (c), B-3 (d), B-2 (e).

5.11.7. Occurrence of Failure Mechanisms

The occurrence of the observed fatigue mechanisms (Paragraph 5.11.6) was classified in terms of the increasing pulsed-current period (increasing amplitudes of temperature & strain). The distribution of the fatigue deterioration mechanisms was found to be fairly random, Table 5-15. It was observed, however, that all the described fatigue mechanisms are present in samples which experienced large cyclic plasticity (e.g. Sample E-1).

Table 5-15. Distribution of fatigue mechanisms in the samples investigated.

Sample	Short cracks – crack initiation	Crack propagation	Film debonding & lifting	Cavities & craters	Grooves
E-1	✓	✓	✓	✓	✓
E-2	✓	✓	✓		
E-3					
E-4			✓		✓
E-5		✓	✓		
E-6	✓	✓		✓	✓
E-7					✓

The random distribution of the observed fatigue deterioration mechanisms is attributed to the fact that fatigue testing for each sample was suspended after fuse operation. Hence, as the time period decreased the magnitude of the cyclic shear strain also decreased, but at the same time the test time and the total number of cycles increased. Consequently, the accumulation of damage for all samples was approximately identical.

5.12. Conclusions

A finite element CAD tool for life prediction of the manufactured substrate fuse, when subjected to cyclic-current loading, has been presented. Additionally, an experimental set-up was devised to enable lifetime prediction of fuses subjected to repetitive current pulses.

The lifetime of the manufactured substrate fuse subjected to pulsed-currents of varying time period was determined computationally and experimentally. The computer predictions were found to be in a good agreement with the experimental findings. The fuse samples were dismantled after testing and various fatigue deterioration mechanisms were observed. These were, mainly, cracking of the conductive film, conductive film de-bonding and the film lifting off the substrate.

It was observed that sufficient care must be taken at all stages of modelling & simulation to avoid the build-up of errors. Wherever possible, the FE models were verified to ensure that the computer predictions are accurate.

Further experimental work is necessary to produce accurate elevated-temperature fatigue data for common fuse element materials.

Chapter 6.

Conclusions and Recommendations

6.1. Summary

My PhD study aimed at enhancing the knowledge of the electrical, thermal and mechanical behaviour of thin conductive films, carrying electric currents, laid on non-conductive substrates. Comprehensive results of the analyses, in the electro-thermal domain, including current, temperature and heat flux distributions, were presented for the fuse element carrying steady-state electric current. The effect of sandwiching the fuse element between two substrates and the effect of additional heat sink(s) attached to the substrate(s), on the pre-arcing current-carrying capacity and short-circuit performance of thin-film substrate fuses, was also investigated.

The emphasis, however, was placed on the mechanical behaviour, as this area had not so far been fully investigated by other researchers. The distributions and magnitudes of the electro-thermally induced stresses, strains & deformation in substrate fuses were presented. Major modes of fatigue deterioration, namely conductive film cracking and de-bonding from the substrate, were identified. Critical stress & strain components contributing to fatigue failure, and their locations, were also identified. The magnitudes of the critical stresses, strains and displacements were computed for varying thickness of the conductive film and the substrate, and for various combinations of single-layer and multi-layer films laid on alumina and pyrex substrates. The techniques to achieve a reduction in the magnitude of the critical stresses & strains were investigated for a number of single-layer, two-layer and three-layer fuse models.

A finite element model of a commercially available manufactured substrate fuse was developed to enable theoretical life prediction of notched thin-film fuses when subjected to current pulses. Additionally, an experimental set-up, for pulsed-current fuse testing, was devised to enable comparison of the theoretical findings with empirical data. The computed lifetimes were found to be in a good agreement with the experimental findings. After pulsed-current testing cracks of various lengths were found in the conductive film. Most of these cracks initiated along the interfacial film/substrate notch edge, which were in agreement with the computer-predicted location of the maximum shear stresses & strains. The large shear stresses, occurring along the interfacial film/substrate notch edge, are also responsible for the conductive film de-bonding from the substrate. Likewise, large compressive direct stresses in the conductive film were shown to be responsible for film lifting from the substrate. Both film de-bonding and film lifting were observed in the tested fuse samples.

6.2. Evaluation of Study

The main advantages of the FE CAD methodology demonstrated in the thesis are:

- it constitutes a versatile and economical means for simulating the electrical, thermal and mechanical behaviour of thin-film substrate fuses (Chapters 4 & 5);
- it can be applied to any substrate fuse geometry and any type of intermittent current loading (e.g. Paragraphs 4.3.4 & 4.3.5, 5.7);
- the technique can be used successfully for life prediction of substrate fuses subjected to intermittent-current loading (Chapter 5);
- to improve the accuracy of the predictions, constitutive model behaviour[10] and material properties can be enhanced continually [104-105].
- it enables comprehensive and cost-effective evaluation of the pre-arcing performance of new substrate (and possibly other) fuse designs.

The FE CAD methodology can be used for substrate fuse design to assist the designer with:

- estimation of the critical electro-thermal parameters, e.g. fuse element & fuse body temperature and power loss, for the intended rated current (e.g. Paragraphs 4.4 & 5.6);
- estimation of the time-current characteristic (Paragraph 5.5);
- the effect of possible modification(s) of the design on the electro-thermal characteristics of the fuse (Paragraphs 4.3.4 & 4.3.5);
- estimation of the magnitude of the electro-thermally induced stresses, and possible design modifications to reduce these stresses (Paragraphs 4.4 & 4.5);

---

[10] Constitutive model – an ABAQUS model, describing material's behaviour. For example, for a component subjected to a simple tension test an isotropic, linear elastic material with no temperature dependence would be sufficient. However, if the component might be subjected to rapid and severe overload, elasto-rate dependent plastic, work-hardening, temperature-dependent model might be required [104].

- estimation of the amplitude of cyclic stresses & strains, occurring under intermittent-current loading, and possible design modifications to reduce those stresses & strains (Paragraphs 5.9, 4.4.3, 4.4.4, 4.4.5, 4.5);
- life prediction for the intended intermittent-current application (Paragraph 5.10).

6.3. Recommendations for Future Work

In order to further refine the accuracy of life predictions the following ought to be investigated, and the enhanced material properties and constitutive model behaviour, resulting from these investigations ought, ideally, to be incorporated into the computer models:

- ambient and elevated-temperature elasto-plastic properties of copper/silver films;
- creep properties of the conductive film material;
- cyclic strain softening/hardening properties of the conductive film material;
- fatigue properties of common fuse element materials (silver, copper) need to be obtained, for the working temperature range of thin-film fuses (100~300°C).

The following are considered to be rich seams for further investigation:

- Crack growth in the conductive film was not studied due to limitations of the software (ABAQUS). However, third-party software can be used to analyse crack growth [108]. The software [111] models the growing crack by replacing the original mesh with a cracked mesh. This step must be performed every time the crack length is increased. Even using the complex third-party crack-growth prediction software, however, the analysis of the electro-thermally induced crack growth, under cyclic-current loading, would require sequential electro-thermal, thermal stress and crack-growth analyses, at time intervals set according to the pulsed-current period. This was seen as too complex (at the time of writing) and too expensive to justify and, hence, was not investigated further in my project. Given that the computing power of modern workstations doubles every few years, the computation of the above mentioned analysis should be feasible in the near future.
- Since the occurrence of large cyclic interfacial shear stresses & strains was found to be the primary reason for cracking and substrate fuse failure, it is envisaged that the use of flexible substrates, of low modulus of elasticity, would reduce the critical stresses & strains and, hence, prolong fuse life. Consequently, samples of fuse elements laid on to flexible substrates were obtained for investigation [83]. The initial evaluation of the novel

substrate fuse design technique, wherein the conductive film is laid onto a flexible paper-like substrate, is presented in Paragraph 6.3.1. It is envisaged that further research into flexible-substrate fuse design may produce promising findings resulting, hopefully, in a new industrial standard for semiconductor protection substrate fuses.

6.3.1. Novel Substrate Fuse Design

A novel fabrication technique for thin-film electronic circuit boards, developed by Peter Evans et al, opens new possibilities for future substrate fuse designs. In this emerging fabrication technique circuit tracks are formed on paper-like substrates by depositing films of a metal-loaded ink via a standard conductive lithographic film (CLF) printing process [29]. Although the new technique was developed for printed circuit fabrication purposes, its application to substrate fuse design was considered hopeful.

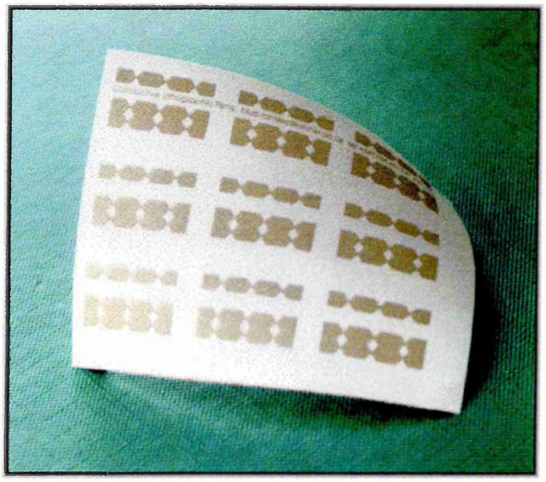

Figure 6-1. Novel fuse element design on paper-like substrate.

Several fuse samples were fabricated using the CLF technique for further investigation, Figure 6-1 [83], and preliminary tests showed that the CLF fuses are able to successfully clear small fault currents, Figure 6-2.

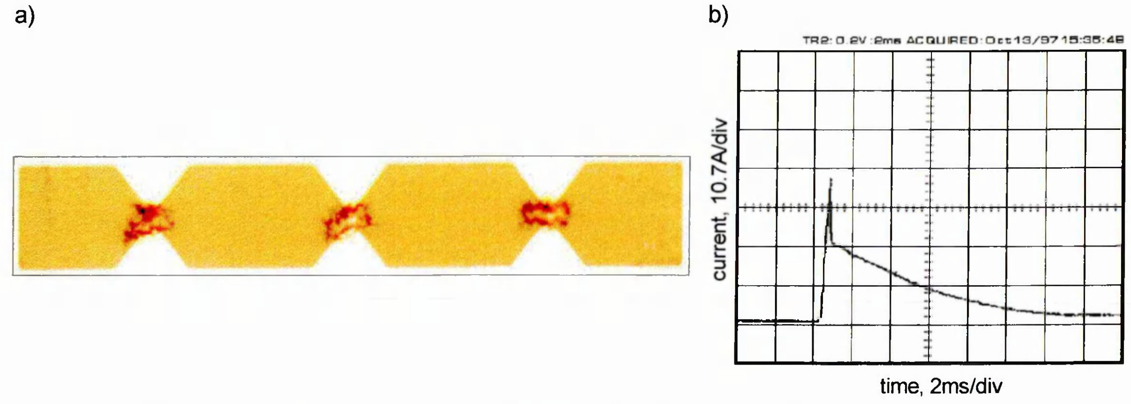

Figure 6-2. Fault current clearance by the CLF fuse; a) fuse element after operation; b) current waveform, t=2 ms/div, I=10.7 A/div.

The principal advantages of the new technique are:

- lightweight design;
- smaller external fuse dimensions;
- lower cost.

This technique, however, has a few disadvantages. These are:

- the lithographic printing process restricts the film thickness to around 5 microns;
- resistivity of the ink, that consists primarily of an electrically conductive metallic particulate suspended in an organic resin, is about twelve times larger than that of pure copper (~0.15Ω/sq. for cured sheet resistivity) and about six times larger than that of screen-printed films;
- the process's resolution limits lie between 0.1mm and 0.01mm.

An improvement in the flexible substrate fuse fatigue life-span under pulsed current-loading conditions is a postulated possibility. This proposition is based on the fact that CLF substrates (e.g. *polyart* – high density expanded polyethylene paper, *teslin* – polyethylene substrate, *gloss art paper*) are more flexible than traditional substrates (alumina, pyrex). The smaller modulus of elasticity indicates that the CLF substrates can expand more freely, hence the stresses can be reduced.

The flexible substrates were also subjected to high-temperature withstand tests. These tests involved placing the three substrates in a furnace at a setting of 250°C, examined, and subsequently heated to 500°C. The results of the tests are presented in Table 6-1.

Table 6-1. High-temperature withstand performance of the CLF substrates.

Substrate → **Temperature**	**Gloss Art**	**Polyart**	**Teslin**
250°C	slightly carbonised	50% carbonised extremely brittle	almost intact
500°C	100% carbonised extremely brittle	100% carbonised extremely brittle	25% carbonised substantially brittle

From the results of this test it is concluded that only the *teslin* substrate exhibits satisfactory high-temperature withstand properties, since the existence of carbon in any substantial quantity is likely to cause the fuse to fail due to excessive arcing.

The general conclusion is such that the CLF process is unsuitable for substrate fuses, however, the verification of this application necessitates further study.

6.4. Contributions to Knowledge

The following is a list of the main contributions to knowledge resulting from the work carried out in this thesis:

1. The effect of sandwiching the fuse element between two substrates, and the effect of attaching heat sink(s) to the substrate(s), on the pre-arcing current-carrying capacity and short-circuit performance of thin-film substrate fuses (Paragraphs 4.3.4 & 4.3.5).
2. Distribution of the electro-thermally induced stresses, strains and deformation in single-layer, single-notch and multi-notch, thin-film substrate fuse element geometries (Paragraph 4.4).
3. The effect of varying the thickness of the conductive film and the substrate on the magnitudes of the stresses & deformation (Paragraphs 4.4).
4. The effect of the thermo-elastic properties of the substrate material on the electro-thermo-mechanical behaviour of thin-film substrate fuses (Paragraphs 4.3.3, 4.4.5, 4.5.3).
5. Identification of the critical components of stress & strain, and their location, contributing to crack initiation & growth, and conductive film de-bonding and lifting off the substrate (Paragraphs 4.5 & 5.8).
6. Distribution and magnitudes of the stress & strain, for various two-layer and three-layer film metal combinations, in thin-film substrate fuses carrying steady-state electric current. (Paragraph 4.5).
7. The suitability of the ABAQUS coupled thermal-electrical procedure, for the prediction of the magnitude of the temperature, up to the melting temperature, due to Joulean heating, in complex non-linear finite element models of wire and thin-film substrate fuses (Appendix B, Paragraphs 3.8 & 5.4).
8. The application of the FE CAD methodology to the prediction of the time-current characteristic of thin-film substrate fuses, using 3D models comprising all parts of the fuse and the test-rig connectors, utilising temperature-dependent material properties for all parts of the model, and non-linear coefficient of surface heat transfer (Paragraph 5.5).
9. Comprehensive finite element CAD methodology, for computational life prediction of thin-film substrate fuses, when subjected to intermittent current loading (Chapter 5).

10. Experimental determination of lifetime and fatigue deterioration effects, e.g. crack formation, conductive film de-bonding and lifting from the substrate, in thin-film substrate fuses subjected to current pulses (Paragraph 5.11).
11. Initial evaluation of the applicability of the CLF technique to thin-film substrate fuse design (Paragraph 6.3.1).

6.5. Publications

The following paper has so far been submitted and accepted for publication:

[1] M. Wilniewczyc, D. Crellin, P.M. McEwan: *'Finite Element Analysis of Thermally-Induced Film De-bonding in Thick/Thin Film Substrate Fuses'*, Sixth International Conference on Electric Fuses and their Applications, Torino-Italy, Sept. 1999.

References

[1] Wright, A. & Newbery, P.G.: *'Electric Fuses'*, Peter Pereggrinus Ltd., IEE London 1982.

[2] Jacks, E.: *'High Rupturing Capacity Fuses'*, E.&F.N. Spon Ltd., London 1975.

[3] Ossowicki, J. & Sulikowski J.: *'Bezpieczniki Warstwowe na Podłożu Szklano-Krystalicznym'*, Prospects of Development of Current Breaking Techniques, Electrical Engineering Faculty, Technical University of Gdańsk, Gdańsk, Poland 1996.

[4] Harrison, Robert: *'Development and Characterisation of Thin Film Electric Fuselinks'*, Ph.D. Thesis, University of Nottingham, May 1994.

[5] Wilniewczyc, M.: *'2nd Progress Report on Research into Computer Prediction of Stress Distribution in Single and Multi-Layer Thin-Thick Film Substrate Fuse Elements'*, Internal Report, Sheffield Hallam University, Sheffield, January 1997.

[6] Rosen, P. & Newbery, P.G.: *'Recent Advances in HRC Fuse Technology'*, Electronics & Power, IEE, pp.495–498, June 1983.

[7] Wilkins, R. & Cline, H. Cynthia: *'An Advanced Applications Tool to Enhance the Fuse Protection of Power Semiconductors'*, IEEE Industry Applications Society Annual Meeting', Vol. 2, pp.1226–1230, 1993.

[8] McEwan, P.M.: '*Numerical Prediction of the Pre-Arcing Performance of HRC Fuses*', Ph.D. Thesis, Liverpool Polytechnic, Liverpool, October 1975.

[9] Gomez, J.C. & McEwan, P.M.: *'Investigation of the Pre-Arcing Behaviour of Dissimilar Uniform Double-Elemented Filled Fuses Using FE CAD Techniques'*, Proc. ICEFA, Nottingham, Sept.1991, pp.65-67.

[10] Brown, R.E., McEwan, P.M.: *'Unduloid Formation and Causation of Current Interruption in Current-Carrying Wires'*, Sixth Int. Conf. on Electric Fuses and their Applications, Torino (Italy), 20-22 Sept. 1999.

[11] Gomez, J.C., McEwan, P.M.: *'Experimental Investigation of Wall-Stabilised Arc Mechanisms of Wires in Fuse Filler'*, ICEFA, Ilmenau (Germany), Sept.1995, pp.243-250.

[12] TYPOWER ALOX Semiconductor Fuses Developed for Extreme Applications, BUSSMANN, Publication No 170Q.

[13] Summers, W.J.: *'YODEN Fuses – Preliminary Examination'*, GEC ALSTHOM Technical Report No.: B92/12, May 1992.

[14] Hiroyuki Takahashi: *'A Semiconductor Fuse-link on a Ceramic Substrate'*, Proc. of Int. Conf. on Electric Fuses and their Applications, Nottingham, U.K., Sept. 1991, pp.92-95.

[15] Lipski, T.; *'Bezpieczniki niskonapięciowe'*, (Low Voltage Fuses), Wydawnictwa Naukowo-Techniczne, Warszawa 1968.

[16] HRC Fuse Links, GEC ALSTHOM (Liverpool), Low Voltage Equipment Catalogue.

[17] Rosen, P. & Newbery, P.G.: *'Recent Advances in HRC Fuse Technology'*, Electronics & Power, IEE, pp.495–498, June 1983.

[18] Newbery, P.G., *'A Fuse Update for Semiconductor Protection'*, Power Conversion International Conference Proceedings, pp.123–133, USA, October 1986.

[19] Breen, Barry: *'Thin Film Surface Mount Fuses'*, 41st Electronic Components and Technology Conference Proceedings, Vol.1, pp.428-430, Atlanta, 11-16 May 1991.

[20] Lindmayer, M. et al: *'Fusing and Short-Circuit Interruption Behaviour of Metal Film Fuses'*, Proc. ICEFA, Nottingham, Sept.1991, pp.107–113.

[21] Cogan, D de: *'TLM Modelling of the Thermal Behaviour of Conducting Films on Insulating Substrates'*, Journal of Physics D, 1987, vol.20, pp.1445-1450.

[22] Marriage, A.J. et al: *'High Speed Thick Film Fuses'*, 5th European Hybrid Microelectronics Conference Proceedings, Italy 1985, pp.282–287.

[23] Mollet, Ronald E.: *'Overcurrent Protection of High Power Semiconductors with High Speed Fuses'*, Power Conversion International Conference Proceedings, U.S.A., 1983, pp.102–112.

[24] Inameti, E.E.: *'Thermal Studies of Thin-Film Fuses'*, Ph.D. Thesis, University of Nottingham, August 1988.

[25] Cogan, de D et al: *'Temperature Measurements of Thin Films on Substrates'*, Proc. IEE, Part I, Vol.132, No.3, June 1985.

[26] Howe, A.F. et al: *'Measuring the Pre-Arcing Temperature of HBC Fuselinks by Thermal Imaging'*, Proc. of Int. Conf. on Electric Fuses and their Applications, Trondheim, Norway, June. 1984, pp.12-23.

[27] Aktieselkabet Laur. Knudsen Nordisk Electricities, U.S. patent 4,331,947.

[28] Dorman Smith Fuses Ltd., U.K. patent 2,110,485A.

[29] Ramsey, B.J., Evans, P.S.A., Harrison, D.: *'A Novel Circuit Fabrication Technique Using Offset Litography'*, Journal of Electronics Manufacturing, 1997, Vol.7, No.1, pp.63-67.

[30] Dziedzic, A. et al: *'Analysis of Ageing Effects in Polymer Thick-Film Resistors based on DC Measurements and Impedance Spectroscopy'*, Proc. of 10th European Microelectronics Conf., Copenhagen Denmark, May 1995, pp.238-246

[31] Cięż, M.: *'Failure Mechanisms in Thick-Film Layers'*, European Hybrid Microelectronics Conference Proceedings, Copenhagen Denmark, May 1983, pp.1-11.

[32] Bacher, Rudolf J. et al: *'Firing Process-Related Failure Mechanisms in Thick Film Copper Multilayers'*, Electronic Components Conference Proceedings, U.S.A. 1986, pp.471-480.

[33] Perecherla, Raju et al: *'Adhesion Failure Modes In Copper Thick Film Conductors'*, International Journal of Microcircuits and Electronic Packaging', Volume 18, Number 1, First Quarter 1995, pp.29-40.

[34] Milgram, A.A.: *'Influence of Metallic Diffusion on the Adhesion of Screen Printed Silver Films'*, Metallurgical Transactions, Volume 1, March 1970, pp.695-700.

[35] Lund, R.E. and Gorres, J.M.: *'A New Failure Mechanism in Thin Film Resistors'*, Electronic Components Conference Proceedings', U.S.A. 1981, pp.67-74.

[36] Cogan, D. de, et al: *'A Transient Thermal Failure Mode in Metal Film Resistors'*, Journal of Physics D, 1987, Volume 20, pp.1454-1456.

[37] Dasgupta, Abhijit et al: *'Material Failure Mechanisms and Damage Models'*, IEEE Transactions on Reliability , Dec.1991, Volume 40, No.5, pp.531-536.

[38] Dasgupta, Abhijit: *'Failure Mechanism Models for Cyclic Fatigue'*, IEEE Transactions on Reliability , Dec.1991, Volume 42, No.4, Dec.1993, pp.548-555.

[39] Coffin, L.F.: *'A Study of the Effects of Cyclic Thermal Stresses on a Ductile Metal'*, Transactions of the ASME, Vol.76, August 1954, pp.931-950.

[40] Bruno A. Boley et al.: *'Theory of Thermal Stresses'*, Robert E. Krieger Publishing Company, Malabar, Florida 1985.

[41] Bannatine, J.A. et al: *'Fundamentals of Metal Fatigue Analysis'*, Prentice Hall, New Jersey 1990.

[42] Sandor, B.I.: *'Fundamentals of Cyclic Stress and Strain'*, University of Wisconsin Press, 1972.

[43] Manson, S.S.: *'Thermal Stress and Low-Cycle Fatigue'*, McGraw-Hill, Inc., Malabar, Florida 1981.

[44] Skelton, R.P.: *'Fatigue at High Temperature'*, Applied Science Publishers, London, 1983.

[45] Xiang, Gui et al: *'Thermal Simulation of Thin-Film Interconnect Failure Caused by High Current Pulses'*, IEEE Transactions on Electron Devices, Volume 42, No.7, July 1995, pp.1386-1388.

[46] Czucha, J.: *'On the Proper Co-ordination of Fuses with Semiconductor Devices in the Heavy Short-Circuit Region'*, Proc. of Int. Conf. on Electric Fuses and their Applications, Trondheim, Norway, June 1984, pp.95-105.

[47] Bradley, M.: '*Dynamic Fuse Model for Electromigration Failure of Polycrystalline Metal Films*', The American Physical Society, 3rd Series, Vol.50, No.2, Part A, pp.631-634.

[48] Cogan, de Donald: '*Non-linear Thermal Effects in Metal/Non-metal Systems*', 4th Int. Workshop on the Electronic Properties of Metal/Non-metal Microsystems, Sheffield Hallam University, Sheffield UK, 3 September 1993, pp.459-466.

[49] Szeloch, R.F. et al: '*Computer-Controlled Step-Stress Method for Thick-Film Resistive Layers Testing*', Proc. of the 7th Symposium on Reliability in Electronics, Budapest, 1988, pp.606-611.

[50] Wilkins, R.: '*Endurance of Semiconductor Fuses under Cyclic Loading*', Proc. ICEFA, Nottingham, Sept. 1991, pp.43-48.

[51] Sloot, J.G.J. et al: '*Fuse Characteristics Determined by Melting or Ageing?*', Prospects of Development of Current Breaking Techniques, The Scientific Papers of Electrical Engineering Faculty, Technical University of Gdańsk, Gdańsk 1996, pp.119-123.

[52] Daalder, J.E.: '*Ageing in Fuses with M-Effect*', Proc. ICSAP, Łódź Poland, 1981, pp.295-298.

[53] Harrison, R.D.: '*Ageing of Film Fuses on Substrates*', Proc. ICEFA, Nottingham, Sept.1991, pp.85-91.

[54] Arai, S.: '*Deteriorations and Cycles to Failure of H.V. Current-Limiting Fuses Subjected to Cyclic Loading*', Proc. ICEFA, Trondheim 1984, pp.252-261.

[55] Stevenson, G.: '*Cyclic Loading of Fuses for the Protection of Semiconductors*' Proc. ICEFA, Liverpool 1976, pp.276-282.

[56] Meng, X.Z.: '*Lifetime Predictions of Miniature Fuses and Semiconductor Protection Fuses*', Ph.D. Thesis, Eindhoven University of Technology, 1995.

[57] Morgan, V.T.: '*Rating of Conductors for Short-Duration Currents*', Proc. IEE, Vol.118, No.3/4, March/April 1971.

[58] Newman, J.C. Jr.: '*Finite Element Analysis of Crack Growth Under Monotonic and Cyclic Loading*', Cyclic Stress-Strain and Plastic Deformation Aspects of Fatigue

Crack Growth, ASTM STP 637, American Society for Testing and Materials, St. Louis, Mo., 2-8 May.1976, pp. 56-80.

[59] Kline, R.A.: '*Stress Analysis of Adhesively Bonded Joints*', Int. Symposium on Adhesive Joints: Formation, Characteristics and Testing', Kansas City, MO, 12-17 Sept. 1982, Plenum Publishing 1984, pp.239-242.

[60] Li, W., et al: '*Stress Analysis of Adhesive Bonded Tee Joints*', 2nd Int. Conf. on Contact Mechanics, Ferrara, Italy, July 1995, pp.63-71.

[61] Meera, N.K. et al: '*Notch Stress-Strain Analysis and Life Prediction in Multi-axial Fatigue*', Int. Symposium on Fatigue Design, Helsinki, Finland, 5-8 Sept. 1995, pp.291-308.

[62] Zsary, A.: '*Stress Analysis of Coating in the Practice of Design Engineer*', Proc. of the 9th Congress on Material Testing, Budapest, Hungary, 29 Sept. – 3 Oct. 1986, pp.651-655.

[63] Bacmann, J.J.: '*Texture and Stress Analysis of Sputtered Thin Films*', Proc. of the Joint 4th Int. Symposium on Trends and New Applications in Thin Films (TATF'94) and the 11th Conf. on High Vacuum, Interfaces, and Thin Films (HVITF'94), Dresden, Germany, 7-11 March 1994, pp.297-302.

[64] Wakasa, K. et al: '*Interfacial Stress Distribution Between Bovine Dentine and Resin Composite in Dentine Bonding Systems*', Journal of Materials Science – Materials in Medicine, Vol.7, pp.617-621.

[65] Ozmat, B.: '*A Non-linear Thermal Stress Analysis of Surface Mount Solder Joints*', 40th Electronic Components & Technology Conference, Las Vegas, N.V. U.S.A., 20-23 May 1990, pp.959-973.

[66] Aivazzadeh, S.: '*Stress Analysis at the Interface in Adhesive Joints by Special Finite Elements*', International Journal of Adhesion and Adhesives, 1986, Vol.4, pp.185-188.

[67] Kapur, S.: '*Stress Analysis of Polyamide Copper Thin Film Structure on Glass Ceramic/Copper Multilevel Substrate*', 42nd Electronic Components and Technology Conference, San Diego CA, U.S.A., 18-20 May 1992, pp.129-133.

[68] Lau J., et al: '*Thermal Stress Analysis of Tape Automated Bonding Packages and Interconnections*', 39th Electronic Components Conference, Houston TX, U.S.A., 22-24 may 1989, pp.456-463.

[69] Chandler, H.D.: '*Determination of Creep, Stress Relaxation and Stress-Strain Curves in Copper*', 5th Int. Conf. on Creep and Fracture of Engineering Materials and Structures, Swansea, 1993, pp.63-71

[70] Burdekin, F.M.: '*Engineering Design Against Fracture at Stress Concentrators*', Proc. of the 3rd Int. Conf. on Fracture at Stress Concentrators, Cambridge, UK, Sept. 1984, pp.14-20.

[71] Smith, R.A.: '*Propagation of Fatigue Cracks from Notches*', Proc. of the 3rd Int. Conf. on Fracture at Stress Concentrators, Cambridge, UK, Sept. 1984, pp.34-40.

[72] Sarihan, V.: '*A Methodology for Fatigue Life Prediction of Solder Joints*', Proceedings of the ABAQUS Users' Conference, Paris, France, May 1995, pp. 743-754.

[73] Morin, G.: '*Thermo-Mechanical Fatigue Analysis of Engine Collector Rings*', Proceedings of the ABAQUS Users' Conference, Paris, France, May 1995, pp. 619-632.

[74] Lukáš, P. et al: '*High Cycle Fatigue Life of Metals*', Materials Science and Engineering, 15 (1974), pp.239-245.

[75] Kettunen, P. et al: '*Fatigue of Polycrystalline Copper at Constant and Variable Plastic Strain Amplitudes*', Fatigue Fracture of Engineering Materials and Structures, Vol.8, No.3, 1985, pp.277-285.

[76] Benham, P.P.: '*Torsional-Strain-Cycling Fatigue of Copper at Low Endurance*', Journal of the Institute of Metals, Vol.91, 1962-63, pp.404-407.

[77] Kemsley, D.S.: '*Effects of Cyclic Stress and Frequency on Deformation Markings in Fatigued Copper*', Journal of the Institute of Metals, Vol85, 1956-57, pp.153-157.

[78] Thompson, N. et al: '*The Origin of Fatigue Fracture in Copper*', Phil. Mag., Ser.8, Vol.I, Pl.3, pp.113-126.

[79] Mughrabi, H.: '*The Cyclic Hardening and Saturation Behaviour of Copper Single Crystals*', Materials Science and Engineering, 33 (1978), pp.207-223.

[80] Benham, P.P.: *'Axial-Load and Strain-Cycling Fatigue of Copper at Low Endurance'*, Journal of the Institute of Metals, 1961, pp.328-335.

[81] British Standards 88: Parts 1–4. 1998, British Standards Institution.

[82] GEC Alsthom: '*Experimental Verification of the Minimum Fusing Current of the 20A Manufactured Substrate Fuse*', Internal Report, May 1998.

[83] Evans, P.: Cleaner Electronics Research Group, Brunel University, Private communication.

[84] Carslaw, H.S.: '*Conduction of Heat in Solids*', Oxford University Press, Oxford 1959.

[85] Benham, P.P.: '*Mechanics of Solids and Structures*', Pitman Books Limited, London 1981.

[86] Dieter, George E.: *'Mechanical Metallurgy'*, McGraw-Hill Book Company Inc., London 1961.

[87] Kobayashi, Albert S.: *'Manual of Engineering Stress Analysis'*, Prentice-Hall, New Jersey, 1982.

[88] Brandes, E.: '*Smithells Metals Reference Book*', Butterworths, London 1983.

[89] Samsonov, G.V.: *'Handbook of the Physicochemical Properties of the Elements'*, Oldbourne, London 1968.

[90] Davis, Joseph R. et al: *'Metals Handbook – Properties & Selection – Non-ferrous Alloys and Special Purpose Materials'*, Vol.2, ASM Int., Oct. 1990.

[91] Boyer, H.E. et al: *'Metals Handbook'*, American Society for Metals, Ohio 1985.

[92] Scott D. Henry et al: *'ASM Handbook – Fatigue and Fracture'*, Vol.19, ASM Int. Handbook Committee, USA 1996.

[93] Morrell, R. *'Handbook of Properties of Technical & Engineering Ceramics'*, Part 2: High Alumina Ceramics, HMSO publication, London 1987.

[94] Alper, M. Allen: '*High Temperature Oxides. Part III: Magnesia, Alumina, Beryllia Ceramics: Fabrication, Characterisation & Properties*', Academic Press, New York and London 1970.

[95] Leon, I, et al: '*Handbook of Thin Film Technology*', McGraw-Hill Book Company, 1983.

[96] Elshabini, Aicha: '*Thin Film Technology Handbook*', McGraw-Hill Companies, New York 1998.

[97] Berry, R. et al: '*Thin Film Technology*', D. Van Nostrand Company Ltd., U.S.A. 1968.

[98] Neelamkavil, F.: '*Computer Simulation and Modelling*', John Wiley & Sons, London 1987.

[99] Bulgren W.: '*Discrete System Simulation*', Prentice-Hall Inc., N.J. U.S.A. 1982.

[100] Silvester, P.P. et al: '*Finite Elements for Electrical Engineers*', Cambridge University Press, Cambridge 1990.

[101] Dziedzic, Andrzej. Institute of Electronic Technology. Technical University of Wrocław, Poland. Private Communication.

[102] Crellin, D. GE POWER CONTROLS LTD., Liverpool UK, Private Communication.

[103] Sulikowski, Jan. Technical University of Gdańsk, Poland. Private Communication.

[104] ABAQUS ver.5.5/5.6 User's Manuals, Hibbit Karlsson & Sorensen Inc., 1995.

[105] ABAQUS News/Answers, 1994-1999.

[106] PATRAN ver.1.4 User's Manuals, The MacNeal-Schwendler Corporation, Los Angeles, May 1995.

[107] Wilniewczyc, M.: '*POWERFUSE – User's Manual*', Sheffield Hallam University, Sheffield, July 1998.

[108] Timbrell, C. et al: '*Application of ABAQUS to Analysis of 3D Cracks and Fatigue Crack Growth Prediction*', Proc. of ABAQUS Users' Conf., Newport, June 1994, pp.527-541.

[109] Leonida, Giovanni: '*Handbook of Printed Circuit Design, Manufacture, Components & Assembly*', Electrochemical Publications, Ayr 1982.

Internet references:

[110] *'Thermal Fatigue of a Surface Mount Assembly'*,
http://www.abaqus.com/applications/surface-mount/index.html

[111] *'ZENCRACK – 3D Crack Analysis Software and Automatic Crack Growth Prediction'*
http://www.zentech.co.uk/software.htm#Zencrack

[112] Hibbit Karlsson & Sorensen Inc.
http://www.abaqus.com/

Appendix A. Nomenclature

Film terminology.

For **two-layer films**, the film deposited on the substrate is referred to as the ***substrate-bonded film*** (SBF), and the film deposited on top of the *substrate-bonded film* is referred to as the ***metal-bonded film*** (MBF).

For **three-layer films**, the film deposited on the substrate is again referred to as the *substrate-bonded film,* and the film deposited on top of the *substrate-bonded film* is referred to as the ***lower metal-bonded film*** (LMBF). The film deposited on top of the *lower metal-bonded film* is referred to, finally, as the ***upper metal-bonded film*** (UMBF). This terminology is clarified in Figure A-1.

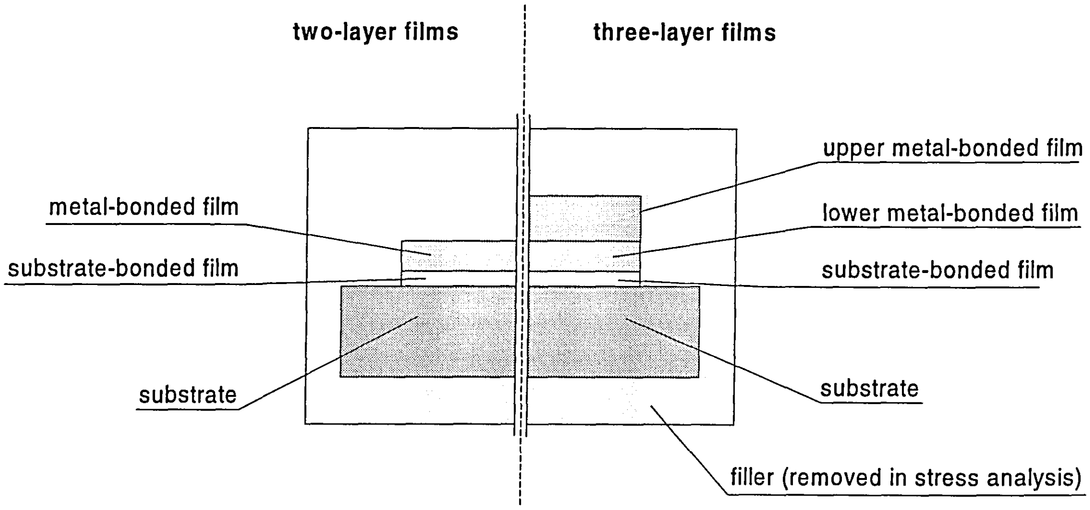

Figure A-1. Multilayer film and substrate terminology.

Definitions of the critical stress axes and points.

The stresses presented in this thesis are directional in relation to the fuse element-substrate geometry. The location of the co-ordinate axes, and the location of the critical stress axes and points are shown in Figure A-2, and are defined as follows.

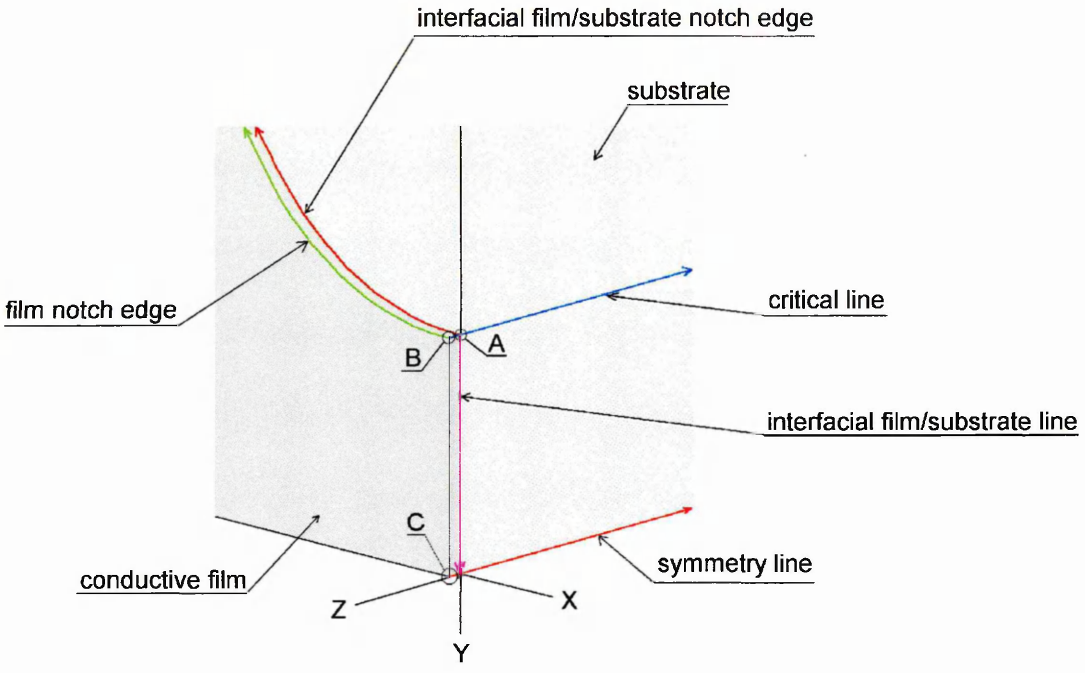

Figure A-2 Fuse element-substrate model showing critical stress points and directions.

Point A	Point on the film/substrate interface at the minimum cross-section of the notch – termed the **critical point**.
Point B	Point on the edge of the conductive film, at the minimum cross-section of the notch.
Point C	Point on the surface of the conductive film co-incident with the 'Z' axis of model symmetry.
Critical line	The (blue) line projected orthogonally from the Point B, through the conductive film and substrate thickness.
Symmetry line	The (red) line projected from Point C, along the 'Z' axis of symmetry, through the conductive film and substrate thickness.
Interfacial film/substrate line	The (pink) line along the 'Y' axis, on the film/substrate interface, whose beginning is at Point A,.
Interfacial film/ substrate notch edge	The (brown) line, whose beginning is at Point A.
Film notch edge	The (green) line whose beginning is at Point B.

Appendix B. Suitability of the ABAQUS Software for the Prediction of Current-Induced Temperature Distribution in 3D Media.

The ABAQUS software was verified with respect to the accuracy of the prediction of the thermal-electrical procedure. A 3D ABAQUS FE model of a wire fuse, and a mathematical model of a wire fuse, developed by McEwan [8], were used for this study. The mathematical model was built into a custom-made computer program [107]. The results produced by ABAQUS were compared with the predictions produced by the computer program and, additionally, with experimental data [102].

ABAQUS Finite Element Model of a Wire Fuse

The ABAQUS FE model of a section of a quarter of the wire fuse is shown in Figure B-1.

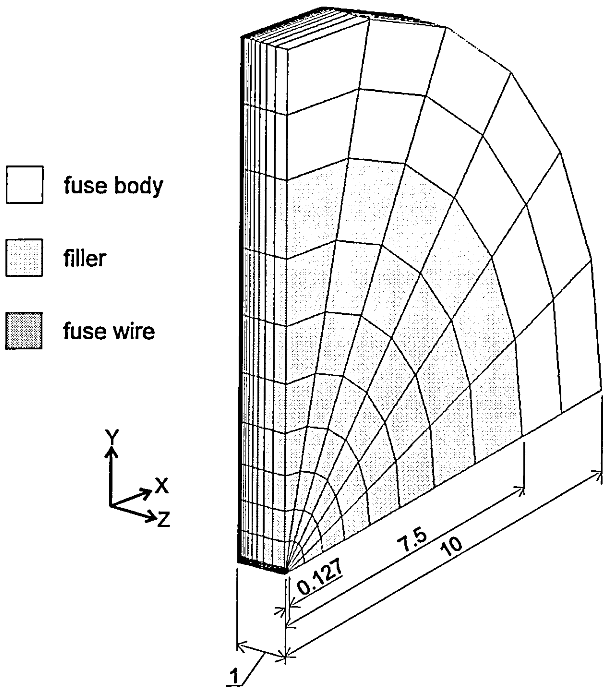

Figure B-1. The ABAQUS finite element model of a wire fuse.

The fuse wire was surrounded by a quartz sand filler, and both were encapsulated in a ceramic body. The study assumed that the lateral and axial heat fluxes were negligible, which in effect reduced the problem to a 1D Joulean heat generation & flow. Despite the problem being one-dimensional, however, 3D modelling was adopted[11]. The reason for doing this was

---

[11] The ABAQUS library of finite elements includes 1D and 2D axisymmetric elements, which could be used to solve the problem discussed.

such that both the electro-thermal procedure *and* the 3D DC3D8E and DC3D8 finite elements, used to construct the model, could be verified simultaneously. The DC3D8(E) elements were used to construct all other electro-thermal FE models, hence if accurate predictions could be obtained for the wire fuse model investigated, the other models were also presumed to produce accurate results.

The ABAQUS input file for the wire fuse model:

```
*HEADING

    ABAQUS verification of the accuracy of the prediction
    of the Time/Current characteristic of the wire fuse.

    3D elements used: DC3D8(E)

    Electrical current is injected at one end of wire.

    Voltage is fixed at 0 volts at the other end of the fuse wire.

    Wire material:     COPPER
    Filler material:   QSAND
    Body material:     ALUMINA

*PREPRINT, MODEL=NO, HISTORY=NO, ECHO=NO
**
*RESTART, WRITE, OVERLAY
**
*NODE, INPUT=WIRE_FUSE_NODES
**
*ELEMENT, TYPE=DC3D8E, ELSET=WIRE, INPUT=WIRE_FUSE_ELMS_WIRE
**
*ELEMENT, TYPE=DC3D8, ELSET=FILLER, INPUT=WIRE_FUSE_ELMS_FILLER
**
*ELEMENT, TYPE=DC3D8, ELSET=BODY, INPUT=WIRE_FUSE_ELMS_BODY
**
*************************************************************************
** Minimize the wavefront
*************************************************************************
**
*WAVEFRONT MINIMIZATION, NODES, METHOD=1
            1,    1337
**
*************************************************************************
** Define node sets
*************************************************************************
**
*NSET, NSET=ALLNODES, GENERATE
    1,  1391
**
*************************************************************************
** Define properties of solid elements
*************************************************************************
**
*SOLID SECTION, ELSET=WIRE, MATERIAL=COPPER
          1.,
**
*SOLID SECTION, ELSET=FILLER, MATERIAL=QSAND
          1.,
**
*SOLID SECTION, ELSET=BODY, MATERIAL=ALUMINA
          1.,
**
*************************************************************************
** Define thermal-electrical properties of materials
*************************************************************************
**
*MATERIAL, NAME=COPPER
**
** Melting point 1083 deg C
** Boiling point 2560 deg C
**
*DENSITY
    8.89E-6,     0.
    8.84E-6,   100.
    8.80E-6,   200.
    8.65E-6,   500.
```

```
    8.48E-6,  800.
    8.33E-6, 1082.
**
*CONDUCTIVITY, TYPE=ISO
    0.403,      0.
    0.401,     25.
    0.395,    100.
    0.389,    200.
    0.341,    538.
    0.244,   1037.
    0.230,   1082.
**
*ELECTRICAL CONDUCTIVITY
  62.89E03,      0.
  43.86E03,    100.
  33.56E03,    200.
  19.30E03,    500.
  13.28E03,    800.
  10.91E03,   1000.
  10.12E03,   1082.
**
*SPECIFIC HEAT
    380,      0.
    382,     20.
    393,    100.
    406,    200.
    446,    500.
    519,    962.
**
** ALUMINA
**
** Nominal Al O  content 96.5-99.0 %
**           2 3
**
*MATERIAL, NAME=ALUMINA
**
*DENSITY
     3.75E-6,
**
*CONDUCTIVITY, TYPE=ISO
    0.0250,        20.
    0.0200,       100.
    0.0150,       200.
    0.0100,       400.
    0.0081,       600.
    0.0071,       800.
    0.0069,      1000.
    0.0064,      1200.
**
*SPECIFIC HEAT
      780,     25.
      911,    100.
     1023,    200.
     1175,    500.
**
*MATERIAL, NAME=QSAND
**
*DENSITY
      1.8E-6,
**
*CONDUCTIVITY, TYPE=ISO
  0.002127,     27.
  0.001432,    127.
  0.001091,    227.
  0.000873,    327.
  0.000709,    427.
  0.000586,    527.
  0.000491,    627.
  0.000422,    727.
  0.000381,    827.
  0.000354,    927.
  0.000340,   1027.
  0.000326,   1127.
  0.000312,   1227.
  0.000299,   1327.
**
*SPECIFIC HEAT
       1176.,
**
***************************************************************************
** Define initial temperatures at all nodes
***************************************************************************
**
*INITIAL CONDITIONS, TYPE=TEMPERATURE
  ALLNODES,   20.0
```

```
**
***************************************************************************
** Begin a step
***************************************************************************
**
*STEP, INC=1000
 STEP 1: JOULE HEATING ANALYSIS
**
*COUPLED THERMAL-ELECTRICAL, DELTMX=100,  END=PERIOD
   0.1,   1000,    ,   ,   0.001
**
***************************************************************************
** Reset solution controls
***************************************************************************
**
*CONTROLS, PARAMETERS=TIME INCREMENTATION
   10,    12,    9,   16,    10,     1,  12,      5,    6,    6
** 0.5,  0.5,  0.5,  0.85,  0.5,  0.25,   1,  0.75
** 0.8,    1, 1.25,     1,    1,   0.1,   1,     1,  0.95
**
***************************************************************************
** Define node sets
***************************************************************************
**
*NSET, NSET=EXTERNAL, GENERATE
       1,      91,       1
*NSET, NSET=SYMMETRY, GENERATE
     911,     947,       1
*NSET, NSET=INJECT_C, GENERATE
     971,     971,       1
     981,     981,       1
     999,     999,       1
    1013,    1013,       1
    1027,    1027,       1
    1030,    1031,       1
    1092,    1093,       1
    1102,    1102,       1
    1117,    1117,       1
    1128,    1128,       1
    1137,    1138,       1
    1162,    1183,       1
**
***************************************************************************
** Specify fixed boundary conditions
***************************************************************************
**
*BOUNDARY, OP=NEW
  EXTERNAL, 11, 11,         20.
**
*BOUNDARY, OP=NEW
  SYMMETRY,  9,  9,         0.0
**
***************************************************************************
** Inject current
***************************************************************************
**
** Inject current
**
** total # of nodes: 36
** I_node = I_symm/36 = (I_total / 4) / 36
** i.e. Inode=Itotal/144
**
*CECURRENT
  INJECT_C,   9,   0.1215277
**
***************************************************************************
** Request output
***************************************************************************
**
*NODE PRINT, FREQ=1
NT,      EPOT
**
**
*NODE FILE, FREQ=999
NT,      EPOT
**
*EL PRINT, POSITION=INTEGRATION POINT, FREQ=99
**
*EL FILE, POSITION=INTEGRATION POINT, FREQ=99
**
*EL PRINT, POSITION=NODES, FREQ=0
**
*EL FILE, POSITION=NODES, FREQ=0
**
*EL PRINT, POSITION=CENTROIDAL, FREQ=99
```

```
EPG,      ECD
ECURS,    ELJD,     NCURS
JENER
HFL
*EL FILE, POSITION=CENTROIDAL, FREQ=99
EPG,      ECD
ECURS,    NCURS
HFL
**
*EL PRINT, POSITION=AVERAGED AT NODES, FREQ=0
**
*EL FILE, POSITION=AVERAGED AT NODES, FREQ=0
**
*ENERGY FILE, FREQ=99
 ALLJD
**
*ENERGY PRINT, FREQ=99
 ALLJD
**
*MODAL PRINT, FREQ=99
**
*MODAL FILE, FREQ=99
**
*PRINT, FREQ=1
**
*END STEP
```

Mathematical Model of a Wire Fuse

For the mathematical model of a wire fuse it was assumed, as in the previous case, that the lateral and axial heat fluxes were negligible, which reduced the problem to one dimensional Joulean heat generation & flow. The solution was based on the computation of time-varying temperature distribution for axi-symmetric Joulean heating in long circular conductors surrounded by thermally conductive media. Crank-Nicholson formulation was adopted for this study. The wire fuse model is shown in Figure B-2.

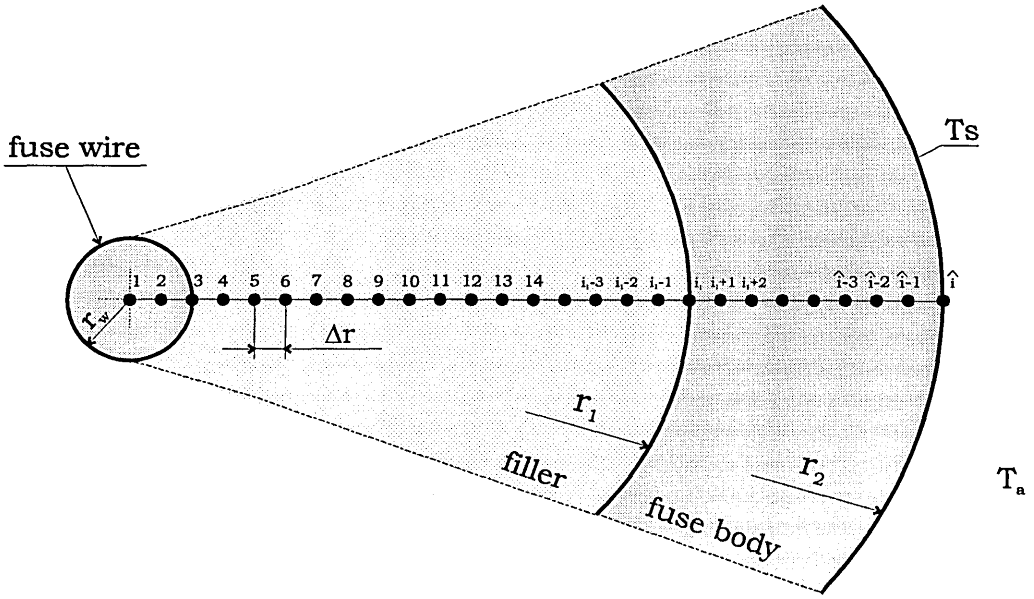

Figure B-2. The wire fuse model adopted for the Crank-Nicholson formulation.

The governing transient heat flux equation for a three-dimensional conductive body with internal heat generator is given by:

$$c\rho\frac{\partial T}{\partial t} = \nabla(K\nabla T) + \frac{J^2}{\delta} = K\nabla^2 T + \frac{J^2}{\delta} \qquad \text{[Eq.B-1]}$$

where:

c – thermal capacity;

ρ – media density;

J – current density;

Due to axi-symmetry of the model the Cartesian co-ordinate difference equation must be transformed to polar co-ordinate form:

$$c\rho\frac{\partial T}{\partial t} = K\left\{\left(\frac{\partial^2 T}{\partial r^2} + \frac{1}{\partial r^2}\cdot\frac{\partial^2 T}{\partial \varphi^2} + \frac{\partial^2 T}{\partial z^2}\right) + \frac{J^2}{\delta K}\right\} \qquad \text{[Eq.B-2]}$$

The following assumptions are made:

- Axi-symmetric conditions apply, hence $\frac{\partial^2 T}{\partial \varphi^2} = 0$;
- Axial heat flow is negligible, hence $\frac{\partial^2 T}{\partial z^2} = 0$;

Given the above assumptions and substituting $\kappa = \frac{K}{c\rho}$, where κ – diffusivity of media, equation B-2 can be rewritten as:

$$\frac{1}{\kappa}\frac{\partial T}{\partial t} = \frac{1}{r}\left(\frac{\partial}{\partial r}\left(r\frac{\partial T}{\partial r}\right)\right) + \frac{J^2}{\delta K} \qquad \text{[Eq.B-3]}$$

Equation B-3 must be substituted by difference equations appropriate to the points (nodes) within all media (conductor, filler, fuse body) and at the conductor/filler and filler/body boundaries.

Adopted notation:

T_i^n – is the temperature at time instant nΔT, at the ith node, i.e. at radius (i-1)·Δr, where $\Delta r = \frac{r_c}{2}$, and Δt is the iterative time interval;

$$\frac{\partial T_i^n}{\partial t} \cong \frac{T_i^{n+1} - T_i^{n-1}}{2\Delta t}$$

$$\frac{\partial^2 T_i^n}{\partial r^2} \cong \frac{T_{i-1}^n - T_{i+1}^n - 2T_i^n}{\Delta r^2}$$

$$i_1 = \left| \frac{r_1}{\Delta r} + 1 \right|$$

$$\hat{i} = \left| \frac{r_2}{\Delta r} + 1 \right|$$

Subscripts:

c – conductor;

f – filler;

b – fuse body;

Critical boundaries:

$r = 0 \Rightarrow i = 1$

$r = r_c \Rightarrow i = 3$

$r = r_1 \Rightarrow i = i_1$

$r = r_2 \Rightarrow i = \hat{i}$

$T_{\hat{i}} = T_s$

Homogenous media:

$0 < r < r_c \Rightarrow i = 2$

$r_c < r < r_1 \Rightarrow 3 < i < i_1$

$r_1 < r < r_2 \Rightarrow i_1 < i < \hat{i}$

Radial time-varying difference equations:

Condition 1. $r = 0$ ($i = 1$)

Because r = 0 de l'Hospital's Rule $\left(\nabla^2 T = 2\frac{\partial^2 T}{\partial r^2} \right)$ must be applied to the thermal flux equation:

$$\frac{1}{\kappa_c}\frac{\partial T}{\partial t} = 2 \cdot \frac{1}{r}\left(\frac{\partial}{\partial r}\left(r\frac{\partial T}{\partial r} \right) \right) + \frac{J^2}{\delta K_c}$$

where:

$$\kappa_c = \frac{K_c}{c_c \rho_c}.$$

Hence:

$$\frac{1}{\kappa_c}\frac{T_i^{n+1}-T_i^n}{\Delta t}=\frac{1}{\Delta r^2}\left\{2\left[2T_{i+1}^n-2T_i^n\right]+\frac{J^2\Delta r^2}{\sigma K_c}\right\}$$

from which:

$$T_i^{n+1}=T_i^n+\frac{\kappa_c\Delta t}{\Delta r^2}\left\{4\left(T_{i+1}^n-T_i^n\right)+\frac{J^2\Delta r^2}{\sigma K_c}\right\} \qquad \text{[Eq.B-4]}$$

Condition 2. $0 < r < r_c$ $(i = 2)$

$$\frac{1}{\kappa_c}\frac{\partial T}{\partial t}=\frac{1}{r}\left(\frac{\partial}{\partial r}\left(r\frac{\partial T}{\partial r}\right)\right)+\frac{J^2}{\sigma K_c}$$

$$\frac{1}{\kappa_c}\frac{T_i^{n+1}-T_i^n}{\Delta t}=\frac{1}{\Delta r^2}\left\{\left(1+\frac{1}{2i}\right)T_{i+1}^n+\left(1-\frac{1}{2i}\right)T_{i-1}^n-2T_i^n\right\}+\frac{J^2\Delta r^2}{\sigma K_c}$$

from which:

$$T_i^{n+1}=T_i^n+\frac{\kappa_c\Delta t}{\Delta r^2}\left\{\left(1+\frac{1}{2i}\right)T_{i+1}^n+\left(1-\frac{1}{2i}\right)T_{i-1}^n-2T_i^n+\frac{J^2\Delta r^2}{\sigma K_c}\right\} \qquad \text{[Eq.B-5]}$$

Condition 3. $r = r_c$ $(i = 3)$

$$\frac{1}{\kappa_{cf}}\frac{\partial T}{\partial t}=\frac{1}{r}\left(\frac{\partial}{\partial r}\left(r\frac{\partial T}{\partial r}\right)\right)+\frac{J^2}{\sigma K_{cf}}$$

where:

$$\kappa_{cf}=\frac{1}{2}\left(\frac{K_c}{c_c\rho_c}+\frac{K_f}{c_f\rho_f}\right)$$

$$K_{cf}=\frac{1}{2}\left(K_c+K_f\right)$$

Hence:

$$T_i^{n+1}=T_i^n+\frac{\kappa_{cf}\Delta t}{\Delta r^2}\left\{K_f T_{i+1}^n+K_c T_{i-1}^n-\left(K_f+K_c\right)T_i^n+\frac{J^2\Delta r^2}{\sigma K_c}\right\} \qquad \text{[Eq.B-6]}$$

Condition 4. $r_c < r < r_1$ $(3 < i < i_1)$

$$\frac{1}{\kappa_f}\frac{\partial T}{\partial t}=\frac{1}{r}\left(\frac{\partial}{\partial r}\left(r\frac{\partial T}{\partial r}\right)\right)$$

Therefore:

$$\frac{1}{\kappa_f}\frac{T_i^{n+1}-T_i^n}{\Delta t}=\frac{1}{\Delta r^2}\left\{\left(1+\frac{1}{2i}\right)T_{i+1}^n+\left(1-\frac{1}{2i}\right)T_{i-1}^n-2T_i^n\right\}$$

and:

$$T_i^{n+1}=T_i^n+\frac{\kappa_f\Delta t}{\Delta r^2}\left\{\left(1+\frac{1}{2i}\right)T_{i+1}^n+\left(1-\frac{1}{2i}\right)T_{i-1}^n-2T_i^n\right\} \qquad \text{[Eq.B-7]}$$

Condition 5. $r = r_1$ $(i = i_1)$

$$\frac{1}{\kappa_{fb}}\frac{\partial T}{\partial t}=\frac{1}{r}\left(\frac{\partial}{\partial r}\left(r\frac{\partial T}{\partial r}\right)\right)$$

where:

$$\kappa_{fb}=\frac{1}{2}\left(\frac{K_f}{c_f\rho_f}+\frac{K_b}{c_b\rho_b}\right)$$

hence:

$$T_i^{n+1}=T_i^n+\frac{\kappa_{fb}\Delta t}{\Delta r^2}\left\{K_bT_{i+1}^n+K_fT_{i-1}^n-(K_f+K_b)T_i^n\right\} \qquad \text{[Eq.B-8]}$$

Condition 6. $r_1 < r < r_2$ $(i_1 < i < \hat{i})$

$$\frac{1}{\kappa_b}\frac{\partial T}{\partial t}=\frac{1}{r}\left(\frac{\partial}{\partial r}\left(r\frac{\partial T}{\partial r}\right)\right)$$

and:

$$T_i^{n+1}=T_i^n+\frac{\kappa_b\Delta t}{\Delta r^2}\left\{\left(1+\frac{1}{2i}\right)T_{i+1}^n+\left(1-\frac{1}{2i}\right)T_{i-1}^n-2T_i^n\right\} \qquad \text{[Eq.B-9]}$$

Condition 7. $r = r_2$ $(i = \hat{i})$

$$T_i^{n+1}=T_s$$

The Crank-Nicholson formulation:

$$\left[\frac{\partial T_i}{\partial t}\right]^n=\frac{1}{2}\left\{\left[\frac{\partial T_i}{\partial t}\right]^n+\left[\frac{\partial T_i}{\partial t}\right]^{n+1}\right\}$$

Moreover:

$$T_i^n = \frac{1}{2}\left(T_i^n + T_i^{n+1}\right)$$

$$T_{i+1}^n = \frac{1}{2}\left(T_{i+1}^n + T_{i+1}^{n+1}\right)$$

Applying the Crank-Nicholson formulation to equations B-4÷B-9 gives:

$$T_i^{n+1} = T_i^n + M_c\left(T_{i+1}^{n+1} + T_{i+1}^n - T_i^n - T_i^{n+1}\right) + M_cH \qquad [\text{Eq.B-10}]$$

$$T_i^{n+1} = T_i^n + \frac{M_c}{2}\left\{\left(1+\frac{1}{2i}\right)\left(T_{i+1}^n + T_{i+1}^{n+1}\right) + \left(1-\frac{1}{2i}\right)\left(T_{i-1}^n + T_{i-1}^{n+1}\right) - 2T_i^n - 2T_i^{n+1}\right\} + M_cH \qquad [\text{Eq.B-11}]$$

$$T_i^{n+1} = T_i^n + \left(T_{i-1}^{n+1} + T_{i-1}^n - 2T_i^n\right) + \frac{M_f}{M_c}\left(T_{i+1}^{n+1} + T_{i+1}^n - T_i^n - T_i^{n+1}\right) + 2H \qquad [\text{Eq.B-12}]$$

$$T_i^{n+1} = T_i^n + \frac{M_f}{2}\left\{\left(1+\frac{1}{2i}\right)\left(T_{i+1}^n + T_{i+1}^{n+1}\right) + \left(1-\frac{1}{2i}\right)\left(T_{i-1}^n + T_{i-1}^{n+1}\right) - 2T_i^n - 2T_i^{n+1}\right\} \qquad [\text{Eq.B-13}]$$

$$T_i^{n+1} = T_i^n + \left(T_{i-1}^{n+1} + T_{i-1}^n - 2T_i^n\right) + \frac{M_b}{M_f}\left(T_{i+1}^{n+1} + T_{i+1}^n - T_i^n - T_i^{n+1}\right) \qquad [\text{Eq.B-14}]$$

$$T_i^{n+1} = T_i^n + \frac{M_b}{2}\left\{\left(1+\frac{1}{2i}\right)\left(T_{i+1}^n + T_{i+1}^{n+1}\right) + \left(1-\frac{1}{2i}\right)\left(T_{i-1}^n + T_{i-1}^{n+1}\right) - 2T_i^n - 2T_i^{n+1}\right\} \qquad [\text{Eq.B-15}]$$

$$T_i^{n+1} = T_s \qquad [\text{Eq.B-16}]$$

where M_c, M_f and M_b are modal parameters:

$$M_c = \frac{\kappa_c \Delta t}{\Delta r^2},\ M_f = \frac{\kappa_f \Delta t}{\Delta r^2},\ M_b = \frac{\kappa_b \Delta t}{\Delta r^2}$$

and H is the Joulean heat generated in the conductor:

$$H = \frac{J^2 \Delta r^2}{\delta_c K_c}$$

Equations B-10÷B-16 are implicit and must be solved numerically. The flow chart for the Crank-Nicholson numerical solution of the transient temperature distribution in the model discussed is shown in Figure B-3.

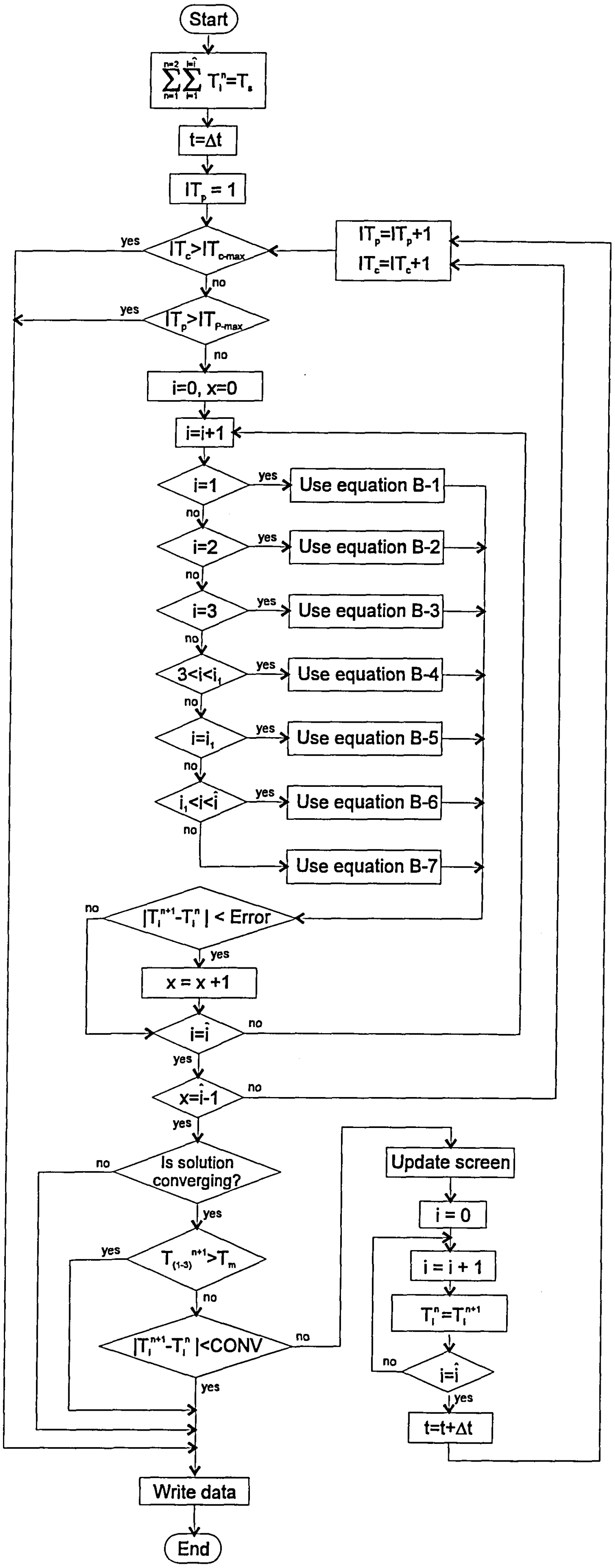

Figure B-3. Flow chart for the numerical solution of the Crank-Nicholson formulation.

Comparison of the Abaqus and PowerFuse Predictions

The I:t characteristics of the wire fuse, produced by the two models, are compared with experimental I:t points in Figure B-4.

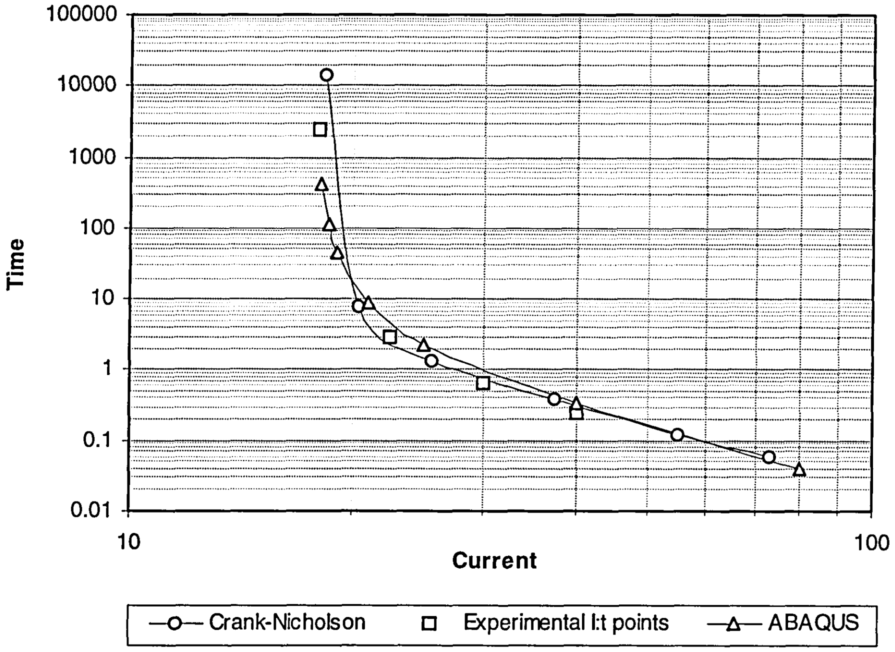

Figure B-4. Comparison of the time-current characteristics.

From Figure B-4 it is observed that the ABAQUS prediction is within acceptable error of the Crank-Nicholson prediction; at all points $\left.\frac{t^{\text{Abaqus}}}{t^{\text{Crank-Nicholson}}}\right|_{I=I_{\text{test}}} < 2$.

Appendix C. Experimental Verification of the Minimum Fusing Current of the Manufactured Substrate Fuse

The experimental verification of the minimum fusing current (MFC) of the manufactured substrate fuse (MSF) was carried out in order to obtain:

- the MFC of the MSF, investigated in Chapter 5, in order to obtain reference 'benchmark current', for the pulsed-current tests;
- the end-cap and the test-rig copper bar temperatures for a range of currents, up to the melting current, to facilitate verification of the accuracy of the ABAQUS electro-thermal predictions (Chapter 5).

The value of the MFC was measured using the experimental set-up shown in Figure C-1. This measurement was carried out using standard test-rig, in accordance with Clause 8.1.4 BS 88 Part 4 [81]. The cross-sectional area of the copper conductors, to which the fuse was fixed, was selected in accordance with Clause 8.3.1, BS 88 Part 4.

Test-Rig Setup

The experimental set-up consisted of the following:

1. Standard test-rig (in accordance with Clause 8.1.4 BS 88 Part 4, copper conductors in accordance with Clause 8.3.1 BS 88 Part 4).
2. Digital thermometers - to measure the temperatures of: i) the top end-cap of the fuse, ii) the test-rig copper bar, 26cm above the fuse terminal; iii) ambient air temperature, approximately 60cm above the fuse; iv) ambient air temperature, 5m away from the fuse.
3. Thermocouple (fixed to the copper bar, 26cm above the fuse terminal).
4. Fuse under test.
5. Six digital ammeters (to ensure that the current in all branches of the resistor bank does not exceed the nominal current).
6. Two analog ammeters (to measure the total current carried by the fuse).
7. Resistor bank (to limit the current carried by the fuse).

A photograph of the test-rig is shown in Figure C-1.

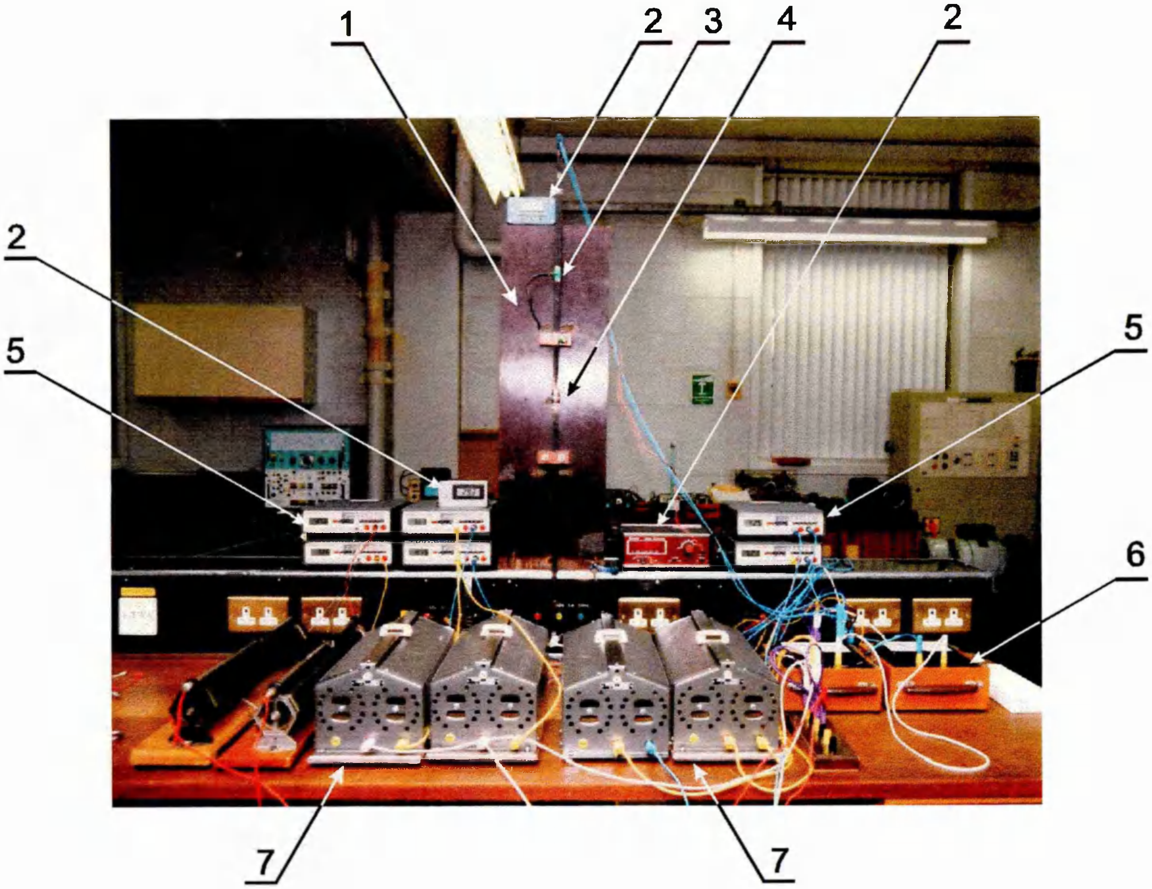

1 – Standard test-rig
2 – Digital thermometer
3 –Thermocouple
4 – Fuse under test
5 – Digital ammeter
6 – Ammeter
7 – Resistor bank

Figure C-1. Experimental set-up for the measurement of the minimum fusing current of the manufactured substrate fuse.

The schematic diagram of the experimental set-up is shown in Figure C-2.

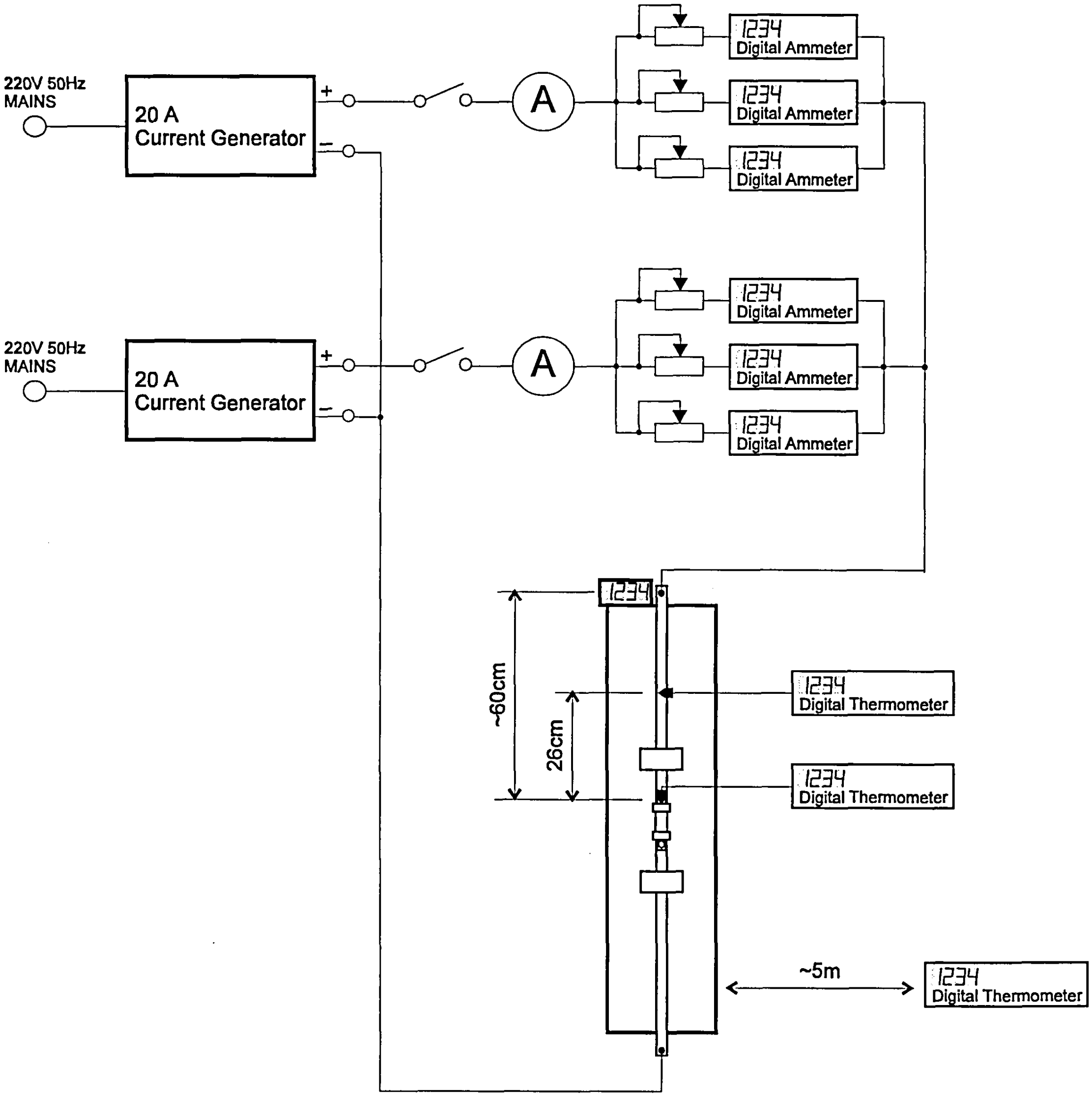

Figure C-2. Schematic diagram of the circuit used for the measurement of the minimum fusing current.

Test Methodology

Initially the resistor bank was set to maximum resistance. At t=0 the circuit was powered up and the resistor bank's resistance was gradually reduced until the current reached 20A, and this value of the current was maintained for one and a half hours. At time instant t=1.5hrs the current was increased by 1A to 21A, and by 1A every half an hour thereafter. The following temperatures were recorded: i) top end-cap temperature; ii) temperature of the test-rig copper bar (26cm above the fuse terminal); iii) ambient air temperature (approx. 60cm above the fuse) and iv) ambient air temperature (approx. 5m away from the test-rig).

Results of the Test

The recorded top end-cap and copper bar temperatures versus current are shown in Figure C-3. Using the experimental data the formulae linking the top end-cap and bar temperatures with fuse current were determined:

$$T_{\text{top end-cap}} = 0.0016 \cdot I^3 - 0.001 \cdot I^2 + 0.0923 \cdot I + 21.6 \qquad \text{[Eq.C-1]}$$

$$T_{\text{connector}} = 0.0159 \cdot I^2 - 0.03 \cdot I + 21.6 \qquad \text{[Eq.C-2]}$$

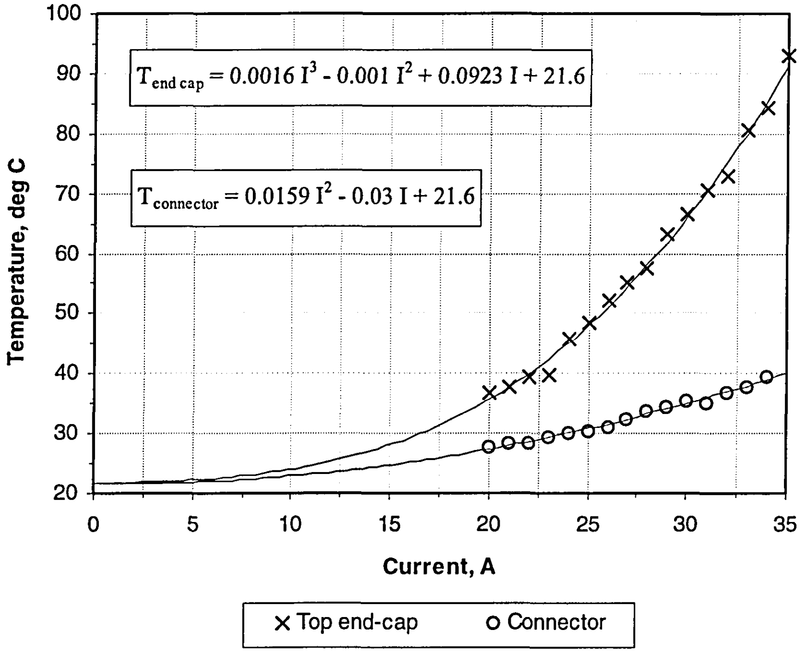

Figure C-3. Top end-cap and copper-bar connector temperatures versus current.

The fuse operated 28 minutes after the current had been adjusted to I_{mfc}=35A.

Results of an Independent Verification of the Minimum Fusing Current of the Manufactured Substrate Fuse

From the results of an independent investigation [82] the value of the minimum fusing current of the 20A manufactured substrate fuse was determined as I_{mfc}=34A.

Appendix D. Computer Programs Written for the Project

Three computer programs were written for this project:

- NodeConv – Node co-ordinates conversion utility;
- Convert – Temperature inter- and extrapolation;
- PowerFuse – Wire fuse performance prediction.

The three programs are described below.

NodeConv – Node co-ordinates conversion utility

NodeConv is a conversion utility which recalculates the X, Y and Z co-ordinates of each node found in the input file. The program was written to facilitate the transition from the output files generated by Patran, to the requirements of the Abaqus input files. The conversion factor is specified by the user. The program can be used to convert from one system of dimensions to another, for example to convert the position of the nodes from *inches* to *millimetres*, a conversion factor of 1/25.4=0.0394 should be used. All insignificant zeroes are omitted from the output file. Additionally, the program can be used to reduce the number of decimal places.

Input file:

FileName.in **Note:** All comment lines must begin with an asterisk ('*').

Field 1:	Column 1-8 :	Node number
Field 2:	Column 10-21:	X co-ordinate
Field 3:	Column 23-34:	Y co-ordinate
Field 4:	Column 36-47:	Z co-ordinate

Characters which separate fields are ignored. An empty field #2, #3 or #4 is translated as 0 (zero).

Output file:

FileName.out **Note:** All comment lines are transferred from the input file to the output file.

Field 1:	Column 1-8:	Node number
Field 2:	Column 10-21:	Converted X co-ordinate
Field 3:	Column 23-34:	Converted Y co-ordinate
Field 4:	Column 36-47:	Converted Z co-ordinate

The last line in the output file is the conversion status message. It reports that the file was either converted successfully or, otherwise, indicates the number of errors found during the conversion.

Example:

The **.in* input file:

```
*NODE
       7,      3018.75,      4.89688
       8,      312.079,       3.5612
       9,      32.2837,      2.26947
      10,      3.64062,      1.01875
      31,      2.83775,       6.8875
      33,      2.14813,      5.89219
*
```

Using a conversion factor of 0.0393 (to convert form *millimetres* to *inches*), and reducing the number of decimal places to four[12], the output file generated by *NodeConv* is presented below:

```
** Node co-ordinate conversion utility.
**
** File converted from C:\NodeConv\test.in
**
*NODE
       7,        118.6,       0.1924,            0
       8,        12.26,       0.1400,            0
       9,        1.269,       0.0892,            0
      10,       0.1431,       0.0400,            0
      31,       0.1115,       0.2707,            0
      33,       0.0844,       0.2316,            0
*
** File converted successfully.
```

The model used was two-dimensional (no values for the 'Z' co-ordinate are present in the **.in* file), hence all the 'Z' co-ordinate values in the **.out* file are equal to zero.

Transcript of the *NodeConv* session:

```
*** Node Co-ordinates File Conversion Program ***
Type input filename: C:\NodeConv\test
Input filename: C:\NodeConv\test.in
Output filename: C:\NodeConv\test.out
Conversion factor: 0.0393
Number of decimal places (min=1 max=8): 4

Converting file...
Processing node number: 33

File converted successfully.
```

---

[12] The *NodeConv* program has a built-in mechanism which proportionally reduces the number of decimal digits for large numbers. The number of decimal digits in the output file is never greater than that requested by the user.

Convert – Temperature extrapolation

Convert is a conversion utility which was written to post-process ABAQUS result files (*.dat). This program interpolates or extrapolates nodal variables, computed by ABAQUS, using a user-defined factor.

Input files:

FileName.out	An ASCII file containing temperatures at all nodes of the finite element model. This file can be generated by editing ABAQUS ASCII results file containing the computed temperatures (*AbqusJobName.dat*). Note: All comment lines should begin with an asterisk.
FileName.nod	An ASCII file containing node numbers which have been retained in the finite element model used for the thermal stress analysis.

Output file:

FileName.con	Output file generated by *Convert.* This file contains extrapolated temperatures at all nodes found in the **.nod* file.

Example:

The **.out* file:

```
*    NODE FOOT-    NT11          EPOT
       10          58.9
       12          53.3
       13          64.6
       26          78.0            0.
       27          94.4            0.
       28          91.6            0.
       29         142.7            0.
       35         152.7            0.
       62         242.7            0.
       76         250.1            0.
**
```

The **.nod* file:

```
*NODE
       26,         4.,       0.075,  0.00999
       27,         4.,     0.05625,  0.00999
       28,         4.,      0.0375,  0.00999
       29,         4.,     0.01875,  0.00999
       35,         4.,   2.693E-9,  0.00800
       62,         4.,   2.693E-9,  0.00800
       76,         4.,   2.693E-9,  0.00800
**
```

Using the **.out* and **.nod* files, and given the interpolation factor of k=0.4, *Convert* generated the **.con* file:

```
** File converted from C:\Convert\test.out
** Maximum temperature in file: 100.0 at node 76
      26,   40.2
      27,   45.9
      28,   44.9
      29,   62.7
      35,   66.1
      62,   97.4
      76,  100.0
**
```

Transcript of the *Convert* session:

```
*** CONVERT ABAQUS Results File Conversion Program ***
Type input filename: C:\Convert\test
Input filename: C:\Convert\test.out
Output filename: C:\Convert\test.con
Required maximum temperature: 100

Searching for maximum temperature in file...
Processing node number: 76
Maximum temperature 250.1 found at node 76

Converting file...
Processing node number: 76

File converted successfully.
```

Nodes #10, #12 and #13 were omitted from the converted **.con* file, because they do not appear in the **.nod* file.

Note: A maximum of 31,500 nodes are allowed in the **.nod* file. For larger FE models the *Convert+* program can be used. The only difference between *Convert* and *Convert+* is such that the *Convert+* program can handle models of unlimited size (up to 99,999,999 nodes). A slower performance, however, is the penalty paid.

PowerFuse – Wire fuse performance prediction

PowerFuse – wire fuse performance prediction computer program – this program was written to enable verification of the accuracy of the Abaqus thermal-electrical predictions (Appendix B). The manual for the program is available in a separate volume [107].

Appendix E. ABAQUS Input Files

Due to the very large size of the ABAQUS input files, some node-set definitions, given in the source codes presented below, were clipped. However, the logical structure and all command definitions were maintained. Since many variations of the finite element models and input files were used during the course of the PhD study, only the primary models are presented in this section.

Abaqus Input Files for the FE Models Analysed in Chapter 4.

Input file for the Thermal-Electrical Analysis:

```
*HEADING

      FE model for the thermal-electrical analysis of a 1-notch
      substrate fuse element.

      Film thickness:       10 um
      Film material:        silver
      Substrate thickness:  0.6 mm
      Substrate material:   Alumina

      NUMBER OF ELEMENTS IS                                        31157
      NUMBER OF NODES IS                                           34164
      NUMBER OF NODES DEFINED BY THE USER                          34164
      TOTAL NUMBER OF VARIABLES IN THE MODEL                       39807
      (DEGREES OF FREEDOM PLUS ANY LAGRANGE MULTIPLIER VARIABLES)
      MAXIMUM D.O.F. WAVEFRONT ESTIMATED AS                         1503
      RMS WAVEFRONT ESTIMATED AS                                    1106

      FILE SIZES - THESE VALUES ARE CONSERVATIVE UPPER BOUNDS

            UNIT          WORDS          MEGABYTES

              2         89378328          715.03
             10          3651336           29.21
             19          3286509           26.29
             21          6449499           51.60
             22          6449499           51.60
             25          7660526           61.28
           -------     -----------      ----------
            TOTAL      116875697          935.01

      IF THE RESTART FILE IS WRITTEN ITS LENGTH WILL BE APPROXIMATELY

                                                                WORDS     MGBS

      WRITTEN IN THE ANALYSIS PREPROCESSOR                     9630629   77.05
      PLUS WRITTEN AT THE BEGINNING OF EACH STEP               8431084   67.45
      PLUS FOR EACH INCREMENT WRITTEN TO THE RESTART FILE      8034007   64.27

**
*PREPRINT, MODEL=NO, HISTORY=NO, ECHO=NO
**
**RESTART, WRITE, OVERLAY
**
*PHYSICAL CONSTANTS, ABSOLUTE ZERO=-273.15
**
**************************************************************************
** Define nodes and elements
**************************************************************************
**
*NODE, INPUT=MM3_NODES, SYSTEM=R
**
*ELEMENT, TYPE=DC3D8, ELSET=FILLER, INPUT=MM3_ELMS_FILLER
**
*ELEMENT, TYPE=DC3D8E, ELSET=FILM_10, INPUT=MM3_ELMS_FILM_10
**
*ELEMENT, TYPE=DC3D8, ELSET=SUBSTRAT, INPUT=MM3_ELMS_SUBSTRAT
**
```

```
************************************************************************
** Define node sets
************************************************************************
**
*NSET, NSET=SYMM_VOLT
    26,     27,     28,     29,     30,     31,     32,     33,     34,     35,    36,
    37,     38,     39,     40,     41,     42,     43,     44,     45,     46,    47,
    48,     49,     50,     51,     52,     53,     54,     55,     56,     57,    58,
    59,     60,     61,     73,     85,     99,    137,    138,    139,    140,   141,
   142,    143,    144,    145,    249,    250,    251,    252,    253,    254,   333,
   346,    359,    416,    417,    418,    419,    420,    421,    422,    423,   424,
   591,    592,    593,    594,    595,    691,    705,    779,    780,    781,   782,
   783,    784,    785,    786,    787,   1000,   1001,   1002,   1003,   1119,  1210,
  1211,   1212,   1213,   1214,   1215,   1216,   1217,   1218,   1487,   1488,  1489,
  1719,   1720,   1721,   1722,   1723,   1724,   1725,   1726,   1727,   2447,  2448,
  2449,   2450,   2451,   2452,   2453,   2454,   2455,   3480,   3481,   3482,  3483,
  3484,   3485,   3486,   3487,   3488,   4576,   4577,   4578,   4579,   4580,  4581,
  4582,   4583,   4584,   5716,   5717,   5718,   5719,   5720,   5721,   5722,  5723,
  5724,   6790,   6791,   6792,   6793,   6794,   6795,   6796,   6797,   6798,  7926,
  7927,   7928,   7929,   7930,   7931,   7932,   7933,   7934,   9009,   9010,  9011,
  9012,   9013,   9014,   9015,   9016,   9017
**
*NSET, NSET=INP_VOLT
      1996,       1997,       2566,       2601,       2636,       2637,       2638,
      2639,       2640,       2641,       2642,       2643,       2644,       2972,
      2973,       2974,       3431,       3616,       3649,       3650,       3651,
      3652,       3653,       3654,       3655,       3656,       3657,       3658,
      3980,       3981,       3982,       3983,       4509,       4510,       4727,
      4728,       4729,       4730,       4731,       4732,       4733,       4734,
      4735,       4736,       4737,       4738,       4739,       4740,       4741,
      4742,       4744,       5631,       5632,       5633,       5880,       5881,
      5882,       5883,       5884,       5885,       5886,       5887,       5888,
      5889,       5890,       5891,       5892,       5893,       5894,       5895,
      5897,       5898,       6687,       6688,       6689,       6690,       6965,
      6966,       6967,       6968,       6969,       6970,       6971,       6972,
      6973,       6974,       6975,       6976,       6977,       6978,       6979,
      6980,       6984,       6985,       6986,       7805,       7806,       7807,
      7808,       7809,       8111,       8112,       8113,       8114,       8115,
      8116,       8117,       8118,       8119,       8120,       8121,       8122,
      8123,       8124,       8125,       8126,       8130,       8131,       8132,
      8133,       8870,       8871,       8872,       8873,       8874,       8875,
      9201,       9202,       9203,       9204,       9205,       9206,       9207,
      9208,       9209,       9210,       9211,       9212,       9213,       9214,
      9215,       9216,       9221,       9222,       9223,       9224,       9225,
     10270,      10271,      10272,      10273,      10274,      10275,      10276,
     10277,      10278,      10279,      10281,      10282,      10283,      10284,
     10285,      11350,      11351,      11352,      11353,      11354,      11355,
     11356,      11357,      11358
**
*NSET, NSET=EXT_NODES
   572,    575,    576,    989,   1005,   1007,   1009,   1010,   1475,   1476,   1479,
  1490,   1501,   1502,   1506,   1995,   2103,   2104,   2112,   2122,   2123,   2125,
  2126,   2127,   2129,   2331,   2380,   2407,   2951,   2971,   3118,   3125,   3126,
      :      :      :      :      :      :      :      :      :      :      :
      :      :      :      :      :      :      :      :      :      :      :
      :      :      :      :      :      :      :      :      :      :      :
 31853,  31854,  31855,  31856,  31861,  31864,  31884,  32421,  32424,  32461,  32464,
 32493,  32609,  32612,  32613,  32616,  32617,  32620,  32621,  32624,  32625,  32626,
 32627,  32628,  32629,  32630,  32631,  32646,  32647,  32648,  32649,  32650,  32651,
 32652,  32659,  33072,  33103,  33188,  33193,  33198,  33203,  33220,  33222,  33226,
**
************************************************************************
** Define properties of solid elements
************************************************************************
**
** FILM_10
**
*SOLID SECTION, ELSET=FILM_10, MATERIAL=SILVER
          1.,
**
** SUBSTRATE
**
*SOLID SECTION, ELSET=SUBSTRAT, MATERIAL=ALUMINA
          1.,
**
** FILLER
**
*SOLID SECTION, ELSET=FILLER, MATERIAL=QUARTZ_S
          1.,
**
************************************************************************
** Define thermal-electrical properties of materials
************************************************************************
**
** SILVER
```

```
**
*MATERIAL, NAME=SILVER
**
** Melting point  961 deg C
** Boiling point 2200 deg C
**
*DENSITY
   10.50E-6,   20.
**
** Following values for the liquid state
    9.35E-6,  961.
**
*CONDUCTIVITY, TYPE=ISO
    0.453,      0.
    0.428,     20.
    0.419,    100.
    0.377,    500.
**
** Following values for the liquid state
    0.175,    961.
    0.176,   1000.
    0.181,   1100.
    0.185,   1200.
    0.189,   1300.
    0.193,   1400.
**
*ELECTRICAL CONDUCTIVITY
  61.73E03,      0.
  59.04E03,     20.
  35.10E03,    200.
  21.10E03,    500.
  13.79E03,    962.
**
** Following values for the liquid state
    6.3E03,    965.
    5.68E3,   1000.
    5.43E3,   1100.
    5.5E03,   1130.
    5.18E3,   1200.
    4.95E3,   1300.
    4.74E3,   1400.
**
*SPECIFIC HEAT
    232.0,      0.
    232.6,     20.
    235.2,    100.
    238.5,    200.
    248.2,    500.
**
** Following values for the liquid state
    263.2,    962.
    283.0,   1100.
    283.0,   1200.
    283.0,   1300.
**
** ALUMINA
**
** Nominal Al O  content 96.5-99.0 %
**          2 3
**
*MATERIAL, NAME=ALUMINA
**
*DENSITY
     3.75E-6,
**
*CONDUCTIVITY, TYPE=ISO
    0.0250,        20.
    0.0200,       100.
    0.0150,       200.
    0.0100,       400.
    0.0081,       600.
    0.0071,       800.
    0.0069,      1000.
    0.0064,      1200.
**
*SPECIFIC HEAT
      780,     25.
      911,    100.
     1023,    200.
     1175,    500.
**
** QUARTZ_SAND
**
*MATERIAL, NAME=QUARTZ_S
**
```

```
*DENSITY
      1.8E-6,
**
*CONDUCTIVITY, TYPE=ISO
    0.000586,
**
*SPECIFIC HEAT
       1176.,
**
******************************************************************************
** Suppress wavefront minimisation
******************************************************************************
**
*WAVEFRONT MINIMIZATION, SUPPRESS
**
******************************************************************************
** Define initial temperatures at nodes
******************************************************************************
**
** Initial_temperature
**
*INITIAL CONDITIONS, TYPE=TEMPERATURE, INPUT=MM3_INITIAL
**
******************************************************************************
** Begin a step
******************************************************************************
**
*STEP, AMPLITUDE=RAMP, INC=100
*COUPLED THERMAL-ELECTRICAL, STEADY STATE
         0.1,          1.
**
******************************************************************************
** Specify fixed boundary conditions (electrical)
******************************************************************************
**
** Symmetry voltage (on symmetry plane)
**
*BOUNDARY, OP=NEW
 SYMM_VOLT,  9,  9,        0.0
**
******************************************************************************
** Inject current
******************************************************************************
**
** 171 nodes on the input surface
** Inode = Isymm / 171 = Itotal / 2 / 171 = Itotal / 342
**
*CECURRENT
   INP_VOLT,  9,   0.130409
**
******************************************************************************
** Specify fixed boundary conditions (thermal)
******************************************************************************
**
** Ambient temperature = 20
**
*BOUNDARY, OP=NEW
 EXT_NODES, 11, 11,         20.
**
******************************************************************************
** Request output
******************************************************************************
**
*NODE PRINT, FREQ=1
NT,  EPOT
**
** Write nodal temperatures to the *.fil file for subsequent
** thermal stress analysis
**
*NODE FILE, FREQ=1
NT,  EPOT
**
*EL PRINT, POSITION=INTEGRATION POINT, FREQ=99
**
*EL FILE, POSITION=INTEGRATION POINT, FREQ=99
**
*EL PRINT, POSITION=NODES, FREQ=0
**
*EL FILE, POSITION=NODES, FREQ=0
**
*EL PRINT, POSITION=CENTROIDAL, FREQ=99
EPG, ECD
ECURS,   ELJD,    NCURS
JENER
HFL
```

```
*EL FILE, POSITION=CENTROIDAL, FREQ=99
EPG, ECD
ECURS,   NCURS
HFL
**
*EL PRINT, POSITION=AVERAGED AT NODES, FREQ=0
**
*EL FILE, POSITION=AVERAGED AT NODES, FREQ=0
**
*ENERGY FILE, FREQ=99
 ALLJD
**
*ENERGY PRINT, FREQ=99
 ALLJD
**
*MODAL PRINT, FREQ=99
**
*MODAL FILE, FREQ=99
**
*PRINT, FREQ=1
**
*END STEP
```

Input file for the Thermal-Stress Analysis:

```
*HEADING

   FE model of a symmetrical part of the 1-notch
   substrate fuse element.

   Thermal stress analysis.

   Units: mm; deg. C; Joule; sec.; kg

   Substrate thickness: 0.6 mm
   Substrate material:  alumina
   1 conductive layer.
   Film thickness:      10 um
   Film material:       silver

   NUMBER OF ELEMENTS IS                              15543
   NUMBER OF NODES IS                                 17946
   NUMBER OF NODES DEFINED BY THE USER                17946
   TOTAL NUMBER OF VARIABLES IN THE MODEL             53838
   (DEGREES OF FREEDOM PLUS ANY LAGRANGE MULTIPLIER VARIABLES)
   MAXIMUM D.O.F. WAVEFRONT ESTIMATED AS               1482
   RMS WAVEFRONT ESTIMATED AS                          1257

   FILE SIZES - THESE VALUES ARE CONSERVATIVE UPPER BOUNDS

     UNIT          WORDS          MEGABYTES

       2         61350829          490.81
      19          5047379           40.38
      21          4756158           38.05
      22          4756158           38.05
    ----      ----------       ----------
   TOTAL        75910524          607.28

   IF THE RESTART FILE IS WRITTEN ITS LENGTH WILL BE APPROXIMATELY

                                                         WORDS     MEGABYTES
                                                       ---------   ---------
   WRITTEN IN THE ANALYSIS PREPROCESSOR                  1350335       10.80
   PLUS WRITTEN AT THE BEGINNING OF EACH STEP             376140        3.01
   PLUS FOR EACH INCREMENT WRITTEN TO THE RESTART FILE   5804266       46.43

**
*PREPRINT, MODEL=NO, HISTORY=NO, ECHO=NO
**
*PHYSICAL CONSTANTS, ABSOLUTE ZERO=-273.15
**
*RESTART, WRITE, OVERLAY
**
***********************************************************************
** Define nodes and elements
***********************************************************************
**
*NODE, INPUT=MM3_STR_NODES, SYSTEM=R
**
*ELEMENT, TYPE=C3D8, ELSET=FILM_10, INPUT=MM3_STR_ELMS_FILM_10
**
```

```
*ELEMENT, TYPE=C3D8, ELSET=SUBSTRAT, INPUT=MM3_STR_ELMS_SUBSTRAT
**
***********************************************************************
** Define node sets
***********************************************************************
**
*NSET, NSET=FIX_Z
 2973, 2974, 3616,  3649,  3650,  3651,  3652,  3653,  3654,  3655,  3656,  3657,  3658,
 3980, 3981, 3982,  3983,  4509,  4727,  4728,  4729,  4730,  4731,  4732,  4733,  4734,
 4735, 4736, 4737,  4738,  4739,  4740,  4741,  4742,  4744,  5631,  5632,  5880,  5881,
 5882, 5883, 5884,  5885,  5886,  5887,  5888,  5889,  5890,  5891,  5892,  5893,  5894,
 5895, 5897, 5898,  6687,  6688,  6689,  6965,  6966,  6967,  6968,  6969,  6970,  6971,
 6972, 6973, 6974,  6975,  6976,  6977,  6978,  6979,  6980,  6984,  6985,  6986,  7805,
    :    :    :      :      :      :      :      :      :      :      :      :      :
    :    :    :      :      :      :      :      :      :      :      :      :      :
    :    :    :      :      :      :      :      :      :      :      :      :      :
25294,25296,25298, 25299, 25300, 26384, 26402, 26408, 26414, 26417, 26420, 26423, 26426,
26429,26430,26431, 27580, 27599, 27616, 27623, 27630, 27634, 27638, 27642, 27646, 27647,
27648,28014,28293, 28707, 28725, 28741, 28749, 28757, 28762, 28763, 28764, 28765, 28766,
29113,29717,29735, 29751, 29761, 29771, 29778, 29780, 29781, 29782
**
*NSET, NSET=FIX_YZ
 1996, 1996, 1997,  1997,  2566,  2566,  2601,  2601,  2636,  2636,  2637,  2637,  2638,
 2638, 2639, 2639,  2640,  2640,  2641,  2641,  2642,  2642,  2643,  2643,  2644,  2644,
 3431, 3431, 4510,  4510,  5633,  5633,  6690,  6690,  7809,  7809,  8875,  8875,  9911,
 9911,10983,10983, 12083, 12083, 13183, 13183, 14283, 14283, 15498, 15498, 16674, 16674,
16696,16696,16716, 16716, 16734, 16734, 16746, 16746, 16758, 16758, 16770, 16770, 17977,
17977,19138,19138, 20107, 20107, 21085, 21085, 22085, 22085, 23102, 23102, 23111, 23111,
23118,23118,24109, 24109, 25301, 25301, 26432, 26432, 27649, 27649, 28767, 28767, 29783
**
*NSET, NSET=FIX_Y
   67,   68,   69,    70,    71,    72,   160,   173,   184,   193,   200,   205,   220,
  235,  296,  306,   314,   324,   325,   326,   327,   328,   329,   330,   331,   332,
  440,  454,  466,   476,   484,   490,   494,   509,   524,   539,   554,   555,   556,
  557,  558,  559,   560,   561,   562,   563,   564,   565,   804,   819,   832,   843,
  852,  859,  864,   867,   882,   897,   912,   927,   942,   957,   958,   959,   960,
    :    :    :      :      :      :      :      :      :      :      :      :      :
    :    :    :      :      :      :      :      :      :      :      :      :      :
    :    :    :      :      :      :      :      :      :      :      :      :      :
33669,33678,33683, 33684, 33697, 33701, 33711, 33714, 33721, 33723, 33727, 33728, 33729,
33846,33851,33852, 33926, 33931, 33932, 33942, 33945, 33952, 33954, 33958, 33959, 33960,
34031,34032,34073, 34074, 34081, 34083, 34087, 34088, 34089, 34124, 34140, 34144, 34145
**
*NSET, NSET=FIX_XY
      30,    30,    35,    35,     52,     52,     54,     54,     58,     58,
      59,    59,    60,    60,    145,    145,    424,    424,    787,    787,
    1218,  1218,  1727,  1727,   2455,   2455,   3488,   3488,   4584,   4584,
    5724,  5724,  6798,  6798,   7934,   7934,   9017,   9017,  10070,  10070,
   11159, 11159, 12277, 12277,  13395,  13395,  14513,  14513,  15764,  15764,
   17054, 17054, 18344, 18344,  19482,  19482,  20430,  20430,  21401,  21401,
   22382, 22382, 23402, 23402,  24395,  24395,  25545,  25545,  26636,  26636,
   27815, 27815, 28905, 28905,  29941,  29941,  29968,  29968,  29993,  29993,
   30014, 30014, 30031, 30031,  30044,  30044,  30053,  30053,  30058,  30058,
   30059, 30059
**
*NSET, NSET=FIX_X
     26,    27,    28,    29,    31,    32,    33,    34,    36,    37,    38,    39,
     40,    41,    42,    43,    44,    45,    46,    47,    48,    49,    50,    51,
     53,    55,    56,    57,    61,    73,    85,    99,   137,   138,   139,   140,
    141,   142,   143,   144,   249,   250,   251,   252,   253,   254,   333,   346,
    359,   416,   417,   418,   419,   420,   421,   422,   423,   591,   592,   593,
  29384, 29385, 29386, 29387, 29388, 29389, 29393, 29394, 29395, 29886, 29887, 29888,
      :      :      :      :      :      :      :      :      :      :      :      :
      :      :      :      :      :      :      :      :      :      :      :      :
      :      :      :      :      :      :      :      :      :      :      :      :
  29889, 29890, 29892, 29894, 29895, 29897, 29913, 29914, 29915, 29916, 29918, 29920,
  29922, 29924, 29925, 29934, 29935, 29936, 29937, 29938, 29939, 29940, 29942, 29943,
  29945, 29947, 29949, 29951, 29953, 29954, 29962, 29963, 29964, 29965, 29966, 29967,
  29970, 29972, 29974, 29976, 29978, 29980, 29981, 29988, 29989, 29990, 29991, 29992,
  29995, 29997, 29999, 30001, 30003, 30004, 30010, 30011, 30012, 30013, 30016, 30018,
  30020, 30022, 30023, 30028, 30029, 30030, 30033, 30035, 30037, 30038, 30042, 30043,
  30046, 30048, 30049, 30052, 30055, 30056,
**
***********************************************************************
** Minimize the wavefront
***********************************************************************
**
*WAVEFRONT MINIMIZATION, NODES, METHOD=1
    30,   28390
**
***********************************************************************
** Define properties for solid elements
***********************************************************************
**
** FILM_10
```

```
**
*SOLID SECTION, ELSET=FILM_10, MATERIAL=SILVER
          1.,
**
** SUBSTRATE
**
*SOLID SECTION, ELSET=SUBSTRAT, MATERIAL=ALUMINA
          1.,
**
**************************************************************************
** Define mechanical properties of materials
**************************************************************************
**
*MATERIAL, NAME=SILVER
**
*DENSITY
      0.0105,
**
*ELASTIC, TYPE=ISO
**
** Yield stress:     29.4 MPa at 20 deg C
** Tensile strength: 300  MPa for commercial fine silver annealed at 100 deg.C
**                   Other sources: 177 MPa at 20 deg C
**
**  Young's Modulus  Poisson's ratio   Temperature
      80000.,        0.37,         20.
      66700.,        0.37,        400.
      35300.,        0.37,        960.
**
*EXPANSION, TYPE=ISO, ZERO=20.
    1.862E-5,         20.
    1.945E-5,        100.
     2.05E-5,        300.
    2.158E-5,        500.
      2.4E-5,        700.
     2.65E-5,        900.
    2.785E-5,       1000.
**
**
*MATERIAL, NAME=ALUMINA
**
*DENSITY
     0.00382,
**
*ELASTIC, TYPE=ISO
**
**  Young's Modulus  Poisson's ratio   Temperature
     340000.,           0.238,            0.
     333000.,           0.241,          200.
     325000.,           0.242,          400.
     316000.,           0.248,          600.
     308000.,           0.25,           800.
**
*EXPANSION, TYPE=ISO, ZERO=20.
      6.0E-6,         20.
      6.4E-6,        100.
      7.1E-6,        200.
      7.8E-6,        300.
      8.2E-6,        400.
      8.4E-6,        500.
      8.6E-6,        600.
      9.4E-6,        800.
      9.8E-6,       1000.
     1.01E-5,       1200.
     1.03E-5,       1400.
**
******************************************************************************
** Begin a step
******************************************************************************
**
*STEP, AMPLITUDE=RAMP, INC=100
**
*STATIC
   0.1,       0.1
**
******************************************************************************
** Read temperatures at nodes from file
******************************************************************************
**
*TEMPERATURE, INPUT=MM3_ALU.CON
**
******************************************************************************
** Fix model in space
******************************************************************************
**
```

```
*BOUNDARY, OP=NEW
    FIX_Z, 3,,     0.
**
******************************************************************************
** Fix model on symmetry planes
******************************************************************************
**
*BOUNDARY, OP=NEW
    FIX_YZ, 2,3,    0.
**
*BOUNDARY, OP=NEW
    FIX_Y, 2, ,     0.
**
*BOUNDARY, OP=NEW
    FIX_XY, 1,2,    0.
**
*BOUNDARY, OP=NEW
   FIX_X, 1, ,      0.
**
******************************************************************************
** Request output
******************************************************************************
**
*NODE PRINT,  FREQ=0
U
CF
*NODE FILE,  FREQ=0
U
CF
**
*EL PRINT,  POSITION=INTEGRATION POINT,  FREQ=0
S
E
*EL FILE,  POSITION=INTEGRATION POINT,  FREQ=0
S
E
**
*EL PRINT,  POSITION=NODES,  FREQ=0
S
*EL PRINT,  FREQ=0
NFORC
*EL FILE,  POSITION=NODES,  FREQ=0
*EL FILE,  FREQ=0
NFORC
**
*EL PRINT,  POSITION=CENTROIDAL,  FREQ=0
ENER
ELEN
*EL FILE,  POSITION=CENTROIDAL,  FREQ=0
ENER
ELEN
**
*EL PRINT,  POSITION=AVERAGED AT NODES,  FREQ=0
**
*EL FILE,  POSITION=AVERAGED AT NODES,  FREQ=0
**
*MODAL PRINT,  FREQ=0
**
*MODAL FILE,  FREQ=0
**
*ENERGY PRINT,  FREQ=0
**
*ENERGY FILE,  FREQ=0
**
*PRINT,  FREQ=0
**
*END STEP
```

Abaqus Input Files for the FE Models Analysed in Chapter 5.

Input file for the thermal-electrical analysis:

```
*HEADING

  ABAQUS input file for the:
  Thermal-electrical analysis of the manufactured substrate fuse.

  Finite element model in accordance with the MSF_standard_NewBar FE model.

  Convection is allowed on all external surfaces
  (body, end_cap, terminal, bar).

  Heat sink is provided at the far end of the bar.
  The heat sink temperature can be varied.

  Electrical current is supplied at all nodes at the far end of the bar.

  Current waveform (PulseLoad #6) : ton=0.73s, toff=0.73s, Ion=40A, Ioff=0A

  HotStart initial conditions, i.e. temperature distribution at all nodes
  at t=0 is same as under steady-state conditions, for Irms=28.3A.

  All units are 'SI' units except for 'millimetre' and 'Celsius'.

  All node co-ordinates translated to 'millimetres'.

  Film thickness:        15  um
  Substrate thickness:   0.6 mm
  Film material:         COPPER
  Substrate material:    ALUMINA
  Filler material:       QSAND
  Body material:         ALUMINA
  Fuse contact material: ALUMINIUM BRASS
  End cap material:      ALUMINIUM BRASS
  Terminal material:     ALUMINIUM BRASS
  Bar material:          COPPER

          ====================================
          PROBLEM SIZE Standard-mesh FE model:
          ====================================

          NUMBER OF ELEMENTS IS                              19369
          NUMBER OF NODES IS                                 21864
          NUMBER OF NODES DEFINED BY THE USER                21864
          TOTAL NUMBER OF VARIABLES IN THE MODEL             29692
          (DEGREES OF FREEDOM PLUS ANY LAGRANGE MULTIPLIER VARIABLES)
          MAXIMUM D.O.F. WAVEFRONT ESTIMATED AS                991
          RMS WAVEFRONT ESTIMATED AS                           650

          FILE SIZES - THESE VALUES ARE CONSERVATIVE UPPER BOUNDS

            UNIT         WORDS          MEGABYTES

              2         31531756          252.25
             19          2590027           20.72
             21          4009383           32.08
             22          4009383           32.08
          -------      ----------      ----------
           TOTAL        42140549          337.12

          IF THE RESTART FILE IS WRITTEN ITS LENGTH WILL BE APPROXIMATELY

                                                            WORDS      MEGABYTES
                                                          ---------    ---------
          WRITTEN IN THE ANALYSIS PREPROCESSOR             1461922        11.70
          PLUS WRITTEN AT THE BEGINNING OF EACH STEP        596565         4.77
          PLUS FOR EACH INCREMENT WRITTEN TO THE RESTART FILE  5035684    40.29

          ================================
          PROBLEM SIZE Fine-mesh FE model:
          ================================

          NUMBER OF ELEMENTS IS                              56171
          NUMBER OF NODES IS                                 59924
          NUMBER OF NODES DEFINED BY THE USER                59924
          TOTAL NUMBER OF VARIABLES IN THE MODEL             73750
          (DEGREES OF FREEDOM PLUS ANY LAGRANGE MULTIPLIER VARIABLES)
          MAXIMUM D.O.F. WAVEFRONT ESTIMATED AS               2802
```

```
          RMS WAVEFRONT ESTIMATED AS                          1806

          FILE SIZES - THESE VALUES ARE CONSERVATIVE UPPER BOUNDS

            UNIT          WORDS          MEGABYTES

              2       268789392          2150.32
             10         6893478            55.15
             19         6448425            51.59
             21        11627397            93.02
             22        11627397            93.02
             25         1400179            11.20
          -------    ----------       ----------
           TOTAL      306786268          2454.29

          IF THE RESTART FILE IS WRITTEN ITS LENGTH WILL BE APPROXIMATELY

                                                                 WORDS     MEGABYTES
                                                                ---------   ---------
          WRITTEN IN THE ANALYSIS PREPROCESSOR                    3885502       31.08
          PLUS WRITTEN AT THE BEGINNING OF EACH STEP              1544702       12.36
          PLUS FOR EACH INCREMENT WRITTEN TO THE RESTART FILE    14504024      116.03


*PREPRINT, MODEL=NO, HISTORY=NO, ECHO=NO
**
*RESTART, WRITE, OVERLAY
**
*PHYSICAL CONSTANTS, ABSOLUTE ZERO=-273.15
**
**************************************************************************
** Define nodes and elements
**************************************************************************
**
*NODE, INPUT=MSF_NODES, SYSTEM=R
**
*ELEMENT, TYPE=DC3D8E, ELSET=FILM_15, INPUT=MSF_ELMS_FILM_15
*ELEMENT, TYPE=DC3D8, ELSET=SUBSTRAT, INPUT=MSF_ELMS_SUBSTRAT
*ELEMENT, TYPE=DC3D8, ELSET=FILLER, INPUT=MSF_ELMS_FILLER
*ELEMENT, TYPE=DC3D8, ELSET=BODY, INPUT=MSF_ELMS_BODY
*ELEMENT, TYPE=DC3D8E, ELSET=END_CAP, INPUT=MSF_ELMS_END_CAP
*ELEMENT, TYPE=DC3D8E, ELSET=TERMINAL, INPUT=MSF_ELMS_TERMINAL
*ELEMENT, TYPE=DC3D8E, ELSET=CONTACT, INPUT=MSF_ELMS_CONTACT
*ELEMENT, TYPE=DC3D8E, ELSET=BAR, INPUT=MSF_ELMS_BAR
**
**************************************************************************
** Minimize the wavefront
**************************************************************************
**
*WAVEFRONT MINIMIZATION, NODES, METHOD=3
        20535,   25818
**
**************************************************************************
** Define node sets
**************************************************************************
**
** All nodes excluding those in the bar
**
*NSET, NSET=ALLEXBAR, GENERATE
  1, 21012
**
** All nodes in the bar
**
*NSET, NSET=ALLINBAR, GENERATE
  25000, 25851
**
** All nodes at the far end of the bar
**
*NSET, NSET=BAR_END, GENERATE
   25814,   25851,       1
**
**************************************************************************
** Define element faces in the bar on which convection/radiation is
** allowed. (Only new element faces after mesh refinement).
**************************************************************************
**
*ELSET, ELSET=BAR_CO_1, GENERATE
   25203,   25472,       1
**
*ELSET, ELSET=BAR_CO_2
   25220,   25238,   25256,   25274,   25292,   25310,   25328,   25346,
   25364,   25382,   25400,   25418,   25436,   25454,    25472
**
*ELSET, ELSET=BAR_CO_3, GENERATE
   25203,   25472,       1
```

```
**
**************************************************************************
** Define properties of solid elements
**************************************************************************
**
** Conductive film
**
*SOLID SECTION, ELSET=FILM_15, MATERIAL=COPPER
          1.,
**
** Substrate
**
*SOLID SECTION, ELSET=SUBSTRAT, MATERIAL=ALUMINA
          1.,
**
** Filler
**
*SOLID SECTION, ELSET=FILLER, MATERIAL=QSAND
          1.,
**
** Fuse body
**
*SOLID SECTION, ELSET=BODY, MATERIAL=ALUMINA
          1.,
**
** End cap
**
*SOLID SECTION, ELSET=END_CAP, MATERIAL=BRASS
          1.,
**
** Terminal
**
*SOLID SECTION, ELSET=TERMINAL, MATERIAL=BRASS
          1.,
**
** Fuse contact
**
*SOLID SECTION, ELSET=CONTACT, MATERIAL=BRASS
          1.,
**
** Bar
**
*SOLID SECTION, ELSET=BAR, MATERIAL=COPPER
          1.,
**
**************************************************************************
** Define thermal-electrical properties of materials
**************************************************************************
**
*MATERIAL, NAME=COPPER
**
** Melting point 1083 deg C
** Boiling point 2560 deg C
**
*DENSITY
    8.89E-6,    0.
    8.84E-6,  100.
    8.80E-6,  200.
    8.65E-6,  500.
    8.48E-6,  800.
    8.33E-6, 1082.
**
** Following values for the liquid state
    8.00E-6, 1083.
**
*CONDUCTIVITY, TYPE=ISO
    0.403,      0.
    0.401,     25.
    0.395,    100.
    0.389,    200.
    0.341,    538.
    0.244,   1037.
    0.230,   1082.
**
** Following values for the liquid state
    0.166,   1083.
    0.170,   1200.
    0.176,   1400.
    0.180,   1600.
**
*ELECTRICAL CONDUCTIVITY
  62.89E03,      0.
  43.86E03,    100.
  33.56E03,    200.
  19.30E03,    500.
```

```
  13.28E03,    800.
  10.91E03,   1000.
  10.12E03,   1082.
**
** Following values for the liquid state
   5.00E03,   1083.
   4.72E03,   1200.
   4.29E03,   1400.
   3.95E03,   1600.
**
*SPECIFIC HEAT
    380,      0.
    382,     20.
    393,    100.
    406,    200.
    446,    500.
    519,    962.
**
** Following values for the liquid state
**
** Aluminium brass
**
*MATERIAL, NAME=BRASS
**
*DENSITY
    8.55E-6,   20
**
*CONDUCTIVITY, TYPE=ISO
    0.103,      0.
    0.101,     25.
    0.099,    100.
    0.097,    200.
    0.085,    538.
    0.061,   1010.
**
*ELECTRICAL CONDUCTIVITY
  20.12E03,      0.
  19.42E03,     20.
  17.00E03,    100.
  14.62E03,    200.
  10.06E03,    500.
   7.46E03,    800.
   6.29E03,   1000.
**
*SPECIFIC HEAT
**
    360,      0.
    385,     20.
    487,    100.
    616,    200.
   1017,    500.
   1728,   1000.
**
** ALUMINA
**
** Nominal Al O  content 96.5-99.0 %
**          2 3
**
*MATERIAL, NAME=ALUMINA
**
*DENSITY
     3.75E-6,
**
*CONDUCTIVITY, TYPE=ISO
    0.0250,        20.
    0.0200,       100.
    0.0150,       200.
    0.0100,       400.
    0.0081,       600.
    0.0071,       800.
    0.0069,      1000.
    0.0064,      1200.
**
*SPECIFIC HEAT
      780,     25.
      911,    100.
     1023,    200.
     1175,    500.
**
** QUARTZ SAND
**
*MATERIAL, NAME=QSAND
**
*DENSITY
      1.8E-6,
```

```
**
*CONDUCTIVITY, TYPE=ISO
  0.00078,     27.
  0.00073,    127.
  0.00070,    227.
  0.00066,    327.
  0.00061,    427.
  0.00057,    527.
  0.00051,    627.
  0.00048,    727.
  0.00045,    827.
  0.00043,    927.
**
*SPECIFIC HEAT
       1176.,
**
***************************************************************************
** Define film properties to allow convection on external surfaces
***************************************************************************
**
** Film property for fuse body (alumina)
**
*FILM PROPERTY, NAME=FILMA
    5E-6,   20.0
   12E-6,   70.0
   16E-6,  150.0
**
** Film property for end cap and terminal (zinc coated brass)
**
*FILM PROPERTY, NAME=FILMB
    5E-6,   20.0
   12E-6,   70.0
   16E-6,  150.0
**
** Film property for the bar (black painted copper)
**
*FILM PROPERTY, NAME=FILMC
    6E-6,   20.0
   14E-6,   70.0
   19E-6,  150.0
**
***************************************************************************
** Define initial temperatures at all nodes
***************************************************************************
**
** This option to be used for 'cold-start' analysis.
**
**INITIAL CONDITIONS, TYPE=TEMPERATURE
** ALLEXBAR,   21.6
**
**INITIAL CONDITIONS, TYPE=TEMPERATURE
**  ALLINBAR,  21.6
**
** This option to be used for 'hot-start' analysis. Irms=28.3A
**
*INITIAL CONDITIONS, TYPE=TEMPERATURE, INPUT=y_standard_NewBar_film15_nt11.nod
**
***************************************************************************
** Define the loading curve for current
***************************************************************************
**
** Load: PulLoad6: ton=0.73s, toff=0.73s, Ion=40A
**
*AMPLITUDE, NAME=PulLoad6, DEFINITION=TABULAR, SMOOTH=0.05
     0.001,  1,      0.73,  1,     0.731,  0,    1.46,  0,
     1.461,  1,      2.19,  1,     2.191,  0,    2.92,  0,
     2.921,  1,      3.65,  1,     3.651,  0,    4.38,  0,
     4.381,  1,      5.11,  1,     5.111,  0,    5.84,  0,
     5.841,  1,      6.57,  1,     6.571,  0,     7.3,  0,
         :   :          :   :          :   :        :   :
         :   :          :   :          :   :        :   :
         :   :          :   :          :   :        :   :
   773.801,  1,    774.53,  1,   774.531,  0,  775.26,  0,
   775.261,  1,    775.99,  1,   775.991,  0,  776.72,  0,
   776.721,  1,    777.45,  1,   777.451,  0,  778.18,  0,
   778.181,  1,    778.91,  1,   778.911,  0,  779.64,  0,
   779.641,  1,    780.37,  1,   780.371,  0,   781.1,  0,
**
***************************************************************************
** Define the variation of the heat sink temperature with time.
***************************************************************************
**
*AMPLITUDE, NAME=SINK, DEFINITION=TABULAR, SMOOTH=0.05
   0,   1.0,    1.0,    1.0
**
```

```
***************************************************************************
** Define the curve for T (bar_end) := f (time)
***************************************************************************
**
** Temperature T=39.4 deg C was found during the MFC test of the MSF
** and is only valid for I=Imfc=35A.
**
** The following option to be used with transient analysis (I=Imfc):
**
*AMPLITUDE, NAME=BAR_END1, DEFINITION=TABULAR, SMOOTH=0.05
    0,  21.6,   500,    37,   1000,   38,   3000,    39.4
**
** The following option to be used with steady-state analysis:
** when I(t=0)=0
**
*AMPLITUDE, NAME=BAR_END2, DEFINITION=TABULAR, SMOOTH=0.05
    0,  21.6,   1.0,    39.4
**
** The following option to be used with steady-state analysis:
** when I(t=0)=0.7 x Itotal
**
*AMPLITUDE, NAME=BAR_END3, DEFINITION=TABULAR, SMOOTH=0.05
    0,  29.5,   1.0,    39.4
**
** The following option to be used with steady-state analysis (load I_2):
** when I(t=0)=0.8 x Itotal
**
*AMPLITUDE, NAME=BAR_END4, DEFINITION=TABULAR, SMOOTH=0.05
    0,  33.2,   1.0,    39.4
**
** The following option to be used with load I_1 i.e. I(t=0)=0.85xI_mfc
**
*AMPLITUDE, NAME=BAR_END5, DEFINITION=TABULAR, SMOOTH=0.05
    0,  35,   1.0,    39.4
**
** The following option to be used with transient analysis (Irms=28.3):
**
*AMPLITUDE, NAME=BAR_END6, DEFINITION=TABULAR, SMOOTH=0.05
    0,  21.6,   500,    31.4,   1000,   32.3,   3000,    33.5
**
***************************************************************************
** Begin a step
***************************************************************************
**
*STEP, INC=1000
   Step 1. Joule heating analysis
**
** Transient analysis
**
*COUPLED THERMAL-ELECTRICAL, DELTMX=350, END=PERIOD
   0.24333333,    1800,     0.24333333,    0.24333333
**
** Steady-state analysis
**
**COUPLED THERMAL-ELECTRICAL, STEADY STATE
**    0.1,   1.0,   0.001,    0.1
**
***************************************************************************
** Adjust {CONTROLS} to address the problem of highly non-linear analysis
***************************************************************************
**
*CONTROLS, PARAMETERS=TIME INCREMENTATION
   10,    12,     9,    16,    10,      1,  12,      5,      6,    6
  0.5,  0.5,   0.5,  0.85,  0.5,  0.25,   1,  0.75
  0.8,     1,  1.25,     1,     1,   0.1,    1,     1,  0.95
**
***************************************************************************
** Specify fixed boundary conditions
***************************************************************************
**
** Set symmetry voltage to 0 Volts
**
*BOUNDARY, OP=NEW
    6685,  9,  9,          0.0
    6687,  9,  9,          0.0
    6689,  9,  9,          0.0
    6699,  9,  9,          0.0
    6802,  9,  9,          0.0
        :  :   :             :
        :  :   :             :
        :  :   :             :
   10950,  9,  9,          0.0
   10955,  9,  9,          0.0
   10958,  9,  9,          0.0
   10960,  9,  9,          0.0
```

```
   20628,  9,  9,         0.0
**
** Inject current at 38 nodes
**
** Total current: 40 A / 2 = 20 / 38 = 0.526315
**
*CECURRENT, AMPLITUDE=PulLoad6, OP=NEW
    BAR_END,  9,     0.526316
**
** Total No of nodes at bar end: 38
**
** Provide heat sink at far end of the bar
**
**BOUNDARY, OP=NEW, AMPLITUDE=BAR_END6
**   BAR_END,  11,   11,      1.0
**
** The following option to be used for 'hot-start' analysis, for I=28.3A
**
*BOUNDARY, OP=NEW
   BAR_END,  11,   11,    33.5
**
**************************************************************************
** Define element faces on which convection is allowed
**************************************************************************
**
** Convection on the surfaces of the bar
**
*FILM, AMPLITUDE=SINK, OP=NEW
      25000,   F2,    21.6,   FILMC
      25000,   F5,    21.6,   FILMC
      25001,   F2,    21.6,   FILMC
      25001,   F5,    21.6,   FILMC
      25002,   F2,    21.6,   FILMC
           :     :        :       :
           :     :        :       :
           :     :        :       :
      25002,   F5,    21.6,   FILMC
      25201,   F4,    21.6,   FILMC
      25201,   F6,    21.6,   FILMC
      25202,   F3,    21.6,   FILMC
      25202,   F4,    21.6,   FILMC
      25202,   F6,    21.6,   FILMC
**
   BAR_CO_1,   F3,    21.6,   FILMC
   BAR_CO_2,   F4,    21.6,   FILMC
   BAR_CO_3,   F5,    21.6,   FILMC
**
** Body - convection
**
*FILM, AMPLITUDE=SINK, OP=NEW
    5145, F2,    21.6,   FILMA
    5146, F2,    21.6,   FILMA
    5168, F2,    21.6,   FILMA
    5175, F2,    21.6,   FILMA
       :   :        :        :
       :   :        :        :
       :   :        :        :
   16763, F2,    21.6,   FILMA
   16764, F2,    21.6,   FILMA
   16765, F2,    21.6,   FILMA
   16766, F2,    21.6,   FILMA
   16767, F2,    21.6,   FILMA
**
** End cap and terminal - convection
**
*FILM, AMPLITUDE=SINK, OP=NEW
    1821, F2,    21.6,   FILMB
    1822, F2,    21.6,   FILMB
    1823, F2,    21.6,   FILMB
    1824, F2,    21.6,   FILMB
    1825, F2,    21.6,   FILMB
       :   :        :        :
       :   :        :        :
       :   :        :        :
   18129, F2,    21.6,   FILMB
   18130, F2,    21.6,   FILMB
   18130, F4,    21.6,   FILMB
   18131, F2,    21.6,   FILMB
   18131, F4,    21.6,   FILMB
**
**************************************************************************
** Request output
**************************************************************************
**
*NODE PRINT, FREQ=1
```

```
NT,      EPOT
**
*NODE FILE, FREQ=1
NT,      EPOT
**
*EL PRINT, POSITION=INTEGRATION POINT, FREQ=99
**
*EL FILE, POSITION=INTEGRATION POINT, FREQ=99
**
*EL PRINT, POSITION=NODES, FREQ=0
**
*EL FILE, POSITION=NODES, FREQ=0
**
*EL PRINT, POSITION=CENTROIDAL, FREQ=99
EPG,     ECD
ECURS,   ELJD,    NCURS
JENER
HFL
*EL FILE, POSITION=CENTROIDAL, FREQ=99
EPG,     ECD
ECURS,   NCURS
HFL
**
*EL PRINT, POSITION=AVERAGED AT NODES, FREQ=0
**
*EL FILE, POSITION=AVERAGED AT NODES, FREQ=0
**
*ENERGY FILE, FREQ=99
 ALLJD
**
*ENERGY PRINT, FREQ=99
 ALLJD
**
*MODAL PRINT, FREQ=99
**
*MODAL FILE, FREQ=99
**
*PRINT, FREQ=1
**
*END STEP
```

Input file for the thermal-stress analysis:

```
*HEADING

     Thermal stress analysis of a symmetrical part of the
     manufactured substrate fuse element.

     Units: mm; deg. C; Joule; sec.; kg

     Finite element mesh in accordance with the FE model: MSF_fine.db

     Only the conductive film and the substrate were retained
     for the thermal stress analysis.

     No of nodes:       26683
     No of elements:    23507

     Substrate thickness:  0.6 mm
     Substrate material:   ALUMINA

     Film thickness:       15 um
     Film material:        COPPER

     Pulse Load #6:

     Two-STEP analysis: thermal stress T= 20 --> T=101 deg C,
                           followed by T=101 --> T= 83 deg C.

     NUMBER OF ELEMENTS IS                                23507
     NUMBER OF NODES IS                                   26683
     NUMBER OF NODES DEFINED BY THE USER                  26683
     TOTAL NUMBER OF VARIABLES IN THE MODEL               80049
     (DEGREES OF FREEDOM PLUS ANY LAGRANGE MULTIPLIER VARIABLES)
     MAXIMUM D.O.F. WAVEFRONT ESTIMATED AS                 2862
     RMS WAVEFRONT ESTIMATED AS                            2166

     FILE SIZES - THESE VALUES ARE CONSERVATIVE UPPER BOUNDS

       UNIT          WORDS           MEGABYTES

         2        173303941           1386.43
```

```
        19        7635679              61.09
        21        8885646              71.09
        22        8885646              71.09
     -------    ----------          ----------
      TOTAL     198710912            1589.69

    IF THE RESTART FILE IS WRITTEN ITS LENGTH WILL BE APPROXIMATELY

                                                            WORDS     MEGABYTES
                                                          ---------   ---------
     WRITTEN IN THE ANALYSIS PREPROCESSOR                  1894923       15.16
     PLUS WRITTEN AT THE BEGINNING OF EACH STEP             568869        4.55
     PLUS FOR EACH INCREMENT WRITTEN TO THE RESTART FILE  10625417       85.00

**
*PREPRINT, MODEL=NO, HISTORY=NO, ECHO=NO
**
*PHYSICAL CONSTANTS, ABSOLUTE ZERO=-273.15
**
*RESTART, WRITE, FREQUENCY=1
**
**************************************************************************
** Define nodes and elements
**************************************************************************
**
*NODE, INPUT=MSF_STR_NODES, SYSTEM=R
**
*ELEMENT, TYPE=C3D8, ELSET=FILM_15, INPUT=MSF_STR_ELMS_FILM_15
**
*ELEMENT, TYPE=C3D8, ELSET=SUBSTRAT, INPUT=MSF_STR_ELMS_SUBSTRAT
**
**************************************************************************
** Minimize the wavefront
**************************************************************************
**
*WAVEFRONT MINIMIZATION, NODES, METHOD=2
    795,   38052
**
**************************************************************************
** Define properties of solid elements
**************************************************************************
**
*SOLID SECTION, ELSET=SUBSTRAT, MATERIAL=ALUMINA
          1.,
**
*SOLID SECTION, ELSET=FILM_15, MATERIAL=COPPER
          1.,
**
**************************************************************************
** Define elasto-plastic properties of materials
**************************************************************************
**
*MATERIAL, NAME=COPPER
**
*DENSITY
      0.00896,
**
*ELASTIC, TYPE=ISO
**
** Yield stress:       69 MPa (annealed)
** Yield stress:      287 MPa (strained)
** Tensile strength:  235 MPa (annealed)
**
**  Young’s Modulus  Poisson's ratio   Temperature
      129000.,         0.343,                20.
      111000.,         0.343,              400.
       95100.,         0.343,              600.
       65000.,         0.343,              950.
*PLASTIC
       69,     0.0
      100,     0.0196
      172,     0.0500
      200,     0.0733
      236,     0.1000
      300,     0.1500
**
*EXPANSION, TYPE=ISO, ZERO=20.
    1.661E-5,         20.
    1.718E-5,        100.
    1.845E-5,        300.
    1.915E-5,        500.
    2.072E-5,        700.
    2.250E-5,        900.
    2.410E-5,       1100.
**
```

```
*MATERIAL, NAME=ALUMINA
**
*DENSITY
    0.00382,
**
*ELASTIC, TYPE=ISO
**
**  Young's Modulus  Poisson's ratio   Temperature
     340000.,          0.238,             0.
     333000.,          0.241,           200.
     325000.,          0.242,           400.
     316000.,          0.248,           600.
     308000.,          0.25,            800.
**
*EXPANSION, TYPE=ISO, ZERO=20.
      6.0E-6,         20.
      6.4E-6,        100.
      7.1E-6,        200.
      7.8E-6,        300.
      8.2E-6,        400.
      8.4E-6,        500.
      8.6E-6,        600.
      9.4E-6,        800.
      9.8E-6,       1000.
     1.01E-5,       1200.
     1.03E-5,       1400.
**
*******************************************************************************
** Define node set
*******************************************************************************
**
*NSET, NSET=ALLNODES, GENERATE
  1, 57408
**
*NSET, NSET=FIX_Z
   132,  135,  144,  279,  282,  285,  444,  447,  450,  459,  588,
   591,  732,  735,  744,  801
**
*NSET, NSET=FIX_YZ
   13252
**
*NSET, NSET=FIX_Y
   101,   102,   123,   124,   125,   812,   813,   814,   823,   824,   825,
   826,   847,   848,  4605,  4606,  4625,  5111,  5118,  5119,  5120,  5133,
  5134,  5141,  5142,  6626,  6633,  6819,  6826,  6986,  7174,  7642, 13245,
 13246, 13247, 13248, 13249, 13250, 13251, 13253, 13254, 13255, 13256, 13257,
 13258, 13259, 13260, 13261, 13262, 13263, 13264, 13265, 13266, 13267, 13268,
 13269, 13518, 13519, 13520, 13521, 13522, 13523, 13524, 13525, 13526, 13527,
 13528, 13529, 13530, 13531, 13532, 13533, 13583, 13584, 13586, 13587, 13588,
 13589, 13590, 13594, 13595, 13596, 13597, 13598, 13599, 13600, 13601, 13602,
 13603, 13604, 13605, 13606, 13607, 13608, 13609, 13610, 13611, 13612, 13613,
 13614, 13615, 14125, 14130, 14229, 14234, 14239, 14244, 14249, 14254, 14259,
 14264, 14269, 14276, 14281, 14286, 14291, 14296, 14301, 14306, 14311, 15051,
 15052, 15053, 15054, 15055, 15056, 15065, 15066, 15067, 15068, 15069, 15070,
 15071, 15072, 15100, 15101, 15102, 15103, 15104, 15105, 15106, 15107, 15153,
 15154, 15155, 15156, 15157, 15158, 15159, 15160, 15209, 15210, 15211, 15212,
 15213, 15214, 15215, 15216, 15283, 15284, 15285, 15286, 15287, 15288, 15289,
 15290, 15345, 15346, 15347, 15348, 15349, 15350, 15351, 15352, 15441, 15442,
 15443, 15444, 15445, 15446, 15447, 15448, 15513, 15514, 15515, 15516, 15517,
 15518, 15519, 15520, 22127, 22167, 22172, 22177, 22182, 22187, 22192, 22197,
 22202, 23282, 23288, 23294, 23300, 23306, 23312, 23318, 23324, 23330, 23336,
 23342, 23348, 23354, 23360, 23366, 23372, 23378, 23384, 23390, 23396, 23402,
 23408, 23414, 23420, 23426, 23432, 23438, 23444, 23450, 23456, 23462, 23468,
 23474, 23480, 23486, 23492, 23498, 23504, 23510, 23516, 26503, 26504, 26505,
 26506, 26507, 26508, 26539, 26545, 26551, 26557, 26563, 26569, 29492, 29493,
 29494, 29495, 29496, 29497, 29498, 29499, 29500, 29501, 29502, 29527, 29528,
 29529, 29530, 29531, 29532, 29551, 29552, 29553, 29554, 29555, 29556, 29587,
 29588, 29589, 29590, 29591, 29592, 29641, 29642, 29643, 29644, 29645, 29646,
 29677, 29678, 29679, 29680, 29681, 29682, 29743, 29744, 29745, 29746, 29747,
 29748, 29790, 29796, 29803, 29810, 29817, 29823, 29829, 29835, 29842, 29849,
 29856, 29862, 29868, 29874, 29881, 29888, 29895, 29901, 29907, 29913, 29920,
 29927, 29934, 29940, 37613, 37724, 37725, 37726, 37727, 37728, 37729, 38000,
 38040, 38045, 38050, 38055, 38060, 38065, 38070, 38075, 38558, 38564, 38570,
 38576, 38582, 38588, 38594, 38600, 38606, 38612, 38618, 38624, 38630, 38636,
 38642, 38648, 38654, 38660, 38666, 38672, 38678, 38684, 38690, 38696, 38702,
 38708, 38714, 38720, 38726, 38732, 38738, 38744, 38750, 38756, 38762, 38768,
 38774, 38780, 38786, 38792, 40197, 40203, 40209, 40215, 40221, 40302, 40303,
 40304, 40305, 40306, 40312, 40318, 40325, 40332, 40339, 40345, 40351, 40358,
 40365, 40372, 40378, 40384, 40391, 40398, 40405, 40411, 40417, 40424, 40431,
 40438, 41191, 41210, 41252, 41319, 41320, 41321, 41322, 41323, 41324, 41325,
 41326, 44251, 44252, 44253, 44254, 44255, 50312, 50320, 50360, 50365, 50370,
 50375, 50380, 50385, 50390, 50395, 50400, 50405, 50410, 50415, 50420, 50425,
 50430, 50435, 51052, 51053, 51054, 51055, 51056, 51057, 51058, 51059, 51087,
 51088, 51089, 51090, 51091, 51092, 51093, 51094, 51140, 51141, 51142, 51143,
 51144, 51145, 51146, 51147, 51196, 51197, 51198, 51199, 51200, 51201, 51202,
```

```
 51203, 51270, 51271, 51272, 51273, 51274, 51275, 51276, 51277, 51332, 51333,
 51334, 51335, 51336, 51337, 51338, 51339, 51428, 51429, 51430, 51431, 51432,
 51433, 51434, 51435, 56513, 56514, 56515, 56516, 56517, 56538, 56539, 56540,
 56541, 56542, 56558, 56559, 56560, 56561, 56562, 56588, 56589, 56590, 56591,
 56592, 56633, 56634, 56635, 56636, 56637, 56663, 56664, 56665, 56666, 56667,
 56718, 56719, 56720, 56721, 56722
**
*NSET, NSET=FIX_XY
    6625, 6625, 37612, 37612, 41187, 41187, 50311, 50311
**
*NSET, NSET=FIX_X
  6621,  6623,  6627,  6662,  6664,  6666,  6706,  6708,  6710,  6712,  6748,
  6750,  6788,  6790,  6792,  6809, 37582, 37583, 37584, 37585, 37586, 37587,
 37588, 37589, 37590, 37591, 37592, 37593, 37594, 37595, 37596, 40900, 40901,
 40902, 40903, 40904, 40905, 40906, 40907, 40908, 40909, 40910, 40911, 40912,
 40913, 40914, 40915, 40916, 50281, 50282, 50283, 50284, 50285, 50286, 50287,
 50288, 50289, 50290, 50291, 50292, 50293, 50294, 50295
**
******************************************************************************
** Initial conditions
******************************************************************************
**
*INITIAL CONDITIONS, TYPE=TEMPERATURE
  ALLNODES,   20.0
**
******************************************************************************
** Step 1 - THERMAL STRESS ANALYSIS: TEMPERATURE CHANGE: 20 --> T=101 deg
******************************************************************************
**
*STEP, AMPLITUDE=RAMP, INC=100
**
*STATIC
   1.0,       1.0
**
******************************************************************************
** Read temperatures at nodes
******************************************************************************
**
*TEMPERATURE, INPUT=y_fine_101.con
**
******************************************************************************
** Fix model in space
******************************************************************************
**
** fix_left_side_xx0
**
*BOUNDARY, OP=NEW
    FIX_Z, 3,,      0.
**
** fix_left_side_x00
**
*BOUNDARY, OP=NEW
    FIX_YZ, 2,3,    0.
**
******************************************************************************
** Fix model on symmetry planes
******************************************************************************
**
** fix_bottom_side_x0x
**
*BOUNDARY, OP=NEW
    FIX_Y, 2, ,     0.
**
** fix_symmetry_line_00x
**
*BOUNDARY, OP=NEW
    FIX_XY, 1,2,    0.
**
** fix_right_side_0xx
**
*BOUNDARY, OP=NEW
   FIX_X, 1, ,      0.
**
******************************************************************************
** Request output
******************************************************************************
**
*NODE PRINT, FREQ=0
U, CF
*NODE FILE, FREQ=0
U, CF
**
*EL PRINT, POSITION=INTEGRATION POINT, FREQ=0
S, E
*EL FILE, POSITION=INTEGRATION POINT, FREQ=0
```

```
S, E
**
*EL PRINT, POSITION=NODES, FREQ=0
S
*EL PRINT, FREQ=0
NFORC
*EL FILE, POSITION=NODES, FREQ=0
*EL FILE, FREQ=0
NFORC
**
*EL PRINT, POSITION=CENTROIDAL, FREQ=0
ENER
ELEN
*EL FILE, POSITION=CENTROIDAL, FREQ=0
ENER
ELEN
**
*EL PRINT, POSITION=AVERAGED AT NODES, FREQ=0
**
*EL FILE, POSITION=AVERAGED AT NODES, FREQ=0
**
*MODAL PRINT, FREQ=0
**
*MODAL FILE, FREQ=0
**
*ENERGY PRINT, FREQ=0
**
*ENERGY FILE, FREQ=0
**
*PRINT, FREQ=0
**
*END STEP
**
******************************************************************************
** Step 2 - THERMAL STRESS ANALYSIS: T=101 --> T=83 deg
******************************************************************************
**
*STEP, AMPLITUDE=RAMP, INC=100
**
*STATIC
   1.0,     1.0
**
******************************************************************************
** Read temperatures at nodes
******************************************************************************
**
*TEMPERATURE, INPUT=y_fine_83.con
**
******************************************************************************
** Fix model in space
******************************************************************************
**
** fix_left_side_xx0
**
*BOUNDARY, OP=NEW
    FIX_Z,  3,,     0.
**
** fix_left_side_x00
**
*BOUNDARY, OP=NEW
    FIX_YZ, 2,3,    0.
**
******************************************************************************
** Fix model on symmetry planes
******************************************************************************
**
** fix_bottom_side_x0x
**
*BOUNDARY, OP=NEW
    FIX_Y, 2, ,     0.
**
** fix_symmetry_line_00x
**
*BOUNDARY, OP=NEW
    FIX_XY, 1,2,    0.
**
** fix_right_side_0xx
**
*BOUNDARY, OP=NEW
   FIX_X, 1, ,      0.
**
******************************************************************************
** Request output
******************************************************************************
**
```

```
*NODE PRINT, FREQ=0
U, CF
*NODE FILE, FREQ=0
U, CF
**
*EL PRINT, POSITION=INTEGRATION POINT, FREQ=0
S, E
*EL FILE, POSITION=INTEGRATION POINT, FREQ=0
S, E
**
*EL PRINT, POSITION=NODES, FREQ=0
S
*EL PRINT, FREQ=0
NFORC
*EL FILE, POSITION=NODES, FREQ=0
*EL FILE, FREQ=0
NFORC
**
*EL PRINT, POSITION=CENTROIDAL, FREQ=0
ENER
ELEN
*EL FILE, POSITION=CENTROIDAL, FREQ=0
ENER
ELEN
**
*EL PRINT, POSITION=AVERAGED AT NODES, FREQ=0
**
*EL FILE, POSITION=AVERAGED AT NODES, FREQ=0
**
*MODAL PRINT, FREQ=0
**
*MODAL FILE, FREQ=0
**
*ENERGY PRINT, FREQ=0
**
*ENERGY FILE, FREQ=0
**
*PRINT, FREQ=0
**
*END STEP
```

Appendix F. Computer Hardware & CAD Software Used for the Project

Computer Hardware

Platform	Sun Ultra 10
RAM	128 MB
DISK RAM	6 GB

Computer Software

Operating system	Sun Solaris 2.6
FE solver	ABAQUS, ver.5.6
Pre-processor	PATRAN, ver.8.0
Post-processor	ABAQUS Post, ver.5.6

Appendix G. Properties of Materials Used in the Study

UNITS: mm; deg. C; sec.; kg; Newton; Joule; Ampere

Electrical And Thermal Properties

```
----------------------------------------
SILVER
----------------------------------------

*MATERIAL, NAME=SILVER
**
** Melting point  961 deg C
** Boiling point 2200 deg C
**
*DENSITY
   10.50E-6,   20.
**
** Following values for the liquid state
    9.35E-6,  961.
**
*CONDUCTIVITY, TYPE=ISO
    0.453,      0.
    0.428,     20.
    0.419,    100.
    0.377,    500.
**
** Following values for the liquid state
    0.175,    961.
    0.176,   1000.
    0.181,   1100.
    0.185,   1200.
    0.189,   1300.
    0.193,   1400.
**
*ELECTRICAL CONDUCTIVITY
  61.73E03,      0.
  59.04E03,     20.
  35.10E03,    200.
  21.10E03,    500.
  13.79E03,    962.
**
** Following values for the liquid state
    6.3E03,    965.
    5.68E3,   1000.
    5.43E3,   1100.
    5.5E03,   1130.
    5.18E3,   1200.
    4.95E3,   1300.
    4.74E3,   1400.
**
*SPECIFIC HEAT
    232.0,      0.
    232.6,     20.
    235.2,    100.
    238.5,    200.
    248.2,    500.
**
** Following values for the liquid state
    263.2,    962.
    283.0,   1100.
    283.0,   1200.
    283.0,   1300.
**

----------------------------------------
COPPER
----------------------------------------

*MATERIAL, NAME=COPPER
**
** Melting point 1085 deg C
** Boiling point 2560 deg C
**
*DENSITY
    8.89E-6,    0.
    8.84E-6,  100.
    8.80E-6,  200.
    8.65E-6,  500.
    8.48E-6,  800.
**
** Following values for the liquid state
    8.00E-6, 1083.
**
*CONDUCTIVITY, TYPE=ISO
    0.403,      0.
    0.401,     25.
    0.395,    100.
    0.389,    200.
    0.341,    538.
    0.244,   1037.
    0.230,   1082.
**
** Following values for the liquid state
    0.166,   1083.
    0.170,   1200.
    0.176,   1400.
    0.180,   1600.
**
*ELECTRICAL CONDUCTIVITY
  62.89E03,      0.
  43.86E03,    100.
  33.56E03,    200.
  19.30E03,    500.
  13.28E03,    800.
  10.91E03,   1000.
  10.12E03,   1082.
**
** Following values for the liquid state
   5.00E03,   1083.
   4.72E03,   1200.
   4.29E03,   1400.
   3.95E03,   1600.
**
*SPECIFIC HEAT
    380,      0.
    382,     20.
    393,    100.
    406,    200.
    446,    500.
    519,    962.
**

----------------------------------------
BRASS
----------------------------------------

*MATERIAL, NAME=BRASS
**
** Melting point 900-965 deg C,
depending on Cu-Zn composition
** Boiling point      deg C
**
*DENSITY
    8.55E-6,   20
**
*CONDUCTIVITY, TYPE=ISO
    0.103,      0.
    0.101,     25.
    0.099,    100.
    0.097,    200.
    0.085,    538.
    0.061,   1010.
**
*ELECTRICAL CONDUCTIVITY
  20.12E03,      0.
  19.42E03,     20.
  17.00E03,    100.
```

```
  14.62E03,    200.
  10.06E03,    500.
   7.46E03,    800.
   6.29E03,   1000.
**
*SPECIFIC HEAT
**
    360,      0.
    385,     20.
    487,    100.
    616,    200.
   1017,    500.
   1728,   1000.
**

----------------------------------------
ALUMINIUM
----------------------------------------

*MATERIAL, NAME=AL
**
** Melting point   660.37 deg C
** Boiling point  2520    deg C
**
*DENSITY
   2.7E-06,    25
**        ,   100
**        ,   200
**        ,   500
**
** Following values for the liquid state
   2.38E-6,   660.
**
*CONDUCTIVITY, TYPE=ISO
    0.236,       0.
    0.237,      27.
    0.240,     100.
    0.240,     127.
    0.237,     227.
    0.232,     327.
    0.226,     427.
    0.220,     527.
    0.213,     627.
**
** Following values for the liquid state
    0.094,     660.
    0.095,     727.
    0.099,     800.
    0.102,     900.
    0.105,    1000.
**
*ELECTRICAL CONDUCTIVITY
  41.37E03,      0.
  37.73E03,     20.
  36.91E03,     25.
  36.59E03,     27.
  25.84E03,    127.
  20.04E03,    227.
  16.31E03,    327.
  13.60E03,    427.
  11.49E03,    527.
   9,82E03,    627.
**
** Following values for the liquid state
   4.13E03,    660.
   4.03E03,    700.
   3.80E03,    800.
   3.60E03,    900.
   3.42E03,   1000.
**
*SPECIFIC HEAT
    897,         0.
    900,        20.
    938,       100.
    984,       200.
   1030,       300.
   1076,       400.
**
** Following values for the liquid state
   1080,       660.
   1080,       900.
**

----------------------------------------
MOLYBDENUM
----------------------------------------

*MATERIAL, NAME=MOLYBDENUM
**
** Melting point 2615 deg C
** Boiling point 4610 deg C
**
*DENSITY
     13.54E-6,    25.
**
** Following values for the liquid state
     9.34E-06,  2617.
**
*CONDUCTIVITY, TYPE=ISO
    0.139,       0.
    0.138,      27.
    0.135,     100.
    0.121,     500.
    0.110,    1000.
    0.082,    1500.
    0.073,    1750.
    0.070,    2000.
**
*ELECTRICAL CONDUCTIVITY
  20.62E03,      0.
  18.73E03,     20.
  18.28E03,     25.
  18.11E03,     27.
  12.47E03,    127.
   9.43E03,    227.
   7.63E03,    327.
   6.32E03,    427.
   5.43E03,    527.
   4.72E03,    627.
   1.65E03,   2607.
**
*SPECIFIC HEAT
    240.,       0.
    247.,      20.
    260.,     100.
    285.,     500.
    298.,     750.
    310.,    1000.
    375.,    1500.
    450.,    2000.
    535.,    2500.
    570.,    2607.
**

----------------------------------------
TITANIUM
----------------------------------------

*MATERIAL, NAME=TITANIUM
**
** Melting point 1667 deg C
** Boiling point 3285 deg C
**
*DENSITY
    4.5E-6,     25.
**
** Following values for the liquid state
    4.11E-6,  1685.
**
*CONDUCTIVITY, TYPE=ISO
    0.016,      20.
    0.015,     100.
    0.015,     200.
    0.014,     400.
    0.013,     600.
    0.013,     800.
**
*ELECTRICAL CONDUCTIVITY
   1.85E03,     20.
   1.43E03,    100.
   1.14E03,    200.
   0.84E03,    400.
   0.66E03,    600.
   0.61E03,    800.
**
** Following values for the liquid state
   0.58E03,   1685.
**
*SPECIFIC HEAT
    519.,      20.
```

```
    540.,     100.
    569.,     200.
    619.,     400.
    636.,     600.
    682.,     800.
**
** Following values for the liquid state
    700.,    1685.
**

----------------------------------------
ALUMINA
----------------------------------------

** ALUMINA
**
** Nominal Al2O3 content 96.5-99.0 %
**
*MATERIAL, NAME=ALUMINA
**
*DENSITY
     3.75E-6,
**
*CONDUCTIVITY, TYPE=ISO
    0.0250,        20.
    0.0200,       100.
    0.0150,       200.
    0.0100,       400.
    0.0081,       600.
    0.0071,       800.
    0.0069,      1000.
    0.0064,      1200.
**
*SPECIFIC HEAT
      780,         25.
      911,        100.
     1023,        200.
     1175,        500.
**


----------------------------------------
PYREX
```

```
----------------------------------------

*MATERIAL, NAME=PYREX
**
** Softening point: 825 deg.C
**
*DENSITY
   0.223E-06,    20.
**
*CONDUCTIVITY, TYPE=ISO
**
    0.00112,      0.
    0.00129,    100.
**
*SPECIFIC HEAT
** mean heat capacity 25-175 deg.C
     850.,       20.
**

----------------------------------------
QUARTZ SAND
----------------------------------------

*MATERIAL, NAME=QSAND
**
*DENSITY
   1.8E-6,     20.
**
*CONDUCTIVITY, TYPE=ISO
  0.00078,     27.
  0.00073,    127.
  0.00070,    227.
  0.00066,    327.
  0.00061,    427.
  0.00057,    527.
  0.00051,    627.
  0.00048,    727.
  0.00045,    827.
  0.00043,    927.
**
*SPECIFIC HEAT
       1176.,
**
```

Mechanical Properties

```
----------------------------------------
SILVER
----------------------------------------

*MATERIAL, NAME=SILVER
**
*DENSITY
      0.0105,
**
*ELASTIC, TYPE=ISO
**
**    Young's   Poisson's   Temperature
**    modulus   ratio
      80000.,       0.37,           20.
      66700.,       0.37,          400.
      35300.,       0.37,          960.
**
*EXPANSION, TYPE=ISO, ZERO=20.
    1.862E-5,         20.
    1.945E-5,        100.
    2.050E-5,        300.
    2.158E-5,        500.
    2.400E-5,        700.
    2.650E-5,        900.
    2.785E-5,       1000.
**

----------------------------------------
COPPER
----------------------------------------

*MATERIAL, NAME=COPPER
**
```

```
*DENSITY
    0.00896,   20.
**
*ELASTIC, TYPE=ISO
**
** Yield stress:
**  69 N/mm2 at 20 deg.C (annealed)
** 287 N/mm2 at 20 deg.C (strained)
**
** Tensile strength:
** 235 N/mm2 at 20 deg.C (annealed)
**
** Following data for Annealed copper
**
**    Young's   Poisson's   Temperature
**    modulus   ratio
    129000.,      0.343,         20.
    111000.,      0.343,        400.
     95100.,      0.343,        600.
     65000.,      0.343,        950.
**
*PLASTIC
       69,     0.0
      100,     0.0196
      172,     0.0500
      200,     0.0733
      236,     0.1000
      300,     0.1500
**
*EXPANSION, TYPE=ISO, ZERO=20.
    1.661E-5,         20.
    1.718E-5,        100.
    1.845E-5,        300.
```

```
    1.915E-5,        500.
    2.072E-5,        700.
    2.250E-5,        900.
    2.410E-5,       1100.
**

----------------------------------------
MOLYBDENUM
----------------------------------------

*MATERIAL, NAME=MO
**
*DENSITY
      0.01022,
**
*ELASTIC, TYPE=ISO
**
** Yield stress, Temperature, deg C
**      438.0,               26.
**      345.0,              870.
**       58.8,             1065.
**
** (fused, hot-rolled and annealed
** at 1230 deg C)
**
**   Young's   Poisson's   Temperature
**   modulus   ratio
    320000.,      0.293,          20.
    280000.,      0.293,         500.
    220000.,      0.293,        1000.
    150000.,      0.293,        1250.
**
*EXPANSION, TYPE=ISO, ZERO=20.
     6.3E-6,        20.
     6.6E-6,       700.
     6.9E-6,      1500.
    11.1E-6,      2500.
**

----------------------------------------
TUNGSTEN
----------------------------------------

*MATERIAL, NAME=W
**
*DENSITY
      0.0193,
**
*ELASTIC, TYPE=ISO
**
**   Young's   Poisson's   Temperature
**   modulus   ratio
**
    411000.,       0.28,         20.
**         ,       0.28,        500.
**         ,       0.28,       1000.
**         ,       0.28,       1250.
**
*EXPANSION, TYPE=ISO, ZERO=20.
     4.5E-6,        20.
     4.5E-6,       100.
     4.6E-6,       500.
     4.6E-6,      1000.
     5.4E-6,      2000.
     6.6E-6,      3000.
**

----------------------------------------
TITANIUM
----------------------------------------

*MATERIAL, NAME=Ti
**
*DENSITY
      0.0045,
**
*ELASTIC, TYPE=ISO
**
**   Young's   Poisson's   Temperature
**   modulus   ratio
**
    120200.,      0.361,          20.
**         ,      0.361,         500.
**         ,      0.361,        1000.
**         ,      0.361,        1250.
```

```
**
*EXPANSION, TYPE=ISO, ZERO=20.
     8.8E-6,        20.
     8.8E-6,       100.
     9.1E-6,       200.
     9.4E-6,       400.
     9.7E-6,       600.
     9.9E-6,       800.
**         ,      3000.
**

----------------------------------------
ALUMINIUM
----------------------------------------

*MATERIAL, NAME=AL
**
*DENSITY
      0.0027,
**
*ELASTIC, TYPE=ISO
**
**   Young's   Poisson's   Temperature
**   modulus   ratio
**
      70600,      0.345,          20.
**         ,      0.345,         500.
**         ,      0.345,        1000.
**         ,      0.345,        1250.
**
*EXPANSION, TYPE=ISO, ZERO=20.
     2.35E-5,       20.
     2.39E-5,      100.
     2.43E-5,      200.
     2.53E-5,      300.
     2.65E-5,      400.
**         ,       700.
**         ,      1500.
**         ,      2500.
**

----------------------------------------
MAGNESIUM
----------------------------------------

*MATERIAL, NAME=Mg
**
*DENSITY
      0.01022,
**
*ELASTIC, TYPE=ISO
**
**   Young's   Poisson's   Temperature
**   modulus   ratio
**
      44700,      0.291,          20.
**         ,      0.291,         500.
**         ,      0.291,        1000.
**         ,      0.291,        1250.
**
*EXPANSION, TYPE=ISO, ZERO=20.
     2.61E-5,       20.
     2.61E-5,      100.
     2.70E-5,      200.
     2.80E-5,      300.
     2.89E-5,      400.
**         ,       700.
**         ,      1500.
**         ,      2500.
**

----------------------------------------
GOLD
----------------------------------------

*MATERIAL, NAME=Au
**
*DENSITY
      0.0193,
**
*ELASTIC, TYPE=ISO
**
**   Young's   Poisson's   Temperature
**   modulus   ratio
**
```

```
     78500,       0.42,          20.
**        ,       0.42,         500.
**        ,       0.42,        1000.
**        ,       0.42,        1250.
**
*EXPANSION, TYPE=ISO, ZERO=20.
    1.42E-5,        20.
    1.42E-5,       100.
    1.52E-5,       500.
    1.67E-5,       900.
**

----------------------------------------
ALUMINA
----------------------------------------

*MATERIAL, NAME=ALUMINA
**
*DENSITY
    0.00382,
**
*ELASTIC, TYPE=ISO
**
**   Young's   Poisson's   Temperature
**   modulus   ratio
**
    340000.,      0.238,           0.
    333000.,      0.241,         200.
    325000.,      0.242,         400.
    316000.,      0.248,         600.
    308000.,      0.250,         800.
**
*EXPANSION, TYPE=ISO, ZERO=20.
      6.0E-6,        20.
      6.4E-6,       100.
      7.1E-6,       200.
      7.8E-6,       300.
      8.2E-6,       400.
      8.4E-6,       500.
      8.6E-6,       600.
      9.4E-6,       800.
      9.8E-6,      1000.
     1.01E-5,      1200.
     1.03E-5,      1400.
**

----------------------------------------
PYREX
----------------------------------------

*MATERIAL, NAME=PYREX
**
*DENSITY
    0.00223,
**
*ELASTIC, TYPE=ISO
**
**   Young's   Poisson's   Temperature
**   modulus   ratio
**
     64000.,        0.20,        20.
     65700.,        0.20,       100.
     66800.,        0.20,       200.
     67800.,        0.20,       300.
     68300.,        0.20,       400.
**         ,            ,       600.
**         ,            ,       800.
**
*EXPANSION, TYPE=ISO, ZERO=20.
**
** Average linear thermal
** expansion 20-350 deg C
      3.3E-6,        20.
      3.3E-6,       350.
**          ,       400.
**          ,       500.
**          ,       600.
**
```